

MECHANISTIC INVESTIGATIONS AND THE DEVELOPMENT OF NEW
TRANSFORMATIONS IN ACRIDINIUM-MEDIATED PHOTOREDOX CATALYSIS

Nathan Ariel Romero

A dissertation submitted to the faculty of The University of North Carolina at Chapel Hill in partial fulfillment of the requirements for the degree of Doctor of Philosophy in the Department of Chemistry.

Chapel Hill
2017

Approved by:

David A. Nicewicz

Jeffrey S. Johnson

Erik J. Alexanian

Jillian L. Dempsey

Thomas J. Meyer

© 2017
Nathan Ariel Romero
ALL RIGHTS RESERVED

ABSTRACT

Nathan Ariel Romero: Mechanistic Investigations and the Development of New Transformations in Acridinium-Mediated Photoredox Catalysis
(Under the direction of David A. Nicewicz)

Photoredox catalysis has rapidly expanded to become an indispensable tool for synthetic chemists. Recent developments in this field have demonstrated the potential for photoredox systems to activate normally unreactive substrates and leverage reactivity that cannot be accessed in classical two-electron pathways. Organic chromophores offer particular advantages over their transition metal counterparts, and an introduction to the principles of photoredox catalysis and the properties of common organic photoredox catalysts is provided. Given the importance of solution phase redox potentials in selecting successful catalyst/substrate combinations, we have utilized computational methods to predict redox potentials for a large set of representative organic compounds, demonstrating the predictive power of the computational approach by comparing the calculated redox potential values with experimentally measured potentials.

The Nicewicz laboratory has made use of acridinium-based photoredox catalysts to accomplish the anti-Markovnikov addition of a number of nucleophiles to alkenes, and these systems were thought to rely on the cooperative activity of the acridinium catalyst and a redox active hydrogen atom donor. An in-depth investigation of the proposed mechanism illuminated key photophysical properties of the acridinium catalyst and confirmed the feasibility of a crucial mechanistic step that unites the activity of the co-catalysts.

Observations in the course of this inquiry prompted us to design more robust acridinium catalysts, one of which was employed the development of a photoredox catalytic aryl C-H amination reaction. This methodology features the use of a nitroxyl radical co-catalyst and oxygen to achieve the net oxidative transformation, which furnishes aryl amines with high site-selectivity. An array of arene/amine combinations were shown to undergo the aryl amination reaction, demonstrating the value of this protocol in generating diverse libraries of functionalized arenes. Kinetic analysis of the reaction manifold revealed that product inhibition is a significant mechanistic factor. This observation could inform strategies to improve the efficiency of the reaction and expand the substrate scope beyond current limitations.

ACKNOWLEDGEMENTS

I am thankful for the opportunity to have studied at UNC-Chapel Hill. This department is filled with wonderful people and excellent scientists, from whom I am continually learning. In particular, I thank the faculty serving on my dissertation committee. Thank you to Jeff Johnson for your eloquence, your support of my career, and for your leadership in this department and as chair of committee. Thank you to Jillian Dempsey for offering insight and instruments as I sought to learn about photophysics and spectroscopy. Thank you to Erik Alexanian for your input and enthusiasm which propelled us to publish our aryl amination work. Thank you to Tom Meyer for laying the ground work and establishing a research program that has made much of my graduate work possible. I also thank Kyle Brennaman for your invaluable training and as a resource on photophysics, and Simon Meek for your service on my preliminary oral defense committee.

I am sincerely grateful to Dave Nicewicz for providing the space and resources for the opportunity to be part of an exciting research program. Thank you for the freedom and encouragement to exercise my creativity, for your support and interest in my career, and for your example as a leader who is always eager to learn. I look forward to learning more from you in the coming years. I am also thankful for all members of the Nicewicz Lab, past and present. Each one of you has taught me something, and I thank you for your patience, leadership, perspective, solidarity, and comic relief.

I am thankful for all of my teachers, particularly the faculty at Calvin College who taught me to think critically, to ponder beauty, and to embrace the world on every scale. I cannot

sufficiently thank Prof. Carolyn Anderson for her mentorship, which has propelled me forward at every turn in my education in science. Thank you for teaching me to be an organic chemist, and for challenging me to be great. Even more, thank you for your empathy, your belief in me, and for being a leader that I will always look up to.

I give my deepest thanks to my family for their patience and support. Thank you to my parents, Omar and Sherry, for the sacrifices and commitment to education you have made to bring me to this point. Most of all, thank you for being wonderful people that have enabled me to think for myself, for celebrating creativity, for working diligently, for listening carefully, and for sharing your desire to never stop learning.

To the joy of my life, Gillian, you have given all of this meaning. Your patience, encouragement, and belief in me are more than I deserve. I am humbled to learn from you for the rest of my life. Thank you.

In honor of my grandparents
Domingo and Mercedes Romero
Donald and Helen Van Beek
The memory of your leadership, commitment to excellence,
service, self-sacrifice, and steadfast love
will never stop inspiring me.

TABLE OF CONTENTS

LIST OF FIGURES	xiii
LIST OF SCHEMES.....	xviii
LIST OF TABLES	xx
LIST OF ABBREVIATIONS AND SYMBOLS	xxiii
CHAPTER 1: Organic Photoredox Catalysis.....	1
1.1 Introduction.....	1
1.1.1 Background and Importance	1
1.1.2 Why Organic Photoredox Catalysts?	2
1.2 Photophysical and Electrochemical Considerations	3
1.2.1 Photophysical Processes	3
1.2.2 Photophysical Properties of Organic Photoredox Catalysts	5
1.2.3 Electrochemistry: Thermodynamics of Electron Transfer and Photoinduced Electron Transfer.....	13
1.3 General Mechanistic Schemes for Photoredox Catalysis	17
1.3.1 Definitions.....	19
1.3.2 Other Mechanistic Considerations	20
CHAPTER 2: Experimental and Calculated Electrochemical Potentials of Common Organic Molecules for Applications to Single-Electron Redox Chemistry	25
2.1 Background: literature precedent and considerations for computational prediction of redox potentials	25

2.2	Results and discussion: Calculation of solution phase redox potentials using Density Functional Theory (DFT)	26
2.3	Associated Content	29
2.4	Acknowledgments.....	29
CHAPTER 3: Mechanistic Insight into the Photoredox Catalysis of Anti-Markovnikov Alkene Hydrofunctionalization Reactions		30
3.1	Introduction.....	30
3.2	Results and Discussion	34
3.2.1	Oxidative Activity of Excited State Mes-Acr ⁺	34
3.2.2	Role of Thiol and Disulfide Co-Catalysts.....	46
3.2.3	Preparative scale reaction kinetics	56
3.2.4	Discussion: Rate Limiting Factors.....	59
3.3	Conclusion	60
3.4	Associated Content	61
3.5	Acknowledgements.....	61
CHAPTER 4: Site-Selective Arene C-H Amination via Photoredox Catalysis.....		62
4.1	Background: Aryl C-H Functionalization.....	62
4.2	Results and Discussion: development of a photoredox-catalyzed arene C-H amination	63
4.3	Conclusion	73
4.4	Associated Content	73
4.5	Acknowledgements.....	73
CHAPTER 5: Mechanistic Studies on Acridinium-Mediated Arene C-H Amination Reactions.....		74
5.1	Introduction.....	74

5.2	Results and Discussion	75
5.2.1	Turnover of the acridinyl radical Mes-(t-Bu) ₂ Acr-Ph•	75
5.2.2	Analysis of photoredox catalyst degradation under aerobic conditions	80
5.2.3	Reaction Progress Kinetic Analysis: differentiating catalyst degradation and product inhibition	84
5.3	Conclusions	92
5.4	Associated Content	93
APPENDIX A: Supporting information for “Experimental and Calculated Electrochemical Potentials of Common Organic Molecules for Applications to Single-Electron Redox Chemistry”		
A.1	Computational Details	94
A.1.1	Geometry optimization and calculation of Gibbs free energy	94
A.1.2	Calculation of solution phase electrochemical redox potentials	94
A.1.3	Plots of experimental redox potentials compared with DFT results for the electrochemical series	97
A.1.4	Additional Statistics for Calculated Redox potentials	114
APPENDIX B: Supporting Information for “Mechanistic Insight into the Photoredox Catalysis of Anti-Markovnikov Alkene Hydrofunctionalization Reactions”		
B.1	General Information	116
B.1.1	General Methods	116
B.1.2	Materials	116
B.1.3	Synthesized Materials	117
B.2	Spectroelectrochemical Measurements	121
B.3	Electrochemical Measurements	122
B.4	Photophysical Measurements	123

B.4.1	Emission Studies.....	124
B.4.2	Stern-Volmer Analyses.....	128
B.4.3	Laser Flash Photolysis/Transient Absorption experiments.....	131
B.4.4	Studies involving Mes-Acr•.....	140
B.5	Disulfide Exchange Experiments.....	147
B.6	Reaction Progress Monitoring	151
B.6.1	Gas Chromatography: Alkenol ROH/Product/PhSH/(PhS) ₂	151
B.6.2	UV-Vis Spectroscopy: Mes-Acr ⁺ /Mes-Acr• monitoring during photolysis.....	152
B.7	Determination of Association Constant for Donor-Acceptor Complex.....	153
B.8	Determination of Quantum Yield of Reaction Using Ferrioxalate Actinometry	155
B.9	Computational Details	156
APPENDIX C: Supporting Information for “Site-Selective Arene C-H Amination via Photoredox Catalysis”		
C.1	General Information: Materials and Methods.....	170
C.1.1	Materials	170
C.1.2	General Methods.....	170
C.1.3	Photoreactor Configuration.....	172
C.2	Additional Optimization Studies.....	173
C.3	Synthetic Procedures.....	176
C.3.1	Preparation of Acridinium Photocatalysts	176
C.3.2	Preparation of Arene Substrates.....	180
C.3.3	Procedures for the Photoredox-Catalyzed Synthesis of Aryl Amines.....	186

C.4	Electrochemical Measurements	221
C.5	NMR spectra of new compounds.....	224
APPENDIX D: Supporting Information for Mechanistic Studies on Acridinium-Mediated Arene C-H Amination Reactions		225
D.1	Materials	225
D.2	Specifications for custom LED array used in test reactions and kinetics	225
D.3	Procedure for kinetic analysis of the photoredox catalyzed aryl amination reaction.....	227
D.4	Analysis of reaction mixtures by HRMS	231
D.5	Test reaction shown in Scheme 5.12.....	232
D.6	Preparation of Mes-(<i>t</i> -Bu) ₂ Acr-Ph•	232
D.7	Fluorescence quenching experiments	233
D.8	Additional Schemes and Figures	234
REFERENCES		235

LIST OF FIGURES

Figure 2.1. Plot of experimental versus calculated redox potentials for a series of organic compounds.	28
Figure 3.1. Anti-Markovnikov Hydrofunctionalization using Mes-Acr⁺ as a photoredox catalyst and PMN , PhSH , or (PhS)₂ as viable HAT catalysts.	32
Figure 3.2. Rehm-Weller Plot for k_1 as determined by Stern-Volmer analysis of Mes-Acr⁺ fluorescence quenching where $[\text{Mes-Acr}^+] = 16 \mu\text{M}$ in DCE.	38
Figure 3.3. Variable temperature fluorescence spectra of Mes-Acr⁺	41
Figure 3.4. Detection of alkenyl cation radicals by Laser Flash Photolysis.	43
Figure 3.5. Direct observation of Mes-Acr[•] turnover by PhS[•] generated during LFP with excitation at 410 nm.	50
Figure 3.6. Determination of the second order rate constant k_5 describing oxidation of Mes-Acr[•] to Mes-Acr⁺ by PhS[•]	52
Figure 3.7. Computed structures for HAT between PhSH (3.17, 3.18[‡]) or PMN (3.19, 3.20[‡]) and benzylic radical 3.4	54
Figure 3.8. Reaction progress for hydroetherification of alkenol 3.1b under conditions C or D	55
Figure 3.9. Recovery of Mes-Acr⁺ absorbance at 450 nm under dark conditions after bleaching at $t = 5$ min.	59
Figure 4.1. Blueprint for site-selective C–H amination of aromatics.	64
Figure 4.2. Reaction development. (A) Catalyst optimization and (B) proposed mechanism.	66
Figure 4.3. Reaction Scope for the C–H Amination.	69
Figure 4.4. Synthesis of Anilines Using Ammonium Salt as Ammonia Equivalent.	72
Figure 5.1. UV-Vis absorption spectrum of Mes-(<i>t</i>-Bu)₂Acr-Ph[•] (5.0×10^{-5} M in DCE) prepared by chemical reduction with CoCp₂	78

Figure 5.2. Reaction progress kinetic analysis, “same excess” experiment	85
Figure 5.3. Reaction progress kinetic analysis, “same excess + pdt ” experiment	86
Figure 5.4. Graphical rate equation for the aryl amination conditions in Scheme 5.7	89
Figure A.1. Aromatic Hydrocarbons and Alkynes	97
Figure A.2. Alkenes	98
Figure A.3. Phenols.....	100
Figure A.4. Aliphatic, Aryl, and Enol Ethers.....	101
Figure A.5. Aliphatic and Aryl Amines and Enamines	102
Figure A.6. Thiols, Sulfides, and Disulfides.....	103
Figure A.7. Aromatic Heterocycles	104
Figure A.8. Alkyl and Aryl Halides.....	105
Figure A.9. Aldehydes	106
Figure A.10. Imines, Oximes, and Hydrazones	107
Figure A.11. Carboxylic acids, Esters, and Nitriles.....	108
Figure A.12. Acyl- and Sulfonyl- Chlorides, and Anhydrides	109
Figure A.13. Amides and Carboxylates	110
Figure A.14. Ketones	111
Figure A.15. Nitro compounds, Organosilanes, Halides	112
Figure A.16. Hypervalent Iodines, nitrobenzene, and <i>N</i> -chlorosuccinimide.....	113
Figure A.17. Histograms of the difference between calculated and experimental redox potentials ($E_{\text{calc}} - E_{\text{exp}}$)	114

Figure A.18. Histograms in Figure A.17 separated into the contributions of oxidation and reduction potentials	115
Figure B.1. UV-Vis absorbance spectra collected before (red) and after (blue) bulk electrolysis at a fixed potential of -1.0 V (nominal) on a 93 μM solution of Mes-AcrBF ₄ in DCE with 0.1 M TBABF ₄ as a supporting electrolyte.....	122
Figure B.2. Cyclic voltammograms for the species examined in this study. The $E_{p/2}$ values shown on each plot referenced to Ag/AgCl in 3 M NaCl. Addition of 30 mV to this value gives the potential v. SCE.....	123
Figure B.3. Steady state absorbance spectrum (red, measured on HP 8453 spectrophotometer) and emission spectra for Mes-Acr ⁺	126
Figure B.4. Time resolved emission spectra for Mes-Acr ⁺ (50 μM , measured on LP920) normalized at 510 nm to show both LE and CT.	126
Figure B.5. Fluorescence lifetime of several 10-methyl-acridinium tetrafluoroborate salts measured at 515 nm by Time-Correlated Single Photon Counting (TCSPC).	127
Figure B.6. Raw variable temperature fluorescence spectra of Xyl-Acr ⁺ in DCE.....	127
Figure B.7. Absorbance corrected fluorescence spectra for Mes-AcrBF ₄ and AcrCl for the determination of the relative quantum yield of fluorescence (Φ_F) for Mes-Acr ⁺ in DCE.	127
Figure B.8. Fluorescence lifetime of Mes-Acr ⁺ (16 μM in DCE) measured at 515 nm at the concentrations of anethole (An) given.....	129
Figure B.9. Stern-Volmer plots of quenching of Mes-Acr ⁺ (16 μM) fluorescence lifetime for each quencher studied.....	130
Figure B.10. Transient absorption spectrum (blue) for Mes-Acr ⁺ T (50 μM in DCE) taken at 20 ns with laser excitation at 430 nm. Difference spectrum for Mes-Acr• shown as calculated from spectroelectrochemical records.	133
Figure B.11. Transient absorption kinetics for Mes-Acr ⁺ (50 μM in DCE) measured at 480 nm with laser excitation at 430 nm.....	133
Figure B.12. Detection of the β -methylstyrene cation radical by LFP of a DCE solution containing Mes-AcrBF ₄ (50 μM) and β -methylstyrene (6 mM).....	136

Figure B.13. Detection of the cation radical R-OTBDMS⁺ by LFP of a DCE solution containing Mes-AcrBF ₄ (50 μM) and R-OTBDMS (6 mM).....	137
Figure B.14. Detection of the cation radical ROH⁺ by laser flash photolysis of a DCE solution containing Mes-AcrBF ₄ (50 μM) and alkenol ROH (6 mM).....	138
Figure B.15. Dependence of transient absorption kinetics for Mes-Acr⁺ (75 μM in DCE) with βMS (6 to 24 mM) measured at 520 nm with laser excitation at 430 nm.....	139
Figure B.16. UV-Vis absorbance spectra for species relevant to Laser Flash Photolysis experiments involving Mes-Acr• oxidation.....	141
Figure B.17. Laser flash photolysis ($\lambda_{\text{ex}} = 410 \text{ nm}$, 8.0 mJ) of Mes-Acr•/CoCp₂BF₄ (50 μM) containing no (PhS) ₂	142
Figure B.18. Laser flash photolysis with (PhS) ₂ in DCE.	145
Figure B.19. Transient absorption signals at 520 nm showing consumption of Mes-Acr• at increasing rate when [Mes-Acr•] is increased.....	147
Figure B.20. Plot showing formation of mixed disulfide (4-Me-PhSSPh) under the photolytic conditions.....	149
Figure B.21. (a) Example Gas Chromatogram of an aliquot after $t = 240 \text{ min}$ (b) Example mass spectrum corresponding to 4-Me-PhSSPh	150
Figure B.22. Absorbance spectrum of 30 mM (PhS) ₂ in DCE (red) overlaid with the spectral output for the Ecoxotic LED lamp used in photolysis (blue, arbitrary units). The overlap between the traces is highlighted in gray.....	150
Figure B.23. Absorption spectra for solutions of Mes-AcrBF₄ in DCE (455 μM) with βMS . Inset shows Δ Absorbance to emphasize the shape of the new absorption.....	154
Figure B.24. Benesi-Hildebrand plot for the calculation of K_{DA} by equation B.10.....	154
Figure B.25. Relative free energies of calculated structures for H-atom transfer.	157
Figure C.1. Photoreactor configuration for aryl amination reactions	172
Figure D.1. Custom LED array with irradiation from beneath the vial	226

Figure D.2. Graphical rate analysis testing the inverse relationship between rate and [para].	229
Figure D.3. Simulated kinetics using the experimentally derived rate law (equation 5.3)	230
Figure D.4. Stern-Volmer plots of Mes-(<i>t</i>-Bu)₂Acr-Ph⁺ fluorescence quenching with the following quenchers: a) anisole and b) pdt	233

LIST OF SCHEMES

Scheme 1.1. Photophysical and Electrochemical Processes and Properties of Photoredox Catalysts	4
Scheme 1.2. Common Organic Photoredox Catalysts.....	9
Scheme 1.3. Oxidative and Reductive Quenching Cycles of a Photoredox Catalyst.....	17
Scheme 1.4. Net Redox Outcomes for Photoredox Transformations	19
Scheme 1.5. Cage Escape and Back Electron Transfer (BET) in Singlet and Triplet Radical Ion Pairs	24
Scheme 2.1. Half reactions for reduction and oxidation	26
Scheme 3.1. Proposed Mechanism for Anti-Markovnikov Hydroetherification	32
Scheme 3.2. Excited State Energy Diagram Adapted from Verhoeven ⁶⁰ and Fukuzumi ¹⁷⁸	35
Scheme 3.3. Disulfide Crossover Experiment Probing Mechanism of Disulfide Homolysis.....	47
Scheme 3.4. Chemical Reduction of Mes-Acr ⁺ and Reoxidation <i>via</i> PhS· by Laser Flash Photolysis of (PhS) ₂	49
Scheme 3.5. Proposed adduct formation between PhS ⁻ and Mes-Acr ⁺	58
Scheme 5.1. Proposed mechanism for the aryl amination (most plausible steps denoted in red)	75
Scheme 5.2. Speculative “inner-sphere” mechanism of oxidation of Mes-(<i>t</i> -Bu) ₂ Acr-Ph• by O ₂	76
Scheme 5.3. Redox chemistry, proton transfer, and HAT pathways for a) O ₂ and b) TEMPO.....	76
Scheme 5.4. Preparation of Mes-(<i>t</i> -Bu) ₂ Acr-Ph• and oxidation with O ₂	78
Scheme 5.5. Analysis of product mixtures by HRMS.....	81

Scheme 5.6. Possible degradation reactions of Mes-(<i>t</i>-Bu)₂Acr-Ph⁺ as a result of HO ₂ [•] generation	82
Scheme 5.7. Conditions for RPKA kinetic runs.....	85
Scheme 5.8. Competitive PET as the proposed origin of product inhibition.....	90
Scheme 5.9. Probe for <i>ipso</i> - substitution at the pyrazole substituent	92
Scheme A.1. Example #1: Reduction potential of benzaldehyde using B3LYP.....	95
Scheme A.2. Example #2: Oxidation potential of anisole using B3LYP.....	96
Scheme D.1. Possible pathways in the oxidative degradation of anisole.....	234

LIST OF TABLES

Table 1.1. Photophysical Properties of Organic Photoredox Catalysts.....	10
Table 1.2. Electrochemical Properties of Organic Photoredox Catalysts	11
Table 3.1. Mes-Acr ⁺ Fluorescence Quenching by Alkenes and HAT Catalysts.....	37
Table 5.1. Thermochemical properties of proposed intermediates related to the turnover of acridinyl radical Mes-(<i>t</i>-Bu)₂Acr-Ph•	77
Table 5.2. Experimental and calculated redox potentials and rates of fluorescence quenching (<i>k_q</i>) of anisole and pdt determined by Stern-Volmer analysis	91
Table A.1. Aromatic Hydrocarbons and Alkynes	97
Table A.2. Alkenes.....	98
Table A.3. Phenols	100
Table A.4. Aliphatic, Aryl, and Enol Ethers	101
Table A.5. Aliphatic and Aryl Amines, and Enamines.....	102
Table A.6. Thiols, Sulfides, and Disulfides	103
Table A.7. Aromatic Heterocycles.....	104
Table A.8. Alkyl and Aryl Halides	105
Table A.9. Aldehydes.....	106
Table A.10. Imines, Oximes, and Hydrazones.....	107
Table A.11. Carboxylic acids, Esters, and Nitriles	108
Table A.12. Acyl- and Sulfonyl- Chlorides, and Anhydrides.....	109
Table A.13. Amides and Carboxylates.....	110

Table A.14. Ketones.....	111
Table A.15. Nitro compounds, Organosilanes, Halides.....	112
Table A.16. Amides and Carboxylates.....	113
Table B.1. Disulfide exchange amounts as determined by GC-MS.....	149
Table B.2. Thermochemistry for SM-a.....	158
Table B.3. Cartesian Coordinates for SM-a.....	158
Table B.4. Thermochemistry for SM-b.....	160
Table B.5. Thermochemistry for SM-b.....	160
Table B.6. Thermochemistry for TS-a.....	162
Table B.7. Cartesian Coordinates for TS-a.....	162
Table B.8. Thermochemistry for TS-b.....	164
Table B.9. Cartesian Coordinates for TS-b.....	164
Table B.10. Thermochemistry for PDT-a.....	166
Table B.11. Cartesian Coordinates for PDT-a.....	166
Table B.12. Thermochemistry for PDT-b.....	168
Table B.13. Cartesian Coordinates for PDT-b.....	168
Table C.1. Initial Optimization.....	173
Table C.2. Alkyl Substrate Optimization.....	174
Table C.3. Aniline Synthesis Optimization.....	175
Table C.4. Electrochemical Half Peak Potentials for ($E_{p/2}$) for the arenes and select amine nucleophiles employed.....	223

Table D.1. Coefficient values used to model kinetics by equation D.1	228
---	-----

LIST OF ABBREVIATIONS AND SYMBOLS

(PhS) ₂	Diphenyl disulfide
μs	Microsecond
¹³ C NMR	Carbon-13 nuclear magnetic resonance
¹ H NMR	Proton magnetic resonance
ABS	Acrylonitrile butadiene styrene
BDE	Bond dissociation enthalpy
BDFE	Bond dissociation free energy
BET	Back electron transfer
Boc	<i>tert</i> -butyloxycarbonyl
BQ	Benzoquinone
Cp	Cyclopentadienyl
CPCM	Conductor-like polarizable continuum model
CT	Charge Transfer
DCE	1,2-Dichloroethane
DCM	Dichloromethane
DFT	Density functional theory
DHQD	Dihydroquinidine
DMA	Dimethylacetamide
DMF	Dimethylformamide
e ⁻	Electron
ε	Molar extinction coefficient
<i>E</i> *	Excited state redox potential

$E_{0,0}$	Excited state energy
$E_{1/2}$	Half-wave potential
$E_{p/2}$	Half-peak potential
EDA	Electron donor-acceptor
EnT	Energy transfer
E_p	Peak potential
ESI	Electrospray ionization
ET	Electron transfer
Et ₂ O	Diethyl ether
EtOH	Ethanol
eV	Electronvolt
\mathcal{F}	Faraday constant
Fc	Ferrocene
FID	Flame ionization detector
GC	Gas chromatography
G or ΔG	Gibbs free energy or change in gibbs free energy
H or ΔH	Enthalpy or change in enthalpy
HAT	Hydrogen atom transfer
hex	Hexyl
HRMS	High resolution mass spectrometry
$h\nu$	photon or energy of a photon
IC	internal conversion
IR	Infrared

ISC	Intersystem crossing
K	Kelvin
<i>K</i>	General symbol for equilibrium constant
<i>k</i>	General symbol for rate constant
LE	Locally excited
LED	Light emitting diode
LFP	Laser flash photolysis
LUMO	Lowest unoccupied molecular orbital
m/z	mass per charge
MCPCB	Metal core printed circuit board
MeOH	Methanol
Mes	Mesityl
MOM	Methoxymethyl
M	Molar or mol L ⁻¹
MS	Mass spectrometry
mV	Millivolt
NHE	Normal hydrogen electrode
nm	Nanometer
ns	Nanosecond
O ₂ ^{•-}	Superoxide
Ac	Acetyl
OD	Optical Density
PET	Photoinduced Electron Transfer.

PhMe	Toluene
PhSH	Thiophenol
PMN	2-Phenylmalononitrile
ps	Picosecond
PTFE	Polytetrafluoroethylene
R	Universal gas constant
RPKA	Reaction progress kinetic analysis
SCE	Saturated calomel electrode
SCRf	Self-consistent reaction field
SCRIP	Singlet contact radical [ion] pair
SHE	Standard hydrogen electrode
S _n	Singlet state (ground state: n=0; excited state n>1)
T	Temperature
TBA	Tetra <i>n</i> -butylammonium
TBDMS	<i>tert</i> -Butyl dimethylsilyl
<i>t</i> -Bu	<i>tert</i> -Butyl
TCRIP	Triplet contact radical [ion] pair
TCSPC	Time correlated single photon counting
TEMPO or TEMPO•	(2,2,6,6-Tetramethylpiperidin-1-yl)oxyl
TEMPO ⁺ or TEMPO _{onium}	2,2,6,6-Tetramethyl-1-oxopiperidin-1-ium
TEMPO-H	2,2,6,6-Tetramethylpiperidin-1-ol
TFA	Trifluoroacetic acid
T _n	Triplet state

UV-Vis	Ultraviolet-visible absorption spectroscopy
ν	Vibrational level
V	Volt
Xyl	Xylyl or 2,6-dimethylphenyl
β MS	Beta-methylstyrene
η	Viscosity
μ M	Micromolar
Φ_F	Quantum yield of fluorescence
Φ_{ISC}	Quantum yield of intersystem crossing
Φ_R	Photochemical quantum yield of reaction
τ_F	Lifetime of fluorescence
λ	Wavelength

CHAPTER 1: ORGANIC PHOTOREDOX CATALYSIS

Reproduced in part with permission from Romero, N. A.; Nicewicz, D. A. *Chem. Rev.* **2016**, *116* (17), 10075–10166. Copyright 2016 American Chemical Society.¹

1.1 Introduction

1.1.1 Background and Importance

The revival of radical chemistry in organic synthesis over the past decade has also initiated resurgence in the interest in photochemistry. Much of this renewed interest has come about due to the reactivity that can be accessed via the intermediacy of open shell reactive species that is otherwise difficult or impossible by other means of chemical catalysis. Radical reactivity often times offers a complementarity to polar or two-electron manifolds. Perhaps one of the most rapidly expanding areas of radical chemistry in synthesis is photoredox catalysis. Many researchers in chemistry ranging from biomedical to materials science are quickly adopting the use of photoredox catalysis as a mild means of achieving unique chemical reactivity.

This review will highlight the advances from the past ~40 years that have laid the groundwork for current advances in photoredox catalysis as well as provide readers with the basic tools to approach the design and implementation of photoredox catalysis in organic

¹This chapter is presented as a truncated version of the review article as it appeared in its original form,¹ for the sake of brevity and in order to serve as an introduction to the fundamental principles of photoredox catalysis. For the remainder of the original article, a survey of the literature on organic photoredox catalysis, see: Romero, N. A.; Nicewicz, D. A. *Chem. Rev.* **2016**, *116* (17), 10075–10166.

synthesis. Importantly, this survey of the literature will be limited to purely organic photoredox catalyst systems and will describe the pros and cons to the use of organic photoredox catalysts over their organometallic and inorganic counterparts. We hope that this is just the start of what promises to be a fruitful area of research for many years to come.

1.1.2 Why Organic Photoredox Catalysts?

Recent literature reviews on photoredox catalysis have focused predominantly on the synthetic applications of transition metal chromophores.²⁻⁸ Ruthenium and iridium polypyridyl complexes stand at the forefront of this class, and their well-demonstrated versatility in organic synthesis has garnered particular recognition of late. Despite the fact that organic chromophores have long been acknowledged for their ability to participate in photoinduced electron transfer (PET) processes, their catalytic use as applied to organic synthesis is somewhat less familiar. Topics in organic photoredox catalysis have been reviewed previously,⁹⁻¹⁷ but are relatively narrow in scope or predate recent important advances in catalyst development and the discovery of new reactivity. A comprehensive survey of the literature that encompasses the numerous organic photoredox classes and provides some historical context for new developments in the field is still lacking. It is our goal to provide this.

Still, one might inquire what organic photoredox catalysts have to offer compared to their transition metal counterparts. We hope the answer to this question will become clear as we explore the properties and reactivity of the organic molecules most commonly employed in synthesis as photoredox catalysts. Specifically, we wish to emphasize that organic photoredox catalysis offers far more than “metal-free” alternatives to transition metal catalyzed examples; namely, the potent reactivity afforded by many organic catalysts allows access to unique chemistries and a broad range of substrates that are unreactive in most synthetic contexts.

Moreover, the diversity of these organic compounds presents a collection that promises to be useful in the discovery and optimization of new synthetic methodologies.

1.2 Photophysical and Electrochemical Considerations

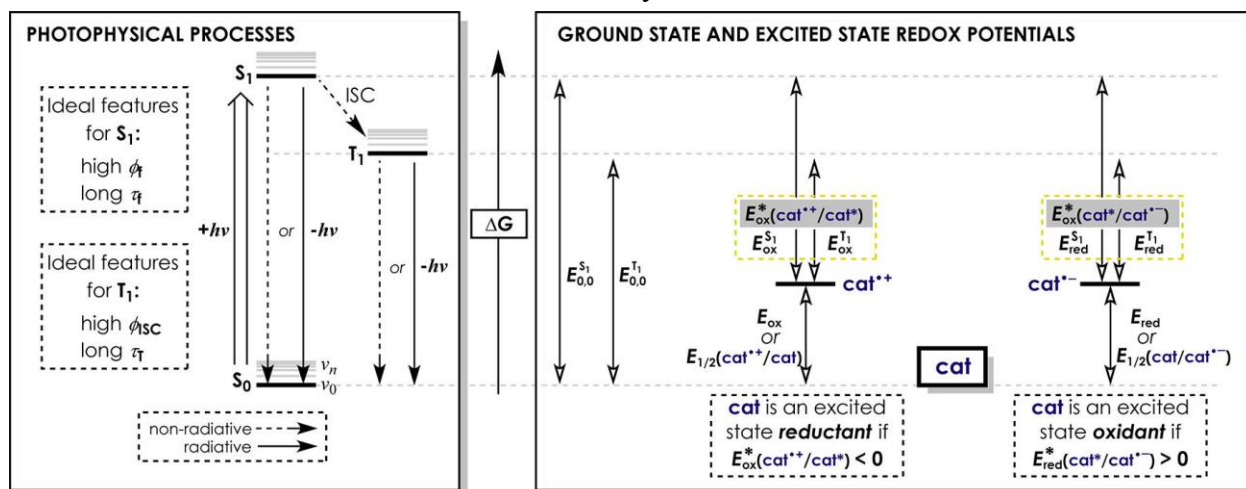
A recurring theme in this review is that the photophysical properties of an electronically excited molecule ultimately govern its photochemical reactivity. Accordingly, consideration of the properties of a photoredox catalyst in both the excited state and the ground state is crucial in effecting a desired reactivity. The recent surge of new synthetic applications for light absorbing molecules was preceded by at least a century of photophysical and electrochemical studies of organic chromophores and ion radicals. Whether directly or indirectly, these efforts to characterize the behavior of excited state chromophores form the basis for their successful deployment as photoredox catalysts. Moreover, mechanistic studies on photoredox catalytic systems frequently rely on the same tools and techniques for analyzing reaction mechanism and shaping the development of more effective catalysts. Given the indispensable role of photophysical studies in this recursive relationship between excited state properties and photochemical reactivity, we believe it is important to precede our survey of synthetic methodologies reported in the literature with a discussion of the photophysical and electrochemical foundations of organic photoredox catalysis.

1.2.1 Photophysical Processes

The rich photochemistry associated with organic molecules originates in a range of excited state energies and the rates which govern their photophysical processes. Simplified state energy diagrams such as the one pictured in **Scheme 1.1** are used to frame the paradigm in which we understand the reactivity of a photoredox catalyst. This paradigm and the ensuing discussion of photophysical processes draw heavily from the treatise *Principles of Molecular*

Photochemistry by Turro, Ramamurthy, and Scaiano.¹⁸ We direct the reader towards this work for a more detailed description of the photophysical underpinnings of molecular excitation and photochemical reactions.

Scheme 1.1. Photophysical and Electrochemical Processes and Properties of Photoredox Catalysts



Absorption of light ($+h\nu$) produces an electronically excited molecule. Typically, promotion of an electron to a higher energy level goes from a ground state singlet (S_0) to a singlet excited state. Depending on the energy of the electromagnetic radiation, a range of singlet excited states with different vibrational energies might be accessed, but within picoseconds, all higher lying excited states relax to the lowest energy, vibrationally equilibrated “first” singlet excited state, S_1 . Considering only the photophysical pathways of an electronically excited molecule in isolation, the fate of S_1 depends on both radiative and non-radiative pathways: radiative pathways are transitions to lower energy states by emitting light ($-h\nu$), while the energy dissipated in a non-radiative transition is lost as heat. S_1 can return to S_0 either by fluorescence (a radiative transition) or by internal conversion, **IC** (a non-radiative transition), or it can proceed to T_1 by a spin-forbidden, non-radiative process known as intersystem crossing (**ISC**). Since the $T_1 \rightarrow S_0$ transition is also spin forbidden, T_1 states tend to be the longest-lived, decaying by

radiative (phosphorescence) and non-radiative pathways as well, although the latter dominates under standard conditions.

With lifetimes stretching from the nanosecond to the millisecond regimes, S_1 and T_1 are the most likely excited states to participate in bimolecular reactions (i.e., reactions with a substrate, or quencher), and each can undergo energy transfer (EnT) and electron transfer (ET). Photoinduced electron transfer, or PET, is a term used to refer to the overall process of excitation and electron transfer between the excited state molecule and a ground state molecule. The specific mechanisms by which each bimolecular process occurs are beyond the scope of this review, but some general principles influencing both energy transfer and electron transfer emerge by considering the energies, lifetimes, and quantum yields of the excited states for a given molecule. Thus, we have compiled some relevant properties for the photoredox catalysts considered in this review (see **Scheme 1.2**) and provide this information in **Table 1.1** and **Table 1.2**. Furthermore, we discuss how these values inform selection of an appropriate photoredox catalyst when probing new reactivity, along with how these properties impact analysis of photoredox reactions. The data illustrate the fact that the structural diversity of organic light-absorbing molecules gives rise to a diverse set of photophysical properties, which, in turn, influence their reactivity in PET processes.

1.2.2 Photophysical Properties of Organic Photoredox Catalysts

1.2.2.1 $\lambda_{\max}^{\text{abs}}$: local absorbance maximum for lowest energy absorption.

One simple application of this value is in determining a source of irradiation for a given photoredox catalyst. The criterion that at least some overlap exists between an absorption of the molecule and emission of the lamp suffices for many purposes. Although excitation of any transition normally results in relaxation to the lowest energy singlet excited state, it is often

desirable to irradiate the lowest energy (i.e., the most red-shifted) absorption from the standpoint of macroscopic energy efficiency and to reduce the likelihood of exciting other reactants with high energy photons, which can lead to competing photochemical reactivity. In this regard, light emitting diodes (LEDs) have emerged as an important tool in photoredox catalysis, as they possess a relatively narrow emission band enabling selective excitation of chromophore and constitute an energy-efficient, high intensity light source.¹⁹⁻²¹ Finally, the $\lambda_{\text{max}}^{\text{abs}}$ value gives some information about how much energy an excited state can contribute to a photoinduced electron transfer. Thus, although irradiation with visible light is attractive for a number of reasons, the longer the wavelength of absorption, the less energy the singlet and triplet excited states will possess.

1.2.2.2 τ_f : lifetime of fluorescence (equal to the inverse of the fluorescence decay rate constant, or $1/k_f$); and ϕ_f : the quantum yield of fluorescence.

These values are helpful in gauging whether the first singlet excited state S_1 can effectively participate in a PET reaction by providing an approximate assessment of the lifetime of S_1 and its propensity towards non-radiative deactivation pathways—namely, IC and ISC. The assumption that the non-radiative decay pathways are significantly slower than emission of a photon allows for the approximation that $\tau_f \cong \tau_{S_1}$ (lifetime of S_1). Fluorescence lifetimes of many organics range from 2 to 20 ns, and a general rule of thumb seems to be that fluorophores with $\tau_f < 1$ ns will not readily participate in PET processes in the singlet state because the excited state decay approaches the rate constant of diffusion ($k_{\text{diff}} \sim 1 \times 10^{10} - 2 \times 10^{10} \text{ s}^{-1}$). Generally speaking, the longer the lifetime of fluorescence, the greater the likelihood of encountering a quencher and undergoing PET. Moreover, ϕ_f provides important information about non-radiative decay pathways: the higher the fluorescence quantum yield, the greater the likelihood of PET in the singlet excited state, because S_1 is not highly susceptible to other deactivation pathways on

the timescale that ET occurs. Fluorescence quantum yields near unity signify that essentially all molecules in S_1 return to the ground state by emission of a photon and that non-radiative pathways are much slower than k_f ; conversely, a low ϕ_f indicates that the rate of non-radiative pathways are competitive with k_f .

1.2.2.3 ϕ_{ISC} : quantum yield of intersystem crossing (frequently used as synonymous with quantum yield of formation of T_1 , ϕ_{T_1}).

When k_{ISC} is fast enough to compete with k_f (and k_{IC}), the T_1 state can be populated, and ϕ_{ISC} can help to predict whether T_1 will be an active excited state in a PET process. Lifetimes for triplet states (τ_{T_1}) are usually several orders of magnitude larger than S_1 and on the order of microseconds to milliseconds. This is a consequence of the fact that the $T_1 \rightarrow S_0$ is symmetry forbidden. We opt not to tabulate τ_{T_1} lifetimes, in part because wide variability in these values is difficult to avoid, owing to the fact that strictly anaerobic conditions are required to preclude quenching by O_2 . Furthermore, decay of the T_1 by phosphorescence or non-radiative pathways is usually orders of magnitude slower than electron transfer reactions. Thus, T_1 are sufficiently long-lived that the efficacy of PET between a substrate and T_1 is not significantly affected by τ_{T_1} .

1.2.2.4 $E_{0,0}^{S_1}$: excited state energy of the first singlet excited state S_1 .

The excited state energy is often named with the subscript “ $_{0,0}$ ”, which refers to the transition between the lowest energy vibrational state ($v = 0$) of S_1 to $v = 0$ of S_0 , which can be estimated at the intersection between normalized symmetrical absorbance and emission spectra after converting the wavelength axis to an energy scale, or by finding the midpoint between absorption and emission maxima (i.e., one-half the Stokes shift). Alternative methods for estimating excited state energy include selecting the energy at the earliest onset (highest energy)

of fluorescence or at the fluorescence maximum. The “earliest onset” method is arbitrary and may overestimate the true excited state energy, while the “fluorescence maximum” method is likely to underestimate $E_{0,0}$.

1.2.2.5 $E_{0,0}^{T_1}$: excited state energy of the first triplet excited state T_1 .

Because $S_0 \rightarrow T_1$ seldom occurs at room temperature, and phosphorescence under the same conditions is also rare, this value is less readily obtained than for S_1 . Moreover, $E_{0,0}^{T_1}$ is most often read from the phosphorescence maximum, which almost always requires cryogenic conditions to maximize phosphorescence as the dominant decay pathway. Under these conditions, the emission spectrum usually exhibits enough structure to allow assignment of E^{T_1} as an $E_{0,0}$.

Note that we present $E_{0,0}^{S_1}$ and $E_{0,0}^{T_1}$ in units of eV to allow for easy combination with electrochemical potential (in units of V) in order to estimate excited state redox potentials. See the discussion below.

Scheme 1.2. Common Organic Photoredox Catalysts

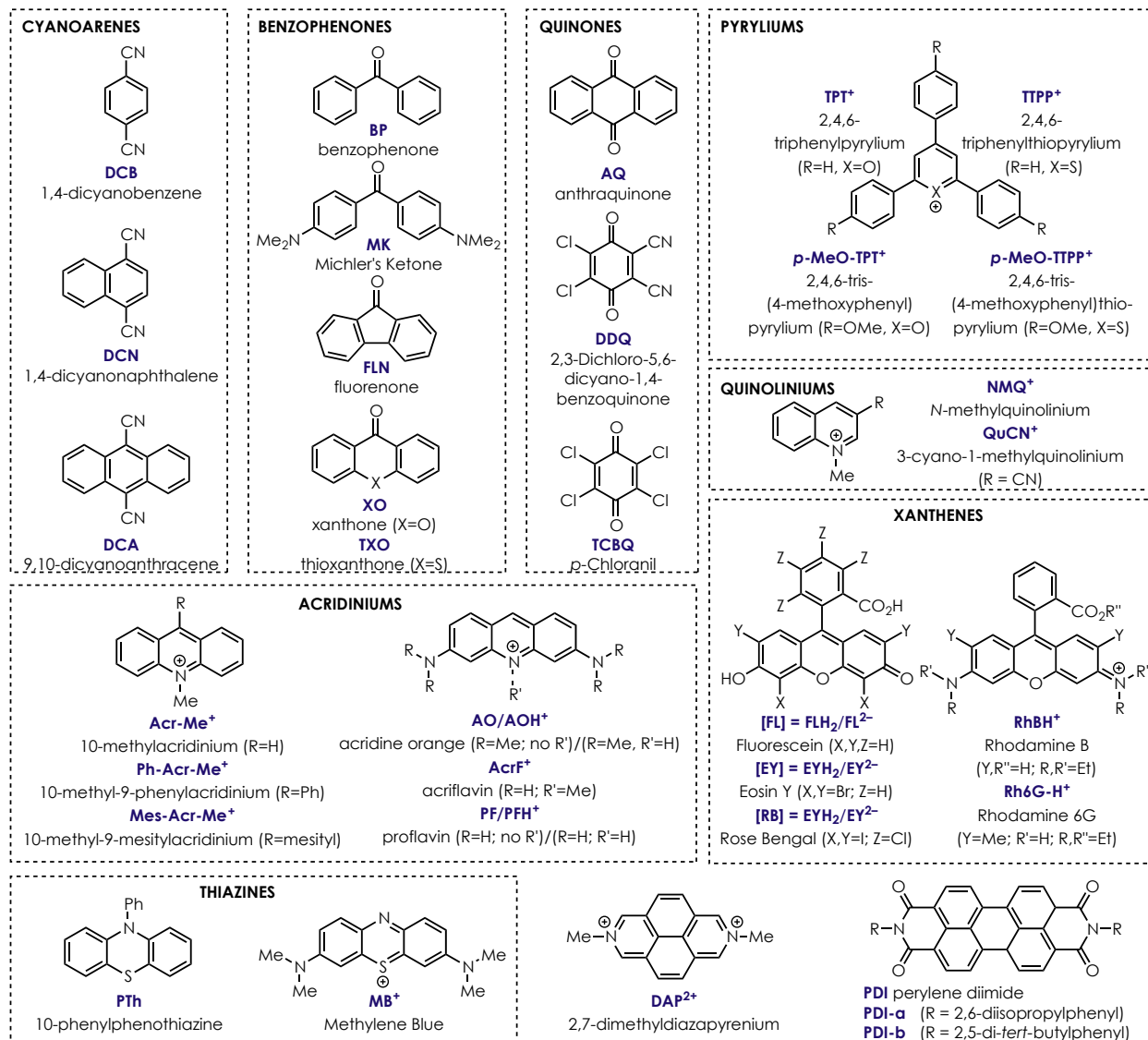


Table 1.1. Photophysical Properties of Organic Photoredox Catalysts

abbreviation	$\lambda_{\text{max}}^{\text{abs}}$ (nm)	τ_f (ns)	ϕ_f	ϕ_{isc}	excited state energies (eV)	
					$E_{0,0}^{S_1}$	$E_{0,0}^{T_1}$ ⁱⁱ
DCB	290 ²²	9.7 ²³			4.01 ²³	3.04 ²⁴
DCN	325 ²⁵	10.3 ²⁶			3.57 ²⁶	2.41 ²⁴
DCA	422 ²⁷	14.9 ²⁶	0.76 ^{iii,28}	0.0085 ²⁹	2.90 ²⁶	1.81 ²⁸
BP	335 ^{iv,30}	0.008 ³¹		1.0 ³²	3.22 ³¹	3.0 ³¹
MK	365 ^{v,33}				2.98 ^{v,33}	2.7 ³¹
FLN	377 ³⁴	16.2 ³²		0.97 ³²		2.31 ³²
XO	340 ³⁵	<0.0 ³²		1.0 ³²	3.4 ³¹	3.22 ³¹
TXO	360 ³⁶	2 ³²		0.99 ³²	3.14 ³¹	2.8 ³¹
TCBQ	450 ³⁷			1.0 ³⁸		2.46 ³⁹
DDQ	~400 ⁴⁰			1.0 ⁴¹		2.67 ⁴⁰
AQ	326 ^{v,42}			1.04 ⁴³		2.73 ^{43,44}
TPT ⁺	415 ^{vi,45}	4.38 ²⁶	0.58 ^{vi,45}	0.42 ⁴⁵	2.83 ²⁶	2.3 ^{vii,46}
<i>p</i> -OMeTPT ⁺	422,470 ^{vii,47}	4.0 ¹⁰	0.95 ¹⁰ 0.49 ⁴⁸	0.03 ⁴⁹	2.34 ^{viii,47}	2.21 ^{vii,46}
TTPP ⁺	414 ⁴⁷	3.6 ^{vi,50}	0.03 ⁵⁰	0.94 ⁴⁹	2.64 ^{viii,47}	2.28 ⁵¹
<i>p</i> -OMeTTPP ⁺	455 ⁴⁷				2.23 ^{viii,47}	
NMQ ⁺	315 ⁵²	20 ⁵³	0.79 ^{ix,54}		3.50 ²³	
QuCN ⁺	329 ⁵⁵	45 ⁵⁶			3.32 ²³	
Acr-Me ⁺		37 ⁵³ , 34 ²⁶	1.0 ^{x,57}		2.80 ²⁶	
Ph-Acr-Me ⁺	424 ⁵⁸	1.5 ⁵⁸	0.063 ⁵⁸			
Mes-Acr-Me ⁺	425 ⁵⁹	6 ⁶⁰	0.035 ⁶⁰ 0.08 ^{xi,61}	0.38 ⁶⁰	LE: 2.67 ⁶⁰ CT: 2.57 ⁶⁰	LE: 1.94 ⁶⁰
AO	425 ⁶²					2.58 ⁶²
AOH ⁺	495 ⁶²	1.8 ⁶³	0.18 ^{x,64}		2.58 ^{iv,65} 2.43 ^{xii,66}	2.07 ⁶⁵ 2.13 ^{xii,66}
AcrF ⁺	470 ^{xii,66}		0.54 ^{x,57}		2.56 ^{xii,66}	2.22 ^{xii,66}
PF	393 ^{x,67}					

ⁱⁱ Determined by highest energy local maximum of phosphorescence spectrum, typically at 77 K in glassy medium; see reference for specific medium

ⁱⁱⁱ In PhMe

^{iv} In MeOH

^v In EtOH

^{vi} In DCM

^{vii} Medium not specified

^{viii} Determined from highest energy fluorescence maximum

^{ix} Fluorescence quantum yield for *N*-ethylquinolinium in aqueous HClO₄/NaClO₄ at pH 5.6

^x In H₂O

^{xi} In DCE (1,2-dichloroethane)

^{xii} In 9:1 EtOH/MeOH

PFH⁺	470 ^{xii,66}	~5 ^{x,68}	0.39 ^{x,64}	0.10 ^{x,69}	2.56 ^{xii,66}	2.22 ^{xii,66}
PTh	<300 ⁷⁰	0.81-2.3 ⁷⁰			2.8 ^{xiii,71}	2.4 ⁷¹
MB⁺	650 ^{xiv,72} 664 ^{x,73}	1.0 ^{xv,74} 0.6 ^{iv,75,76}		0.52 ^{v,77}	1.89 ⁷⁶	1.50 ⁷⁶ 1.85 ⁶⁵
[FL]^{xvi,xvii}	FLH ₂ :437 ^{x,81} FL ²⁻ : 491 ^{x,81}	4.2 ^{iv,78} 4.73 ^{iv,65}	FLH ₂ : 0.2 ⁸¹ FL ²⁻ : 0.93 ⁸¹	0.03 ⁶⁵	2.42 ^{iv,65}	1.94 ⁶⁵
[EY]^{xvii,xvi}	520 ^{iv,78} 533 ^{v,79}	2.1 ^{iv,78} 2.66 ^{iv,65}	0.48 ^{iv,65} 0.19 ^{xviii,57}	0.32 ^{iv,65}	2.31 ^{iv,78}	1.91 ⁶⁵
[RB]^{xvii,xvi}	549 ⁸⁰	0.50 ⁶⁵	0.09 ^{iv,65}	0.77 ^{iv,65}	2.17 ^{iv,65}	1.8 ⁶⁵
[RhB]	550 ^{x,82}	2.45 ^{iv,65}	0.58 ^{iv,65} 0.97 ^{v,57}	0.12 ^{iv,65} 0.0024 ⁸²	2.22 ^{iv,65}	1.80 ⁶⁵
[Rh6G]	530 ^{v,83}	4.13 ^{iv,84}	0.90 ^{x,85}	0.002 ⁸⁶	2.32 ⁸⁷	2.09 ⁸⁶
DAP²⁺	418 ⁸⁸	10.5 ^{x,89}	0.5 ^{x,89}		~3.0 ^{x,89}	
PDI-a/PDI-b	521 ⁹⁰	3.9 ⁹⁰	0.98 ⁹⁰		2.35 ⁹⁰	1.2 ⁹⁰

Table 1.2. Electrochemical Properties of Organic Photoredox Catalysts

abbreviation	ground state redox potentials (V vs. SCE)		excited state redox potentials (V vs. SCE): S ₁		excited state redox potentials (V vs. SCE): T ₁	
	E _{1/2} ^{red}	E _{1/2} ^{ox}	E _{red} ^{S₁}	E _{ox} ^{S₁}	E _{red} ^{T₁}	E _{ox} ^{T₁}
DCB	-1.46 ²³		+2.55 ²³		+1.58 ^{xix,23,24}	
DCN	-1.27 ²⁶		+2.3 ^{xix,26}		+1.14 ^{xix,26,24}	
DCA	-0.91 ²⁶		+1.99 ^{xix,26}		+0.9 ^{xix,26,28}	
BP	-1.72 ³²	+2.39 ³²	+1.5 ^{xix,32,31}	-0.83 ^{xix,32,31}	+1.28 ^{xix,32,31}	-0.61 ^{xix,32,31}
MK	-2.20 ^{xx,92}	+0.86 ⁹³	+0.76 ^{xix,92,33}	-2.12 ^{xix,93,33}	+0.48 ^{xix,92,31}	-1.84 ^{xix,93,31}
FLN	-1.35 ³²	+1.7 ³²			+0.96 ^{xix,32}	-0.61 ^{xix,32}
XO	-1.65 ³²	+1.8 ³²	+1.76 ^{xix,32,31}	-1.61 ^{xix,32,31}	+1.57 ^{xix,32,31}	-1.42 ^{xix,32,31}
TXO	-1.62 ³²	+1.69 ³²	+1.52 ^{xix,32,31}	-1.45 ^{xix,32,31}	+1.18 ^{xix,32,31}	-1.11 ^{xix,32,31}
TCBQ	0.00 ⁹⁴				+2.46 ^{xix,94,39}	
DDQ	+0.49 ⁹⁴				+3.18 ⁴⁰	
AQ	-0.96 ⁹⁴				+1.77 ^{xix,94,43}	
TPT⁺	-0.32 ²⁶		+2.55 ^{xix,45,26}		+2.02 ^{xix,45,46}	
p-OMeTPT⁺	-0.50 ^{xxi,47}		+1.84 ^{xix,47}		+1.71 ^{xix,47,46}	
TTPP⁺	-0.19 ^{xxi,47}		+2.45 ^{xix,47}		+2.09 ^{xix,47,51}	

^{xiii} In DMA

^{xiv} 4:1 MeCN/H₂O

^{xv} In a mixture of diethyl ether/isopentane/EtOH

^{xvi} Neutral form used in ref⁶⁵

^{xvii} Disodium salt disodium used in refs. ⁷⁸, ⁷⁹, ⁸⁰

^{xviii} In 0.1 M aq. NaOH

^{xix} Calculated using the data from the indicated references

^{xx} Potential originally reported relative to the Ag/AgCl reference electrode; referenced to SCE by subtracting 0.039 V from the reported value⁹¹

^{xxi} Potential originally reported relative to NHE; referenced to SCE by subtracting 0.141 V from the value relative to NHE⁹⁵

<i>p</i>-OMeTTPP⁺	-0.33 ^{xxi,47}		+1.9 ^{xix,47}			
NMQ⁺	-0.85 ⁹⁶		+2.70 ⁹⁶			
QuCN⁺	-0.60 ⁹⁷ -0.79 ⁹⁸		+2.72 ⁵⁶			
Acr-Me⁺	-0.46 ²⁶		+2.32 ⁹⁹			
Ph-Acr-Me⁺	-0.54 ^{xxii,100}					
Mes-Acr-Me⁺	-0.49 ⁵⁹ -0.57 ¹⁰¹		LE: +2.18 ⁶⁰ CT: +2.08 ⁶⁰		LE: +1.45 ⁶⁰ CT: +1.88 ¹⁰²	
AO	-2.4 ⁶²				+0.60 ^{xxiii,62}	
AOH⁺	-1.18 ^{xxiii,62}				+0.95 ^{xxiii,62}	
AcrF⁺						
PF						
PFH⁺	-0.74 ^{x,67}		+1.82 ^{xix,67,66}		+1.48 ^{xix,67,66}	
PTh		+0.68 ⁷¹		-2.1 ⁷¹		-1.7 ^{xix,71}
MB⁺	-0.30 ^{iv,xx,65}	+1.13 ^{iv,xx,65}	+1.56 ^{iv,xx,65}	-0.73 ^{iv,xx,65}	+1.60 ^{iv,xx,65} +1.14 ^{xix,65,76}	-0.68 ^{iv,xx,65} -0.33 ^{xix,65,76}
[FL] ^{xxiv,xxv}	-1.17 ^{iv,xx,65} -1.22 ^{iv,xx,78}	+0.87 ^{iv,xx,65} +0.83 ^{iv,xx,78}	+1.25 ^{iv,xx,65}	-1.55 ^{iv,xx,65}	+0.77 ^{iv,xx,65}	-1.07 ^{iv,xx,65}
[EY] ^{xvii,xvi}	-1.08 ^{iv,xx,65} -1.13 ^{iv,xx,78}	+0.76 ^{iv,xx,65} +0.72 ^{iv,xx,78}	+1.23 ^{iv,xx,65}	-1.58 ^{iv,xx,65}	+0.83 ^{iv,xx,65}	-1.15 ^{iv,xx,65}
[RB] ^{xvii,xvi}	-0.99 ^{iv,xx,65} -0.78 ¹⁰⁴	+0.84 ^{iv,xx,65}	+1.18 ^{iv,xx,65}	-1.33 ^{iv,xx,65}	+0.81 ^{iv,xx,65}	-0.96 ^{iv,xx,65}
[RhB]	-0.96 ^{iv,xx,65}	+0.91 ^{iv,xx,65}	+1.26 ^{iv,xx,65}	-1.31 ^{iv,xx,65}	+0.84 ^{iv,xx,65}	-0.89 ^{iv,xx,65}
[Rh6G]	-1.14 ^{xxx,87} -0.92 ^{vi,105}	+1.23 ¹⁰⁶	+1.18 ^{xx,87}	-1.09 ^{xix,87,106}	+0.95 ^{xix,86,87}	-0.86 ^{xix,86,106}
DAP²⁺	-0.46 ^{xxii,88}		+2.54			
PDI-a/PDI-b	-0.43 ^{xxii,107}	+1.63 ^{xxvi,xx,108}	+1.92 ^{xix}	-0.72 ^{xix}	+0.77 ^{xix,107,90}	+0.43 ^{xix,107,108}

^{xxii} In DMF

^{xxiii} Potential originally reported relative to the Fc⁺/Fc couple; referenced to SCE by adding 0.42 V to the reported value¹⁰³

^{xxiv} Neutral form used in ref⁶⁵

^{xxv} Disodium salt disodium used in refs. ^{78, 79, 80}

^{xxvi} In MeCN/CHCl₃

1.2.3 Electrochemistry: Thermodynamics of Electron Transfer and Photoinduced Electron Transfer

1.2.3.1 Electron Transfer in the Ground State

The general equation describing the free energy of a single electron transfer is

Equation 1.1

$$\begin{aligned}\Delta G_{\text{ET}} &= -\mathcal{F}(\Delta E) = -\mathcal{F}(E_{\text{red}} - E_{\text{ox}}) \\ &= -\mathcal{F}(E_{1/2}(\text{A}/\text{A}^{\bullet-}) - E_{1/2}(\text{D}^{\bullet+}/\text{D}))\end{aligned}$$

where \mathcal{F} is the Faraday constant (23.061 kcal V⁻¹ mol⁻¹), and E_{red} and E_{ox} are ground state redox potentials obtained experimentally for each species **A** and **D** undergoing reduction and oxidation, respectively. E_{red} refers to a *reduction potential* and is the common shorthand for $E_{1/2}(\text{A}/\text{A}^{\bullet-})$, or single electron reduction of an acceptor **A** according to the half reaction $\text{A} \rightarrow \text{A}^{\bullet-}$. As experimentally measured by electrochemical means, E_{red} values are negative (<0 V) for most ground state species, since single electron reduction is thermodynamically unfavorable for most compounds under standard conditions. E_{ox} is, by convention, referred to as an *oxidation potential*, but is more accurately written as $E_{1/2}(\text{D}^{\bullet+}/\text{D})$ describing the reduction half reaction $\text{D}^{\bullet+} \rightarrow \text{D}$. This value is generally positive for most molecules of interest because single electron reduction of $\text{D}^{\bullet+}$ is energetically favorable (by equation 1.1). Thus, despite their conventional handles, both E_{red} and E_{ox} actually describe reduction half reactions. This oddity in the convention of naming $E_{1/2}(\text{D}^{\bullet+}/\text{D})$ as E_{ox} is a likely cause for confusion that probably originates in the voltammetric collection of the value, in which the oxidation event occurs at a positive potential.

Moreover, at risk of perpetuating the confusion, use of the terms *reduction potential* and *oxidation potential* in reference to E_{red} and E_{ox} is unavoidable, and may actually have value in describing which half reactions are under discussion for the components of a redox reaction.

Whatever subscript is used, we advocate that the redox couple be parenthetically clarified wherever possible, always writing from right to left the **(reactant/product)** pair of a *reduction* half reaction. For example, we will use the following notation throughout this review: E_{red} or $E_{\text{red}}(\text{A}/\text{A}^{\bullet-})$ is defined by the half reaction $\text{A} \rightarrow \text{A}^{\bullet-}$ and may be referred to as the “reduction potential of A.” E_{ox} or $E_{\text{ox}}(\text{D}^{\bullet+}/\text{D})$ is defined by the half reaction $\text{D}^{\bullet+} \rightarrow \text{D}$ and may be referred to as the “oxidation potential of D.” We also recommend always specifying the reference electrode and, where possible, the solvent used in the determination of a redox potential. All potentials reported in this review can be assumed to be collected in acetonitrile (MeCN) unless otherwise noted.

1.2.3.2 Photoinduced Electron Transfer

The common formulation for determining the free energy of a photoinduced electron transfer (PET) is

Equation 1.2

$$\Delta G_{\text{PET}} = -\mathcal{F}(E_{\text{ox}}(\text{D}^{\bullet+}/\text{D}) - E_{\text{red}}(\text{A}/\text{A}^{\bullet-})) - w - E_{0,0}$$

which is frequently, and incorrectly referred to as the “Rehm-Weller Equation.” We emphasize that IUPAC defines this general equation form as the “Gibbs energy of photoinduced electron transfer” and expressly recommends that it should not be called the “Rehm-Weller equation”,¹⁰⁹ which is an empirical correlation that relates the bimolecular rate constant for PET (k_{PET}) with ΔG_{PET} .^{110–112} An important feature of equation 1.2 is $E_{0,0}$ (in the same units as ΔG in this formulation), or the excited state energy for a given excited state **cat*** (see above).

Equation 1.2 also includes an electrostatic work term w , which accounts for the solvent-dependent energy difference due to the Coulombic impact of charge separation. Rehm and Weller are recognized for including this term in their calculation of ΔG_{PET} which was estimated to be

~0.06 eV in acetonitrile.^{111,112} Generally, this term is larger in magnitude in less polar solvents ($w \propto 1/\epsilon$; ϵ is the solvent dielectric constant), and it depends on the charge of the reactants and the products following ET. Except in detailed photophysical studies where solvent effects are analytically addressed, the w term is frequently omitted on the basis that the correction of w to ΔG_{PET} is a relatively small one (generally < 0.1 eV).¹¹³ Additionally, in depth studies in the past two decades have revealed that the sign and magnitude of w are highly system dependent,^{114–118} precluding adoption of a general model for this correction as addressed in this review. We emphasize that there are certainly cases where the w term can have a significant impact on mechanistic analysis or reaction optimization; however, this is unlikely to be an important consideration when approaching the development of a photoredox reaction, and we omit w in the ensuing discussion.

Moreover, omission of the w term allows for a simpler calculation of the *excited state redox potential* of a given photoredox catalyst **cat**. We find it instructive to consider the excited state redox potentials $E_{\text{red}}^*(\text{cat}^*/\text{cat}^{\bullet-})$ or $E_{\text{ox}}^*(\text{cat}^{\bullet+}/\text{cat}^*)$ as benchmarks when evaluating the plausibility of a substrate reacting with a photoredox catalyst in the excited state. When a PET involves reduction of the excited state **cat**^{*} and oxidation of the ground state substrate “**sub**”,

Equation 1.3

$$\Delta G_{\text{PET}} = -\mathcal{F}(E_{\text{red}}^*(\text{cat}^*/\text{cat}^{\bullet-}) - E_{\text{ox}}(\text{sub}^{\bullet+}/\text{sub}))$$

where E_{red}^* is the *excited state reduction potential* of **cat**. E_{red}^* is calculated by

Equation 1.4

$$E_{\text{red}}^*(\text{cat}^*/\text{cat}^{\bullet-}) = E_{\text{red}}(\text{cat}/\text{cat}^{\bullet-}) + E_{0,0}$$

Note that **cat**^{*} refers to either the S₁ or T₁ excited state, with the corresponding $E_{0,0}$ value ($E_{0,0}^{\text{S}_1}$ or $E_{0,0}^{\text{T}_1}$).

When a PET involves oxidation of the excited state **cat*** and reduction of the ground state **sub**,

Equation 1.5

$$\Delta G_{\text{PET}} = -\mathcal{F}(E_{\text{red}}(\text{sub}/\text{sub}^{\bullet-}) - E_{\text{ox}}^*(\text{cat}^{\bullet+}/\text{cat}^*))$$

where E_{ox}^* is the excited state oxidation potential of **cat**, and is calculated by

Equation 1.6

$$E_{\text{ox}}^*(\text{cat}^{\bullet+}/\text{cat}^*) = E_{\text{ox}}(\text{cat}^{\bullet+}/\text{cat}) - E_{0,0}$$

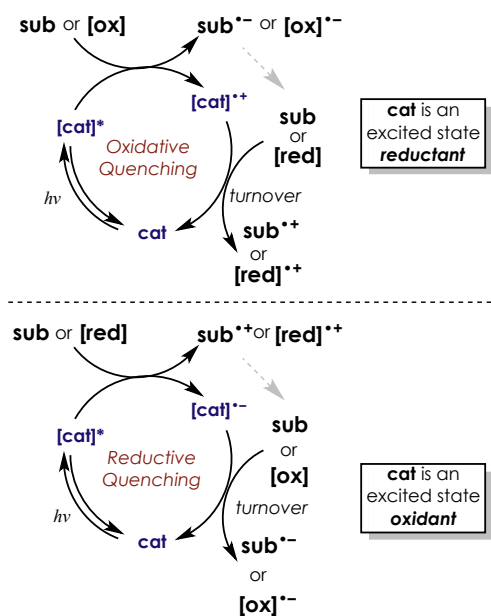
Note that we list $E_{0,0}$ in units of eV, while E_{red} and E_{ox} are in V, but the two are combined in equations 1.4 and 1.6 as if they possess the same units, assuming a conversion factor of 1 eV/V. This is commonplace when approaching a single electron transfer on a per molar basis.

Although equations 1.3 and 1.5 are fundamentally equivalent to equation 1.2 (after the omission of ω), we believe they provide a more intuitive framework when approaching photoredox catalysis from the perspective that the structural and energetic characteristics of photoredox catalysts in the excited state define their unique patterns of PET reactivity. Thus, for a photoredox catalyst acting as an excited state oxidant, E_{red}^* is positive, and for a photoredox catalyst acting as an excited state reductant, E_{ox}^* is negative. Evaluation of a supposed PET process is essentially informed by qualitative estimation of ΔG_{PET} . Accordingly, equations 1.3 and 1.5 make for simple tools when selecting a photoredox catalyst for a desired transformation. If photoinduced oxidation of substrate **sub** is to be feasible, E_{red}^* of photoredox catalyst **cat*** must be more positive than E_{ox} of substrate **sub**. Likewise, if reduction of substrate **sub** is intended, E_{ox}^* of photoredox catalyst **cat*** must be more negative than E_{red} of substrate **sub** for PET to be thermodynamically favorable.

1.3 General Mechanistic Schemes for Photoredox catalysis

Most photoredox catalytic reactions follow one of the two mechanistic schemes depicted in **Scheme 1.3**. Each of these PET cycles is categorized by the primary direction of the ET with respect to the excited state catalyst **cat***: in an oxidative quenching cycle, the excited state **cat*** is quenched by donating an electron either to **sub** or an oxidant **[ox]** present in the reaction mixture; in a reductive quenching cycle, **cat*** is quenched by accepting an electron from **sub** or a reductant **[red]**. The catalyst turnover step involves reduction of the oxidized **[cat]^{•+}** in the oxidative cycle and oxidation of the reduced **[cat]^{•-}** in the reductive cycle. In either case, the substrate, an external redox-active reagent, or an intermediate may be responsible for catalyst turnover.

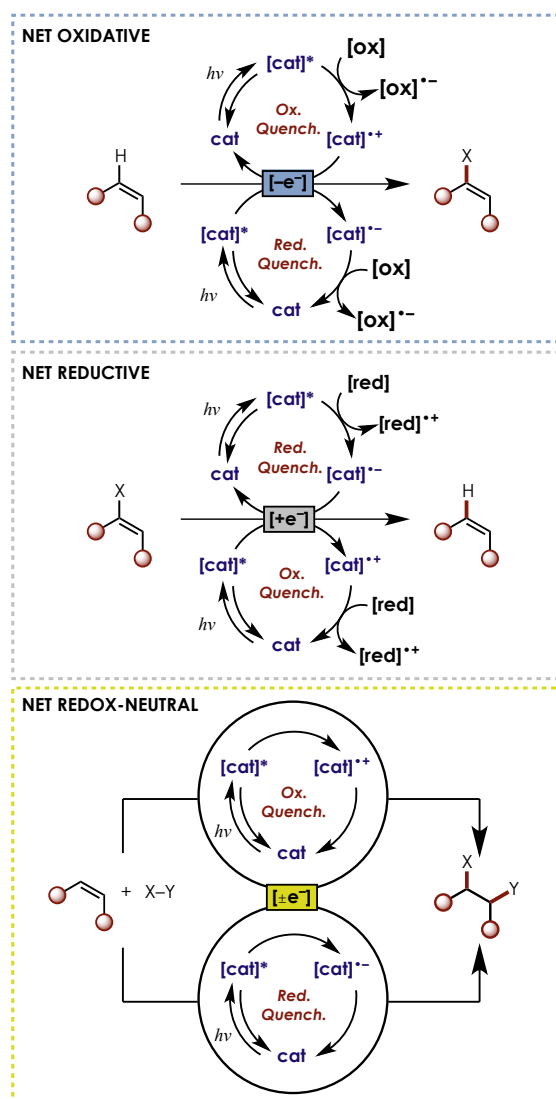
Scheme 1.3. Oxidative and Reductive Quenching Cycles of a Photoredox Catalyst



Regardless of whether the substrate undergoes an ET reaction in the PET step or the turnover step, there are three general redox outcomes possible for the substrate in either quenching manifold: net oxidative, net reductive, and net redox-neutral. **Scheme 1.4** illustrates

these groupings along with a general example for each overall reaction type. A net oxidative reaction requires an external oxidant which can accept electrons in either the PET step or the turnover step. Likewise, net reductive reactions involve an external reductant donating electrons during the PET or turnover steps. Net redox-neutral processes are more complex and often involve return electron transfer with the oxidized or reduced catalyst, sometimes mediated by a redox-active co-catalyst. Additionally, **Scheme 1.4** introduces a symbolic representation for the net redox outcome that we will use throughout this review to denote reaction type. As indicated, $[-e^-]$ refers to a net oxidative reaction, $[+e^-]$ refers to a net reductive reaction, and $[\pm e^-]$ refers to a net redox-neutral reaction. This symbolic representation is intended to be conceptual and does not specify the number of electrons transferred in a given process. Moreover, there are certainly exceptions to this general classification, including overall transformations that consist of multiple sequential photoredox steps, but these delineations are descriptive for a majority of photoredox catalytic reactions.

Scheme 1.4. Net Redox Outcomes for Photoredox Transformations



1.3.1 Definitions

We note that a number of different labels have been used to describe molecules which participate in light driven chemical processes without being consumed, including “photocatalyst”, “photosensitizer” (or simply “sensitizer”), and “PET sensitizer.” However, we believe the term “photoredox catalyst” provides a more precise term for several reasons: (a) “photocatalyst” implies the catalytic involvement of photons, which is relevant in transformations which proceed by chain mechanisms, but is misleading for those that do not; (b) we avoid the usage of any terms related to “sensitizer,” as this is traditionally used to describe a

molecule which participates in energy transfer processes, particularly the “sensitization” of dioxygen (O₂).

Thus, the defining feature of a photoredox catalyst is the ability to undergo a redox reaction in the excited state, and a subsequent turnover step enables participation in light-driven catalytic redox cycles like those shown in **Scheme 1.3**. While the major focus of this review is on synthetic methodologies that employ catalytic quantities of an organic chromophore, we will highlight select cases where stoichiometric loadings are used, particularly in examples that eventually lead to catalytic conditions or in examples that demonstrate the limitations of a given photoredox system. In some of these cases, a photoredox catalytic cycle may be mechanistically tenable, but catalysis is precluded for other reasons.

1.3.2 Other Mechanistic Considerations

1.3.2.1 Chain Mechanisms

The mechanisms shown in **Scheme 1.3** are idealized representations of reactions proceeding exclusively through PET manifolds in a one photon/one product paradigm. Realistically, the efficiencies of many photoredox catalyzed reactions are well below a quantum yield of reaction (ϕ_R) of 1, which is the maximum if only the PET cycles in **Scheme 1.3** are operating. However, in some cases, an intermediate may be capable of donating or accepting an electron to initiate a new chain, rendering possible ϕ_R values greater than unity. Recently, Yoon and Cismesia demonstrated that a number of transition metal photoredox reactions exhibit a significant component of chain transfer,¹¹⁹ and these insights can be extended to analogous reactions using organic photoredox catalysts. Although not often considered as a mechanistic possibility, select cases discussed below confirm that chain transfer is operable in some reactions. Whether a proposed intermediate is capable of chain electron transfer can be estimated

by considering the redox potential of the intermediate, which—although challenging to obtain—have been studied experimentally^{120,121} and computationally.¹²² Furthermore, the groups of Yoon¹¹⁹ and König/Riedle¹²³ have each developed simplified methods for determining ϕ_R and evaluating the extent of chain transfer.

1.3.2.2 EDA complexes and Exciplexes

Occasionally, control experiments reveal that some degree of photolytic reactivity can occur in the absence of a photoredox catalyst, even when the individual reactants are transparent in the wavelength range of irradiation. A noticeable color change upon mixing the two reactants may signal the formation of an electron donor-acceptor (EDA) complex (alternatively referred to as a “charge-transfer complex”). The mechanistic underpinnings and reactivity of these species was established by Kochi^{124–127} and has recently been harnessed by Melchiorre^{128–131} and others¹³² to achieve catalyst-free photolytic transformations using visible light, enabled by the fact that EDA complexes cooperatively absorb a photon at a lower energy (longer wavelength) than either reactant. As a mechanistic consideration in photoredox catalysis, EDA complexes may be responsible for background reactivity (i.e., uncatalyzed), although some examples will be addressed where direct irradiation of a reactant EDA complex leads to a divergent outcome. Moreover, EDA complexation can occur between a substrate and a photoredox catalyst, also resulting in a new, red-shifted absorbance feature. Although rarely characterized in photoredox catalytic methods because the ET outcome is presumably the same, this equilibrium can confer a favorable impact on reactivity through the effects of pre-association and a potentially broader cross-section of irradiation.

Ground state EDA complexes are distinct from exciplexes, which are excited state complexes that cooperatively emit a photon. As it pertains to our discussion, exciplexes are often

in play when an excited state electron-deficient photoredox catalyst, such as a cyanoarene, encounters an electron-rich substrate. Evidence of exciplex formation is observed in the fluorescence spectra as a broad feature which is red-shifted relative to the maximum of the uncomplexed fluorescence. Exciplexes are not always characterized or considered as mechanistic intermediates, probably because these complexes usually lead to the same outcome (i.e., radical [ion] pairs) as if the exciplex did not form. On the other hand, photophysical study of PET processes involving exciplexes has been shown to require special treatment.^{114,115,133}

1.3.2.3 Energy Transfer vs. Electron Transfer

The first synthetic uses of a number of the light absorbing molecules included in this review were as “photosensitizers,” initiating a reaction by transfer of their excited state energy to a substrate.^{134,135} Examples such as Methylene Blue, Rose Bengal, and benzophenone possess relatively high triplet yields and long triplet lifetimes, and are perhaps better known as triplet sensitizers than they are as PET catalysts. One of the most common applications of triplet energy transfer is in the generation of singlet dioxygen ($^1\text{O}_2$)¹³⁶⁻¹³⁹ by photo-sensitization of the ground state triplet dioxygen ($^3\text{O}_2$). Although $^1\text{O}_2$ has useful applications in synthesis, it is often considered an unwelcome byproduct whose high reactivity is expected to interfere with intended chemistries.

By our definition, photoredox catalysis does not include mechanisms involving energy transfer. Although the outcome of energy transfer processes is distinct and recognizable in select cases (e.g., the Schenck-Ene reactivity of olefins and $^1\text{O}_2$ ¹⁴⁰), ET and energy transfer might not be readily distinguishable in other systems. Thus, although we focus only on catalytic manifolds where a PET cycle is presumed, we recognize the possibility that some of the transformations we discuss may proceed partially or completely through energy transfer pathways. We discuss cases

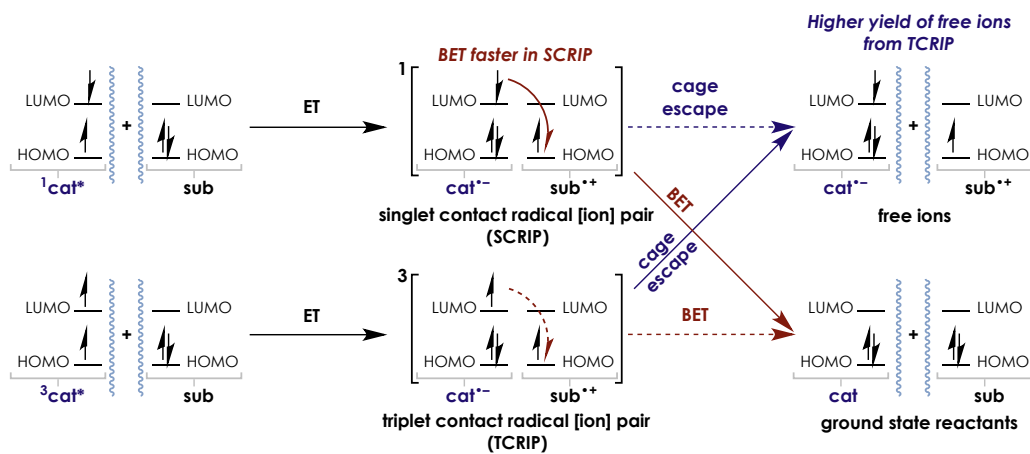
where the primary reports address the possible involvement of both pathways, but we also take note of a general observation that PET mechanisms seem to dominate even in examples where the photoredox catalyst is known to participate in either PET or energy transfer processes. For triplet sensitization, this may be rationalized by considering the relatively high triplet energies for typical organic molecules used as substrates in photoredox reactions, which usually exceed 60 kcal mol^{-1} (2.6 eV).¹⁴¹

1.3.2.4 Singlet or Triplet Excited States: does it matter?

It is clear from **Scheme 1.1** and the data in **Table 1.1** and **Table 1.2** that the S_1 states are more potent oxidants and reductants than the corresponding T_1 states. For this reason, S_1 states have a larger range of oxidizing or reducing capabilities, and can engage substrates with redox potentials high in magnitude. Interestingly, even though ET with a cat^* in the T_1 can occur with a fast bimolecular rate constant comparable to that of S_1 when ΔG_{PET} is largely negative for both states, the T_1 state may actually be less susceptible to back electron transfer (BET) between radical [ion] pairs.

Scheme 1.5 compares ET between **sub** and $^1\text{cat}^*$ or $^3\text{cat}^*$ for a reductive quenching event: the contact radical [ion] pairs following ET retain the overall spin multiplicity of the excited state catalyst. In either case, BET can lead to the free ions or the ground state reactants, but since BET in the triplet contact radical [ion] pair (TCRIP) would require an intersystem crossing, BET in the singlet contact radical [ion] pair (SCRIP) is faster. This is consistent with experimental studies in which the overall efficiency of free ion formation was higher when ET occurred from a triplet $^3\text{cat}^*$,¹⁴² with one study estimating that a $^3\text{cat}^*$ produced twice as many free ions as the corresponding $^1\text{cat}^*$.¹⁴³ Thus, for reactions whose efficiencies suffer from BET, the triplet state of the photoredox catalyst may be the most important excited state.

Scheme 1.5. Cage Escape and Back Electron Transfer (BET) in Singlet and Triplet Radical Ion Pairs



Note: Energy Levels of HOMO and LUMO are arbitrary and not scaled, as is the spacing between

CHAPTER 2: EXPERIMENTAL AND CALCULATED ELECTROCHEMICAL POTENTIALS OF COMMON ORGANIC MOLECULES FOR APPLICATIONS TO SINGLE-ELECTRON REDOX CHEMISTRY

Reproduced in part with permission from Roth, H.; Romero, N.; Nicewicz, D. *Synlett* **2016**, 27 (5), 714–723. Copyright 2015 Georg Thieme Verlag KG.ⁱ

2.1 Background: literature precedent and considerations for computational prediction of redox potentials

The complications associated with measuring accurate electrochemical potentials of organic molecules—particularly when irreversible couples are involved—has prompted the application of computational methods to electrochemical inquiries.^{122,144–148} Previous attempts to correlate redox potentials calculated by Density Functional Theory (DFT) with experimental data mostly rely on redox potentials gathered from multiple sources in the literature.^{122,145} Although these studies generally find at least moderate correspondence between calculation and experiment, comparison with a single source of electrochemical data would eliminate the difficulty in completely accounting for experimental differences (such as working electrode, reference electrode, and scan rate) when concatenating data from various sources. This motivated us to carry out DFT calculations on the data set presented herein.

The general procedure for theoretical prediction of redox potentials primarily involves calculation of the free energy difference ($\Delta G_{1/2}^{\text{o,calc}}$, **Equation 2.1**) between reduced and oxidized

ⁱ This chapter is presented as a truncated version of the article as it appeared in its original form¹⁰³ in order to emphasize the contribution of the first author, H. G. Roth, in collecting and compiling the experimental redox potentials listed in **Appendix A**. For a more complete discussion of the methods used in the collection of the electrochemical data, see Roth, H.; Romero, N.; Nicewicz, D. *Synlett* **2016**, 27 (5), 714–723.

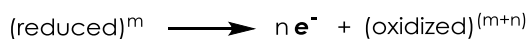
forms (**Scheme 2.1**), which is, in turn, related to $E_{1/2}^0$ by **Equation 2.2** by referencing to an absolute potential for a standard electrode.⁹⁵ Most studies to date have followed a free energy cycle to translate gas phase to solution phase energies,^{122,144} requiring separate calculation of the solvation energy associated with each species (i.e., reduced and oxidized). A related and operationally simpler approach is to calculate the free energies under a solvation model, thus calling for only two distinct steps which require significant computation.¹⁴⁴ By either approach, implicit solvation models can be employed successfully, although the most accurate results have been obtained when “custom” solvation parameters are determined by separate optimization.¹²² We were interested in evaluating a relatively simple computational procedure, with the hope that a more accessible method would be most widely useful.

Scheme 2.1. Half reactions for reduction and oxidation

For reduction:



For oxidation:



Equation 2.1

$$\Delta G_{1/2}^{\text{o,calc}} = G_{298}(\text{reduced}) - G_{298}(\text{oxidized})$$

Equation 2.2

$$E_{1/2}^{\text{o,calc}} = -\frac{\Delta G_{1/2}^{\text{o,calc}}}{n_e \mathcal{F}} - E_{1/2}^{\text{o,ref}}$$

2.2 Results and discussion: Calculation of solution phase redox potentials using Density Functional Theory (DFT)

With this in mind, we calculated the redox potentials for this data set with the frequently used B3LYP^{149,150} and M06-2X¹⁵¹ functionals, the split valence basis set 6-31+G(d,p),^{152,153} and the CPCM solvent continuum approach to account for solvation in MeCN.^{154,155} All calculations were carried out in Gaussian 09.¹⁵⁶ Structures were submitted to geometry optimization, with

frequency calculations performed on the optimized structures both to verify that the geometries were true minima and to calculate free energies at 298 K. The solution phase energies were referenced to SCE by subtraction of 4.281 V (abs. potential of SHE)⁹⁵ and 0.141 V (conversion of SHE to SCE in MeCN).⁹⁵ In some cases, minimized geometries could not be reached, owing to fragmentation of the one electron oxidized or reduced species (a pathway particularly relevant in alkyl and aryl halides), and no further analysis was carried out for these molecules. The potentials successfully computed with both functionals were compared with the experimental electrochemical potentials, and the results are shown in **Figure 2.1**. Both methodologies give a reasonable correlation with the experimental potentials, each exhibiting comparable variation (standard deviation of $(E_{\text{calc}}-E_{\text{exp}})$ for B3LYP = 0.30, and for M06-2X = 0.29; see **Appendix A, Figure A.17** and **Figure A.18**). Ultimately, B3LYP/6-31+G(d,p) offers better overall performance, seen as a near overlay of the regression with the black line representing an ideal agreement between theory and experiment. Whereas B3LYP slightly overestimates reduction potentials and slightly underestimates oxidation potentials, M06-2X overestimates oxidation potentials more significantly (**Appendix A, Figure A.18**), which largely contributes to the global deviation seen for M06-2X. Consideration of individual plots corresponding to the electrochemical series presented in **Figure A.1-Figure A.16 (Appendix A)** provides a measure of the strengths and weaknesses of this general analysis. Specifically, some electrochemical series reveal discrepancies between the calculated and experimental potentials for certain molecules. Conspicuously, DFT calculations overestimate the oxidation potentials for I⁻, Br⁻, and Cl⁻, by approximately 100% for each halide, and this may signal inadequate treatment of solvation, as previous studies found that use of doubly diffuse basis sets led to improved accuracy in anionic species.^{145,157} Other notable deviations in calculated oxidation potentials are

observed in the case of several aromatic heterocycles, such as imidazole and the series of thioamides benzoxazole-2-thione, benzothiazole-2-thione, and benzoimidazole-2-thione (**Figure A.7** and **Table A.7**), for which the potentials are overestimated by about 0.5 to 1.2 V. Although we investigated the 2-mercapto (thiol) form of the benzo-azoles, which showed no significant improvement, one study has suggested that the equilibrium between C=S and C-SH forms shifts towards the C-SH tautomer as the oxidation proceeds.¹⁵⁸ This is likely to complicate the computational analysis.

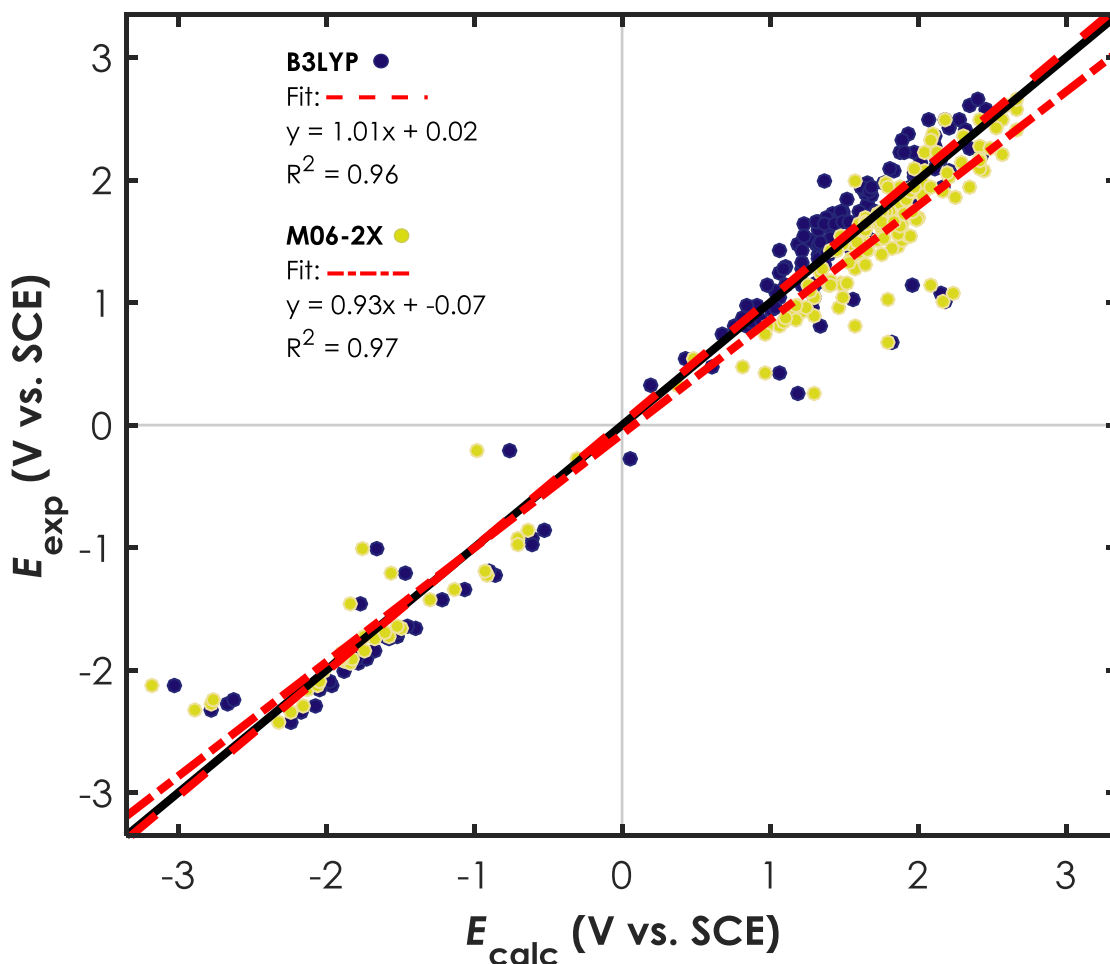


Figure 2.1. Plot of experimental versus calculated redox potentials for a series of organic compounds.

Despite the well-documented pitfalls of DFT in describing the electronic structure of anion radicals,^{159–162} we find that the calculated reduction potentials give a reasonable correlation with experiment. The most noticeable deviations occur in the overestimation of the reduction potentials for trifluoroacetic anhydride (**Figure A.12** and **Table A.12**) and gamma-butyrolactone (**Figure A.11** and **Table A.11**). Notably, the radical anions of these two structures exhibit pyramidalization of a C=O unit, in contrast to the other esters and anhydrides studied which possess extended π systems adjacent to the carbonyl available for delocalization of the added electron density. We speculate that the observed anomalies may be manifestations of DFT's difficulty in describing systems where symmetry or delocalization changes upon ionization.^{163,164}

Overall, the results of these computational studies reveal a reasonable correlation between experimental and theoretical electrochemical redox potentials when using a relatively simple and computationally efficient approach. While B3LYP appears to be the more accurate level of theory, both functionals give rise to deviations in selected cases. Nonetheless, we believe this study validates DFT as a useful tool in predicting solution phase redox potentials.

2.3 Associated Content

Appendix A: Computational details and results grouped by electrochemical series.

2.4 Acknowledgments

This research was supported by an NSF-CAREER grant (CHE-1352490). N.A.R. is also grateful for an NSF Graduate Fellowship.

CHAPTER 3: MECHANISTIC INSIGHT INTO THE PHOTOREDOX CATALYSIS OF ANTI-MARKOVNIKOV ALKENE HYDROFUNCTIONALIZATION REACTIONS

Reproduced with permission from Romero, N. A.; Nicewicz, D. A. *J. Am. Chem. Soc.* **2014**, *136* (49), 17024–17035. Copyright 2014 American Chemical Society.

3.1 Introduction

Alkenes are one of the most versatile chemical feedstocks and are key components of innumerable synthetic transformations. A particularly active field of catalysis utilizes alkene reactants in hydrofunctionalization reactions such as olefin hydroalkoxylation and hydroamination reactions.^{165–167} The vast majority of these alkene hydrofunctionalization reactions proceed with Markovnikov selectivity. In the past decade and a half, there have been significant efforts by a number of research laboratories to develop catalytic protocols to access the opposite regioisomeric hydrofunctionalization adducts,^{168–170} however a more general catalytic platform has yet to be identified.

To address this, our laboratory has recently developed a number of methods for alkene hydrofunctionalization^{171–176} that have demonstrated the unique synthetic control accessible through systems which rely upon the well-defined redox cycles of a photoredox catalyst.¹⁷⁷ These methods display complete anti-Markovnikov selectivity, employing a catalytic quantity of the organic dye 9-mesityl-10-methyl acridinium^{59,60,102,178–190} (**Mes-Acr⁺**)ⁱ as a photooxidant along with a co-catalyst proposed to be a redox-active hydrogen atom donor (**Figure 3.1**).

ⁱ The tetrafluoroborate (BF₄⁻) salt was employed in all studies herein; “Mes-Acr⁺” will be used synonymous to the 9-mesityl-10-methylacridinium cation when the counter-anion is irrelevant. Previous

One initial report from our group featured the use of Mes-AcrClO₄ as a catalytic photooxidant along with 50-200 mol % 2-phenylmalononitrile (**PMN**) as an H-atom transfer (HAT) reagent in a hydroetherification reaction that proceeds with complete regioselectivity.¹⁷¹ This is particularly noteworthy in the context of oxidative alkene functionalizations, which often result in over-oxidation and subsequent difunctionalization.¹⁹¹⁻¹⁹⁴ Further optimization of this and related transformations identified thiophenol (**PhSH**) and, intriguingly, diphenyl disulfide ((**PhS**)₂) as competent HAT catalysts, and these second-generation conditions have allowed for improved yields and drastically shortened reaction times. The increased efficiency rendered by arenethiol-based co-catalysts has enabled extension of this anti-Markovnikov methodology to include a diverse array of nucleophiles, including carboxylic acids,¹⁷² amines,^{173,174} mineral acids such as HF, HCl, and MsOH,¹⁷⁵ as well as propargylic and allylic alcohols and acids in a tandem addition-cyclization sequence.^{195,196} This demonstration of an efficient and broadly applicable complement to Markovnikov-selective protocols is a testament to the value of the alkene cation radical as an intermediate accessible *via* single electron transfer (SET).

studies indicate that the mesityl-acridinium salts of non-coordinating anions (e.g. PF₆⁻, ClO₄⁻) exhibit indistinguishable photophysical behavior.⁶⁰

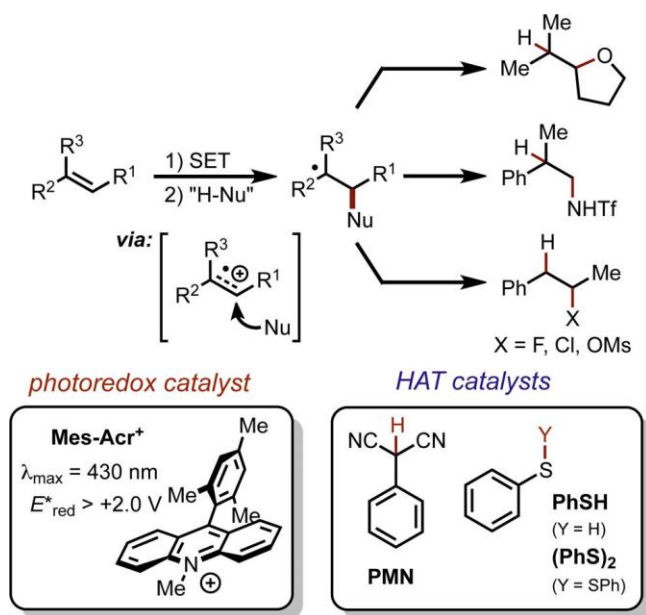
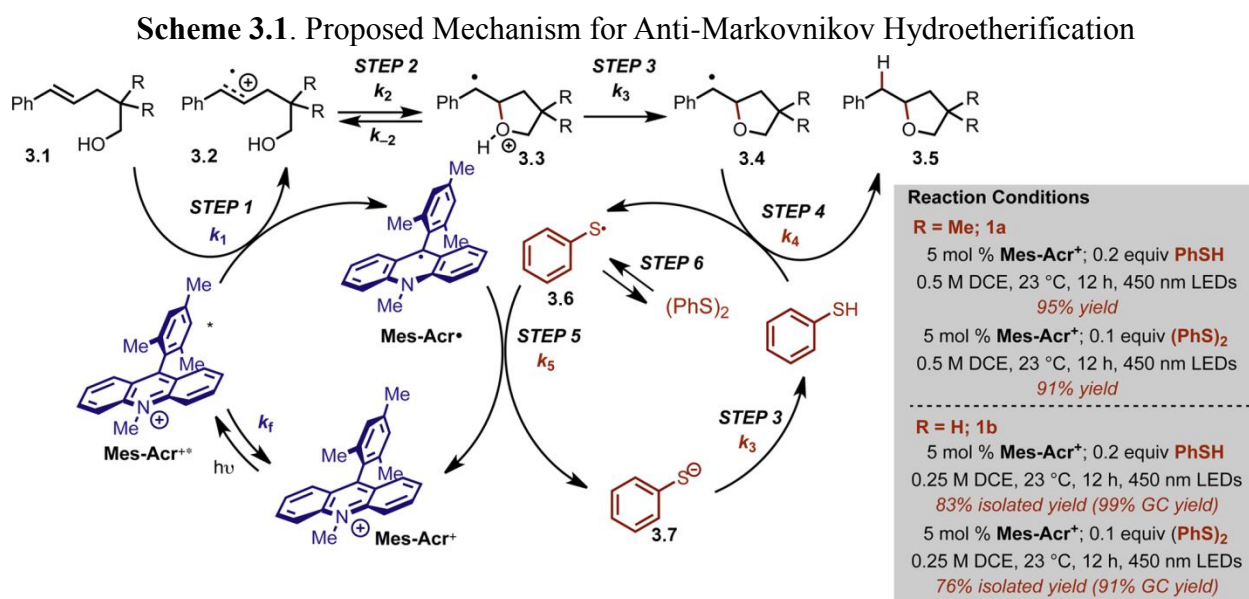


Figure 3.1. Anti-Markovnikov Hydrofunctionalization using **Mes-Acr⁺** as a photoredox catalyst and **PMN**, **PhSH**, or **(PhS)₂** as viable HAT catalysts.



As these transformations are all believed to proceed by a similar mechanism, we were eager to establish a more intimate understanding of the reaction mechanism in order to further expand the synthetic utility of this reaction class. We viewed the intramolecular hydroetherification of alkenols as a model transformation for this study. Our current mechanistic hypothesis is depicted in **Scheme 3.1**, using alkenol hydroetherification as a representative

example. Following single electron transfer from the alkene (**3.1**) to the electronically excited **Mes-Acr⁺**, the pendant alcohol undergoes intramolecular nucleophile addition to the alkenyl cation radical (**3.2**). Deprotonation of distonic cation radical **3.3** and subsequent hydrogen atom transfer (HAT) furnishes the cyclic ether (**3.5**). In the excited state, **Mes-Acr^{+*}** is thought to undergo one electron reduction from the alkene; however, exciplex-mediated cyclization has been implicated in similar systems.¹⁹⁷⁻²⁰³ The HAT catalyst is believed to operate in a concomitant redox cycle where HAT generates phenylthiyl radical (**PhS•**), which serves as a one electron oxidant for the acridine radical (**Mes-Acr•**). In this way, regeneration of ground state **Mes-Acr⁺** and proton transfer to the resulting thiolate (**3.7**) completes a net redox-neutral cycle. The efficacy of the arenethiol-based HAT catalysts has been attributed in part to the oxidizing nature of **PhS•** ($E_{1/2}^{\text{red}} = +0.16$ V vs. SCE),²⁰⁴ which is expected to be an excellent redox partner for oxidation of **Mes-Acr•** ($E_{1/2}^{\text{red}} = -0.55$ V vs SCE).¹⁷⁵

While many photoredox reactions feature additives that can greatly improve reaction efficacy through redox activity in parallel with the photosensitizer, few examples are truly catalytic with respect to the additive. In contrast, our system constitutes an interesting example where a redox active H-atom donor seems to be catalytically relevant in both electron and proton transfer steps. However, mechanistic analysis of such multi-component catalytic systems is notoriously challenging. To understand the interdependent nature of dual catalyst cycles requires an in-depth inquiry beyond macroscopic study of overall rate and reaction order. Thus, we sought to conduct kinetic studies on the elementary steps in the proposed reaction mechanism towards elucidation of the rate limiting factors. We took a tandem approach in our study of the mechanism: steady state and transient absorption and emission spectroscopies were employed in

determining rate constants for steps 1-2 & 5-6, while computational methods were utilized to offer complementary insight where spectroscopic study was impracticable (step 4).

3.2 Results and Discussion

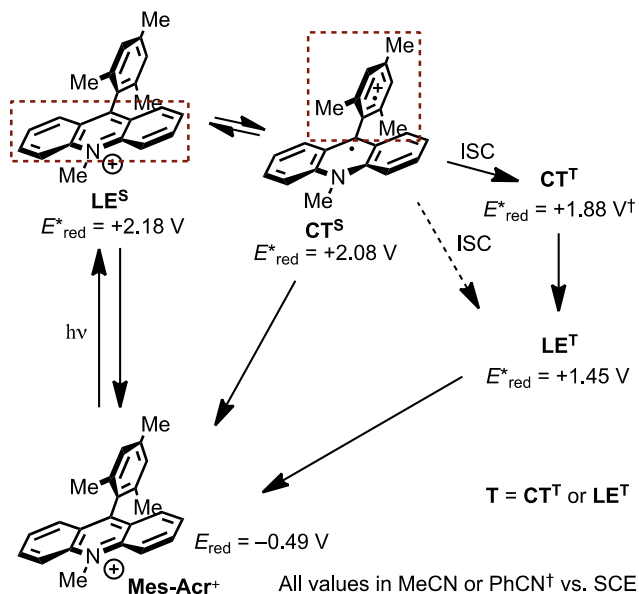
3.2.1 Oxidative Activity of Excited State Mes-Acr⁺

In order to address the photocatalytic activity of Mes-Acr⁺, we focused on the use of transient spectroscopic methods. Although Mes-Acr⁺ has been a well-studied, yet contentious chromophore in recent years, photophysical studies have been mainly directed towards characterization of its excited state topology (**Scheme 3.2**). Verhoeven, *et. al.* report that the first singlet excited state of Mes-Acr⁺, localized on the acridinium system (hereafter referred to as the locally excited singlet state or LE^S) undergoes rapid intramolecular charge transfer from acridinium to the mesityl substituent to form the singlet CT state (CT^S).⁶⁰ LE^S and CT^S are understood to be in thermal equilibrium, and fluorescence from both singlet states is measured on the nanosecond timescale. Moreover, both Fukuzumi and Verhoeven identify a long-lived transient species that is observed to decay on the order of microseconds following laser excitation. Much of the debate has centered on the identity of this microsecond transient species, suggested by Fukuzumi to possess CT character and an excited state reduction potential (E^*_{red}) of +1.88 V vs. SCE,¹⁰² while Verhoeven provides evidence that the species is the locally excited triplet state with $E^*_{\text{red}} = +1.45$ V vs. SCE.⁶⁰ In the absence of unambiguous evidence that the triplet state is comprised of two distinct states or that it is singly a CT or LE triplet, we will simply refer to this long-lived intermediate as the triplet (**T**), noting that **T** may denote CT^T (charge transfer triplet) or LE^T (locally excited triplet), or both.

In the course of our investigation, additional questions arose as to the photophysical nature of the excited state Mes-Acr⁺ in the midst of previous reports which draw varying

conclusions from spectroscopic data. A crucial difference in our work was the use of non-polar solvents such as 1,2-dichloroethane (DCE) rather than acetonitrile (MeCN), which was the medium employed in prior studies. Herein we share new evidence regarding the photophysical characteristics of **Mes-Acr⁺** and its ET behavior in oxidation reactions with alkenes.

Scheme 3.2. Excited State Energy Diagram Adapted from Verhoeven⁶⁰ and Fukuzumi¹⁷⁸



3.2.1.1 Fluorescence quenching: Rate of Primary Electron Transfer k_1 .

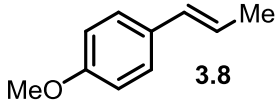
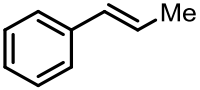
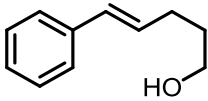
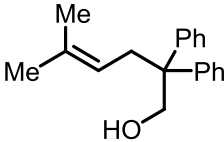
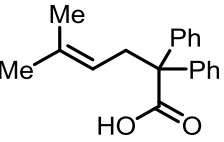
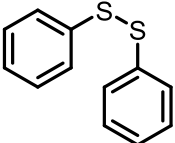
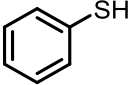
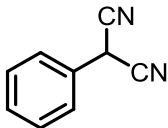
Of the reports where **Mes-Acr⁺** is used as a preparative photolytic oxidant, the long lived transient (**T**) has been primarily implicated in inquiries of its excited state oxidative capacity.^{179,182–184,186,187,205} Although Fukuzumi presents evidence that **T** is responsible for oxidation of arenes with moderate oxidation potentials (e.g., anthracene; $E_{\text{ox}} = +1.19 \text{ vs. SCE}$ ¹⁷⁹), the oxidation potentials of many substrates employed in our methodology (e.g., **3.9-3.11**, **Table 3.1**) approach or exceed the excited state reduction potential of **T** (E_{red}^*), which is estimated to lie between +1.45 V and +1.88 V vs. SCE based on the values reported by Verhoeven and Fukuzumi, respectively. Thus, while we acknowledged the possibility **T** could undergo reduction from more oxidizable alkenes (e.g., **3.8**, **3.9**, and **3.1b** in **Table 3.1** could be oxidized by CT^T), it

seemed unlikely that **T**-mediated oxidation could be general with respect to all alkenes used in our system, on the grounds that SET from alkenes **3.1** to **T** is endergonic in the cases where $E_{p/2}$ of the alkene exceeds +1.88 V. We considered the possibility that a viable pathway for oxidation is through SET to a singlet excited state of **Mes-Acr**⁺ (both **LE**^S and **CT**^S are estimated to have excited state reduction potentials exceeding +2.0 V vs. SCE).⁶⁰ Since both singlet states are fluorescent, we elected to measure the rate of electron transfer by Stern-Volmer analysis of **Mes-Acr**⁺ fluorescence quenching.¹¹³

Employing Time-Correlated Single Photon Counting (TCSPC), we measure a fluorescence lifetime of 6.40 ± 0.03 ns for Mes-AcrBF₄ in DCE.ⁱⁱ Stern-Volmer analysis was carried out on the observed quenching of fluorescence lifetime at increasing concentration of the quenchers given in **Table 3.1**. Anethole (**3.8**) quenches **Mes-Acr**⁺* most efficiently with a second order rate constant ($9.9 \pm 0.1 \times 10^9$ M⁻¹s⁻¹) near the diffusion limit, while even the poorly oxidizable alkenoic acid **3.11** quenches **Mes-Acr**⁺* with a rate constant of $6.1 \pm 0.2 \times 10^8$ M⁻¹s⁻¹. Significantly, quenching of fluorescence is not observed for **PMN**, whereas both **PhSH** and **(PhS)**₂ are competent quenchers at rates competitive with the alkenes studied.

ⁱⁱ Compare with a lifetime of 6.0 ns as measured by Verhoeven with the PF₆⁻ salt.⁶⁰ We also measured the fluorescence lifetime of Mes-AcrBF₄ in MeCN to be 7.3 ns. These values are reasonably consistent with the fluorescence lifetimes reported by Verhoeven, et. al.

Table 3.1. Mes-Acr⁺ Fluorescence Quenching by Alkenes and HAT Catalysts

quencher	K_{SV} (M ⁻¹) ^a	k_1 (M ⁻¹ s ⁻¹) ^b	$E_{p/2}$ ^c
 3.8	63.2	9.85×10^9	1.34
 3.9	44.4 (136) ^d	6.92×10^9 (7.84×10^9) ^d	1.77
 3.1b	37.5	5.85×10^9	1.86
 3.10	7.53	1.18×10^9	2.09
 3.11	3.88	6.10×10^8	2.18
 3.12	40.5	6.40×10^9	1.71
 3.13	53.5	8.47×10^9	1.60
 PMN	–	–	–

^a K_{SV} : Stern-Volmer Constant; error < 5% (estimated from multiple trials). ^b k_1 : bimolecular quenching constant (i.e. k_q) where $k_1 = K_{SV}/\tau_0$; error < 6% (error in $\tau_0 = 0.5\%$). ^cV vs. SCE; Irreversible half wave potential measured by cyclic voltammetry (sweep rate = 100 mV/s). ^dXyl-Acr⁺ as the fluorophore.

Figure 3.2 shows the quenching constant, k_1 , plotted against the thermodynamic driving force ΔG° calculated from one electron oxidation potentials ($E_{p/2}$) of each quencher and the excited state reduction potential for **Mes-Acr⁺** ($E_{\text{red}}^*(\text{LE}^{\text{S}}) = +2.12$ V vs. SCE; Appendix B **Figure B.3**). The trend of this Rehm-Weller plot reveals a plateau in the rate of quenching as k_1 approaches the diffusion limit, characteristic of a mechanism of quenching which proceeds *via* electron transfer.^{113,206} Furthermore, these results indicate that alkene oxidation by way of the singlet excited states of **Mes-Acr⁺** is a feasible pathway for all substrates examined.

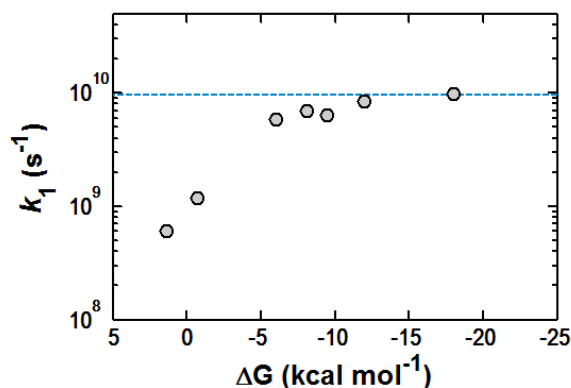


Figure 3.2. Rehm-Weller Plot for k_1 as determined by Stern-Volmer analysis of **Mes-Acr⁺** fluorescence quenching where [**Mes-Acr⁺**] = 16 μM in DCE. Dashed blue line represents the diffusion limit in DCE ($k_{\text{diff}} \approx 9.5 \times 10^9 \text{ s}^{-1}$) estimated using the modified Debye equation.ⁱⁱⁱ

3.2.1.2 Emission Spectroscopy: Role of LE^S and CT^S states in oxidative activity of Mes-Acr⁺.

Although the above fluorescence quenching analysis clarifies that photoinduced electron transfer can be effected by a singlet state, it does not explicitly address whether the singlet state responsible for alkene oxidation is LE or CT in nature. At the wavelength of detection for fluorescence decay (515 nm), the contribution from CT emission is expected to be minimal (see

ⁱⁱⁱ The diffusion limiting rate in DCE is estimated by the modified Debye equation²⁰⁷ of the form: $k_{\text{diff}} = 2RT(2+r_1/r_2+r_2/r_1)/3000\eta$ where R = universal gas constant; $T = 298$ K ; r_1 and r_2 are the collisional radii of the acridinium and quencher, respectively; η (viscosity of DCE at 298 K) = 0.779 mPa·s;²⁰⁸ r_1/r_2 is estimated to be roughly 2, returning a value of $\sim 9.5 \times 10^9 \text{ s}^{-1}$.

Supporting Information (Appendix B), **Figure B.3**), a finding consistent with the records reported by Verhoeven.⁶⁰ Yet, because LE^{S} and CT^{S} exist in equilibrium—a feature emphasized by the variable temperature emission spectra shown in **Figure 3.3**—the particular behavior of each individual singlet state is not easily extracted. Although seemingly a trivial question, we recognized that this detail has important implications in the design of more powerful photooxidants based on the mesityl-acridinium template. For example, if the active oxidant is a CT^{S} state, then the oxidizing power of any mesityl-acridinium possessing a CT^{S} state is approximately limited to the redox potential of the mesityl- cation radical. Alternatively, if the active oxidant is the LE^{S} state, then development of more oxidizing acridinium catalysts should focus on suppressing *intramolecular* charge transfer as a superfluous pathway.

To investigate this behavior, we compared the fluorescence properties of **Mes-Acr⁺** to that of the 9-xylyl analog (**Xyl-Acr⁺** = 9-mesityl-10-methylacridinium tetrafluoroborate),²⁰⁹ which does not form a CT state in DCE,^{iv} yet is seen to undergo fluorescence quenching (see **Table 3.1**, footnote *d*). The emission spectrum of **Mes-Acr⁺** in MeCN shows a strong emission band centered around 570 nm that confirms the existence of a CT^{S} state previously observed.^{58,210} CT^{S} is in equilibrium with LE^{S} , with emission centered around 500 nm (**Figure 3.1a**). Variable temperature emission spectra for **Mes-Acr⁺** reveal a decrease in CT^{S} fluorescence at elevated temperature as thermal repopulation of the LE^{S} becomes more significant, seen also as an increase in the LE^{S} emission component (**Figure 3.1a**).⁶⁰ In DCE, the emission spectrum for **Mes-Acr⁺** exhibits features of both LE^{S} and CT^{S} states, but differs from the spectrum in MeCN in that the LE^{S} appears more pronounced (**Figure 3.1b**). In contrast, **Xyl-Acr⁺** exhibits a

^{iv} Kuruvilla and Ramaiah²⁰⁹ report that the iodide salt of Xyl-Acr⁺ possesses a CT-singlet state in an aqueous buffer, exhibiting a contracted fluorescence lifetime ($\tau = 3.6$ ns) compared the value measured in DCE in our hands ($\tau = 17$ ns).

comparatively narrow emission band and lacks CT fluorescence on the low-energy side as seen in **Mes-Acr**⁺ (**Figure 3.1c**). Variable temperature studies on **Xyl-Acr**⁺ reveal no change in the shape of fluorescence, and only a decrease in quantum yield (Appendix B, **Figure B.6**) is seen as temperature is increased, leading to the conclusion that the locally excited singlet state of **Xyl-Acr**⁺ is most prominent in DCE.

Having confirmed that **Xyl-Acr**⁺ exhibits no discernible CT fluorescence, we compared the rate of fluorescence quenching in **Xyl-Acr**⁺ to that of **Mes-Acr**⁺. We discovered that **Xyl-Acr**⁺ exhibits an enhanced fluorescence lifetime of 17 ± 0.8 ns, and is quenched by β -methylstyrene (**3.9**) with an even larger rate constant ($k_1 = 7.8 \pm 0.3 \times 10^9 \text{ M}^{-1}\text{s}^{-1}$) than is **Mes-Acr**⁺ ($6.9 \pm 0.3 \times 10^9 \text{ M}^{-1}\text{s}^{-1}$). Because emission from **Xyl-Acr**⁺ occurs primarily from an **LE**^S state, this finding demonstrates that the **CT**^S is not required for productive quenching. Furthermore, observation of a significantly longer fluorescence lifetime ($\tau_{\text{LE}}^{\text{S}}$) for **Xyl-Acr**⁺ emphasizes that **CT**^S is formed by intramolecular quenching of **LE**^S in **Mes-Acr**⁺.^{58,60,210} That **Xyl-Acr**^{+*} undergoes SET from alkenes faster than **Mes-Acr**^{+*} suggests that the **CT**^S is an unnecessary photophysical pathway for catalysts of this type. In fact, formation of **CT**^S may decrease the likelihood of alkene oxidation by competitive quenching of the longer-lived **LE**^S. While this example does not preclude that the active oxidant in **Mes-Acr**⁺ is the **CT**^S, it does reveal that an intramolecular charge transfer state is not essential to the oxidative activity of this acridinium class. We view these results as having important implications for catalyst development through future modifications to the currently deployed scaffold.

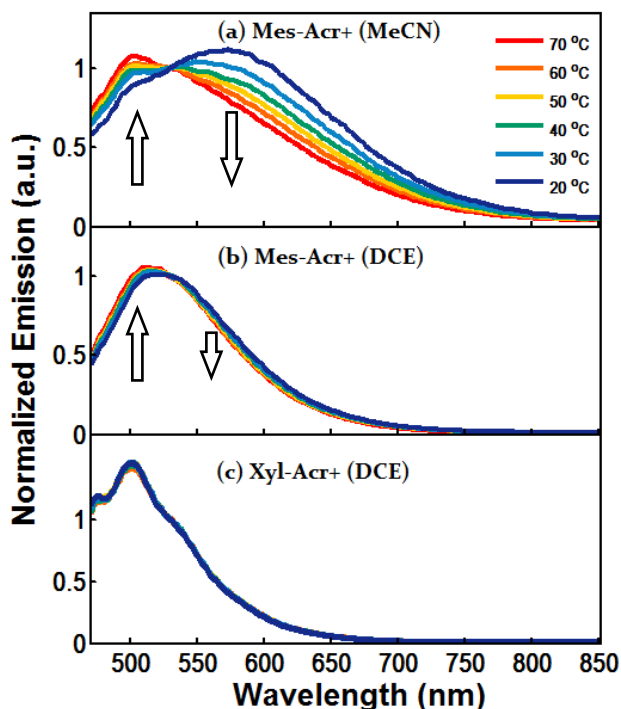


Figure 3.3. Variable temperature fluorescence spectra of **Mes-Acr⁺** in (a) MeCN and (b) DCE and of (c) **Xyl-Acr⁺** in DCE ($\lambda_{\text{ex}} = 450 \text{ nm}$). Spectra normalized to 530 nm to show decrease in CT and increase in LE components with increasing temperature.

3.2.1.3 Laser Flash Photolysis: Detection of Cation Radical Intermediates.

While absorbance spectra for styrenyl cation radicals have been reported upon generation in a solid matrix,²¹¹ key studies by Johnston and Schepp elucidated the solution phase spectra and kinetic behavior of styrenyl cation radicals when reacted with various nucleophiles.^{212–216} In light of this precedent, we felt confident that we could observe cation radicals (**3.2**) as intermediates upon Laser Flash Photolysis (LFP) with **Mes-Acr⁺**, given that the absorption for the cation radical ($\lambda_{\text{max}} = 590\text{-}600 \text{ nm}$) was expected to be spectrally separated from the transient signal for both **T** ($\lambda_{\text{max}} = 500 \text{ nm}$) and **Mes-Acr•** ($\lambda_{\text{max}} = 520 \text{ nm}$).

Laser flash photolysis was first performed on a 50 μM solution of Mes-AcrBF₄ in DCE in order to determine the transient absorption spectrum for **T** and to establish a point of reference with prior photophysical studies. Although the transient absorption spectrum for the triplet matches the previously reported spectra closely, the observed microsecond transient decays with

complicated kinetics (Appendix B, **Figure B.10** and **Figure B.11**). The kinetic model used to achieve a best fit to the signal decay at 480 nm contained a first-order exponential ($\tau_T = 36 \mu\text{s}$) and a second-order term ($\tau_T = 0.25 \mu\text{s}$). The lifetime of the first order decay constant is similar to that calculated by Verhoeven in MeCN, while a second-order decay component has been observed by Fukuzumi, who determined that bimolecular decay results from formation of a **T···T** dimer.¹⁸⁵

When laser flash photolysis is performed on **Mes-Acr**⁺ with anethole (**3.8**), the anethole cation radical **3.8**⁺• is detected by a new feature at 600 nm in the transient absorption spectrum after laser excitation of **Mes-Acr**⁺ at 430 nm (**Figure 3.4a**). The absorption spectrum for the anethole cation radical is calculated by subtraction of the contribution from **Mes-Acr**•, which was determined by spectroelectrochemical analysis (Appendix B, **Figure B.1** and **Figure B.10**). The anethole cation radical **3.8**⁺• possesses a maximum near 600 nm, and is in close agreement with the spectrum reported previously.²¹² Styrenyl cation radicals were also detected at a 20 ns time delay for β -methylstyrene (**3.9**), alkenol **3.1b** and TBDMS-protected alkenol **3.14** using the same method of Laser Flash Photolysis (**Figure 3.4b**; see Appendix B, **Figure B.12-Figure B.14** for curve fitting procedure). Centered roughly at 590 nm, these spectra likewise match the absorption spectra for β -alkyl cation radicals reported in the literature.^{211,217} The difference spectrum for protected alkenol cation radical **14** exhibits a maximum at 590 nm, and a corresponding absorbance for free alkenol **3.1b** is observed with a maximum at the same wavelength, though this signal is significantly lessened at the 20 ns time delay.

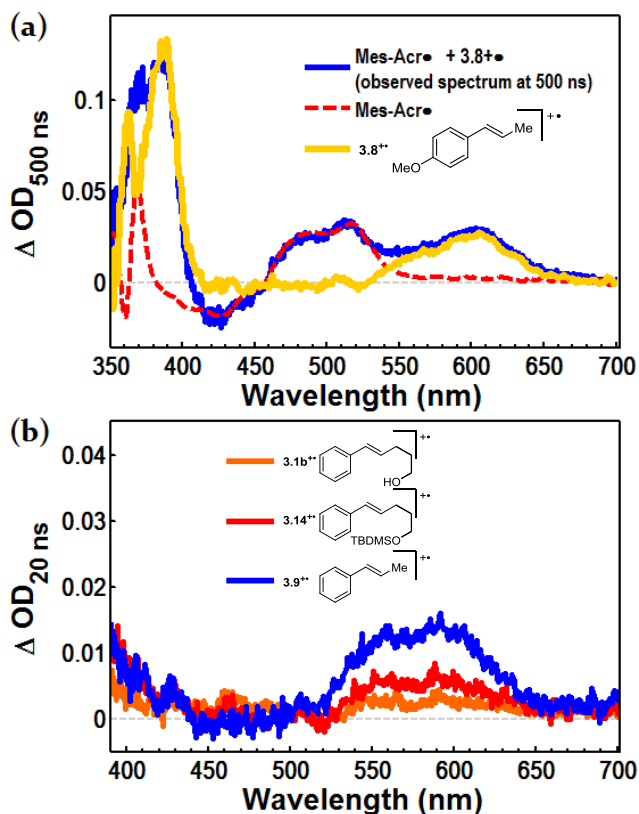


Figure 3.4. Detection of alkenyl cation radicals by Laser Flash Photolysis where $[\text{Mes-Acr}^+] = 50 \mu\text{M}$ in DCE. (a) The differential absorption spectrum for $\mathbf{8}^{\dagger\bullet}$ (yellow) obtained by subtraction of **Mes-Acr** \cdot from the transient absorption spectrum at 500 ns. (b) The differential absorbance spectra for cation radicals $\mathbf{3.1b}^{\dagger\bullet}$, $\mathbf{3.14}^{\dagger\bullet}$, and $\mathbf{3.9}^{\dagger\bullet}$ (orange, red and blue, respectively) obtained by subtraction of **Mes-Acr** \cdot and LE^{T} from the transient absorption spectrum recorded 20 ns after the laser pulse. OD = optical density, or absorbance.

Comparison between the lifetime of each cation radical **3.1b** and **3.9** allows for estimation of the rate of cyclization (k_2). Single wavelength kinetic decay (Appendix B, **Figure B.12-Figure B.14**) of the signal at 590 nm for TBDMS-protected alkenol **3.14** persists well into the microsecond regime ($\tau = 5.9 \mu\text{s}$), while a signal for cation radical **3.1b** cannot be detected at 590 nm at a time delay of 40 ns. We interpret this comparison to signify consumption of the styrenyl cation radical by nucleophilic addition of the tethered oxygen-nucleophile in **3.1b**. Based on the observation that cation radical **3.1b** cannot be detected beyond 40 ns, the first-order

rate constant for intramolecular nucleophile addition is estimated to have an approximate lower limit of $2.5 \times 10^7 \text{ s}^{-1}$ for this class of alkenols.^v

3.2.1.4 Triplet or Singlet?

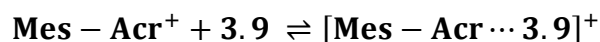
While quenching of singlet state **Mes-Acr**^{+*} is observed for all substrates in **Table 3.1** with large bimolecular rate constants k_1 , we noted that the efficiency of fluorescence quenching is generally low due to the short fluorescence lifetime of 6.4 ns. For example, when alkene **3.9** is the quencher, roughly 20% of fluorescence is quenched at a concentration of $[\mathbf{3.9}] = 6.0 \text{ mM}$ (Appendix B, **Figure B.9**). In combination with a poor quantum yield of fluorescence ($\Phi_F = 8\%$; Appendix B, **Figure B.7**), this corresponds to an oxidation quantum yield of roughly 1.6% at this concentration. Under the conditions where cation radical **3.9**⁺• was detected by transient absorption spectroscopy (**Figure 3.4b**; $[\mathbf{3.9}] = 6.0 \text{ mM}$, $[\text{Mes-AcrBF}_4] = 0.050 \text{ mM}$), the estimated maximum concentration of both **3.9**⁺• and **Mes-Acr**• is $0.8 \mu\text{M}$ following quenching of the singlet. However, based on the absorption for **Mes-Acr**• at 20 ns (Appendix B, **Figure B.12**), the actual concentration of **Mes-Acr**• (and **3.9**⁺•) is $2.4 \mu\text{M}$. Thus, regarding singlet **Mes-Acr**^{+*} as the sole oxidant is inconsistent with the ca. 3-fold greater formation of **3.9**⁺• than is predicted. This disparity leads us to believe that the singlet manifold of **Mes-Acr**⁺ is not the *exclusive* pathway for oxidation in the case of **3.9**.

As previously noted, the triplet state **T** may be sufficiently oxidizing to undergo reduction by **3.9** (and other alkenes with less positive oxidation potentials). Indeed, given that the singlet excited states are insufficient to explain the degree of cation radical formation in **Figure 3.4b**, it

^v This is in good agreement with values published by Johnston and Schepp on the rate of nucleophilic addition to substituted styrene cation radicals by various nucleophiles.²¹² Addition of alcohols to β -methylstyrene takes place with second order rate constants ranging from 1.0×10^6 to $1.1 \times 10^7 \text{ M}^{-1}\text{s}^{-1}$. One would expect the intramolecular addition to occur even faster.

is our conclusion that **3.9** can be oxidized by both the singlet and triplet excited states of **Mes-Acr⁺**. However, in our attempt to address the dynamics of alkene oxidation, we discovered that **Mes-Acr⁺** forms ground state donor-acceptor complexes with alkenes (Equation 3.1; see also Appendix B, **Figure B.23** and **Figure B.24**), resulting in some degree of pre-association of the quencher with **Mes-Acr⁺**. For the portion of **Mes-Acr⁺** complexed with the alkene as [**Mes-Acr⋯3.9**]⁺, excitation of the acridinium chromophore to **LE^S** can be followed by rapid electron transfer, likely faster than diffusion or excited state deactivation by fluorescence or intersystem crossing.¹²⁵ Thus, if the efficiency of this electron transfer is assumed to be unity, the concentration of **3.9⁺** generated from irradiation of [**Mes-Acr⋯3.9**]⁺ can be estimated as the concentration of the complex [**Mes-Acr⋯3.9**]⁺ upon determination of the equilibrium constant K_{DA} .

Equation 3.1



Using the Benesi-Hildebrands method,^{218–220,vi} we estimate the equilibrium constant K_{DA} to be 0.96 M⁻¹. When applied to the conditions used in the spectroscopic analysis of **Figure 3.4b**, an additional 0.3 μM **3.9⁺** can be accounted for as originating from a donor-acceptor complex. In combination with the 0.8 μM generated by diffusion-limited quenching of the singlet state, we estimate that singlet **Mes-Acr⁺** is responsible for roughly 45% (1.1 μM) of **3.9⁺** shown in **Figure 3.4b**, while the other 55% is most likely formed by reductive quenching of a triplet **T**. In this case, ET to **LE^T** would be disfavored, so the probable identity of **T** is **CT^T** according to the assignment by Fukuzumi ($E^*_{red} = +1.88$ V vs. SCE for **CT^T**).

^{vi} Although we are aware of the propensity of the Benesi-Hildebrand Method towards erroneous results,²¹⁹ the value for K_{DA} obtained is within reason of the association constant estimated previously for an acridinium donor acceptor complex.²²⁰

Importantly, we note that the preparative reactions are carried out at drastically higher concentrations than those used in spectroscopic studies (see **Scheme 3.1**). At higher concentrations, the proportion of $[\text{Mes-Acr}\cdots\mathbf{3.9}]^+$ approaches that of free Mes-Acr^+ , which has the effect of increasing the efficiency of $\mathbf{3.9}^+$ formation, even though the solutions are optically dense (i.e., $\text{Absorbance}_{450\text{nm}} \gg 2.0$). Thus, while increasing the overall concentration does not increase the number of photons absorbed, it may increase the efficiency of oxidative quenching due to increased donor-acceptor complexation. Interestingly, the photochemical quantum yield of reaction (Φ_R) was determined to be $\sim 1.7\%$ at full conversion for the reaction of **3.1b** with 0.1 eq. PhSH as the H-atom donor.^{vii} At earlier time points ($t < 20$ min), Φ_R is slightly higher ($\sim 2.3\%$), consistent with additional efficiency conferred by complexation when the substrate concentration is highest. Notably, the overall quantum efficiency of the reaction is compatible with the degree of fluorescence quenching observed for this substrate, supporting our mechanistic hypothesis for alkenes with high oxidation potentials.

3.2.2 Role of Thiol and Disulfide Co-Catalysts

3.2.2.1 Disulfide Exchange Experiments

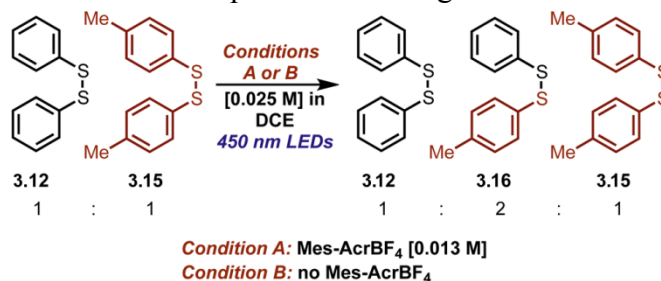
Our lab has reported the use of diphenyl disulfide (PhS)₂ as a HAT co-catalyst in place of **PhSH**. Although initially puzzling, we proposed that the activity of (PhS)₂ could be understood to operate on the same mechanistic landscape as **PhSH** if either $\text{PhS}\cdot$ or PhS^- was generated *in situ* from the disulfide (step 6). In this respect, it is important to note that (PhS)₂ can be isolated as a minor byproduct when **PhSH** is used as an HAT catalyst. Conversely, significant amounts of **PhSH** are detected in reactions employing (PhS)₂, implicating a possible equilibrium between

^{vii} The photochemical quantum yield of reaction was determined by chemical actinometry using Potassium Ferrioxalate. See Supporting Information for details.

the two species. Thus, we were eager to understand how the activity of the **(PhS)₂** and **PhSH** might be mechanistically related.

Given the sulfur-sulfur bond dissociation energy of **(PhS)₂**,²²¹ we reasoned that a homolytic mechanism was more likely than reductive cleavage in a redox system which lacks a strong reductant, given the highly negative reduction potential of **(PhS)₂** ($E_p = -1.65$ V vs. Ag/AgCl).^{222,223} Both oxidative^{224–226} and triplet-sensitized²²⁷ mechanisms of S-S cleavage have been proposed for aryl- and alkyl-disulfides. While direct homolytic mechanisms are well known in the literature,²²⁸ we were unaware of any previous report where an aryl disulfide is cleaved by irradiation with visible light. In order to evaluate the possibility of homolytic disulfide cleavage, we designed a crossover experiment with disulfide **(4-MePhS)₂** (**3.15**) as a “labeled” analogue to **(PhS)₂**.²²⁷ Disulfide **3.15** was selected as a suitable “labeled” phenyl-disulfide as it affords a tractable difference in chromatographic mobility and mass-spectral signature without possessing a significant difference in dissociative behavior.^{221,viii} In the event of homolysis, crossover of the arylthiyl units would be observed (whether by radical-radical recombination or by a homolytic substitution mechanism), which could be detected by gas chromatography as the symmetrical disulfides **3.12** and **3.15** exchange to form mixed disulfide **3.16** (**Scheme 3.3**).

Scheme 3.3. Disulfide Crossover Experiment Probing Mechanism of Disulfide Homolysis

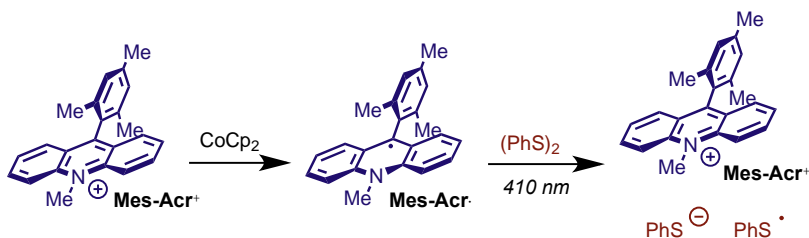


^{viii} Although we were unable to locate any report of the BDE for **(4-MePhS)₂**, the S-H BDE for 4-MePhSH (~78-85 kcal mol⁻¹) differs very little from that for PhSH (~79-84 kcal mol⁻¹) as noted by Luo.²²¹

Under conditions directly analogous to the preparative reaction conditions (i.e., total disulfide concentration = 25 mM), the rate of exchange was monitored by GC-MS. Under irradiation of an equimolar solution of (**PhS**)₂ (**3.12**), (4-MePhS)₂ (**3.15**) and Mes-AcrBF₄ (13 mM in each) with a blue LED lamp (Condition A), we observed disulfide crossover, with **3.16** formed in a ratio of 2:1:1 with respect to the symmetrical disulfides after approximately 120 minutes (Appendix B, **Figure B.20**). We were surprised to find that irradiation in the absence of Mes-AcrBF₄ (Condition B) gave rise to disulfide **3.16**, with apparent zero-order behavior until the equilibrium disulfide amounts were reached. Dark control experiments show no exchange within the analytical limits of the experiment at both room temperature and heating to 40 °C. Although we are unaware of any precedent where an aryl disulfide was cleaved with such low energy radiation, the spectral overlap between the disulfide solution and the emission output of the LED lamp is evident (Appendix B, **Figure B.22**).

These results indicate that the aryl disulfide bond can be homolytically cleaved directly in a light-dependent reaction, consistent with the zero-order behavior seen when **Mes-Acr**⁺ is absent. Presumably, the mechanism of disulfide exchange is different in the presence of the **Mes-Acr**⁺, as the mixed disulfide **3.16** forms with more complicated kinetics under Condition A. Considering that (**PhS**)₂ quenches **Mes-Acr**^{+*} fluorescence (**Table 3.1**), oxidation of (**PhS**)₂ to the cation radical (**PhS**)₂⁺• followed by sulfur-sulfur cleavage seems like a plausible mechanistic step. Additionally, triplet sensitization and subsequent homolysis is also possible. However, as it relates to the preparative reactions, we observe that **Mes-Acr**⁺ bleaches after approximately 3 minutes (*vide infra*) before the disulfide undergoes significant exchange. Thus, because **Mes-Acr**⁺ is not present in a photo-active form for a majority of the reaction, direct photolytic homolysis is the most mechanistically relevant possibility.

Scheme 3.4. Chemical Reduction of Mes-Acr⁺ and Reoxidation *via* PhS• by Laser Flash Photolysis of (PhS)₂



3.2.2.2 Laser Flash Photolysis: Direct Observation and Rate of Mes-Acr• Oxidation (k_5) by PhS•

We viewed the photooxidant regeneration step 5 as vital in understanding the efficacy of the HAT catalyst and how the rate of this step affects the overall kinetics. Although there is literature precedent suggesting that the phenyl-thiyl radical **PhS•** would be capable of oxidizing the crucial intermediate **Mes-Acr•**,^{204,229} a fast dimerization process (Step 6) might be expected to compete with electron transfer (Step 5). Having characterized **Mes-Acr•** in isolation by spectroelectrochemical methods, we were optimistic that we could take advantage of the persistence of this acridinyl radical in a kinetic study of the regeneration event described by the rate constant k_5 . We anticipated that laser-induced generation of **PhS•** by LFP^{204,227,230–234} would allow us to monitor the oxidation of **Mes-Acr•** by transient absorption spectroscopy. To this end, we successfully prepared **Mes-Acr•** by chemical reduction with stoichiometric CoCp₂ (**Scheme 3.4**).^{235–237} The acridinyl radical **Mes-Acr•** was indefinitely persistent at room temperature under dark, anaerobic conditions (Appendix B, **Figure B.16**).

To generate **PhS•** by photolysis of (PhS)₂ while minimizing excitation of **Mes-Acr•**, we selected a laser excitation wavelength of $\lambda_{\text{ex}} = 410$ nm, where **Mes-Acr•** absorption is at a minimum. We confirmed that **PhS•** could be generated under these conditions, decaying by second order kinetics ($2k_r = 2.7 \times 10^6 \text{ M}^{-1}\text{s}^{-1}$, Appendix B, **Figure B.18a**)²³³ independent of pump wavelength. When **Mes-Acr•** was prepared in a solution containing (PhS)₂ and subjected to laser

photolysis at 410 nm, a bleach in the signal at 520 nm was observed concomitant with a recovery of the **Mes-Acr**⁺ absorption at 445 nm. The bleach at 520 nm can be fit to a monoexponential curve with an observed rate constant $k = 2.5 \pm 0.4 \times 10^5 \text{ s}^{-1}$ (**Figure 3.5a**). At this wavelength, absorbance due to **PhS**[•] is insignificant. However, the kinetics of **Mes-Acr**⁺ appearance at 445 nm are more complex due to the absorption of **PhS**[•] in this wavelength range ($\epsilon \approx 2000 \text{ M}^{-1}\text{cm}^{-1}$ at 460 nm).²³⁸

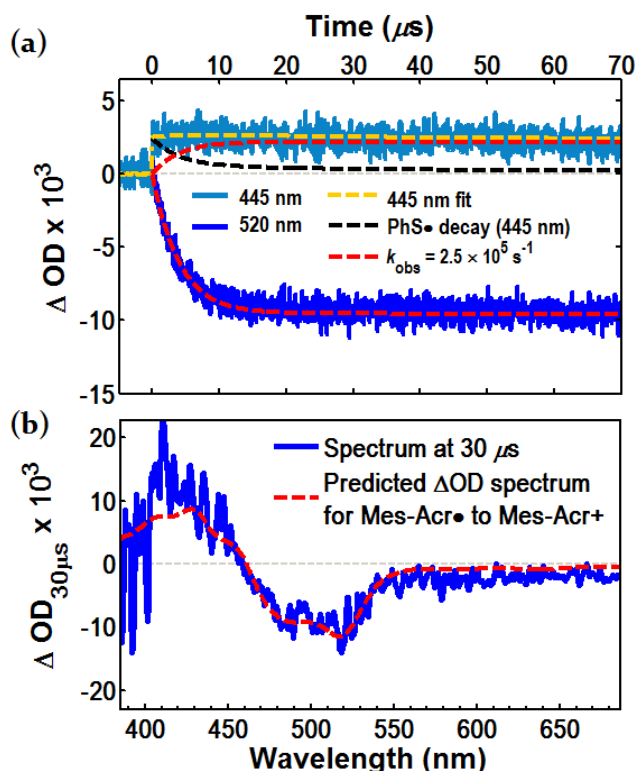


Figure 3.5. Direct observation of **Mes-Acr**[•] turnover by **PhS**[•] generated during LFP with excitation at 410 nm. (a) Bleach in absorbance at 520 nm (blue) corresponding to consumption of **Mes-Acr**[•]; fit to a monoexponential curve (dashed red) with an observed rate constant of $2.5 \pm 0.4 \times 10^5 \text{ s}^{-1}$; growth of the signal at 445 nm (light blue) corresponds to appearance of **Mes-Acr**⁺ and decay of **PhS**[•] and is fit to a curve (dashed yellow) consisting of a single exponential describing **Mes-Acr**⁺ appearance (dashed red) and mixed-order decay of **PhS**[•] (dashed black). (b) Transient difference spectrum at a 30 μs time delay. The dashed red trace is the predicted difference spectrum for 1:1 conversion of **Mes-Acr**[•] to **Mes-Acr**⁺.

As shown in **Figure 3.5a**, the transient signal at 445 nm is a combination of **Mes-Acr⁺** growth and **PhS•** decay^{ix} from an initial maximum of ~2.5 mΔOD (OD = optical density, or absorbance). After taking **PhS•** decay into account,^{230,239–242} a single exponential fit describes the growth of **Mes-Acr⁺** with an observed rate constant $k = 2.5 \times 10^5 \text{ s}^{-1}$, confirming that **Mes-Acr⁺** grows in at the same rate that **Mes-Acr•** disappears. To a reasonable approximation, the concentration of **Mes-Acr⁺** at $t < 50 \mu\text{s}$ matches the amount of **Mes-Acr•** consumed, as determined from the ΔOD at 445 nm and 520 nm, respectively. Comparison of the transient spectrum at 30 μs (**Figure 3.5b**) with the predicted differential absorption spectrum (i.e., the opposite of the **Mes-Acr•** transient difference spectrum) yields strong similarity, further validating a direct conversion of **Mes-Acr•** to **Mes-Acr⁺**. In control experiments excluding (**PhS**)₂, we are unable to observe any significant transient signal exceeding baseline absorbance (Appendix B, **Figure B.17**), supporting our interpretation that the radical **PhS•** is an oxidant for **Mes-Acr•**.^x

^{ix} PhS• decay at 445 nm is a combination of pseudo-first order decay from reaction with Mes-Acr• and second order decay from bimolecular radical-radical recombination. While more sophisticated models are required to truly describe the mixed order kinetics of PhS• disappearance,^{230,239–242} we make the simplification that each decay mode is separate. See Appendix B for details.

^x We also take this as evidence that CoCp₂⁺ is inert to the redox activity of Mes-Acr• and PhS•, and therefore, not a significant perturbation to the system. As additional support to this point, the steady-state UV-Vis absorption spectrum of Mes-Acr• / CoCp₂⁺ was unchanged after subjection to >200 laser pulses during analysis by LFP.

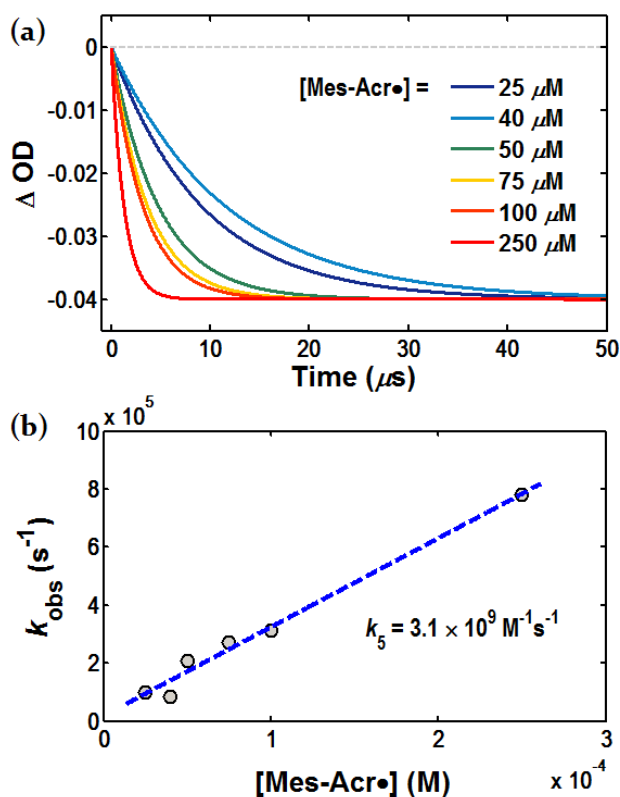


Figure 3.6. Determination of the second order rate constant k_5 describing oxidation of **Mes-Acr•** to **Mes-Acr⁺** by **PhS•**. (a) Normalized monoexponential fitting for **Mes-Acr•** disappearance at 520 nm where $[\text{Mes-Acr•}]$ ranges from 25 to 250 μM . (b) The observed rate constants for **Mes-Acr•** disappearance plotted against $[\text{Mes-Acr•}]$; the second order rate constant k_5 is determined from the slope of the linear regression as $3.1 \pm 0.5 \times 10^9 \text{ M}^{-1}\text{s}^{-1}$ (error estimated from regression statistics).

In order to obtain a second-order rate constant k_5 , a pseudo-first order kinetic study²⁴³ was conducted. The low photolytic yield of **PhS•** with laser photolysis at 410 nm precluded consistent generation of the thiyl radical over a range of **Mes-Acr•** concentrations. LFP was instead performed with 355 nm laser excitation.²³² At this wavelength, photolysis of **(PhS)₂** is consistent over a range of **Mes-Acr•** concentration, and the concentration of **PhS•** generated in a 3 mM solution of **(PhS)₂** is estimated to be less than 6 μM . Varying the concentration of **Mes-Acr•** under pseudo-first order conditions results in a linear increase in the rate of oxidation, measured as the rate of disappearance of the signal at 520 nm (**Figure 3.6a**). The second order rate constant k_5 is taken as the slope of the line fit to the pseudo-first order plot in **Figure 3.6b**,

and is calculated at $3.1 \pm 0.5 \times 10^9 \text{ M}^{-1}\text{s}^{-1}$. The magnitude of k_5 is on the same order as k_1 (k_{ET}), consistent with the expectation that ET between **Mes-Acr•** and **PhS•** is significantly exothermic.^{xi} Control experiments under conditions where **Mes-Acr⁺** and **(PhS)₂** are respectively excluded show no significant bleaching at 520 nm. We believe this experiment offers further evidence in support of our mechanistic proposal that **Mes-Acr•** is oxidized by **PhS•** in a key step that unites the cooperative activity of the photoredox and HAT co-catalysts.

3.2.2.3 Computational Results: Rate of HAT (k_4)

We viewed steps 3 and 4 (proton transfer and HAT, respectively) more difficult to address experimentally. Thus, we turned to computational methods for estimating the rates of these steps. Although Arnold disclosed an *ab initio* study on the regioselective addition of methanol to alkene cation radicals,²⁴⁴ we wanted to model the intramolecular reaction using modern DFT methods. We recognized that a number of post-Hartree-Fock methodologies suffer from systematic errors in describing open shell systems where charge and spin localization are required, as in a cation radical.^{245–247} For this reason, we could not obtain meaningful information from inquiries into cation radicals **3.3** using the (U)B3LYP methodology.^{xii} Thus, we focused our attention on step 4 (HAT) with calculations performed at the UB3LYP/6-311+G(d) level of theory.^{149,150,152,253,254,xiii}

^{xi} Based on $E_{\text{red}}^{1/2} = +0.16 \text{ V v. SCE}$ for **PhS•** reported by Larsen, et. al.²⁰⁴ and $E_{\text{red}}^{1/2} = -0.55 \text{ V v. SCE}$ for **Mes-Acr⁺**. $\Delta G = f(\Delta E) = 23.061 \text{ kcal mol}^{-1} \text{ eV}^{-1} (-0.55 \text{ V} - 0.16 \text{ V}) = -17 \text{ kcal mol}^{-1}$ ($f = \text{Faraday Constant}$).

^{xii} Even though B3LYP has been employed in previous computational studies of organic cation radicals,^{191,248–252} our attempts to model transition structures for alkenol cation-radical cyclization and deprotonation (steps 2 and 3) with this popular functional resulted in erroneous geometries and frequencies. We could not discern whether these computations were mechanistically significant or the result of systematic methodological error.

^{xiii} Computations were carried out using the Gaussian 09 software package (Frisch, M. J.; et al. *Gaussian 09*, revision D.01; Gaussian, Inc.: Wallingford, CT, 2009). See Appendix B for additional details and the full citation for *Gaussian 09*.

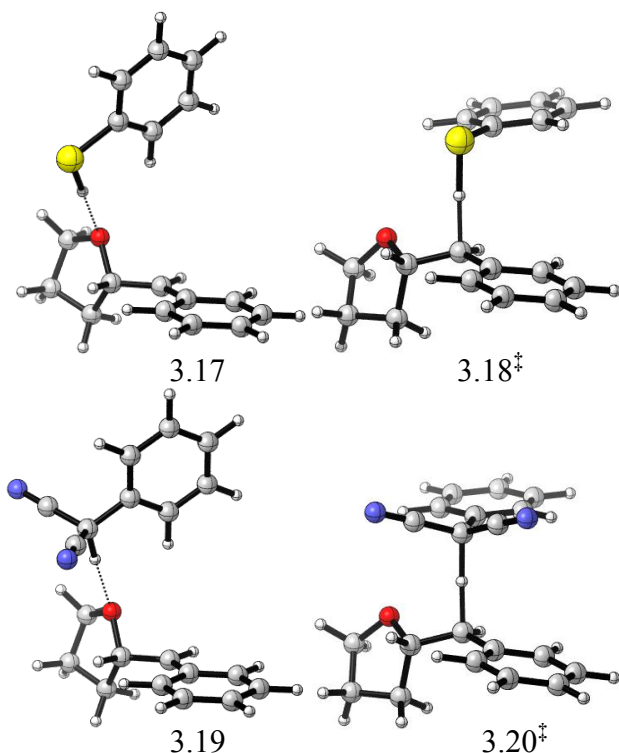


Figure 3.7. Computed structures for HAT between **PhSH** (**3.17**, **3.18[‡]**) or **PMN** (**3.19**, **3.20[‡]**) and benzylic radical **3.4**. Structures **3.17** and **3.19** are local minima; structures **3.18[‡]** and **3.20[‡]** are transition states for HAT.

The lowest energy configuration of radical **3.4/PhSH** (structure **3.17**) following deprotonation is shown in **Figure 3.7** to possess a hydrogen-bonding interaction between O and S-H groups. Radical **3.4** and **PMN** possess a similar H-bonded conformation (structure **3.19**). In both cases, this structural configuration lies on the reaction coordinate for suprafacial HAT. The lowest energy transition structures computed for **PhSH** and **PMN** both exhibit geometries where the phenyl ring of the co-catalyst is perpendicular to the bond undergoing cleavage in the transition state (structures **3.18[‡]** and **3.20[‡]**). For both H-atom donors, this requires ca. 90 degree rotation of the dihedral angle, which, owing to double –CN substitution in **PMN**, is less energetically costly for **PhSH**. Additionally, the benzylic carbon atom of **PMN** is seen to undergo a change in hybridization in the transition state. The calculated activation free energy

barrier (ΔG^\ddagger) for HAT is 9.5 kcal mol⁻¹ for **PhSH**, as compared with 15.1 kcal mol⁻¹ for **PMN**, likely reflecting the requirements for structural reorganization in **PMN**. This difference in activation barrier corresponds to a ca. 10⁴-fold difference in rate, where HAT with **PhSH** is estimated to proceed with a rate constant of approximately 6.2 × 10⁵ M⁻¹s⁻¹ at 298 K (cf. k_4 with **PMN** computed at 5.0 × 10¹ M⁻¹s⁻¹). The calculated rate constant k_4 is in good agreement with experimentally determined rates for HAT between **PhSH** and alkyl and benzylic radicals (e.g., $k = 3.13 \times 10^5$ for PhCH₂• in hexane).^{255,256} Moreover, the drastic lowering in activation energy for HAT with **PhSH** over **PMN** is likely to contribute to the enhanced efficacy of **PhSH** as an HAT co-catalyst.

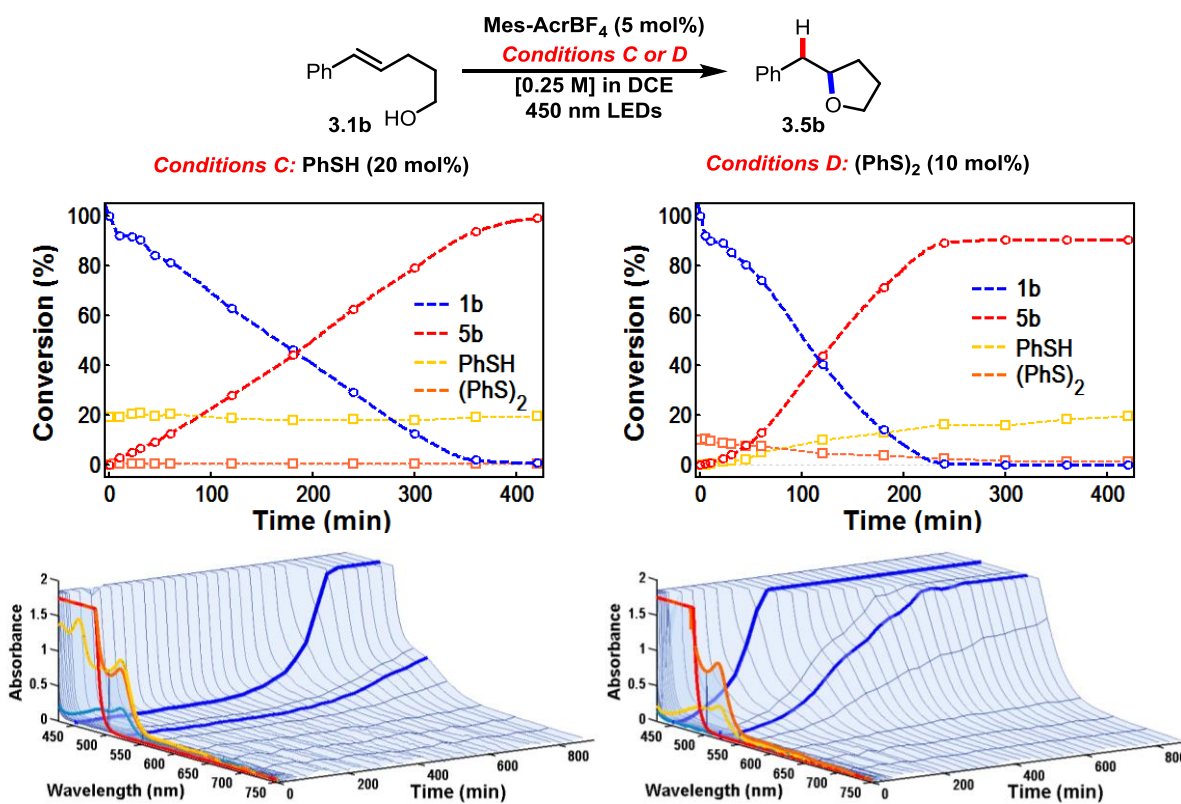


Figure 3.8. Reaction progress for hydroetherification of alkenol **3.1b** under conditions C or D (scale: approximately 0.5 mmol alkenol **3.1b**). (a) and (b): conversion of **3.1b** to **3.5b** (**PhSH** and (**PhS**)₂ also shown in units of mol% relative to [**3.1b**]₀) as determined by Gas Chromatography with dodecane as an internal standard. (c) and (d): Monitoring Mes-Acr⁺/Mes-Acr[•] during reaction by UV-Vis. Highlighted spectral traces: red = 0 min, orange = 1 min,

yellow = 2 min, cyan = 3 min. Time traces of absorbance at 450 and 520 nm are highlighted in blue. Absorbance cut off above 1.75 absorbance units.

3.2.3 Preparative scale reaction kinetics

The kinetic studies reported above predict fast alkene oxidation and intramolecular *O*-addition with catalyst turnover occurring on the nanosecond timescale. Furthermore, computational analysis predicts HAT to be relatively fast when **PhSH** is the H-atom donor. Yet, the rate to completion of the preparative reaction is empirically slow. Therefore, we aimed to identify a resting state in both catalytic cycles in order to understand the key rate limiting factors.

3.2.3.1 HAT Catalyst Resting State and Substrate Conversion: Gas Chromatography (GC).

Kinetic analysis of alkenol **3.1b** conversion (as shown in **Figure 3.8**) was conducted by sampling the mixture over the course of the reaction. A side-by-side comparison of **PhSH** and **(PhS)₂** as HAT catalysts reveals a marked difference between the activity of **PhSH** and **(PhS)₂**. When the HAT catalyst is **PhSH** (Condition C), alkenol consumption and ether formation are approximately linear until reaction completion. In contrast, the overall rate of ether formation is significantly faster when **(PhS)₂** is employed (Conditions D), and the reaction goes to completion after 4 hours, but only after an induction period where the rate of product formation is somewhat delayed. Notably, the yield of ether **3.5b** at full conversion is roughly 10% less (90% yield) for the reaction with **(PhS)₂** than with **PhSH** (essentially quantitative yield), possibly reflecting a bias toward reduction of the disulfide bond by $2\text{H}^+/2\text{e}^-$.

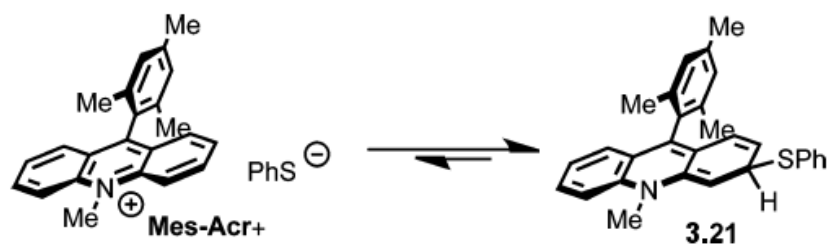
Monitoring the relative quantities of **PhSH** and **(PhS)₂** as the reactions proceed lends important insight into the resting state of the HAT catalyst. Under Condition C (**Figure 3.8a**), the amount of **PhSH** present (yellow) changes very little, and is maintained at approximately 17-19 mol % when **PhSH** is the HAT catalyst. In these cases, the remaining molar balance can be

accounted for as **(PhS)₂** (orange), formed in roughly 1 mol % over the course of the reaction. In contrast, when 10 mol % **(PhS)₂** is employed, the disulfide is progressively converted to **PhSH** as the reaction goes to completion (**Figure 3.8b**, yellow/orange traces). This conversion is correlated with the formation of ether **3.5b**, and in both reactions (Conditions C and D), the final amounts of **PhSH** and **(PhS)₂** are ca. 18 mol % and 1 mol % respectively, further evidence that **(PhS)₂** and **PhSH** share a common catalytic role.

3.2.3.2 Mes-Acr Resting State: UV-Vis Time Evolution.

When **Mes-Acr⁺** (13 mM) with alkenol **3.1b** (250 mM) and either **PhSH** (Condition C) or **(PhS)₂** (Condition D) were continuously irradiated in a cuvette with 450 nm LEDs while monitored by UV-Vis, the absorption for **Mes-Acr•** quickly grew in ($\lambda_{\text{max}} = 520 \text{ nm}$), but then decayed sharply, disappearing entirely by $t = 4 \text{ min}$ when **PhSH** is the HAT catalyst (Condition C) or $t = 3 \text{ min}$ when **(PhS)₂** is used (Condition D). Under the preparative conditions, the absorbance for 13 mM **Mes-Acr⁺** is too intense to be measured; however, this absorption band ($\lambda = 400\text{-}460 \text{ nm}$) likewise disappeared after only 3 minutes of irradiation. In the case of Condition C (HAT catalyst = **PhSH**), absorption at both 450 and 520 nm begin to return at ca. 6 hours, corresponding to reappearance of **Mes-Acr⁺** and **Mes-Acr•**, respectively. For Condition D (HAT catalyst = **(PhS)₂**), both absorptions increase from baseline after only 1 hour, reaching significant levels after ca. 4 hours. Although the absorptions for both **Mes-Acr⁺** and **Mes-Acr•** disappear early in the reaction, the kinetics in **Figure 3.8** clearly indicate steady product formation during this period, verifying that the catalytic activity is not depleted.

Scheme 3.5. Proposed adduct formation between **PhS⁻** and **Mes-Acr⁺**



Given that Mes-AcrBF₄ can be isolated after the reaction is complete, we considered the possibility that the period when **Mes-Acr⁺/Mes-Acr•** absorbance is not detectable represents formation of a reversible adduct^{257–260} as a resting state. Shown in **Scheme 3.5**, we postulated that the **PhS⁻** could add to **Mes-Acr⁺** following oxidation of **Mes-Acr•**. If this addition is reversible, a steady state concentration of **Mes-Acr⁺** is available for immediate excitation and photoinduced ET with alkene **3.1b**. In support of this hypothesis, we observe reappearance of the **Mes-Acr⁺** absorption in the dark when irradiation is ceased after reaching depletion of **Mes-Acr⁺/Mes-Acr•** absorbance under Conditions C (**Figure 3.9**). Absorbance for **Mes-Acr⁺** at 450 nm returns slowly, validating that **Mes-Acr⁺** is catalytically relevant even after apparent bleaching. Similar behavior is observed when 0.1 eq. (**PhS**)₂ is employed (Condition D); however, **Mes-Acr⁺** reappears faster in this case (**Figure 3.9**). In both experiments, absorbance at 520 nm remains at baseline, indicating that **Mes-Acr•** is not formed. Attempts to observe a thiolate-acridinium adduct by ¹H NMR or to isolate an adduct (e.g. **3.21**) synthetically were unsuccessful, but efforts to characterize the resting state behavior of the **Mes-Acr⁺** manifold are ongoing.

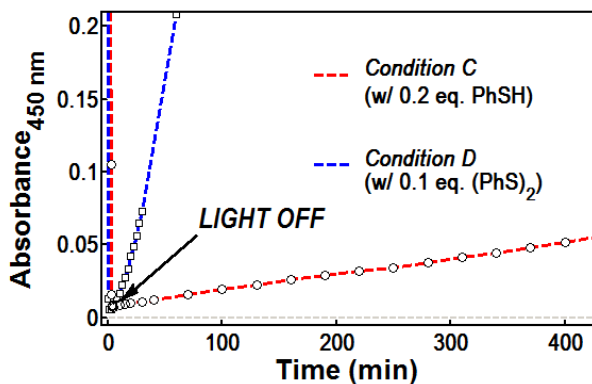


Figure 3.9. Recovery of Mes-Acr^+ absorbance at 450 nm under dark conditions after bleaching at $t = 5$ min.

3.2.4 Discussion: Rate Limiting Factors

We believe the difference in overall reaction rate when comparing **PhSH** and $(\text{PhS})_2$ is consistent with deprotonation (step 3, **Scheme 3.1**) having rate limiting influence. Because $(\text{PhS})_2$ does not depend on HAT for generation of thiyl radical $\text{PhS}\cdot$ in the early stages of reaction (i.e., before ca. 50% conversion), fast oxidation of $\text{Mes-Acr}\cdot$ results in a higher steady state concentration of PhS^- , leading to a higher rate of deprotonation. On the other hand, **PhSH** is required to encounter radical **3.4** before generating $\text{PhS}\cdot$ at all points in the reaction. Although HAT is expected to be fast, concentration of radical **3.4** is in turn limited by the rate of deprotonation, to the effect of decreased PhS^- concentration, and thus, a slower overall rate.

One consequence of the overlap between the catalytic cycles of Mes-Acr^+ and HAT reagent is that the effect of a single rate limiting step could be amplified by preventing formation of intermediates crucial in the turnover of either cycle. Thus, the rate limiting step may change as the reaction progresses. If proton transfer is rate limiting as we suggest, the expected buildup of PhS^- is consistent with the observation that Mes-Acr^+ is occupied in an off-cycle intermediate. We acknowledge the possibility that such a step might also result in a rate limiting equilibrium. Pending current investigations into the rate of deprotonation (k_4) and the putative equilibrium of

the **Mes-Acr**⁺ catalyst and an as yet unidentified adduct, it is plausible that both steps have a combined limiting effect on the overall reaction rate when **PhSH** or **(PhS)**₂ is employed as the hydrogen-atom donor catalyst.

3.3 Conclusion

Through the use of transient and steady state spectroscopic techniques, we have addressed the rate constants describing the elementary steps in our proposed mechanism for anti-Markovnikov alkene hydrofunctionalization, using an alkenol as an intramolecular model system. Detection of alkene cation radical intermediates validates that the mechanism proceeds by electron transfer rather than by formation of an exciplex between the catalyst and alkene as has been postulated in prior alkene hydrofunctionalization reactions involving photocatalysts. We found that all alkenes examined are oxidized on the nanosecond timescale by a singlet **Mes-Acr**^{+*} state, while alkenes with moderate oxidation potentials can also be oxidized by the triplet state. Moreover, direct observation of **Mes-Acr**[•] turnover by **PhS**[•] supports the intermediacy of a key step which unites the parallel catalytic cycles of photoredox and HAT catalysts. Exchange studies reveal that disulfides are competent HAT catalysts which operate on the same cycle as the corresponding thiophenols by way of photolytic thiyl radical generation. We estimate the rate of HAT to be fast, with **PhSH** reacting at a rate ca. 10⁴ times faster than **PMN**. Given that the rate constants addressed explicitly herein are estimated to be fast, our working hypothesis is that deprotonation may be rate limiting in some capacity. Observation that **Mes-Acr**⁺ is engaged in an off-cycle equilibrium is consistent with buildup of thiolate **PhS**⁻ and further suggests the possibility that reversible adduct formation might have additional rate limiting influence. Many of the insights gained through this mechanistic analysis can be applied to other anti-Markovnikov hydrofunctionalizations reported by our group, although reaction specific

considerations are the subject of an ongoing research program, along with current efforts towards photoredox catalyst development based on the acridinium scaffold.

3.4 Associated Content

Appendix B: Experimental procedures and spectral data.

3.5 Acknowledgements

A portion of this work was performed in the UNC-EFRC Instrumentation Facility established by the UNC EFRC (Center for Solar Fuels, an Energy Frontier Research Center funded by the U.S. Department of Energy, Office of Science, Office of Basic Energy Sciences under Award Number DE-SC0001011). This work was also supported by Award No. R01 GM098340 from the National Institute of General Medical Sciences. N.A.R. also acknowledges an NSF Predoctoral Fellowship. We are grateful to Dr. M. Kyle Brennaman, Prof. Alex Miller, and Prof. Jillian Dempsey for insightful conversations and assistance with spectroscopic measurements.

CHAPTER 4: SITE-SELECTIVE ARENE C-H AMINATION VIA PHOTOREDOX CATALYSIS

Reproduced with permission from Romero, N. A.; Margrey, K. A.; Tay, N. E.; Nicewicz, D. A. *Science* **2015**, *349* (6254), 1326–1330. Copyright 2015 by the American Association for the Advancement of Science.

4.1 Background: Aryl C-H Functionalization

The development of catalytic procedures for selective modification of carbon–hydrogen ($C-H$) bonds carries the promise of streamlined and sustainable syntheses of high-value chemicals. Direct transformation of aryl $C-H$ bonds into carbon–carbon ($C-C$), carbon–oxygen ($C-O$), and carbon–nitrogen ($C-N$) bonds can provide efficient access to arenes with diverse structural properties.^{261,262} In particular, interest in aryl $C-H$ amination (construction of $C-N$ bond from $C-H$ bond) is driven by the ubiquity of aryl $C-N$ bonds in pharmaceuticals, natural products, agrochemicals, pigments and optoelectronic materials. In contrast to the Buchwald-Hartwig^{263,264} and Chan-Lam^{265,266} aminations, which stand as the current preferred methods for catalytic aryl $C-N$ bond construction, a $C-H$ amination strategy could circumvent the need for prior functionalization of the arene as halide, triflate or boronic acid. This synthetic advantage is augmented by the application of $C-H$ amination to late stage functionalization of synthetic targets, wherein libraries of complex aryl amines could be generated in a single step for medicinal chemistry screening.

Many of the recent advances in aryl $C-H$ amination have been propelled by the ability of transition metals to activate $C-H$ bonds. Although regioselective addition to an arene that lacks strong electronic or steric bias is an intrinsic challenge of aryl $C-H$ functionalization, a number

of researchers, including Buchwald and co-workers,²⁶⁷ Daugulis and co-workers,²⁶⁸ Shen and co-workers,²⁶⁹ and Nakamura and co-workers,²⁷⁰ have achieved *ortho*-selective addition by relying on Lewis-basic substituents to direct the site of metalation. Beyond transition metal catalyzed approaches, imidation of arenes and heteroarenes has been achieved by Sanford and co-workers in a photoredox mediated system,²⁷¹ as well as by Chang²⁷² and DeBoef²⁷³ and their respective co-workers, who employ $\text{PhI}(\text{OAc})_2$ as an oxidant (Ph, phenyl; OAc, acetate). In these cases, regioselectivity is modest at best. Of the intermolecular *C–H* amination examples reported in the literature, few operate with the arene as a limiting reagent. Exceptional in this regard are the systems reported by Ritter,²⁷⁴ Baran,²⁷⁵ and Itami,²⁷⁶ yet each method appears to be exclusive to a single nitrogen coupling partner.

Taken together, this body of precedent illustrates a number of remaining challenges in aryl *C–H* amination chemistry: (i) achievement of site-selective addition; (ii) extension of nitrogen coupling partner beyond amides and imides, including the direct synthesis of primary anilines; and (iii) achievement of atom-economical and mild synthetic conditions. In this report, we describe our efforts to develop a *C–H* amination methodology that addresses these limitations and demonstrates the combination of organic photoredox catalysis with nitroxyl radicals as co-catalysts.

4.2 Results and Discussion: development of a photoredox-catalyzed arene C-H amination

We hypothesized that an arene cation radical could serve as a key reactive intermediate in a direct, intermolecular *C–H* aryl amination. We believed that an amine could form σ -adduct **4.2** with an arene cation radical **4.1**, generated upon photoinduced electron transfer (PET) from the arene to an excited state photoredox catalyst (cat*) (**Figure 4.1**).^{177,277–280} The subsequent deprotonation of distonic cation radical **4.2** followed by oxidative aromatization of intermediate

4.3, would deliver the desired aminated arene. As this process constitutes a two-electron and two-proton loss, an equivalent of a two-electron oxidant would be required for each photocatalyst turnover. In addition to an earlier report of an intramolecular cyclization initiated by PET,²⁸¹ several recent investigations suggested to us that such a process was feasible. First, Yoshida and co-workers reported the synthesis of aryl amines by means of electrochemical oxidation.^{282–284} Essential to this achievement was the use of protected amines in order to insulate the C–N coupled products from subsequent oxidative degradation. Accordingly, an additional synthetic step was required to liberate the desired targets. Second, Fukuzumi and co-workers have studied the addition of bromide and fluoride anions to arene cation radicals, generated upon PET, via an organic photoredox catalyst.^{285,286} Dioxygen (O₂) served as a terminal oxidant and was believed to play a role in both the regeneration of the photoredox catalyst and the aromatization to furnish the aryl halide.

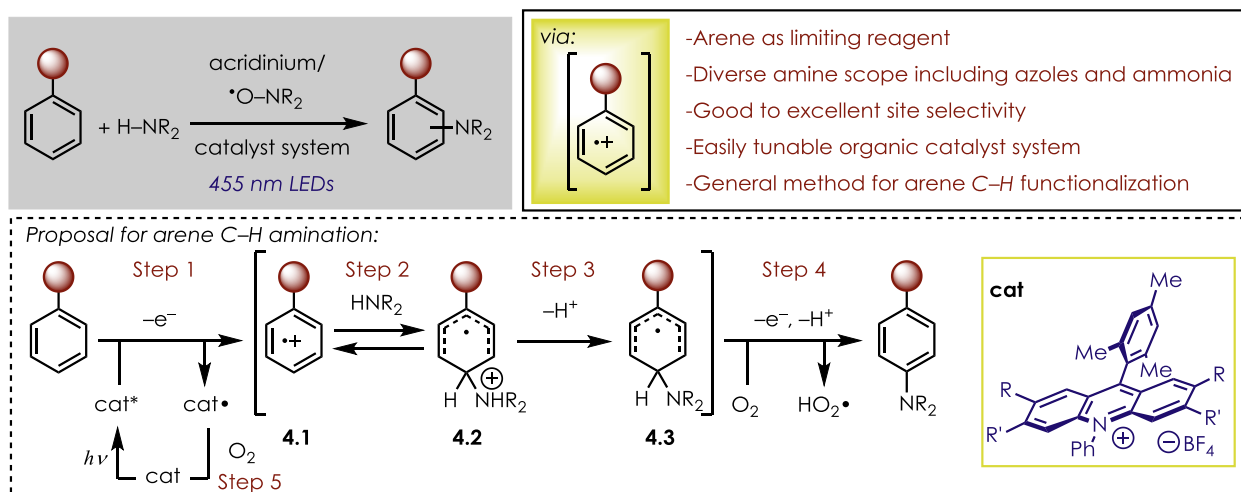


Figure 4.1. Blueprint for site-selective C–H amination of aromatics.

LEDs, light-emitting diodes; $h\nu$, light.

These studies lend support for the arene amination blueprint outlined in Fig. 1, and given that aerobic conditions have been employed in previous oxidative photoredox processes, O₂ was an attractive choice as a terminal oxidant and was our starting point for investigation.

In our initial screens for reactivity, we employed commercially available acridinium catalysts **A** and **B** (**Figure 4.2**, inset), as they have highly positive excited state reduction potential [$E_{\text{red}}^* = +2.20$ V and $+2.09$ V versus the saturated calomel electrode (SCE), respectively] and robustness in the presence of strong nucleophiles. We selected pyrazole (**4.5**) as a representative nucleophile and anisole (**4.4**) as the arene coupling partner.¹⁷⁴ Under the conditions given in **Figure 4.2A**, but in the absence of oxygen, little *C–N* coupled arene adduct (**4.6a** & **4.6b**) was observed. However, when the reaction was run under a balloon of O₂, a combined 47% yield of **4.6a** and **4.6b** was observed, with good *para:ortho* selectivity (ratio of 6.7:1). Subsequent first-pass optimization efforts produced no gain in yield for the catalyst, concentration, solvent, or other oxidants.

This plateau in yield could have several causes. First, aryl amine products **4.6a** and **4.6b** ($E_{\text{p}/2} = +1.50$ V vs. SCE) possess lower oxidation potentials than anisole does ($E_{\text{p}/2} = +1.87$ V vs. SCE), and **4.6a** and **4.6b** could competitively reduce excited state acridinium (cat⁺*), resulting in product inhibition. Second, analysis of the reaction mixture revealed that phenyl formate was the major byproduct, indicating that, in addition to product inhibition, side reactions of the arene reactant were problematic under these conditions. Finally, after failing to detect catalyst **A** or **B** in crude proton nuclear magnetic resonance (¹H NMR) spectra, we questioned the stability of the catalyst under the reaction conditions. Moreover, both anisole (**4.4**) and acridinium are susceptible to degradation reactions in the presence of oxygen-centered radicals;²⁸⁷ we therefore surveyed a number of additives that we hoped would mitigate any highly reactive radical intermediates such as peroxy radicals.

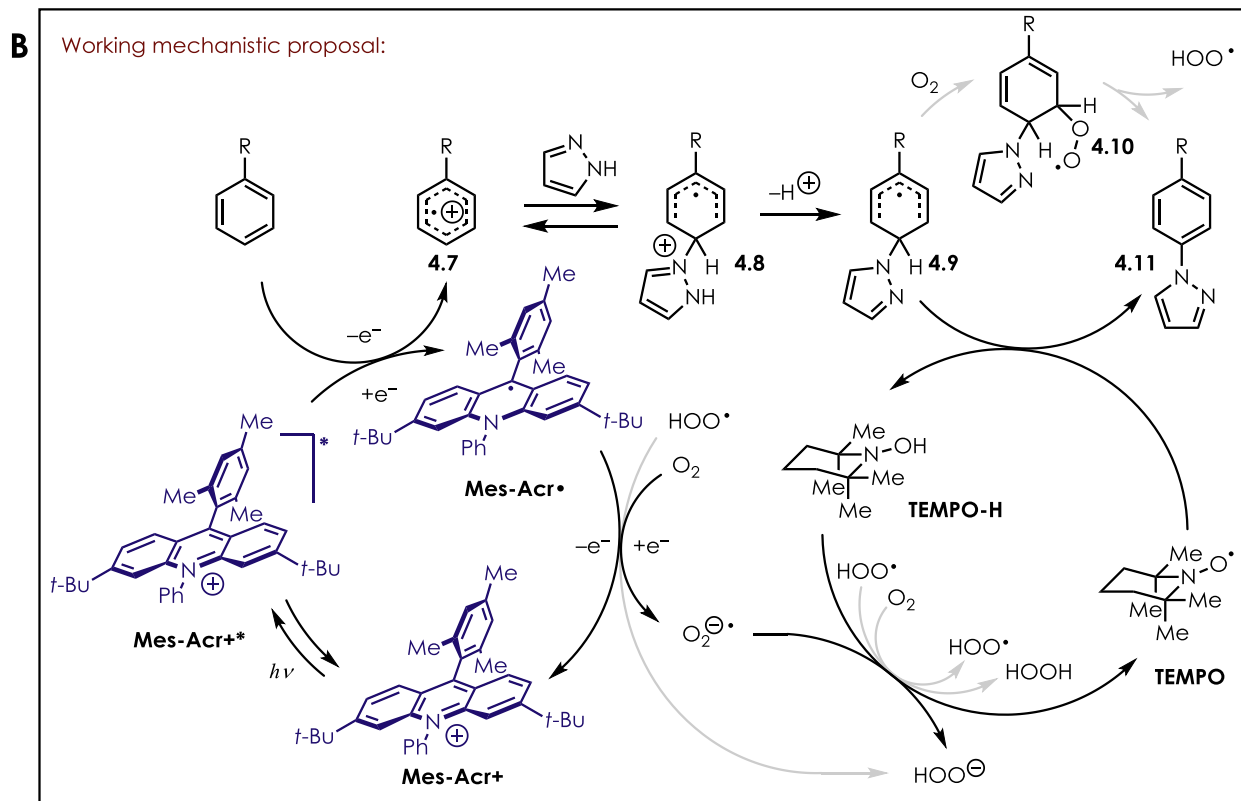
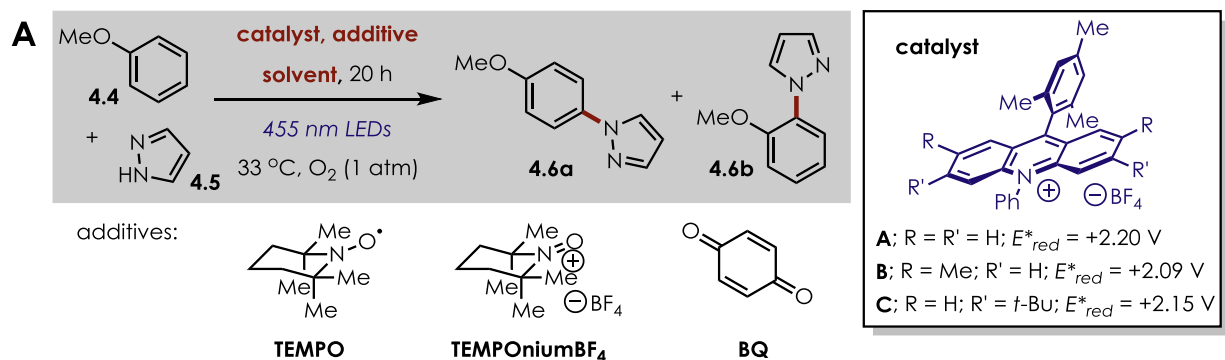


Figure 4.2. Reaction development. (A) Catalyst optimization and (B) proposed mechanism. Reactions run with 1.0 equiv of **4.4** and 2.0 equiv of **4.5** unless otherwise noted. E^*_{red} values for A-C versus SCE (see Appendix C.4 for details). BQ, 1,4-benzoquinone.

We found that 10 mol % TEMPO improved the yield of **4.6a/4.6b** to 65%. We also observed that the remaining mass balance was almost entirely unreacted anisole. Increased equivalents of TEMPO afforded a yield of 74% that decreased with higher loadings.

As an additional measure to prolong the viability of the acridinium catalyst, we modified the acridinium structure to confer stability against addition by nucleophiles or radicals, as in the

case of (9-mesityl-3,6-di-*tert*-butyl-10-phenylacridiniumtetrafluoroborate, **C**). The use of this catalyst provided the best results to date, producing compound **4.6** in 88% yield after 20 hours. A 97% yield was achieved under an atmosphere of air after irradiation for 3 days. The use of immobilized TEMPO on polystyrene resulted in a 65% yield of the aminated arene and facilitated its recovery and reuse via simple filtration.

The mechanism of this reaction is currently the subject of detailed investigation. We believe the role of TEMPO is to aromatize radical intermediate **4.9** directly by H-atom abstraction (**Figure 4.2B**). Alternatively, radical **4.9** could be trapped by O₂ to form 1,3-cyclohexadienyl peroxy radical **10**, from which internal elimination would furnish product **4.11** and hydroperoxyl radical HO₂[•].²⁸⁸ As proposed by Fukuzumi,²⁸⁵ O₂ can oxidize acridine radical **Mes-Acr[•]**, regenerating acridinium **Mes-Acr⁺** and superoxide O₂^{-•}, although other putative intermediates might be capable of catalyst turnover (e.g., HOO[•], **Figure 4.2B**). The strongly basic superoxide should deprotonate intermediate **10**, then subsequently undergo HAT with TEMPO-H, ultimately forming H₂O₂ and regenerating TEMPO. The decrease in undesired byproducts when TEMPO was included is consistent with the proposed activity of TEMPO-H, which is expected to scavenge reactive oxygen centered radicals, such as hydroperoxyl radical HO₂[•]. Although the half-wave redox potential of TEMPO [$E_{1/2}(\text{TEMPO}^{\bullet}/\text{TEMPO}^+) = +0.62 \text{ V}$ vs. Ag/AgCl]²⁸⁹ points to the possibility of oxidization by **cat^{+•}**, the use of 20 mol% TEMPONium-BF₄ gives comparable results to TEMPO in the aryl amination reaction (Table C.2, entry 13). By our current understanding, this suggests that a common mechanistic intermediate is accessible—namely, TEMPO—presumably generated by electron transfer from **cat[•]** ($E_{1/2}(\text{cat}^+/\text{cat}^{\bullet}) = -0.47$ to -0.58 V versus SCE) to TEMPONium. In the absence of **cat⁺**, none of aryl

amine **4.11** is generated with 20 mol % TEMPO, although trace product formation was detected when 20 mol % TEMPO⁺BF₄⁻ was used and the acridinium photocatalyst was omitted.

The optimized conditions were successfully extended to the coupling of pyrazole with a variety of monosubstituted aromatics, including CH₂OCH₃ (MOM)- and *tert*-butyldimethylsilyl (TBS)-protected phenol as well as biphenyl (**4.12-4.15, 18; Figure 4.3**). Halogenated anisole derivatives were excellent substrates for the transformation and afforded *N*-arylpyrazoles **4.19** and **4.20**, with complete regioselectivity *para*- to the methoxy substituent. Likewise, regiochemical discrimination is possible on biaryls bearing electronically distinct aromatic groups. Despite the availability of eight unique aryl *C-H* bonds in 2-chloro-2'-methoxy-1,1'-biphenyl, biaryl **4.21** was formed in 75% yield, with completely site-selective addition *para*- to the methoxy group, reflective of the electronic influences on this manifold. Heterocycles bearing electron-releasing substitution are competent substrates: dimethoxypyridine **4.22** and methoxyquinoline **4.23** were isolated in modest yields, but as single products. Heterocyclic motifs such as quinazoline dione, 1-methyl indazole, and dihydrocoumarin readily underwent *C-H* amination with pyrazole to produce adducts **4.24-4.26**. In all cases, a regioselectivity ratio of >15:1 was observed.

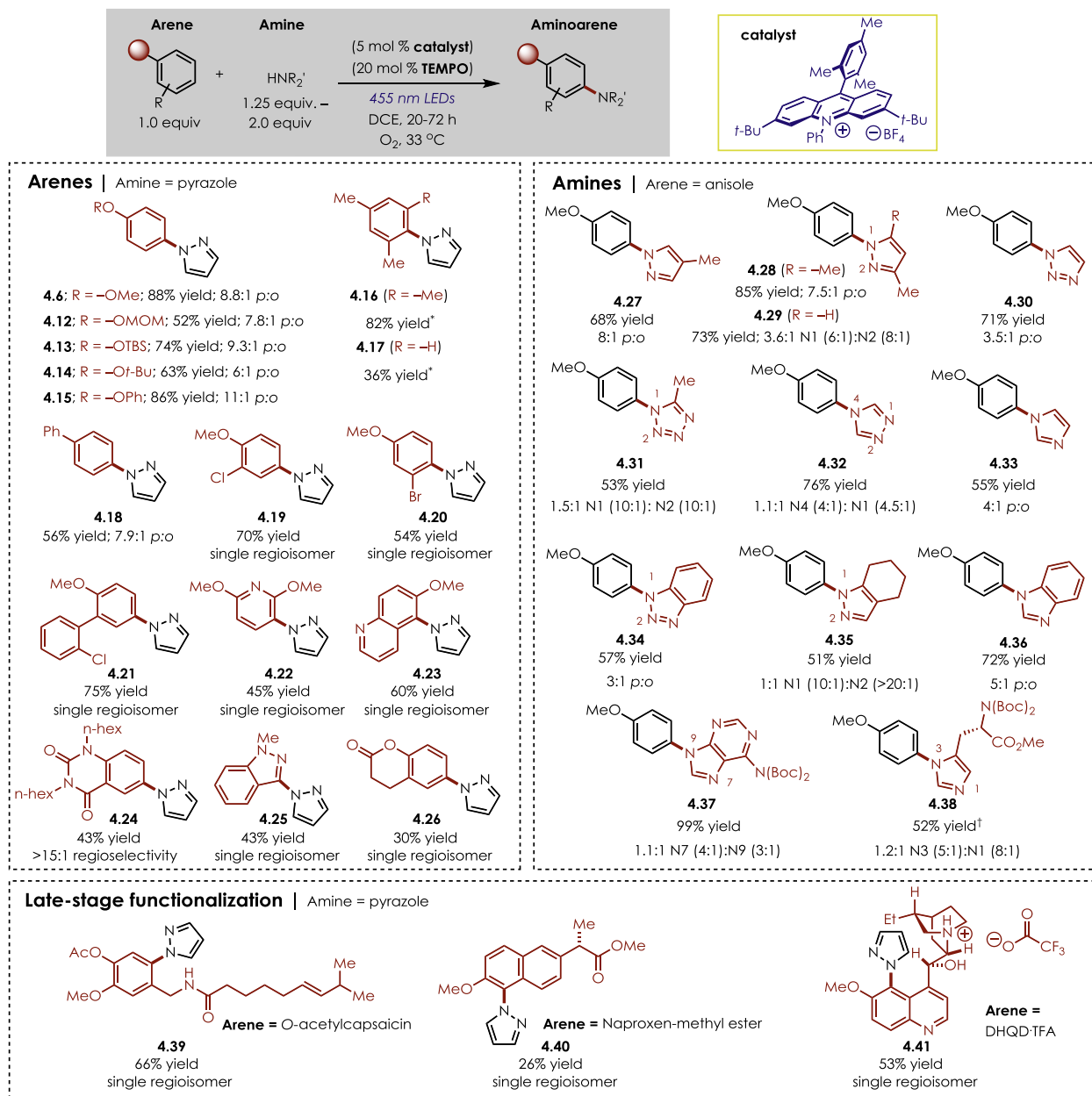


Figure 4.3. Reaction Scope for the C–H Amination.

Parentenetical ratios refer to *p:o* selectivity for that given *N*-isomer. Reactions run in DCE at 0.1 M concentration with respect to the arene limiting reagent. (*) indicates a reaction run with 2.0 equiv. of arene, 1.0 equiv. amine, 1.0 equiv. TEMPO under an N₂ atmosphere for 44 h. (†) indicates a reaction run under N₂ with 1.0 equiv. TEMPO.

One of the challenges associated with oxidative functionalization of arenes is the presence of weak benzylic C–H bonds, particularly in arene cation radicals, which have a documented propensity for H-atom and/or proton loss at these positions.²⁹⁰ For example, under

Yoshida's electrochemical oxidation conditions, alkyl-substituted arenes give rise to benzylic amination over aryl amination. Our initial attempts to apply the previously optimized conditions to the coupling of pyrazole with mesitylene were hampered by competitive benzylic oxidation to the aryl aldehyde (**Table C.2**), a reactivity previously documented by Fukuzumi.¹⁸⁶ Excluding O₂ suppressed benzylic oxidation, and increasing the TEMPO loading to 1.0 equivalent enabled addition of pyrazole to the aromatic ring of mesitylene, forming **4.16** in excellent yield (82%). No products resulting from benzylic oxidation were observed. Likewise, *m*-Xylene reacted under these conditions, albeit in lower yields (36%); the remainder of the mass balance was simply attributed to unreacted starting material. Even modest yields are notable in this context given the oxidation potential of *m*-xylene ($E_{p/2} = +2.28$ V versus SCE) and the excited state reduction potential of catalyst **C**. Considering the acidity of alkylbenzene cation radicals (pK_a [PhMe]⁺⁺ = – 20)²⁹¹, it is remarkable that productive aryl *C–H* amination occurs for mesitylene and *m*-xylene.

Azoles are a privileged structural unit in pharmacologically active compounds^{292,293} and in the architectures of transition metal-catalysts and organocatalysts. Yet, the most reliable methods for construction of aryl-azoles require at least two synthetic steps. We were pleased to find that a diverse range of *N*-heterocyclic nucleophiles could be directly coupled to an arene in our reaction protocol. In addition to pyrazoles (**4.27–4.29**), we found that 1,2,3- and 1,2,4-triazoles (**4.30**, **4.32**), tetrazole (**4.31**), imidazole and benzimidazole (**4.33** & **4.36**), benzotriazole (**4.34**) as well as tetrahydro-indazole (**4.35**) produced good to excellent yields of the *C–N* adducts (53–85% yields). A di-Boc-protected adenine gave nearly quantitative yields (99%) of purines **4.37** in a 1.1:1 *N*-regioisomeric ratio.

To evaluate whether this catalyst system could be applied to late-stage functionalization, we tested the *C–N* bond-forming protocol with representative druglike molecules as shown in

Figure 4.3 (bottom). The successful coupling of Boc-histidine methyl ester with **4.4** offers a new strategy for modification of biologically relevant structures containing this amino acid. When reacted with pyrazole, *O*-acetylcapsaicin, naproxen methyl ester, and dihydroquinidine·trifluoroacetic acid (DHQD·TFA) are transformed into single regioisomers of the adducts (**4.38-4.41**). Despite heteroatom substitution at the benzylic position, no oxidation of the benzylic *C-H* bonds was observed in either *O*-acetylcapsaicin or DHQD·TFA in the reactions forming **4.39** and **4.41**, respectively. Likewise, naproxen-methyl ester contains a sensitive benzylic *C-H* bond that remains undisturbed in the coupling reaction. These results demonstrate the mildness and practicality of the protocol.

The regioselectivities observed in these transformations are challenging to interpret, given the diversity of substituents on the arene coupling partner. Previous studies have found qualitative correlations between the observed site selectivity and LUMO coefficients²⁸² or partial atomic charges.²⁸⁵ The aforementioned work is consistent with the expectation of nucleophilic addition to a cation radical at positions that afford a stabilized radical; in arenes bearing a single substituent, addition at the *ortho*- and *para*- positions is favored over *meta*-addition. Other differentiating factors, such as steric effects, may be intertwined with arene electronics, and future mechanistic studies could clarify the key contributions to the regioselectivities observed.

Last, we explored whether anilines could be forged directly from this catalytic sequence by simply employing either ammonia or an ammonium salt as the nitrogen source. Traditionally, a nitration-hydrogenation sequence is used to access anilines directly. The latter protocol requires rigorous optimization to ensure safe dissipation of the heat associated with the exothermic reaction profile; potentially explosive intermediates and toxic byproducts are also concerns. Only very recently has the Buchwald-Hartwig amination of aromatic halides been accomplished with

ammonia as the nitrogen source.²⁹⁴ A *C-H* amination protocol of benzene with ammonia, developed by DuPont, employs a NiO-ZrO₂ catalyst system at 350 °C and 300-400 atm, furnishing aniline in a 14% maximum yield.^{295,296}

After screening of a variety of commercially-available ammonium salts such as H₄N⁺OAc⁻, H₄N⁺HCO₃⁻, and (H₄N⁺)₂CO₃²⁻, we found that ammonium carbamate (H₄N⁺H₂NCO₂⁻) was best suited for this role (see **Table C.3**). This benchtop-stable solid salt is less costly on a molar basis than liquid ammonia. Using 4.0 equivalents of ammonium carbamate with anisole under catalytic conditions nearly identical to those applied to azoles resulted in the formation of a 1.6:1 mixture of *para*- and *ortho*-anisidine in 59% isolated yield (**4.42**; **Figure 4.4**).

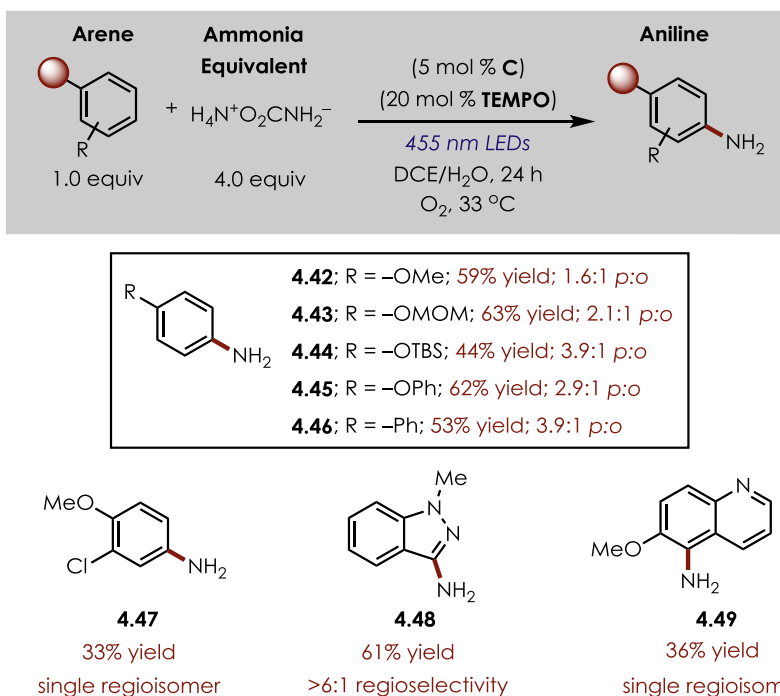


Figure 4.4. Synthesis of Anilines Using Ammonium Salt as Ammonia Equivalent. Reactions run in DCE/H₂O (10:1) at 0.1 M concentration with respect to the arene limiting reagent.

The scope of the aniline-forming reaction was similar to the azole-coupling transformations. Protected phenols (4.43-4.45), haloarenes (4.47), and nitrogen heteroaromatics such as *N*-methylindazole (4.48) and 6-methoxyquinoline (4.49) were aminated under this protocol, albeit with modest regioselectivities in the case of the monosubstituted aromatics.

4.3 Conclusion

Overall, these *C–N* bond-forming reactions are powerful tools for the synthesis of complex aromatics using an organic photooxidant and nitroxyl radical catalyst system. From the substrate scope investigation, it is clear that free alcohols, esters, silyl ethers, halides, amides, alkenes and protected amines are all compatible functionalities. The mildness of this protocol makes it appealing for a variety of applications. Moreover, we anticipate that this general method for the activation of arenes will result in development of additional transformations.

4.4 Associated Content

Appendix C. Experimental Procedures and Spectral Data

4.5 Acknowledgements

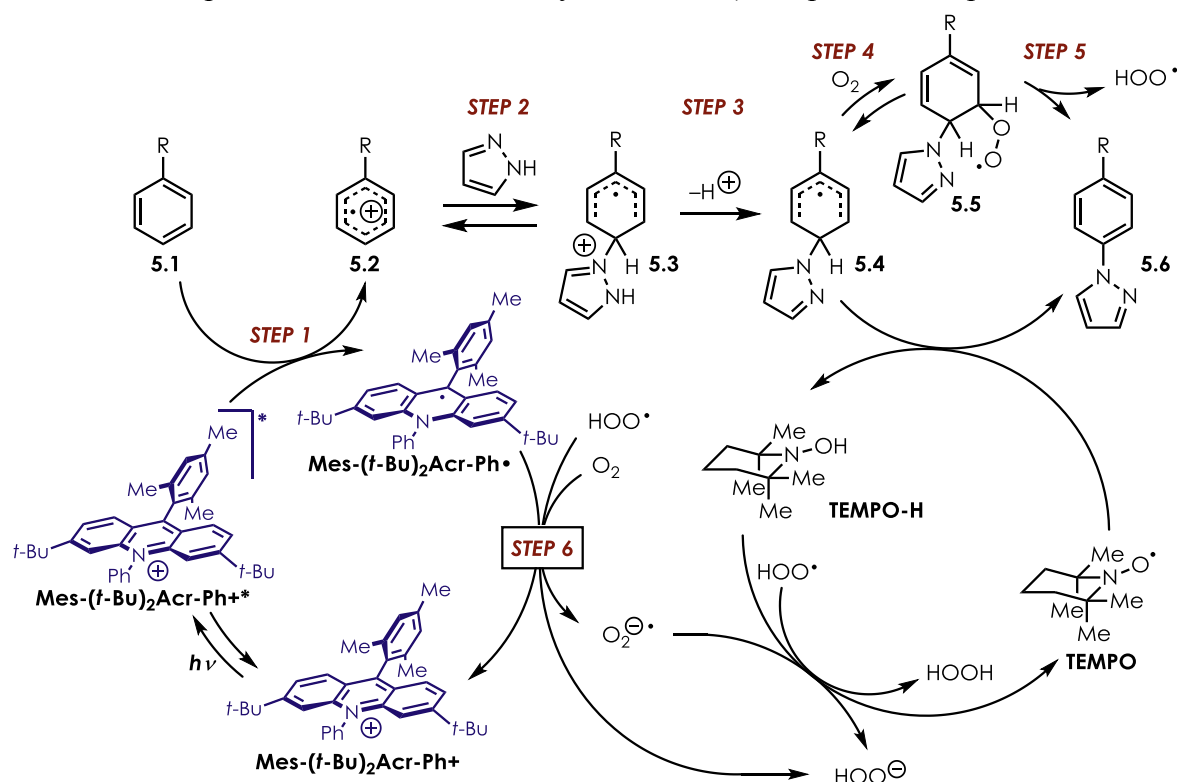
Financial support was provided by the David and Lucile Packard Foundation, Merck, and an Amgen Young Investigator Award. N.A.R is grateful for an NSF Graduate Fellowship, and K.A.M. was supported by a Francis Preston Venable Graduate Fellowship. A provisional patent has been filed on the methods presented here (U.S. patent application no. 62/170,632).

CHAPTER 5: MECHANISTIC STUDIES ON ACRIDINIUM-MEDIATED ARENE C-H AMINATION REACTIONS

5.1 Introduction

The proposed mechanism for the photoredox-mediated aryl amination reaction as presented in **Scheme 5.1** offers a reasonable description of the catalytic process consistent with mechanisms proposed in the literature for similar systems. Yet, a number of questions remain regarding selectivity, the specific roles of reagents, and the generality of the substrate scope. Some of these questions include: a) What is the primary oxidant that turns over the catalytic cycle? b) How robust is the acridinium catalyst if oxygen centered radicals are generated in catalyst turnover? c) Why do we not observe “over-addition” to form multiply-aminated arenes? d) What is the origin of the high *para*-:*ortho*- selectivity in mono-substituted arenes and the high site selectivity in other substrates? e) Which elementary steps exert rate limiting influence? f) What is the particular role of TEMPO in enabling high yields? Is TEMPO merely a radical inhibitor that suppresses unwanted arene degradation and catalyst degradation? Or is does it play a more complex role, involved in multiple steps, such as the aromatization step?

Scheme 5.1. Proposed mechanism for the aryl amination (most plausible steps denoted in red)



In order to address these questions, we have undertaken a comprehensive investigation of the reaction mechanism with the hope that an improved understanding will lead to expansion of the substrate scope beyond the current limitations of the method.

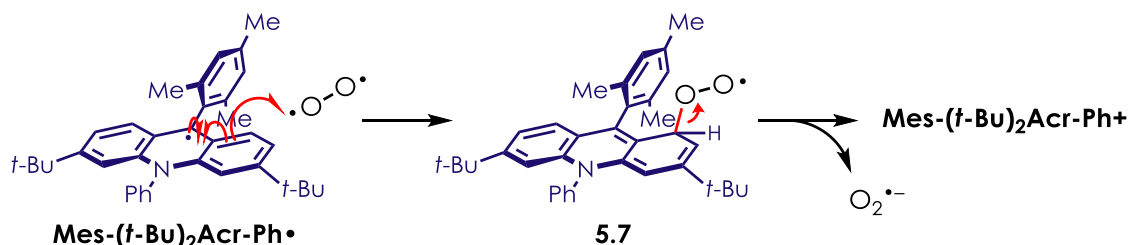
5.2 Results and Discussion

5.2.1 Turnover of the acridinyl radical Mes-(*t*-Bu)₂Acr-Ph•

The aryl C-H amination reaction formally constitutes a 2e⁻(2H⁺) oxidation process, and we began our investigation by seeking to identify the ultimate electron acceptor(s) and elucidate the elementary steps en route to the net transfer of 2e⁻ to the terminal oxidant. A key step in achieving productive catalysis is the turnover of the acridinyl radical Mes-(*t*-Bu)₂Acr-Ph•, shown in **Scheme 5.1** as Step 6. As discussed in Section 4.2 above, we hypothesized that O₂ is reduced to O₂^{•-} in this step, citing prior reports where acridinium photoredox catalysts were used

in net-oxidative processes under aerobic conditions, in which the authors proposed that O_2 was the primary oxidant for acridinyl radical turnover.^{179,182,186,187,285} However, we noted that, considering the reduction potential for **Mes-(*t*-Bu)₂Acr-Ph•** ($E_{1/2}(\text{Mes-(*t*-Bu)₂Acr-Ph+}/\text{Mes-(*t*-Bu)₂Acr-Ph•}) = -0.52 \text{ V vs. SCE}$)²⁹⁷ and O_2 ($E_{1/2}(O_2/O_2^{\cdot-}) = -0.75 \text{ V vs. SCE}$ in MeCN, see **Scheme 5.3** and **Table 5.1**), ET from **Mes-(*t*-Bu)₂Acr-Ph•** to O_2 is expected to be endergonic. Furthermore, we believed **TEMPO** to be an even more unlikely oxidant in the turnover step, as it is a poor single electron oxidant ($E_p(\text{TEMPO}^{\cdot+}/\text{TEMPO}^{\cdot-}) = -1.91 \text{ V vs. Fc}^+/\text{Fc}$)²⁹⁸). Yet, given the wide range of reported redox potentials and apparent medium dependence for the reduction of O_2 , we did not preclude the possibility that O_2 is involved in Step 6, and we speculated that an “inner sphere” mechanism of oxidation by O_2 might lead to the same outcome (**Scheme 5.2**). Thus, we sought to test whether turnover of **Mes-(*t*-Bu)₂Acr-Ph•** by O_2 was a tenable mechanistic step.

Scheme 5.2. Speculative “inner-sphere” mechanism of oxidation of **Mes-(*t*-Bu)₂Acr-Ph•** by O_2



Scheme 5.3. Redox chemistry, proton transfer, and HAT pathways for a) O_2 and b) **TEMPO**

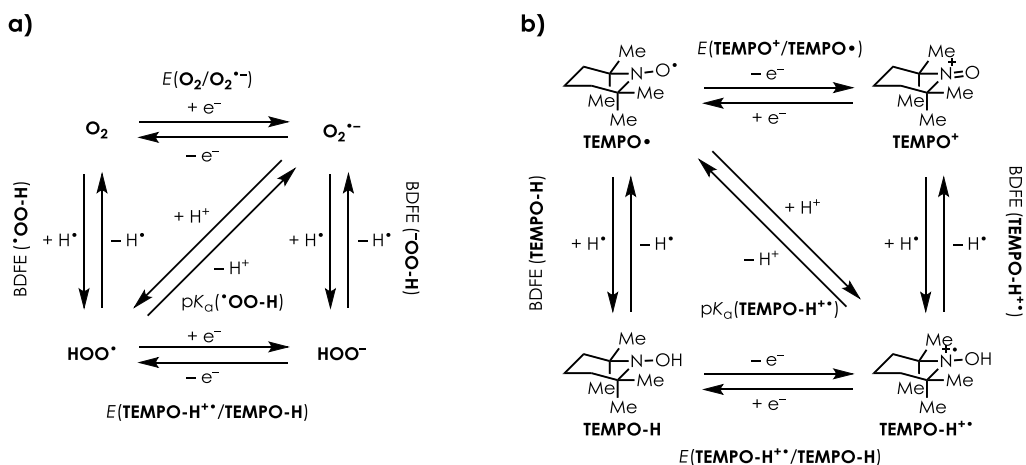


Table 5.1. Thermochemical properties of proposed intermediates related to the turnover of acridinyl radical **Mes-(*t*-Bu)₂Acr-Ph•**

property	value	solvent
$E_{1/2}(\text{TEMPO}^+/\text{TEMPO}^\bullet)$	+0.65 V (vs. SCE) ²⁹⁹	MeCN
$E_p(\text{TEMPO-H}^{++}/\text{TEMPO-H})$	+0.8 V (vs. AgNO ₃ /Ag) ³⁰⁰	MeCN
$E_p(\text{TEMPO}^\bullet/\text{TEMPO}^-)$	-1.91 V (vs. Fc ⁺ /Fc) ²⁹⁸	MeCN
$E_{1/2}(\text{O}_2/\text{O}_2^{\bullet-})$	-1.27 V (vs. Fc ⁺ /Fc) ³⁰¹	DMSO
	-0.75 V (vs. SCE) ³⁰²	MeCN
	-0.16 V (vs. NHE) ³⁰¹	H ₂ O
$E(\text{O}_2^{\bullet-}/\text{O}_2^{2-})$	< -2.0 V (vs. SCE) ³⁰³	DMSO
$E_{1/2}(\text{HO-O}^\bullet/\text{HO-O}^-)$	+0.76 V (vs. NHE) ³⁰¹	H ₂ O
BDFE (TEMPO-H)	71.0 kcal/mol ³⁰¹	H ₂ O
BDFE (TEMPO-H⁺)	56 kcal/mol ^a	MeCN
BDFE (HOO-H)	91.0 kcal/mol ³⁰¹	H ₂ O
BDFE (•OO-H)	60.6 kcal/mol ³⁰¹	H ₂ O
BDFE (^-OO-H)	81.6 kcal/mol ³⁰¹	H ₂ O
$pK_a(\text{TEMPO-H}^{++})$	-4 ³⁰¹	MeCN
$pK_a(\text{HO-O}^\bullet)$	4.9 ³⁰¹	H ₂ O
	~12 ³⁰⁴	DMSO
$pK_a(\text{HO-OH})$	11.6 ³⁰¹	H ₂ O
$pK_a(\text{pyrazole-H}^+)$	2.6 ^{305,306}	H ₂ O

^aThis value is calculated according to the equation used by Mayer, et. al.³⁰⁷: BDFE (in MeCN) = $nFE^\circ + 2.303RTpK_a + 54.9$, where n = number of electrons (i.e., 1), F = Faraday constant, R = gas constant, and T = temperature (298.15 K); values of $E_{1/2}(\text{TEMPO}^+/\text{TEMPO}^\bullet) = +0.24$ V (vs. Fc⁺/Fc, MeCN)³⁰¹ and $pK_a(\text{TEMPO-H}^{++}) = -4$.

Based on our previous studies on acridinyl radical turnover⁶¹ (see Section 3.2.2 above), a solution of **Mes-(*t*-Bu)₂Acr-Ph•** was successfully prepared by chemical reduction of **Mes-(*t*-Bu)₂Acr-Ph⁺** with **CoCp₂** (Scheme 5.4) under an inert atmosphere. The UV-Vis absorption spectrum of **Mes-(*t*-Bu)₂Acr-Ph•** (Figure 5.1) is very similar to that of **Mes-Acr-Me•**, exhibiting broad absorptions on the low energy side centered at 635 nm ($\epsilon = 580 \text{ M}^{-1}\text{cm}^{-1}$) and higher energy transitions at 520 nm ($\epsilon = 4600 \text{ M}^{-1}\text{cm}^{-1}$) and 363 nm. After sparging the solution with O₂ for 10 seconds, the acridinyl radical **Mes-(*t*-Bu)₂Acr-Ph•** was quantitatively converted to **Mes-(*t*-Bu)₂Acr-Ph⁺**, evidenced by complete recovery of the absorbance at 420 nm (Figure 5.1).

Scheme 5.4. Preparation of **Mes-(*t*-Bu)₂Acr-Ph•** and oxidation with O₂

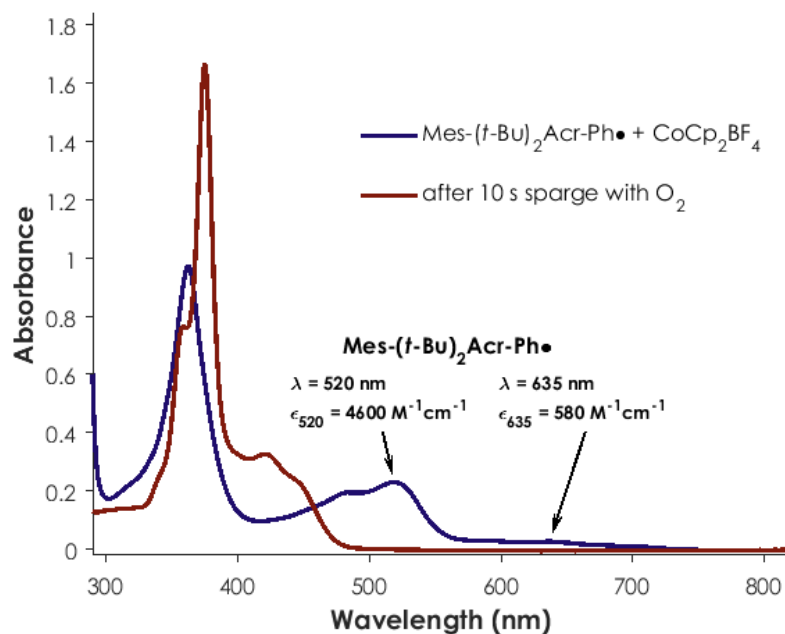
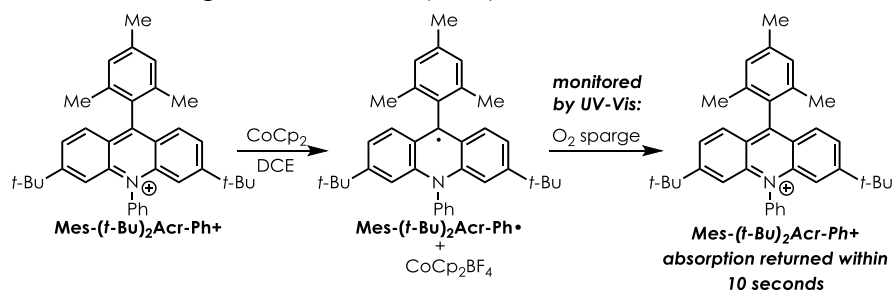


Figure 5.1. UV-Vis absorption spectrum of **Mes-(*t*-Bu)₂Acr-Ph•** (5.0×10^{-5} M in DCE) prepared by chemical reduction with **CoCp₂**; (blue) before and (red) after sparging with O₂ for 10 seconds

Although this experiment does not provide any information regarding the rate of Step 6, the result qualitatively confirms that O₂ is capable of oxidizing **Mes-(*t*-Bu)₂Acr-Ph•**, even though the redox potentials suggest otherwise. We also considered the possibility that other putative intermediates might be competent oxidants for this step. Superoxide (O₂^{•-}), the product of single electron reduction of O₂, is relatively stable in the absence of protons³⁰¹ but is an extremely poor single electron oxidant (see **Table 5.1**). However, O₂^{•-} can be protonated to form hydroperoxyl radical **HOO•** ($\text{p}K_{\text{a}}(\text{H-OO}^{\bullet}) = 4.9$)³⁰¹, which is reactive towards single electron

reduction ($E_{1/2}(\mathbf{HOO}^{\bullet}/\mathbf{HOO}^{-}) = +0.76$ V vs. NHE in H_2O).³⁰¹ Similarly, while \mathbf{TEMPO}^{\bullet} is itself a poor single electron oxidant, in the presence of acid, \mathbf{TEMPO}^{\bullet} is protonated to form $\mathbf{TEMPO-H}^{+}$,^{308,309} which disproportionates to \mathbf{TEMPO}^{+} and $\mathbf{TEMPO-H}$, and both \mathbf{TEMPO}^{+} and $\mathbf{TEMPO-H}^{+}$ should be capable of oxidizing $\mathbf{Mes-(t-Bu)_2Acr-Ph}^{\bullet}$ according to the values listed in **Table 5.1**. We note that the protons required for acid-induced disproportionations of both $\text{O}_2^{\bullet-}$ and \mathbf{TEMPO}^{\bullet} could be supplied by deprotonation of the distonic cation radical **5.2**, whose acidity is expected to be approximately that of pyrazolium ($\text{p}K_{\text{a}}(\text{pyrazole-H}^{+}) = 2.6$ in H_2O).^{305,306}

Moreover, that initial catalyst turnover likely generates oxygen centered radicals as the result of O_2 reduction led us to consider more closely how these reactive intermediates could entrain undesirable side reactions. Specifically, the relatively high O-H bond strength of hydrogen peroxide ($\text{BDE}(\mathbf{HOO-H}) = \sim 88$ kcal/mol²²¹ or $\text{BDFE}(\mathbf{HOO-H}) = 91.0$ kcal/mol³⁰¹) enables H-atom abstraction of relatively weak C-H bonds. Organic peroxy radicals formed by reaction of a carbon centered radical with O_2 can react similarly, and organic peroxides (ROOR)ⁱ can homolyze to form oxyl radicals (RO^{\bullet}) capable of HAT at even stronger C-H bonds.

The formation of such reactive oxygen centered radicals is the likely origin of undesired oxygenation reactions of substrates containing relatively weak C-H bondsⁱ observed in optimization efforts (i.e., Section 4.2). Additionally, the presence of 9 benzylic C-H bonds on the mesityl group of $\mathbf{Mes-(t-Bu)_2Acr-Ph}^{+}$ renders this portion of the catalyst structure susceptible to oxidative degradation in the presence of oxygen centered radicals. To address this latter possibility, we undertook an investigation of photoredox catalyst decomposition.

ⁱ For a possible mechanism for the formation organic peroxy radicals in this system, see **Scheme D.1**.

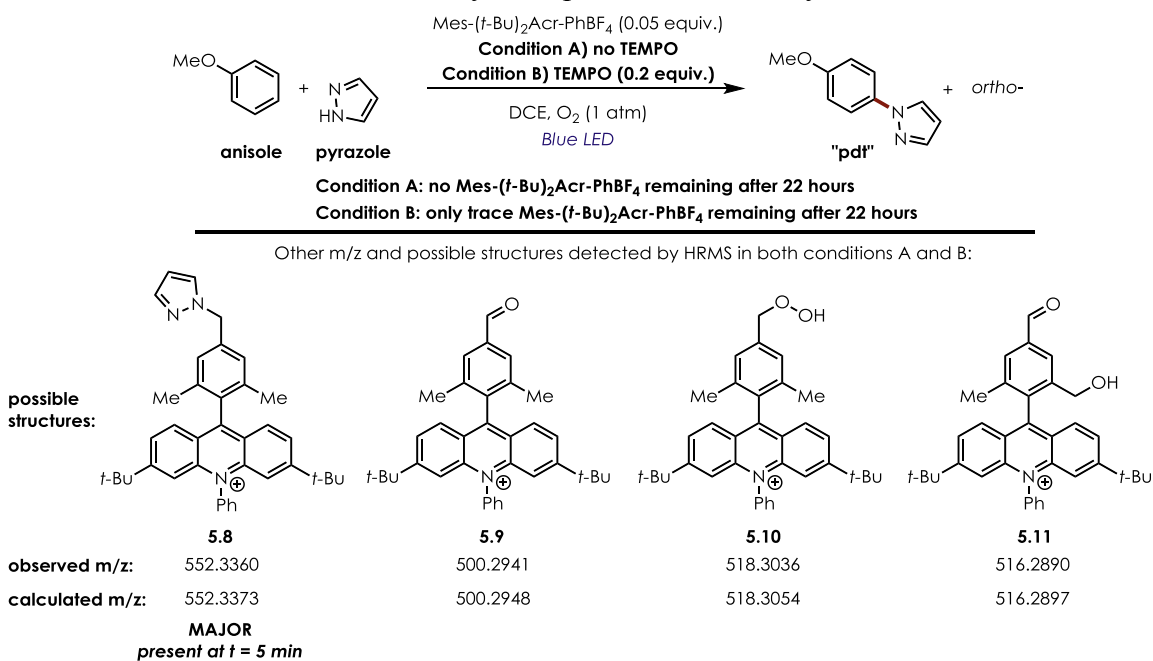
5.2.2 Analysis of photoredox catalyst degradation under aerobic conditions

We employed high resolution mass spectrometry (HRMS) to analyze reaction mixtures for products of photoredox catalyst decomposition. HRMS is a technique that is well suited for an investigation of photoredox catalyst decomposition in this context. The mass spectrometerⁱⁱ used in our analysis is capable of providing mass resolution at the ppm level, precision which is necessary to enable identification of the functional groups involved in catalyst functionalization. Additionally, when run with electrospray ionization in positive mode (ESI+), this system is particularly sensitive to the detection of acridinium cations and functionalized cationic derivatives.

After irradiation for 22 hours, reactions A and B shown in **Scheme 5.5** were analyzed by HRMS in order to determine whether the catalyst had undergone functionalization. For reaction A, run under an atmosphere of O₂ but in the absence of **TEMPO**, no trace of **Mes-(*t*-Bu)₂Acr-Ph⁺** could be detected. Instead, a number of new higher molecular weight species were present, consistent with varying degrees of oxygenation as well as C-H amination of the catalyst with pyrazole as the amine. **Scheme 5.5** shows possible structures corresponding to the measured *m/z* values, although it should be emphasized that these structures are not unequivocally determined structural isomers. For example, structure **5.8** is proposed for the observed *m/z* = 552.3360 (calc. 552.3373), although other regioisomers are possible for this *m/z*. Additionally, structure **5.10** is pictured as a benzylic peroxide, but the observed *m/z* could also correspond to a diol instead of a peroxide. Nonetheless, it is apparent that **Mes-(*t*-Bu)₂Acr-Ph⁺** undergoes a significant degree of oxidative functionalization under these conditions.

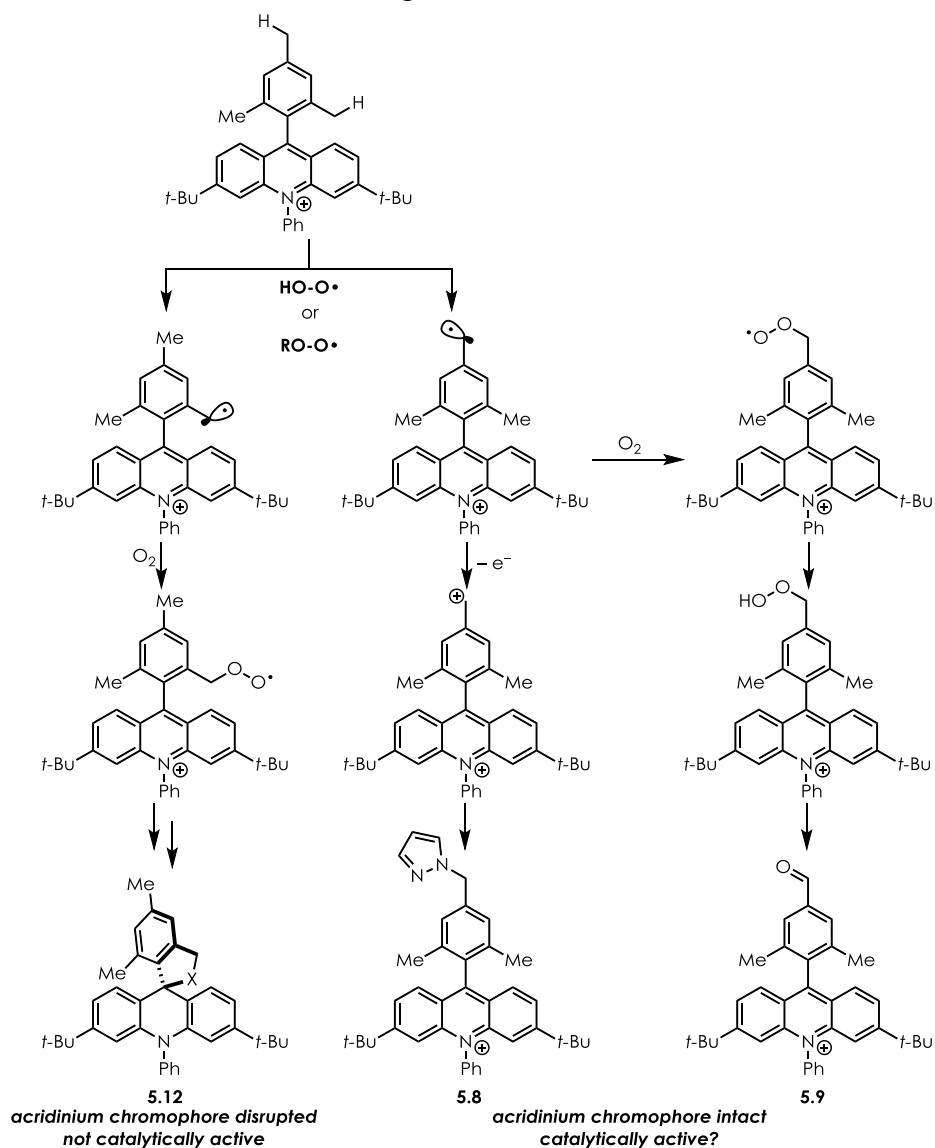
ⁱⁱ See Appendix D for experimental details.

Scheme 5.5. Analysis of product mixtures by HRMS



We believe the benzylic positions on the mesityl unit of **Mes-(*t*-Bu)₂Acr-Ph⁺** are the most likely sites of functionalization based on previous evidence that benzylic oxidation at these positions occurs in the related **Mes-Acr-Me⁺** when irradiated in the presence of O₂.³¹⁰ A proposed mechanism leading to the formation of the major putative byproducts detected by HRMS is shown in **Scheme 5.6**. The primary step leading to the depicted degradation pathways is benzylic H-atom abstraction, most likely by a peroxy radical, either **HO-O[•]** or an organic peroxy **RO-O[•]** formed by reaction of a carbon-centered radical with O₂. We also suggest in **Scheme 5.6** that benzylic functionalization at the 2'- and 6'- methyl groups may be more likely to result in deactivation of the photoredox catalyst. Acridinium salts bearing nucleophilic heteroatoms at these positions are known to cyclize to the corresponding spiro-acridans (e.g. **5.12**), which do not absorb at wavelengths greater than 350 nm.^{311,312} Such a disruption of the acridinium chromophore, as depicted in **Scheme 5.6**, is expected to result in the deactivation of the photoredox catalyst, as it would no longer absorb blue light.

Scheme 5.6. Possible degradation reactions of **Mes-(*t*-Bu)₂Acr-Ph⁺** as a result of HO₂[•] generation



One proposed explanation for the beneficial addition of **TEMPO** in this system is that it inhibits the radical chain reactivity leading to oxidative degradation of the acridinium photoredox catalyst.ⁱⁱⁱ If a lesser proportion of oxidative degradation byproducts were detected when the aryl

ⁱⁱⁱ For a description of a likely mechanism by which **TEMPO** can inhibit autoxidation processes in hydrocarbons, see the work of Pratt, et al.^{308,309}

amination reaction was run with **TEMPO** present as an additive than when **TEMPO** is absent, this could indicate that **TEMPO** does suppress deleterious degradation reactions of **Mes-(*t*-Bu)₂Acr-Ph⁺** and thus improves catalytic performance. When samples were analyzed by HRMS after running the aryl amination reaction under conditions B (**Scheme 5.5**), **Mes-(*t*-Bu)₂Acr-Ph⁺** could be detected in the reaction mixture, but only in trace amounts. The composition of the detected *m/z* values was largely similar to that of conditions A, consistent with oxygenation and C-H amination of **Mes-(*t*-Bu)₂Acr-Ph⁺**, but in this case, with **TEMPO** as an additive. Even in the early stages of reaction, products of catalyst C-H amination (**5.8**) and oxygenation (**5.9-5.11**) could be observed (i.e., as early as 5 minutes after the onset of irradiation). Although the addition of **TEMPO** seems to improve the longevity of **Mes-(*t*-Bu)₂Acr-Ph⁺**, that only trace amounts of the catalyst remain in the product mixtures suggests this improvement is marginal.

Moreover, the discovery of significant catalyst modification at early stages of the reaction is somewhat surprising, considering that productive catalysis still occurs in this regime. We considered several interpretations of this observed activity, including: a) the products of catalyst modification are catalytically active and kinetically comparable to the activity of the unmodified **Mes-(*t*-Bu)₂Acr-Ph⁺**, or b) the products of catalyst degradation are catalytically inactive, but catalysis occurs in a kinetic regime wherein a decreased [**Mes-(*t*-Bu)₂Acr-Ph⁺**] has minimal impact on the rate of product formation. In order to address these possibilities, we undertook a study of the reaction kinetics, drawing from the Reaction Progress Kinetic Analysis (RPKA) approach.

5.2.3 Reaction Progress Kinetic Analysis: differentiating catalyst degradation and product inhibition

Reaction Progress Kinetic Analysis (RPKA) is an approach to elucidating reaction mechanism championed by Donna Blackmond and involves the construction of “graphical rate laws” using data collected from relatively few experiments.³¹³ This methodology allows for determination of key mechanistic influences and is particularly well suited to the analysis of catalytic reactions, as it provides a framework for identifying when catalyst degradation and product inhibition are kinetically significant.³¹⁴ For this reason, we looked to the tools provided by RPKA to understand how the observed functionalization of **Mes-(*t*-Bu)₂Acr-Ph+** impacts the reaction kinetics.

We began our inquiry by collecting kinetic data for the aryl amination reaction under the “standard” optimized conditions (**Scheme 5.7**) by GC analysis of reaction aliquots.^{iv} The concentration of anisole ($[\text{anisole}]_t$) over the course of the reaction is shown in **Figure 5.2a**. Whereas the reaction rate is high at early timepoints – roughly 20% conversion is reached within 10 minutes – the reaction is slow to achieve full conversion. The $[\text{anisole}]_t$ data was transformed into instantaneous reaction rates by fitting the $[\text{anisole}]_t$ versus time data to an arbitrary function

^{iv} Typical analyses employing RPKA involve graphical manipulations of instantaneous reaction rates from a single kinetic run, so the best results are normally obtained using data collected from differential kinetic measurements (which measure reaction rate directly; e.g. calorimetry) or integral measurements (which allow for the measurement of concentration; e.g., such as in situ infrared (IR) spectroscopy) with sufficient time resolution to allow for accurate differentiation of the concentration versus time data. Our attempts to collect kinetic data using in situ IR measurements were obfuscated by overlapping absorptions of reaction components, which precluded the use of this technique. However, we were able to obtain high quality kinetic data by GC analysis. Although this method of gathering kinetics is comparatively time consuming, it can be done under the identical conditions used for the aryl amination reactions. Moreover, it has been demonstrated that some RPKA operations can be implemented without differentiation of the raw concentration versus time data.³¹⁴ Thus, we determined that RPKA would be fruitful when GC analysis was performed on aliquots sampled over the course of reaction.

and differentiating with respect to each time point.^v A plot of reaction rate vs. $[\text{anisole}]_t$ (**Figure 5.2b**, blue trace) reveals that the reaction rate decreases steadily in the first hour of irradiation, and further slows as anisole conversion nears completion.

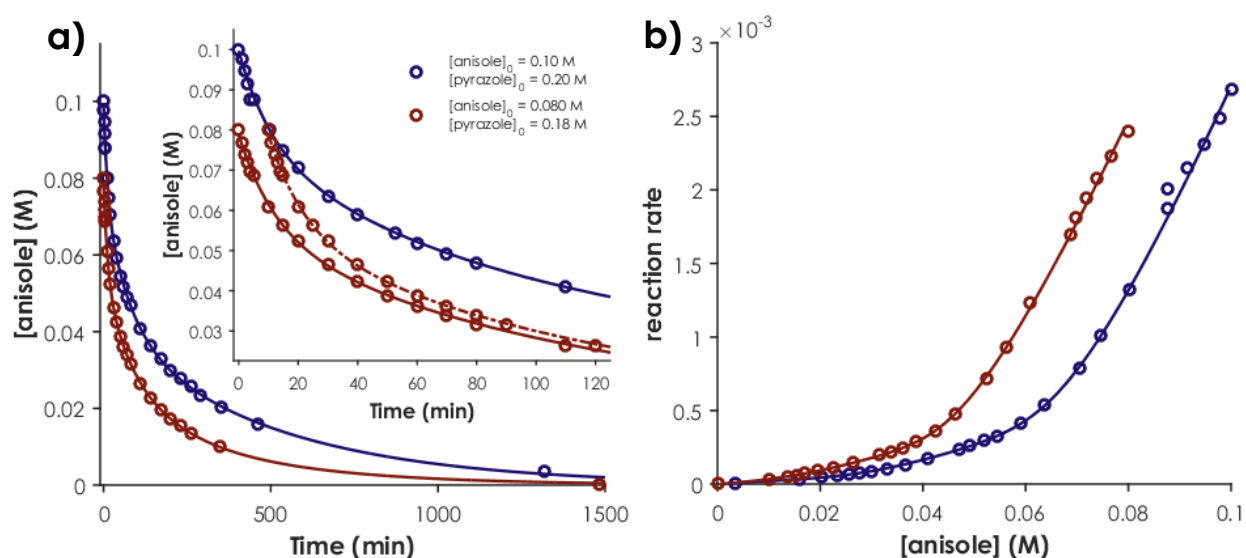
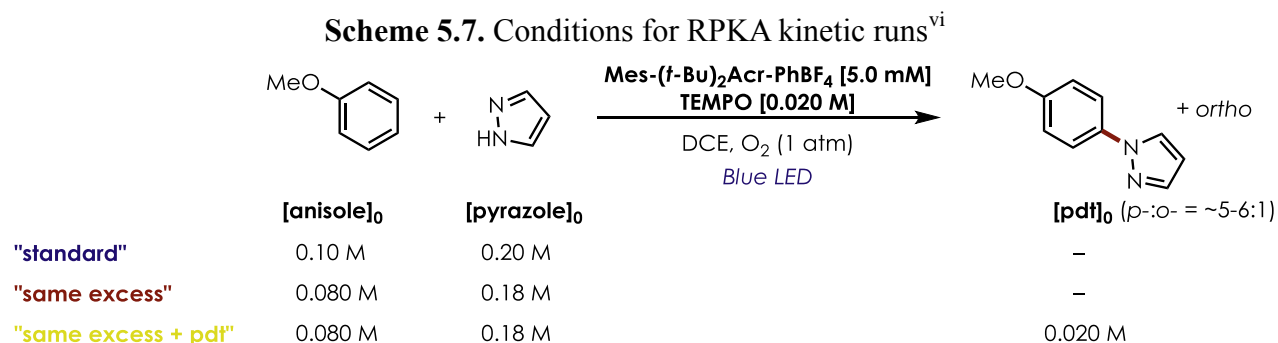


Figure 5.2. Reaction progress kinetic analysis, “same excess” experiment: a) kinetics, “standard” (blue) and “same excess” (red) experiments, inset shows unaltered kinetics (solid red line) and time-offset kinetics (dashed red line) for “same excess”. b) rate vs. $[\text{anisole}]$ for “standard” (blue) and “same excess” (red) experiments

^v See Appendix D for details about curve fitting and differentiation procedures.

^{vi} We use the abbreviation “pdt” to refer to both *para*- and *ortho*- isomers of the depicted structure. When referring to a specific isomer, we will use the notation **para** or **ortho**.

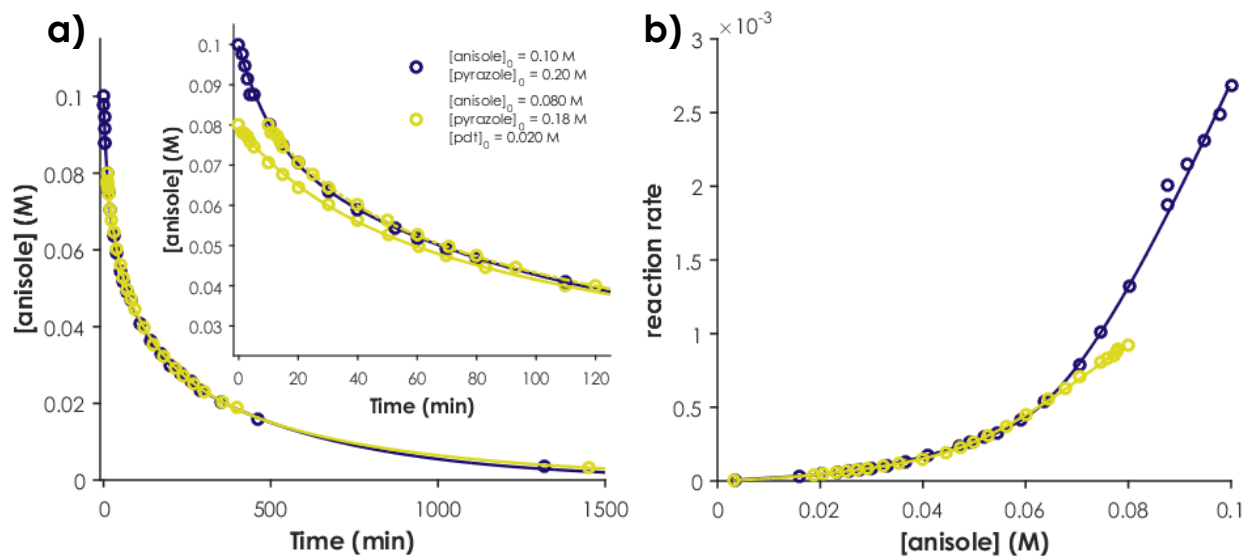


Figure 5.3. Reaction progress kinetic analysis, “same excess + **pdt**” experiment: a) kinetics, “standard” (blue) and “same excess + **pdt**” (yellow) experiments, inset shows unaltered kinetics (solid yellow line) and time-offset kinetics (dashed yellow line) for “same excess + **pdt**”. b) rate vs. [anisole] for “standard” (blue) and “same excess + **pdt**” (yellow) experiments

To investigate how catalyst decomposition affects the reaction rate, the reaction can be conducted at a different concentration of anisole, but the “same excess” of pyrazole.^v In this case, a plot of rate versus [anisole]_t will overlay if catalyst decomposition is not kinetically significant. To this end, the reaction was conducted at 0.080 M anisole with the “same excess” concentration of pyrazole (i.e., 0.18 M pyrazole; “same excess” experiment, **Scheme 5.7**). The plot of rate versus [anisole]_t for this experiment does not overlay with that of the standard conditions, and reveals that, at a given [anisole]_t, the rate remains significantly higher at any given [anisole] in the “same excess” conditions compared to the “standard” conditions (**Figure 5.2b**). Another way to compare these data is to offset the time axis of the “same excess” kinetics by a time interval equal to the time point where [anisole]_t is equal to 0.080 M in the standard conditions kinetics (i.e., [anisole]₀ = 0.08 M in the “same excess” run, see **Figure 5.2a**, inset, dashed red trace). In the absence of mechanistic factors such as catalyst degradation or product inhibition, the kinetic profiles should overlay when offsetting the “same excess” kinetics by this time interval (in this

case, 10 minutes). However, as in the plots of rate vs. [anisole] (**Figure 5.2b**), the time-offset kinetics do not overlay. This signifies that new mechanistic influences which negatively impact the reaction rate have emerged by the time the standard conditions reach 0.080 M anisole. There are two possible explanations for this behavior: a) **Mes-(*t*-Bu)₂Acr-Ph⁺** has undergone decomposition, or b) catalysis is subject to product inhibition.

To discriminate between catalyst decomposition and product inhibition, a reaction was conducted at identical concentrations as the “same excess” experiment, but with 0.020 M **pdt**^{vii} included at the beginning of the reaction. These conditions are intended to mimic the exact conditions present in the standard run at $t = 10$ min in the absence of significant catalyst degradation. In fact, the plots of rate vs. [anisole] (**Figure 5.3b**) and the time-offset kinetics (**Figure 5.3a**, inset) for the “same excess + **pdt**” experiment each overlay with the corresponding plots for the “standard” conditions. This result indicates that the mechanism for the aryl amination reaction is significantly influenced by product inhibition and not by catalyst deactivation.

These results lead to the prediction that the overall reaction rate law will exhibit some degree of negative order in [**pdt**], which is expressed by equation 5.1 below.

Equation 5.1

$$\text{rate} \propto \frac{a[\text{anisole}]^x}{b[\text{pdt}]^y} \quad \text{or} \quad \text{rate} \times b[\text{pdt}]^y \propto a[\text{anisole}]^x$$

However, we plotted the quantity “rate \times [**para**]^{viii} vs. [anisole] and found that the plots did not satisfactorily overlay for all three conditions in **Scheme 5.7** (see **Figure D.2**), indicating that the

^{vii} The sample of **pdt** used in this experiment was a 5:1 mixture of *para*- to *ortho*- isomers.

^{viii} Because the *ortho*- isomer of **pdt** (i.e., **ortho**) is formed in small amounts, the concentration data of [**ortho**] is noisy because of the limits on accurate integration of the GC peak. Thus, we use only the

rate law does not precisely follow the form given in equation 5.1. Ultimately, we found that plotting the quantities “[aniso] / rate” vs. $[\text{para}]^2$ resulted in linear plots that overlay for all three experiments (**Figure 5.4**). These plots can be fit to a linear regression of the form:

Equation 5.2

$$\frac{[\text{aniso}]}{\text{rate}} = \frac{[\text{para}]^2 + k_P}{k_A}$$

Where k_P and k_A are constants derived from the linear regression at the y-intercept and the slope.

Thus, a rate law can be constructed by rearrangement of equation 5.2 and is given in equation 5.3 below:

Equation 5.3

$$\text{rate} = \frac{k_A[\text{aniso}]}{[\text{para}]^2 + k_P}$$

To test the validity of the experimentally derived rate law, we simulated the kinetics ($[\text{aniso}]_t$ vs. time) according to the equation 5.3 and confirmed that the simulated kinetics overlay with the experimental kinetics nicely (see **Figure D.3**).^{ix}

$[\text{para}]$ data in the plots in **Figure 5.4** to reduce noise. Furthermore, we believe that **ortho** is likely to have a minor influence on product inhibition, both because **para** is formed in higher amounts and on the basis that the calculated redox potential for **para** is 0.35 V higher than for **ortho** (**Table 5.2**). Note also that under the “standard” and “same excess” conditions, the final **para:ortho** ratio is 6:1, but the sample used in the “same excess + **pdt**” conditions is 5:1 **para:ortho**. We believe this discrepancy is negligible and likely smaller than other sources of experimental uncertainty.

^{ix} Equation 5.3 is a differential equation, and the simulated kinetics were plotted using a numerical differential equation solver in MATLAB as described in Appendix D.

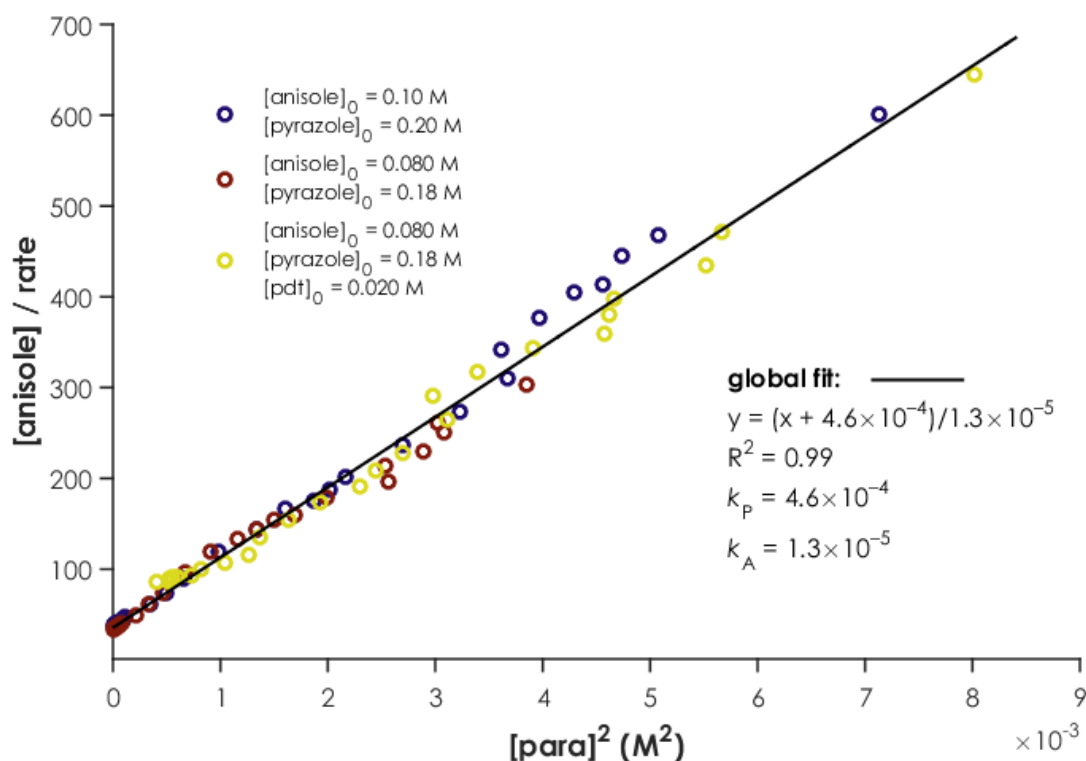


Figure 5.4. Graphical rate equation for the aryl amination conditions in **Scheme 5.7** where the quantities “[aniso]/rate” exhibits linear dependence on $[\text{para}]^2$; the solid line shows the global fit according the equation 5.2.

Moreover, the derived rate law can provide insight into our earlier observation that higher yields were obtained when running the reactions at lower concentrations.²⁹⁷ Because the rate is inversely proportional to the square of the product concentration ($[\text{para}]^2$), and $[\text{para}]$ is dependent on $[\text{aniso}]$ by the mass balance relationship,^x the denominator of equation 5.3 increases faster than the numerator decreases. Thus, a lower $[\text{aniso}]_0$ results in a lower $[\text{para}]$ at all time points and should delay the onset of product inhibition and lessen its impact by shrinking the denominator in equation 5.3. In other words, at lower $[\text{aniso}]_0$, a higher $[\text{para}]$ is required to achieve the same impact on the reaction rate. We can quantify this effect by defining $[\text{para}]_{50\%}$ as the concentration $[\text{para}]_t$ required to reduce the initial reaction rate (i.e., the rate at

^x See equations D.3 and D.4 in Appendix D.

$t=0$) by 50%. The derived rate law can be used to generate an expression that gives $[\text{para}]_{50\%}$ as a function of $[\text{anisole}]_0$ (see equation D.7), which results in $[\text{para}]_{50\%} = 0.017 \text{ M}$ for the “standard” conditions and $[\text{para}]_{50\%} = 0.016 \text{ M}$ for the “same excess” experiment.

We suggest in **Scheme 5.8** a mechanism to account for the observed product inhibition. This model takes into account our prior rationale that **pdt** and anisole compete to quench the excited state $[\text{Mes-(}t\text{-Bu)}_2\text{Acr-Ph}]^*$ by PET. Presumably, back electron transfer (BET) is possible between $\text{pdt}^{+\bullet}$ and $\text{Mes-(}t\text{-Bu)}_2\text{Acr-Ph}\bullet$ (as well as between $\text{anisole}^{+\bullet}$ and $\text{Mes-(}t\text{-Bu)}_2\text{Acr-Ph}\bullet$), and each sequence of excitation, quenching, and BET constitutes an unproductive, net redox neutral cycle.

We previously noted that **pdt** possesses a lower redox potential ($E_{p/2} = +1.50 \text{ V}$ vs. SCE, measured as a mixture of *para*- and *ortho*- isomers)²⁹⁷ than anisole ($E_{p/2} = +1.84 \text{ V}$ vs. SCE). The comparatively lower redox potential of **pdt** is expected to result in a higher rate constant of quenching (k_q)⁹⁹ for **pdt** than for anisole (i.e., $k_{q,\text{rel}} = k_q(\text{pdt})/k_q(\text{anisole}) > 1$). Indeed, we measured k_q for anisole and **pdt** by Stern-Volmer analysis of fluorescence quenching (**Table 5.2**), and we found that $k_q(\text{pdt})$ was 3.2 times that of $k_q(\text{anisole})$ ($k_{q,\text{rel}} = 3.2$).

Scheme 5.8. Competitive PET as the proposed origin of product inhibition

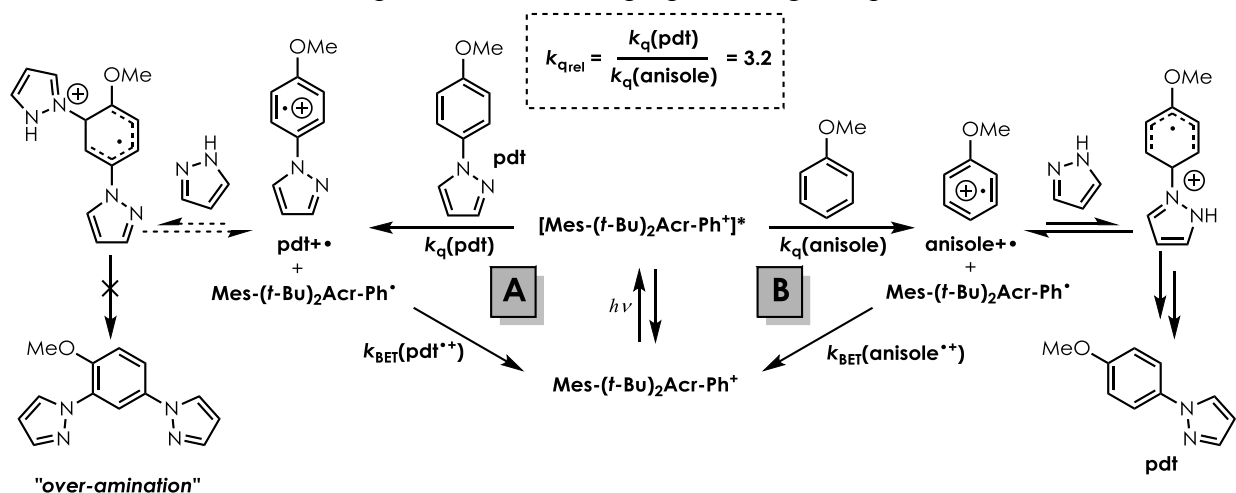


Table 5.2. Experimental and calculated redox potentials and rates of fluorescence quenching (k_q) of anisole and **pdt** determined by Stern-Volmer analysis

quencher	$E_{p/2}(D^{+}/D) / V$ vs. SCE	$E_{calc}(D^{+}/D) / V$ vs. SCE ^a	k_q (M ⁻¹ s ⁻¹)
anisole	1.84 ^b	1.65 ¹⁰³	2.1×10^9 ^c
pdt	1.50 ^{c,297}	1.29 ^d (1.64 ^e)	6.7×10^9 ^c

^aCalculated using B3LYP/6-31+G(d,p) by the identical method described in ¹⁰³ and Appendix A.

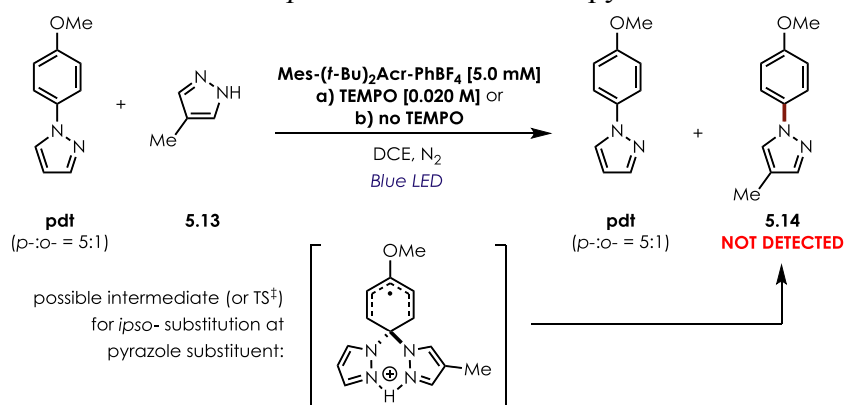
^bAverage of the values reported in references ¹⁰³ and ²⁹⁷. ^cMeasured as a ~5:1 mixture of *para*- and *ortho*- isomers. ^dCalculated for **para**. ^eCalculated for **ortho**.

Given that $k_{q,rel} = 3.2$, the rate of quenching for anisole is equal to that of **pdt** when $[pdt] = [anisole]/3.2$. We define the “critical concentration” of **pdt**, or $[pdt]_c$, to be the concentration of **pdt** at which the quenching rates are equal, and is determined when the expression $[pdt] = [anisole]/3.2$ is satisfied. In other words, when $[pdt]$ exceeds $[pdt]_c$, the rate of quenching for **pdt** becomes higher than the rate of quenching for anisole. This is analogous to $[para]_{50\%}$, which is a measure of $[para]_t$ at which product inhibition begins to dominate the rate law. Interestingly, under the reaction conditions studied here, $[para]_{50\%}$ occurs at a roughly similar concentrations relative to $[anisole]$ as $[pdt]_c$: the average $[anisole]_{50\%}/[para]_{50\%}$ for the “standard” and “same excess” experiments is 4.4, while $[anisole]_0/[pdt]_c$ is 3.2. We have yet to derive a rate law *a priori* that incorporates the kinetics of competitive quenching into the overall rate expression and unambiguously ties the macroscopic product inhibition to the quenching step, and we are currently investigating how the relative rates of BET impact the kinetics of competitive quenching. Nonetheless, that product inhibition emerges in the macroscopic kinetics at a similar relative concentration to that observed in the relative rates of fluorescence quenching may suggest that competitive PET is one origin of product inhibition.

This simplified model assumes that **pdt**⁺ reacts only with **Mes-(*t*-Bu)₂Acr-Ph•** to give their ground state counterparts, or it reacts reversibly and unproductively with pyrazole. Under

standard reaction conditions, we detect no products resulting from “over-addition” of pyrazole to **pdt**. We submitted **pdt** to reactions with 4-methylpyrazole **5.13** as a nucleophile to test whether the amine can add to **pdt**⁺ and displace pyrazole by *ipso*-substitution (**Scheme 5.9**), which would be otherwise untraceable with pyrazole as a nucleophile; however, none of the “crossover” product **5.14** was formed with and without **TEMPO** present. Thus, we assume that addition of pyrazole to **pdt**⁺ is unfavorable or there exists no irreversible downstream step in pathway A (**Scheme 5.8**) to ultimately effect a second aryl C-N bond formation. In contrast, productive catalysis does occur in pathway B through **anisole**⁺ if addition of pyrazole is followed by a subsequent irreversible step. Although we have yet to establish the identity of this irreversible step, we believe the observed product inhibition can be rationalized by a partitioning of **pdt** and anisole into unproductive cycles of successive PET and BET, with successful product formation proceeding through addition of pyrazole to **anisole**⁺.

Scheme 5.9. Probe for *ipso*-substitution at the pyrazole substituent^{xi}



5.3 Conclusions

By preparing the acridinyl radical **Mes-(*t*-Bu)₂Acr-Ph•** and studying it in isolation, we determined that O₂ is capable of turning over the catalytic cycle to regenerate the acridinium

^{xi} Reactions conducted under anaerobic conditions to prevent oxidative degradation

Mes-(*t*-Bu)₂Acr-Ph⁺. We also observed that **Mes-(*t*-Bu)₂Acr-Ph⁺** undergoes a significant degree of functionalization over the course of reaction, but, based on our analysis of the reaction kinetics, we believe the products of catalyst functionalization retain catalytic activity. Moreover, we confirmed that the reaction rate is negatively impacted by product formation, and we suggest that the mechanistic origin of this product inhibition is competitive quenching of the excited state **Mes-(*t*-Bu)₂Acr-Ph⁺***. This was corroborated by measuring the relative rates of fluorescence quenching, which revealed that **pdt** quenches **Mes-(*t*-Bu)₂Acr-Ph⁺*** with a rate constant 3.2 times that of anisole. It is expected that other arene-amine combinations are likewise subject to product inhibition, and the kinetic relationships borne out of this study may suggest strategies to exceed current limitations on synthetic yields, possibly by lowering initial reactant concentrations or sequestration of the product to prevent competitive PET. Although catalyst functionalization appears to have minimal impact on the optimized aryl amination system, it may yet be important in related transformations.

Efforts are currently underway to assemble a more comprehensive mechanistic framework for understanding this system. Additional kinetic experiments could allow for construction of a complete rate law that accounts for order in each component, with the aim of elucidating the key rate limiting factors. We also hope to fully understand the origin of the beneficial inclusion of **TEMPO** as a co-catalyst, and whether or not it plays a role beyond mediating oxidative side reactions. Ultimately, we wish to clarify the factors behind the site selectivity of this reaction with the goal of developing predictive models that can be accurately applied to all classes of substrates.

5.4 Associated Content

Appendix D. Experimental Procedures and Spectral Data

APPENDIX A: SUPPORTING INFORMATION FOR “EXPERIMENTAL AND CALCULATED ELECTROCHEMICAL POTENTIALS OF COMMON ORGANIC MOLECULES FOR APPLICATIONS TO SINGLE-ELECTRON REDOX CHEMISTRY”

A.1 Computational Details

A.1.1 Geometry optimization and calculation of Gibbs free energy

All DFT calculations were carried out using the Gaussian 09 software package¹⁵⁶ at the (U)B3LYP^{149,150} and (U)M06-2X¹⁵¹ levels of theory with the 6-31+G(d,p) basis set.^{152,153} For the structures containing Fe or I, the LanL2DZ³¹⁵⁻³¹⁷ basis set was used to describe the Fe or I atoms, while 6-31+G(d,p) was used for all other atoms in the molecule. Geometry optimizations were carried out for the reduced and oxidized forms of each molecule, and frequency calculations were performed on the minimized structures in the same sequence by specifying the “freq” keyword in the route section. The CPCM formalism for the Self Consistent Reaction Field (SCRF) model of solvation was employed in all calculations to account for solvation in acetonitrile, and the default parameters as implemented in Gaussian were used (i.e., radii defined by the UFF parameters). All optimized structures used to calculate the redox potentials herein were confirmed to reside on local minima, as they lacked imaginary frequencies. Gibbs free energies at 298 K (G_{298}) were obtained from the calculation output as the “Sum of electronic and thermal Free Energies.”

A.1.2 Calculation of solution phase electrochemical redox potentials

Ultimately, two free energies are required for the calculation of redox potentials

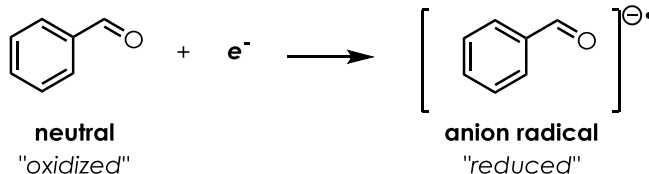
$E_{1/2}^{\text{o,calc}}$ according to the following expanded form of **Equation 2.4** (see main text):

Equation A.1

$$E_{1/2}^{\text{o,calc}} = -\frac{(G_{298}[\text{reduced}] - G_{298}[\text{oxidized}])}{n_e \mathcal{F}} - E_{1/2}^{\text{o,SHE}} + E_{1/2}^{\text{o,SCE}}$$

Where n_e is the number of electrons transferred (in all calculations here, $n_e = 1$ and is accordingly omitted from all subsequent expressions), \mathcal{F} is the Faraday constant (value 23.061 kcal mol⁻¹ V⁻¹), $E_{1/2}^{\text{o,SHE}}$ is the absolute value for the standard hydrogen electrode (SHE, value = 4.281 V)⁹⁵ and $E_{1/2}^{\text{o,SCE}}$ is the potential of the saturated calomel electrode (SCE) relative to SHE in acetonitrile (value = -0.141 V)⁹⁵, and $G_{298}[\text{oxidized}]$ and $G_{298}[\text{reduced}]$ are the Gibbs free energies in acetonitrile as gathered from DFT calculations. Example calculations for both reduction and oxidation potentials are shown below.

Scheme A.1. Example #1: Reduction potential of benzaldehyde using B3LYP



$$G_{298}[\text{neutral}] = -345.526186 \text{ Hartree}$$

$$G_{298}[\text{anion radical}] = -345.622680 \text{ Hartree}$$

$$\Delta G_{1/2}^{\text{o}} = (G_{298}[\text{anion radical}] - G_{298}[\text{neutral}])$$

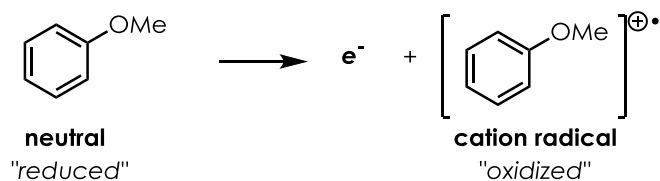
$$= (-345.622680 - -345.526186 \text{ Hartree}) \times 627.5 \text{ kcal mol}^{-1} \text{Hartree}^{-1}$$

$$= -60.55 \text{ kcal mol}^{-1}$$

$$E_{1/2}^{\text{o,calc}} = -\frac{\Delta G_{1/2}^{\text{o}}}{n_e \mathcal{F}} - E_{1/2}^{\text{o,SHE}} + E_{1/2}^{\text{o,SCE}} = -\frac{-60.55 \text{ kcal mol}^{-1}}{23.061 \text{ kcal mol}^{-1} \text{V}^{-1}} - 4.281 \text{ V} - 0.141$$

$$= -1.80 \text{ V vs. SCE}$$

Scheme A.2. Example #2: Oxidation potential of anisole using B3LYP



$$G_{298}[\text{neutral}] = -346.700459 \text{ Hartree}$$

$$G_{298}[\text{cation radical}] = -346.477141 \text{ Hartree}$$

$$\Delta G_{1/2}^{\circ} = (G_{298}[\text{neutral}] - G_{298}[\text{cation radical}])$$

$$= (-346.700459 - -346.477141 \text{ Hartree}) \times 627.5 \text{ kcal mol}^{-1} \text{Hartree}^{-1}$$

$$= -140.13 \text{ kcal mol}^{-1}$$

$$E_{1/2}^{\text{o,calc}} = -\frac{\Delta G_{1/2}^{\circ}}{n_e \mathcal{F}} - E_{1/2}^{\text{o,SHE}} + E_{1/2}^{\text{o,SCE}} = -\frac{-140.13 \text{ kcal mol}^{-1}}{23.061 \text{ kcal mol}^{-1} \text{V}^{-1}} - 4.281 \text{ V} - 0.141 \text{ V}$$

$$= \mathbf{1.65 \text{ V vs. SCE}}$$

A.1.3 Plots of experimental redox potentials compared with DFT results for the electrochemical series

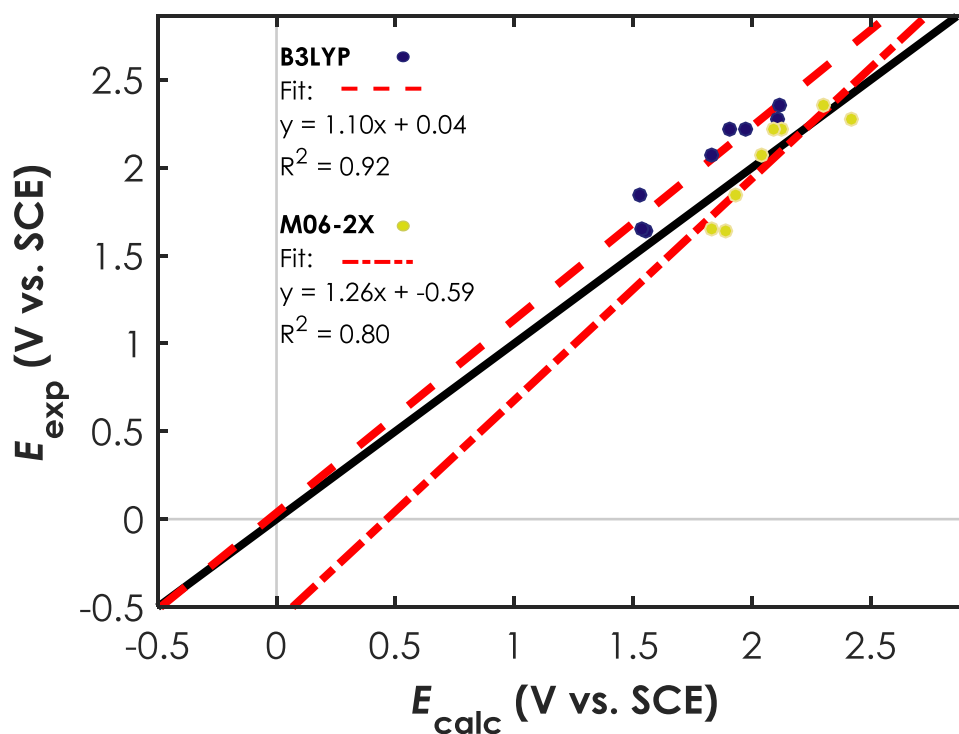


Figure A.1. Aromatic Hydrocarbons and Alkynes

Table A.1. Aromatic Hydrocarbons and Alkynes				
Name	CAS #	$E_{p/2}^{\text{exp}}$ (V vs. SCE)	$E_{1/2}^{\text{B3LYP}}$ (V vs. SCE)	$E_{1/2}^{\text{M06-2X}}$ (V vs. SCE)
Toluene	108-88-3	2.36	2.12	2.30
<i>o</i> -Xylene	95-47-6	2.22	1.91	2.12
<i>m</i> -Xylene	108-38-3	2.22	1.97	2.09
Mesitylene	108-67-8	2.07	1.83	2.04
Naphthalene	91-20-3	1.64	1.55	1.89
Phenylacetylene	536-74-3	2.27	2.11	2.42
Diphenylacetylene	501-65-5	1.84	1.52	1.93
1-ethynyl-4-methoxybenzene	768-60-5	1.65	1.54	1.83

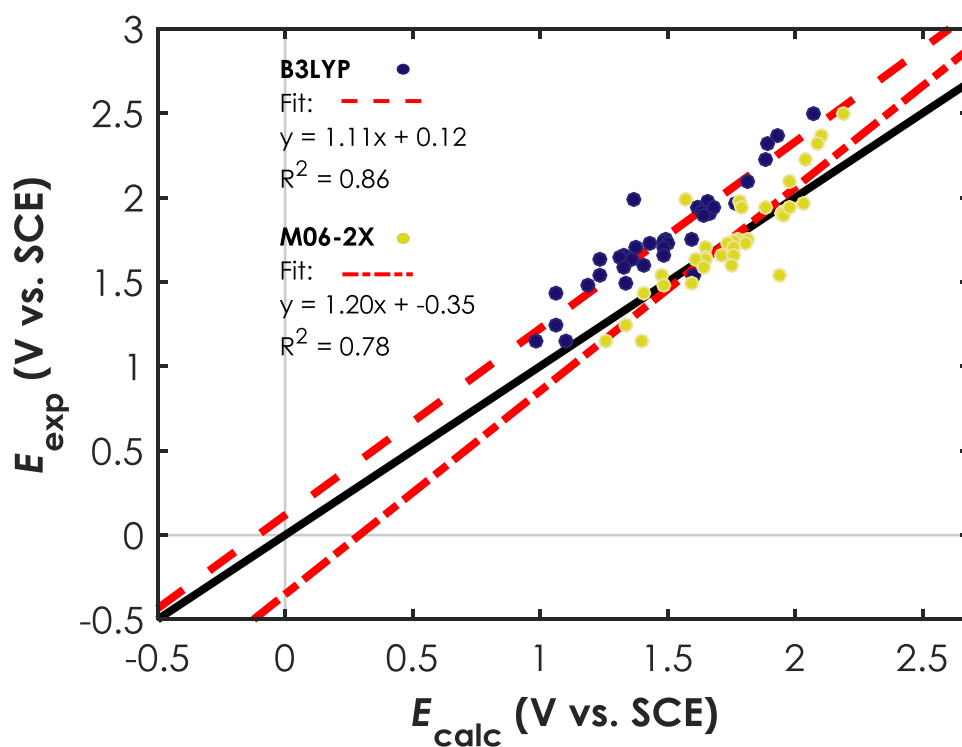


Figure A.2. Alkenes

Table A.2. Alkenes				
Name	CAS #	$E_{p/2}^{\text{exp}}$ (V vs. SCE)	$E_{1/2}^{\text{B3LYP}}$ (V vs. SCE)	$E_{1/2}^{\text{M06-2X}}$ (V vs. SCE)
2-Methyl-1-pentene	763-29-1	2.50	2.07	2.19
Cyclohexene	110-83-8	2.37	1.93	2.10
Cyclopentene	142-29-0	2.32	1.89	2.09
Norbornene	498-66-8	2.22	1.88	2.04
3-Methyl-2-buten-1-ol	556-82-1	2.10	1.82	1.98
2,4-Dimethyl-1,3-pentadiene	1000-86-8	1.98	1.37	1.57
2-Methyl-2-butene	513-35-9	1.98	1.65	1.78
Styrene	100-42-5	1.97	1.76	2.03
2-Chloro- <i>trans</i> - β -methylstyrene	13271-10-8	1.94	1.62	1.88
1-Methylcyclohexene	591-49-1	1.94	1.62	1.79
3-Bromo- <i>trans</i> - β -methylstyrene	50618-01-4	1.92	1.64	1.95
α -Methylstyrene	98-83-9	1.91	1.67	1.95
3-Chloro- <i>trans</i> - β -methylstyrene	26293-11-8	1.89	1.64	1.95
Methyl (<i>E</i>)-4-(prop-1-enyl)benzoate	158475-38-8	1.94	1.68	1.98
1-Methylcyclopentene	693-89-0	1.75	1.60	1.78
4-Bromo- <i>trans</i> - β -methylstyrene	4489-23-0	1.75	1.49	1.82

<i>trans</i> - β -methylstyrene	873-66-5	1.74	1.48	1.76
3-Methyl- <i>trans</i> - β -methylstyrene	17271-70-4	1.73	1.43	1.73
4-Chloro- <i>trans</i> - β -methylstyrene	1879-53-4	1.73	1.50	1.80
4-Fluoro- <i>trans</i> - β -methylstyrene	699-01-4	1.71	1.48	1.76
2-Methyl- <i>trans</i> - β -methylstyrene	2077-34-1	1.70	1.38	1.65
1,3-Di(1-propenylbenzene)	123884-49-1	1.66	1.33	1.72
Indene	95-13-6	1.66	1.49	1.76
4- <i>tert</i> -Butyl- <i>trans</i> - β -methylstyrene	68175-34-8	1.65	1.32	1.65
1-Phenylcyclohexene	771-98-2	1.64	1.36	1.65
1,2-Di(1-propenylbenzene)	33996-35-9	1.64	1.24	1.61
3-Methoxy- <i>trans</i> - β -methylstyrene	52956-26-0	1.60	1.41	1.76
4-Methyl- <i>trans</i> - β -methylstyrene	2077-30-7	1.59	1.33	1.64
1,3-Cyclohexadiene	592-57-4	1.54	1.24	1.48
1,2-Diphenylethylene	530-48-3	1.54	1.60	1.94
2-Methoxy- <i>trans</i> - β -methylstyrene	2077-36-3	1.48	1.19	1.49
1,4-Di(1-propenylbenzene)	46125-60-4	1.43	1.06	1.41
1-(3-thiophenyl)-(<i>E</i>)-1-propene	112114-38-2	1.49	1.33	1.59
<i>trans</i> -Anethol	4180-23-8	1.24	1.06	1.34
3,4-Dimethoxystyrene	6380-23-0	1.15	1.10	1.40
Isosafrole	120-58-1	1.15	0.98	1.26

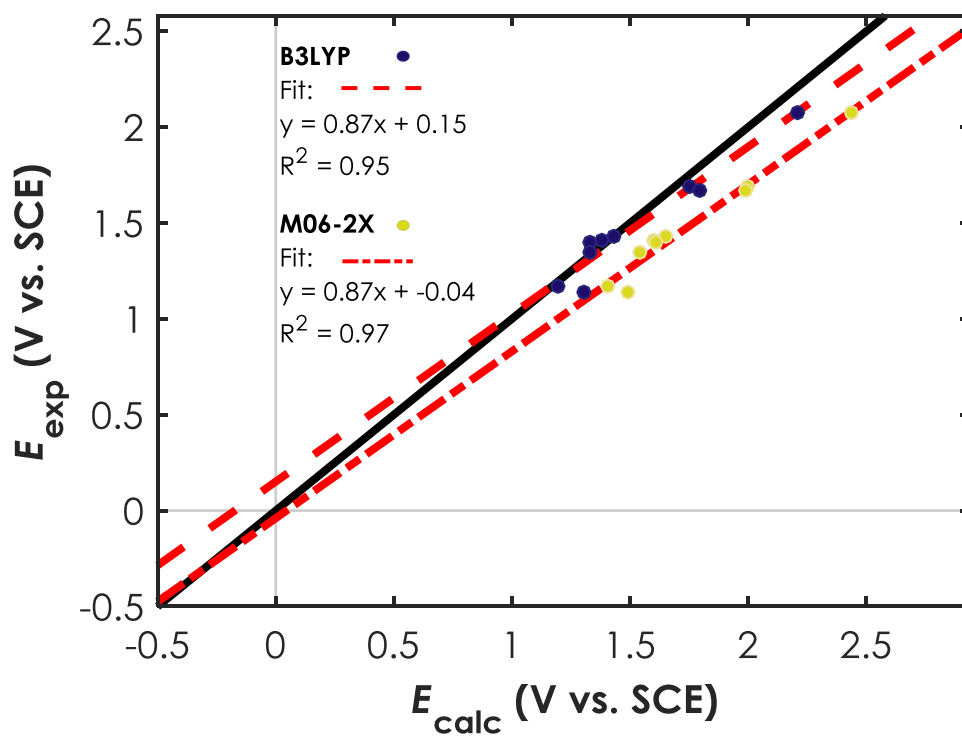


Figure A.3. Phenols

Table A.3. Phenols				
Name	CAS #	$E_{p/2}^{\text{exp}}$ (V vs. SCE)	$E_{1/2}^{\text{B3LYP}}$ (V vs. SCE)	$E_{1/2}^{\text{M06-2X}}$ (V vs. SCE)
4-Cyanophenol	767-00-0	2.08	2.21	2.44
4-Bromophenol	106-41-2	1.69	1.75	2.00
Phenol	108-95-2	1.63	1.79	1.99
3,4-Dimethylphenol	95-65-8	1.43	1.43	1.65
Guaiacol	90-05-1	1.41	1.38	1.60
2-Naphthol	135-19-3	1.40	1.33	1.61
2,4,6-Trimethylphenol	527-60-6	1.35	1.33	1.54
4-Methoxyphenol	150-76-5	1.17	1.19	1.41
Hydroquinone	123-31-9	1.14	1.30	1.49

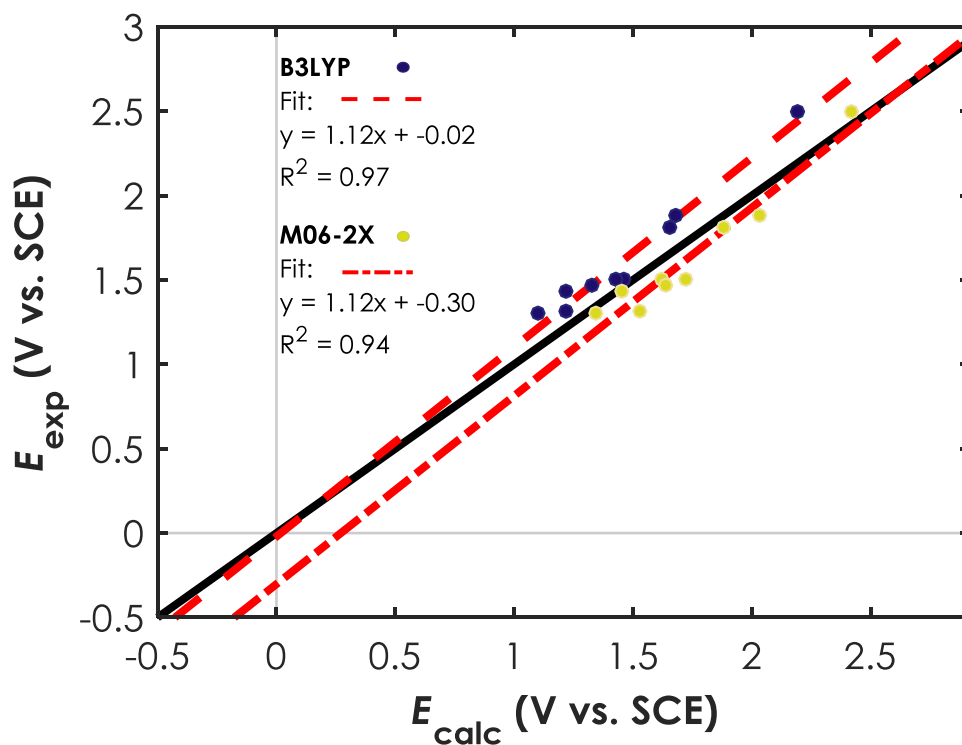


Figure A.4. Aliphatic, Aryl, and Enol Ethers

Table A.4. Aliphatic, Aryl, and Enol Ethers				
Name	CAS #	$E_{p/2}^{\text{exp}}$ (V vs. SCE)	$E_{1/2}^{\text{B3LYP}}$ (V vs. SCE)	$E_{1/2}^{\text{M06-2X}}$ (V vs. SCE)
1,4-Dioxane	123-91-1	2.50	2.19	2.42
Diphenyl ether	101-84-8	1.88	1.68	2.03
Anisole	100-66-3	1.81	1.65	1.88
3,4-Dihydro-2 <i>H</i> -pyran	110-87-2	1.51	1.46	1.62
<i>m</i> -Dimethoxybenzene	151-10-0	1.50	1.43	1.72
1,3-Di(iso-propoxy)benzene	79128-08-8	1.47	1.33	1.64
<i>o</i> -Dimethoxybenzene	91-16-7	1.43	1.21	1.46
2-Methoxynaphthalene	93-04-9	1.32	1.21	1.53
<i>p</i> -Dimethoxybenzene	150-78-7	1.30	1.10	1.34

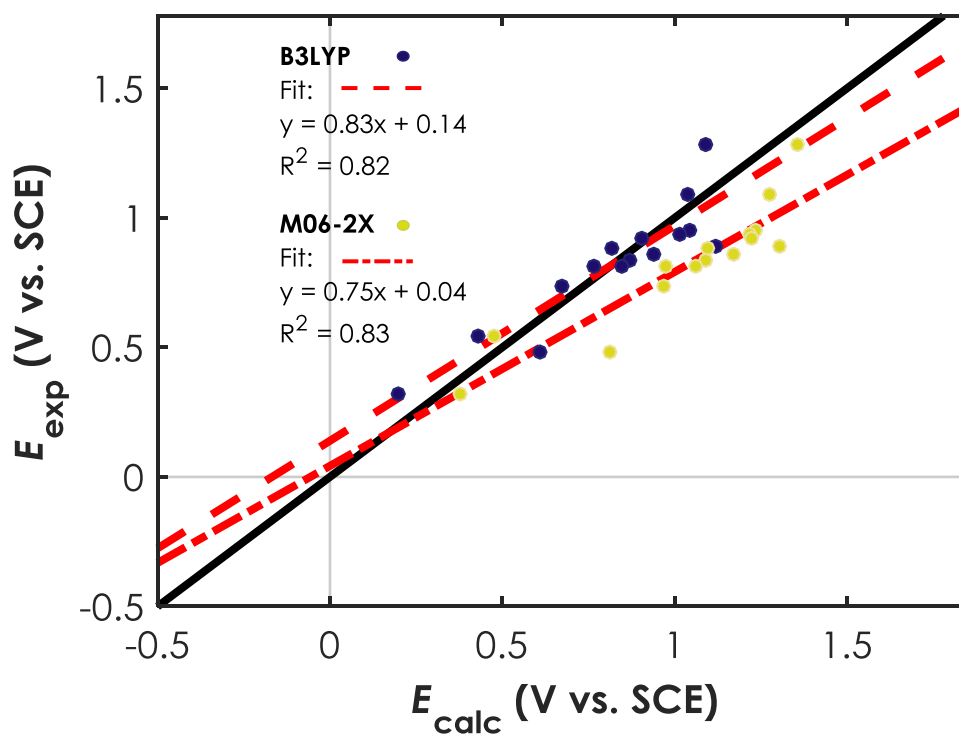


Figure A.5. Aliphatic and Aryl Amines and Enamines

Table A.5. Aliphatic and Aryl Amines, and Enamines				
Name	CAS #	$E_{p/2}^{\text{exp}}$ (V vs. SCE)	$E_{1/2}^{\text{B3LYP}}$ (V vs. SCE)	$E_{1/2}^{\text{M06-2X}}$ (V vs. SCE)
1,8-Diazabicyclo[5.4.0]undec-7-ene	6674-22-2	1.28	1.09	1.36
Diisopropylamine	108-18-9	1.09	1.04	1.27
Aniline	62-53-3	0.95	1.04	1.24
Piperidine	110-89-4	0.94	1.02	1.22
Diphenylamine	122-39-4	0.92	0.90	1.22
Pyrrolidine	123-75-1	0.89	1.12	1.30
<i>N</i> -Phenylmorpholine	92-53-5	0.88	0.82	1.10
<i>m</i> -Anisidine	536-90-3	0.86	0.94	1.17
2,6-Di(iso-propyl)aniline	24544-04-5	0.84	0.87	1.09
<i>p</i> -Toluidine	106-49-0	0.81	0.85	1.06
Triethylamine	121-44-8	0.83	0.76	0.98
<i>N,N</i> -Dimethylaniline	121-69-7	0.74	0.67	0.97
1-Morpholinocyclohexene	670-80-4	0.54	0.43	0.48
<i>o</i> -Phenylenediamine	95-54-5	0.48	0.61	0.81
1-Cyclohex-1-enylpyrrolidine	1125-99-1	0.32	0.20	0.38

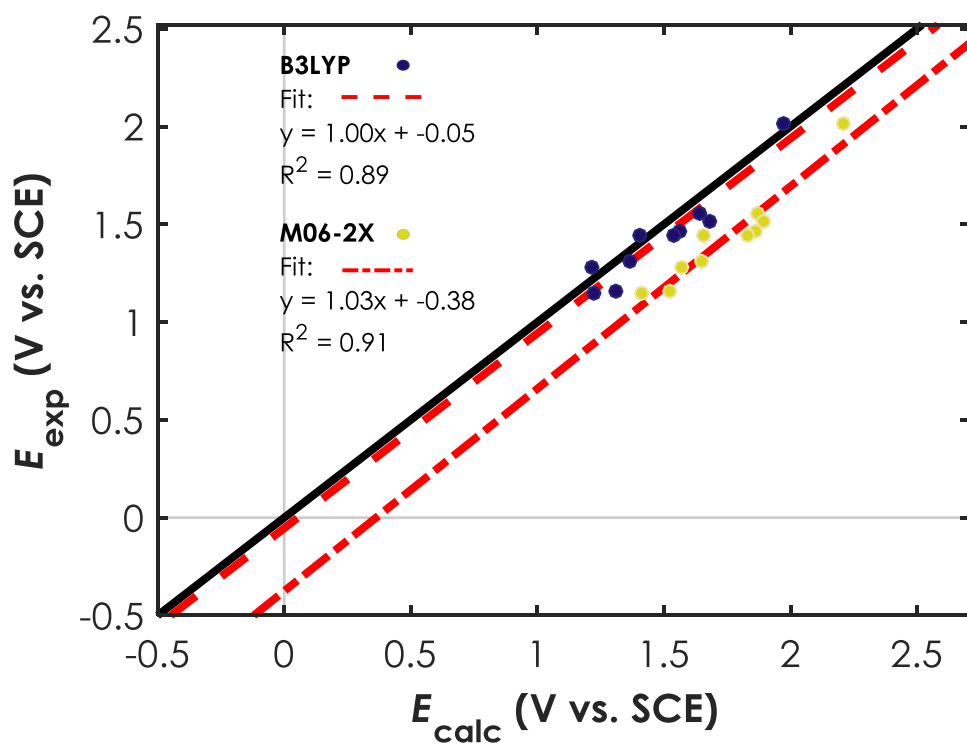


Figure A.6. Thiols, Sulfides, and Disulfides

Table A.6. Thiols, Sulfides, and Disulfides				
Name	CAS #	$E_{\text{p}/2}^{\text{exp}}$ (V vs. SCE)	$E_{1/2}^{\text{B3LYP}}$ (V vs. SCE)	$E_{1/2}^{\text{M06-2X}}$ (V vs. SCE)
<i>p</i> -Nitrophenyl disulfide	100-32-3	2.02	1.97	2.21
Phenyl disulfide	882-33-7	1.56	1.64	1.87
Thiophenol	108-98-5	1.51	1.68	1.89
<i>p</i> -Tolyl disulfide	103-19-5	1.46	1.56	1.86
Thioanisole	100-68-5	1.44	1.40	1.66
2,6-Dimethylthiophenol	118-72-9	1.44	1.54	1.83
2-Naphthalenethiol	91-60-1	1.33	1.37	1.65
<i>p</i> -Methoxyphenyl disulfide	5335-87-5	1.28	1.22	1.57
1,4-Benzenedithiol	624-39-5	1.16	1.31	1.52
4-Methoxythiophenol	696-63-9	1.15	1.22	1.42

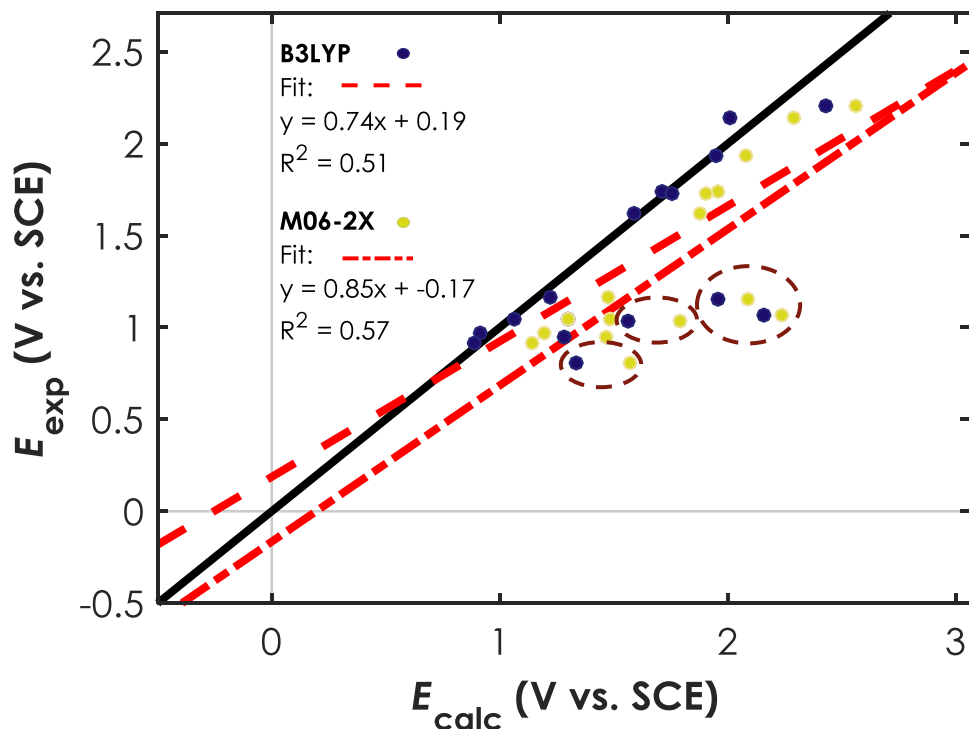


Figure A.7. Aromatic Heterocycles

Table A.7. Aromatic Heterocycles				
Name	CAS #	$E_{p/2}^{\text{exp}}$ (V vs. SCE)	$E_{1/2}^{\text{B3LYP}}$ (V vs. SCE)	$E_{1/2}^{\text{M06-2X}}$ (V vs. SCE)
Pyrazole	288-13-1	2.21	2.43	2.56
Quinoline	91-22-5	2.14	2.01	2.29
Furan	110-00-9	1.94	1.95	2.08
2,3-Benzofuran	271-89-6	1.74	1.71	1.96
Furfuryl alcohol	98-00-0	1.73	1.75	1.90
Thianaphthene	95-15-8	1.62	1.59	1.88
Indole	120-72-9	1.16	1.22	1.47
Imidazole	288-32-4	1.15	1.96	2.09
2-Mercaptobenzoxazole	2382-96-9	1.07	2.16	2.24
<i>N</i> -Methylpyrrole	96-54-8	1.04	1.30	1.49
5-Methoxyindole	1006-94-6	1.04	1.06	1.30
2-Mercaptobenzothiazole	149-30-4	1.03	1.56	1.79
4-Methoxyindole	4837-90-5	0.97	0.91	1.19
2-Aminothiazole	96-50-4	0.95	1.28	1.47
6-Methoxyindole	3189-13-7	0.92	0.89	1.15
2-Mercaptobenzimidazole	583-39-1	0.81	1.34	1.57

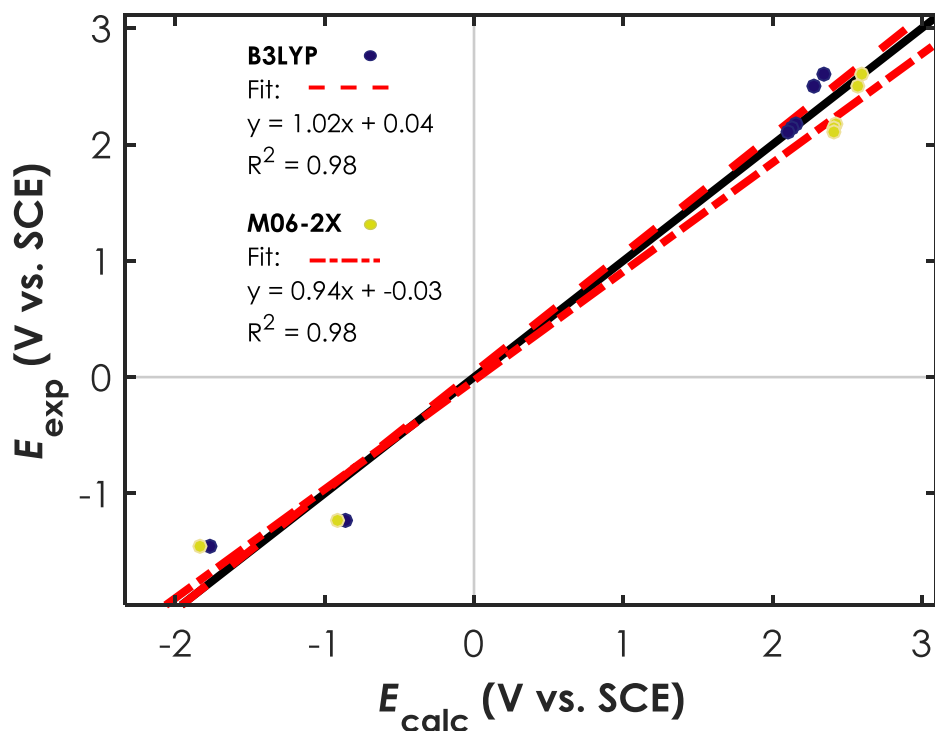


Figure A.8. Alkyl and Aryl Halides

Table A.8. Alkyl and Aryl Halides				
Name	CAS #	$E_{p/2}^{\text{exp}}$ (V vs. SCE)	$E_{1/2}^{\text{B3LYP}}$ (V vs. SCE)	$E_{1/2}^{\text{M06-2X}}$ (V vs. SCE)
Chlorobenzene	108-90-7	2.61	2.35	2.60
Bromobenzene	108-86-1	2.50	2.28	2.57
Iodobenzene	591-50-4	2.17	2.16	2.42
1-Chloro-4-iodobenzene	637-87-6	2.15	2.13	2.41
1-Chloro-4-iodobenzene	637-87-6	-1.94	D	D
1-Bromo-4-iodobenzene	589-87-7	2.10	2.11	2.41
1-Bromo-4-iodobenzene	589-87-7	-1.95	D	D
1-Fluoro-4-nitrobenzene	350-46-9	-1.23	-0.86	-0.91
Diiodomethane	75-11-6	-1.82	D	D
1,2-Dichloroethane	107-06-2	-1.92	D	D
Carbon tetrachloride	56-23-5	-2.48	D	D
Dibromomethane	74-95-3	-2.48	D	D
α -Bromoacetophenone	70-11-1	-1.46	-1.77	-1.84
ethyl 2-bromoacetate	105-36-2	-1.08	D	D
diethyl 2-bromomalonate	685-87-0	-0.62	D	D

“D” signifies that the structure could not be minimized due to spontaneous dissociation during geometry optimization

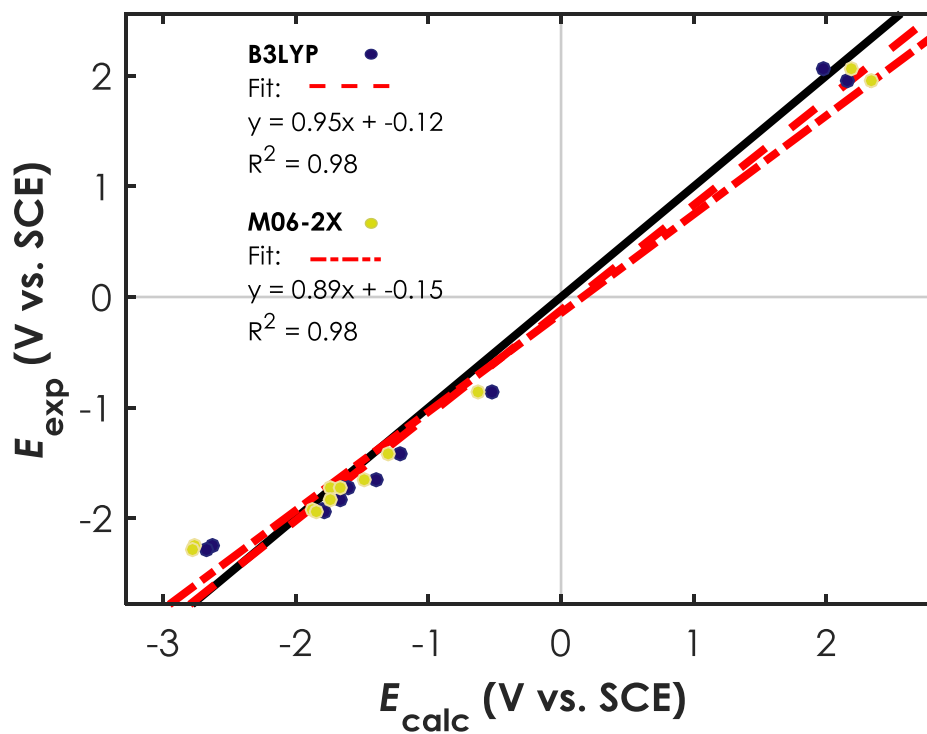


Figure A.9. Aldehydes

Table A.9. Aldehydes				
Name	CAS #	$E_{p/2}^{\text{exp}}$ (V vs. SCE)	$E_{1/2}^{\text{B3LYP}}$ (V vs. SCE)	$E_{1/2}^{\text{M06-2X}}$ (V vs. SCE)
<i>p</i> -Anisaldehyde	123-11-5	2.06	1.98	2.19
<i>p</i> -Hydroxybenzaldehyde	123-08-0	1.95	2.16	2.34
<i>p</i> -Nitrobenzaldehyde	555-16-8	-0.86	-0.53	-0.63
<i>p</i> -Cyanobenzaldehyde	105-07-7	-1.42	-1.21	-1.30
<i>p</i> -Trifluoromethylbenzaldehyde	455-19-6	-1.66	-1.40	-1.49
Biphenyl-4-carboxaldehyde	3218-36-8	-1.72	-1.65	-1.74
2-Naphthaldehyde	66-99-9	-1.73	-1.60	-1.66
<i>p</i> -Chlorobenzaldehyde	104-88-1	-1.85	-1.67	-1.74
Benzaldehyde	100-52-7	-1.93	-1.80	-1.87
<i>o</i> -Tolualdehyde	529-20-4	-1.94	-1.79	-1.84
3-Methylbutyraldehyde	590-86-3	-2.24	-2.63	-2.77
Cyclohexanecarboxaldehyde	2043-61-0	-2.28	-2.67	-2.78

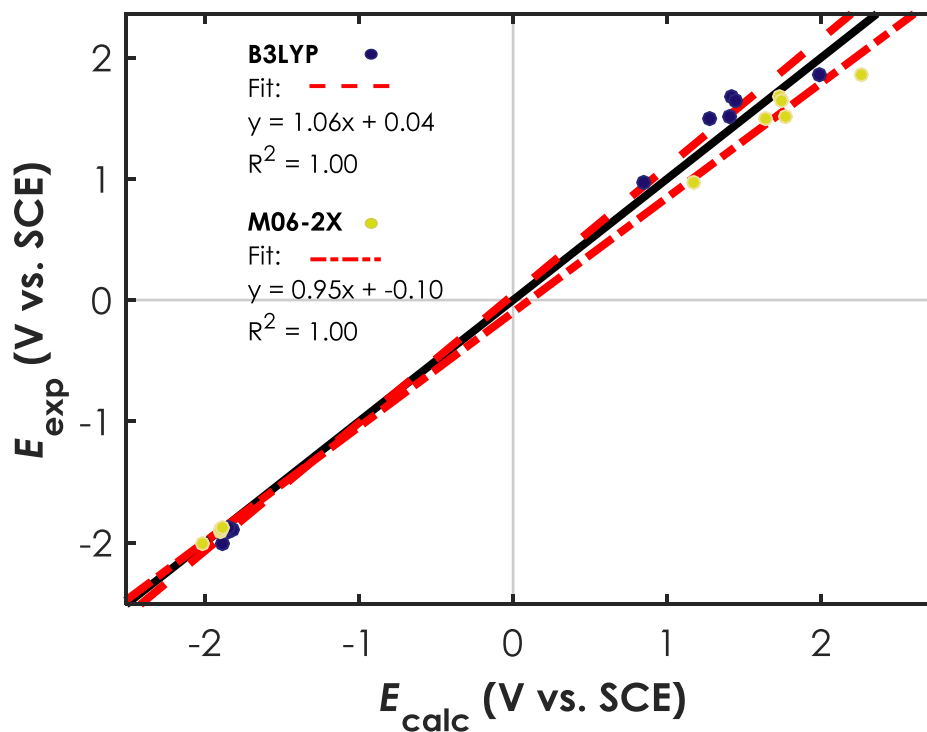


Figure A.10. Imines, Oximes, and Hydrazones

Table A.10. Imines, Oximes, and Hydrazones				
Name	CAS #	$E_{p/2}^{\text{exp}}$ (V vs. SCE)	$E_{1/2}^{\text{B3LYP}}$ (V vs. SCE)	$E_{1/2}^{\text{M06-2X}}$ (V vs. SCE)
Benzaldoxime	932-90-1	1.86	1.99	2.26
(<i>E</i>)- <i>N</i> -(Phenylmethylene)benzenamine	1750-36-3	1.67	1.41	1.73
(<i>E</i>)- <i>N</i> -(Phenylmethylene)benzenamine	1750-36-3	-1.91	-1.85	-1.89
(<i>E</i>)- <i>N</i> -Benzylidene-4-fluoroaniline	83306-62-1	1.64	1.44	1.74
(<i>E</i>)- <i>N</i> -Benzylidene-4-fluoroaniline	83306-62-1	-1.90	-1.82	-1.89
(<i>E</i>)- <i>N</i> -Benzylidene-3-methoxyaniline	5877-59-8	1.52	1.41	1.77
(<i>E</i>)- <i>N</i> -Benzylidene-3-methoxyaniline	5877-59-8	-1.88	-1.85	-1.89
(<i>E</i>)- <i>N</i> -Benzylidene-4-methylaniline	1613-92-9	1.50	1.28	1.63
(<i>E</i>)- <i>N</i> -Benzylidene-4-methylaniline	1613-92-9	-2.01	-1.88	-2.01
Benzaldehyde diphenyl hydrazone	966-88-1	0.97	0.84	1.17

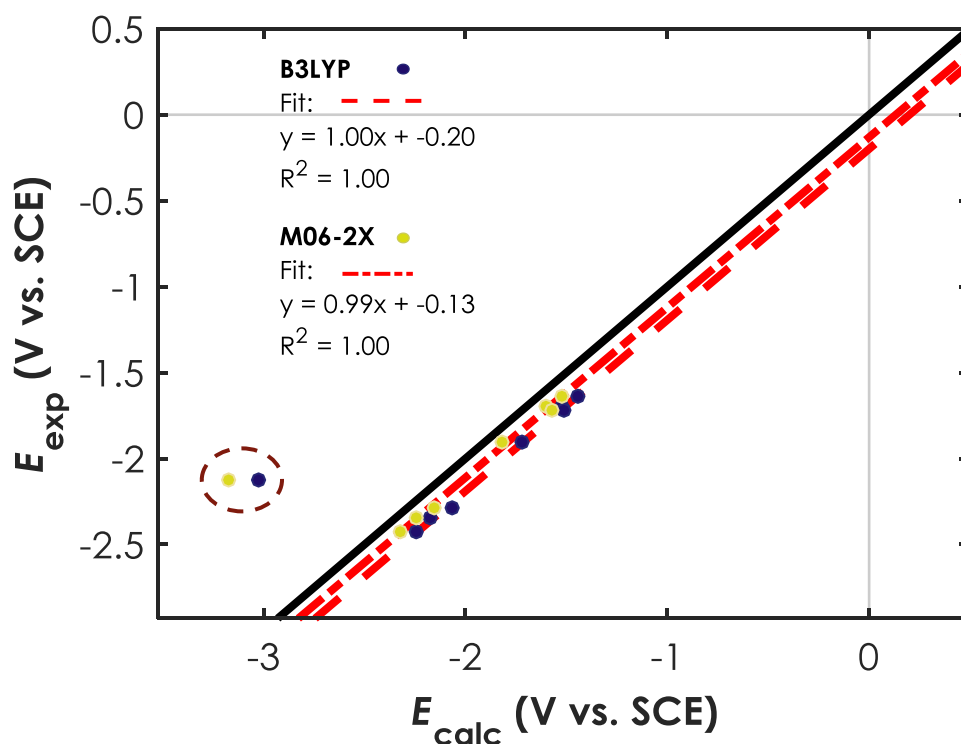


Figure A.11. Carboxylic acids, Esters, and Nitriles (NOTE: γ -butyrolactone (highlighted) is not in the linear regression)

Table A.11. Carboxylic acids, Esters, and Nitriles				
Name	CAS #	$E_{p/2}^{\text{exp}}$ (V vs. SCE)	$E_{1/2}^{\text{B3LYP}}$ (V vs. SCE)	$E_{1/2}^{\text{M06-2X}}$ (V vs. SCE)
<i>p</i> -Dicyanobenzene	623-26-7	-1.64	-1.45	-1.52
<i>o</i> -Dicyanobenzene	91-15-6	-1.70	-1.52	-1.60
<i>m</i> -Dicyanobenzene	626-17-5	-1.90	-1.72	-1.82
Benzonitrile	100-47-0	-2.43	-2.24	-2.32
Methyl 4-cyanobenzoate	1129-35-7	-1.72	-1.51	-1.57
γ -Butyrolactone	96-48-0	-2.13	-3.02	-3.17
Methyl benzoate	93-58-3	-2.34	-2.17	-2.24
Benzoic acid	65-85-0	-2.29	-2.07	-2.15

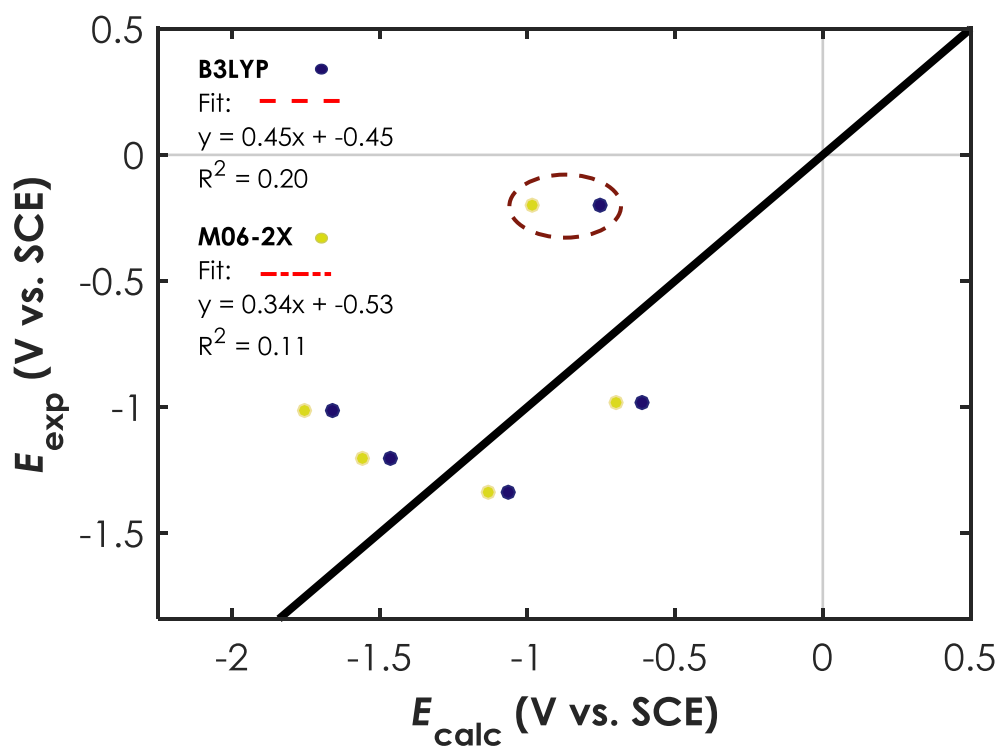


Figure A.12. Acyl- and Sulfonyl- Chlorides, and Anhydrides

Table A.12. Acyl- and Sulfonyl- Chlorides, and Anhydrides				
Name	CAS #	$E_{p/2}^{\text{exp}}$ (V vs. SCE)	$E_{1/2}^{\text{B3LYP}}$ (V vs. SCE)	$E_{1/2}^{\text{M06-2X}}$ (V vs. SCE)
3,5-Bis(trifluoromethyl)-benzenesulfonyl chloride	39234-86-1	-0.45	D	D
2-Nitrobenzenesulfonyl chloride	1694-92-4	-0.51	D	D
Benzoyl chloride	98-88-4	-1.20	-1.47	-1.56
<i>p</i> -Toluenesulfonyl chloride	98-59-9	-1.37	D	D
2-Mesitylenesulfonyl chloride	773-64-8	-1.45	D	D
Trifluoroacetic anhydride	407-25-0	-0.20	-0.75	-0.98
Maleic anhydride	108-31-6	-0.98	-0.61	-0.70
Benzoic anhydride	93-97-0	-1.01	-1.66	-1.75
Phthalic anhydride	85-44-9	-1.34	-1.07	-1.14

“D” signifies that the structure could not be minimized due to spontaneous dissociation during geometry optimization

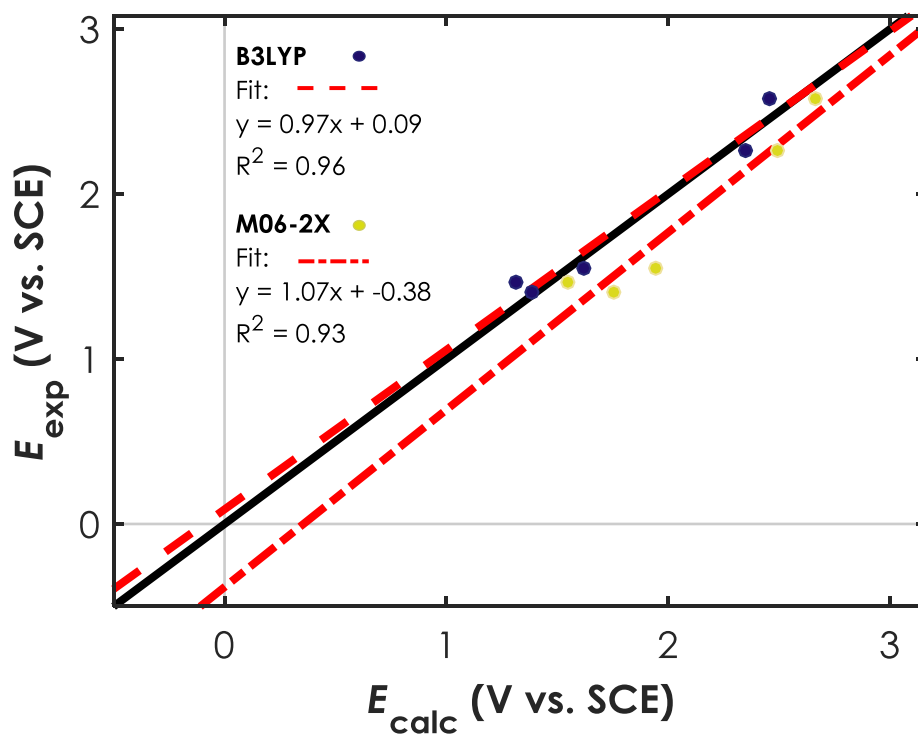


Figure A.13. Amides and Carboxylates

Table A.13. Amides and Carboxylates				
Name	CAS #	$E_{p/2}^{\text{exp}}$ (V vs. SCE)	$E_{1/2}^{\text{B3LYP}}$ (V vs. SCE)	$E_{1/2}^{\text{M06-2X}}$ (V vs. SCE)
δ -Valerolactam	675-20-7	2.58	2.45	2.66
<i>N,N</i> -Dimethylformamide	68-12-2	2.26	2.35	2.49
1,3-Dimethyl-3,4,5,6-tetrahydro-2(1 <i>H</i>)-pyrimidone	7226-23-5	1.55	1.62	1.94
Tetrabutylammonium pivalate	29650-96-2	1.26	D	D
Tetrabutylammonium benzoate	18819-89-1	1.40	1.39	1.75
Tetrabutylammonium acetate	10534-59-5	1.47	1.31	1.55

“D” signifies that the structure could not be minimized due to spontaneous dissociation during geometry optimization

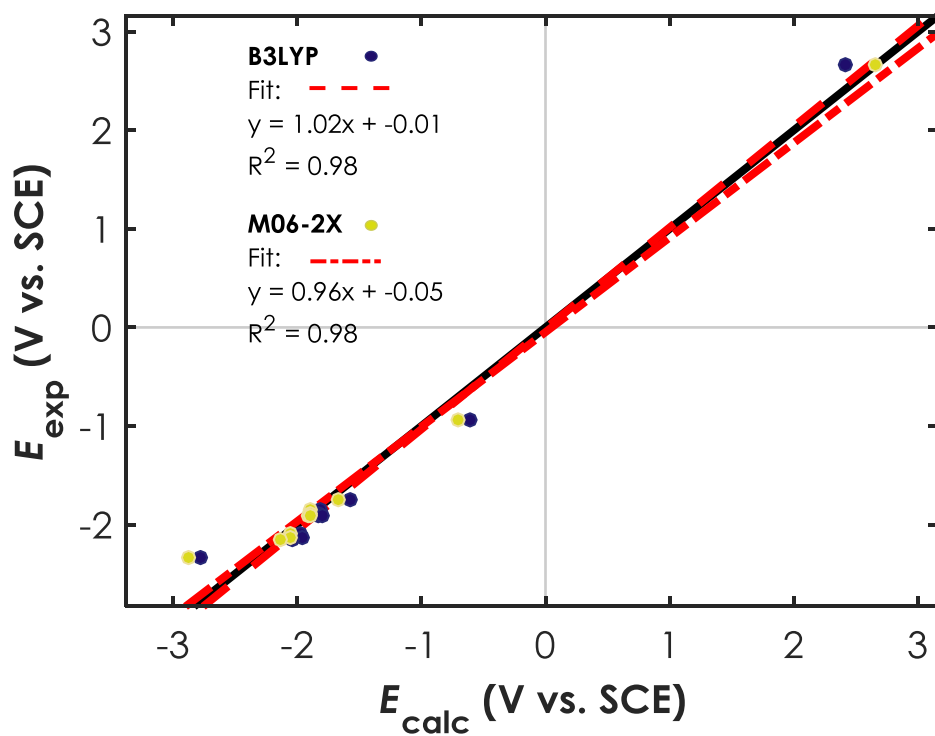


Figure A.14. Ketones

Table A.14. Ketones				
Name	CAS #	$E_{p/2}^{\text{exp}}$ (V vs. SCE)	$E_{1/2}^{\text{B3LYP}}$ (V vs. SCE)	$E_{1/2}^{\text{M06-2X}}$ (V vs. SCE)
Cyclohexyl methyl ketone	823-76-7	2.66	2.41	2.66
4'-Nitroacetophenone	100-19-6	-0.93	-0.60	-0.71
4'-Trifluoromethylacetophenone	709-63-7	-1.74	-1.58	-1.67
4'-Iodoacetophenone	13329-40-3	-1.85	-1.82	-1.90
4'-Bromoacetophenone	99-90-1	-1.89	-1.83	-1.89
4'-Chloroacetophenone	99-91-2	-1.91	-1.84	-1.91
4-Acetylbiphenyl	92-91-1	-1.91	-1.80	-1.89
Acetophenone	98-86-2	-2.11	-1.97	-2.05
4'-Fluoroacetophenone	403-42-9	-2.13	-1.96	-2.06
4'-Methylacetophenone	122-00-9	-2.16	-2.05	-2.13
Cyclohexanone	108-94-1	-2.33	-2.78	-2.88

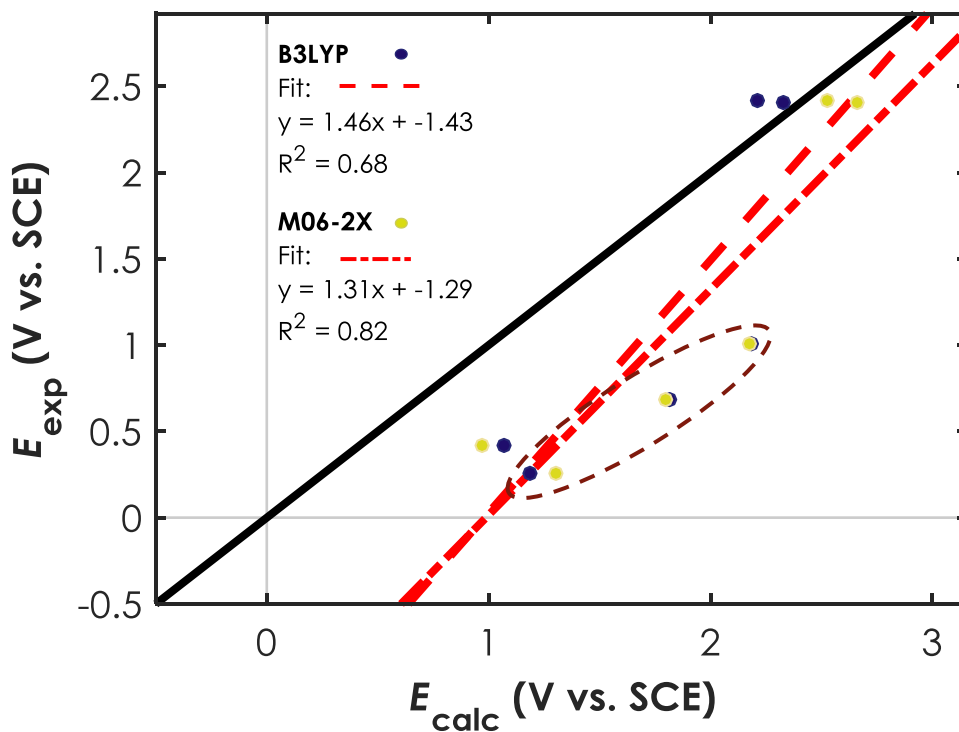


Figure A.15. Nitro compounds, Organosilanes, Halides

Table A.15. Nitro compounds, Organosilanes, Halides				
Name	CAS #	$E_{p/2}^{\text{exp}}$ (V vs. SCE)	$E_{1/2}^{\text{B3LYP}}$ (V vs. SCE)	$E_{1/2}^{\text{M06-2X}}$ (V vs. SCE)
Triphenylsilane	789-25-3	2.42	2.21	2.53
Chlorotriphenylsilane	76-86-8	2.41	2.32	2.66
Ferrocene	102-54-5	0.42	1.07	0.97
Ammonium cerium(IV) nitrate	16774-21-3	0.98	not calculated	not calculated
Tetrabutylammonium Iodide	311-28-4	0.26	1.19	1.30
Tetrabutylammonium Bromide	1643-19-2	0.71	1.82	1.80
Tetrabutylammonium Chloride	1112-67-0	1.01	2.19	2.18

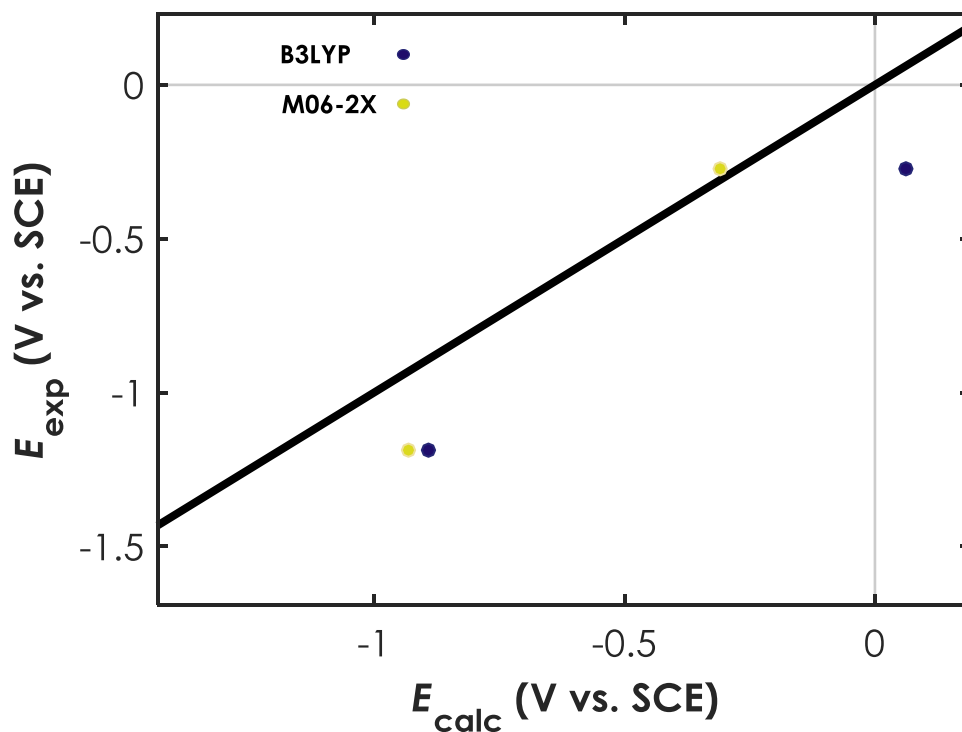


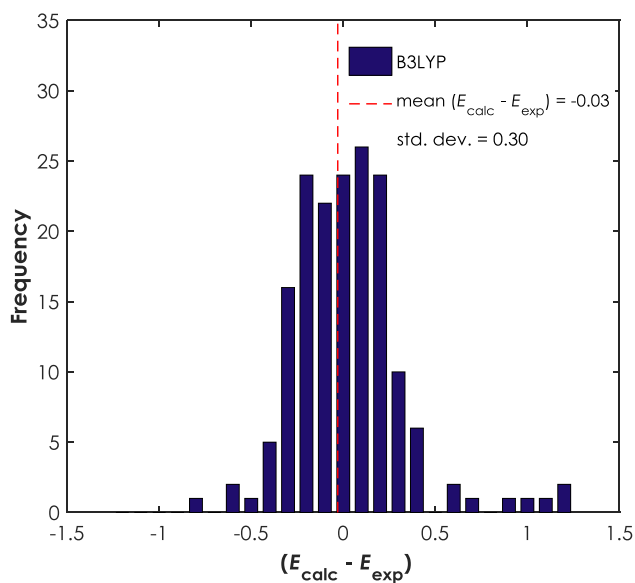
Figure A.16. Hypervalent Iodines, nitrobenzene, and *N*-chlorosuccinimide

Table A.16. Amides and Carboxylates				
Name	CAS #	$E_{\text{p}/2}^{\text{exp}}$ (V vs. SCE)	$E_{1/2}^{\text{B3LYP}}$ (V vs. SCE)	$E_{1/2}^{\text{M06-2X}}$ (V vs. SCE)
Nitrobenzene	98-95-3	-1.19	-0.89	-0.93
(Diacetoxy)iodobenzene	3240-34-4	-1.12	D	D
[Bis(trifluoroacetoxy)]iodobenzene	2712-78-9	-0.26	D	D
<i>N</i> -Chlorosuccinimide	128-09-6	-0.27	0.06	-0.31

“D” signifies that the structure could not be minimized due to spontaneous dissociation during geometry optimization

A.1.4 Additional Statistics for Calculated Redox potentials

(a) B3LYP



(b) M06-2x

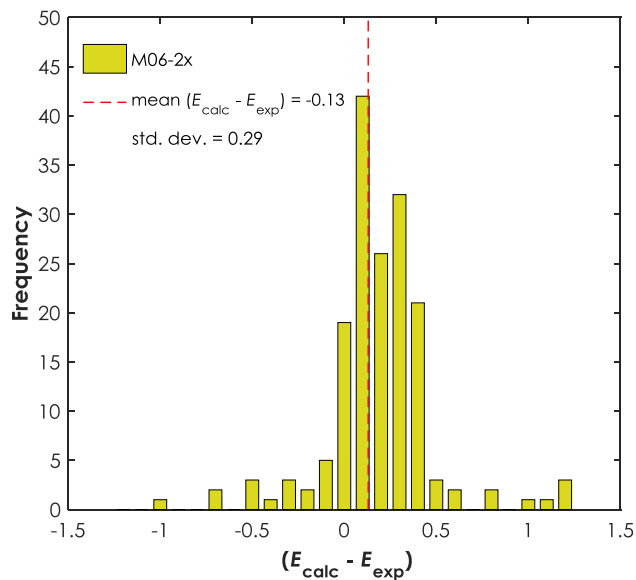


Figure A.17. Histograms of the difference between calculated and experimental redox potentials ($E_{\text{calc}} - E_{\text{exp}}$) for (a) B3LYP and (b) M06-2X

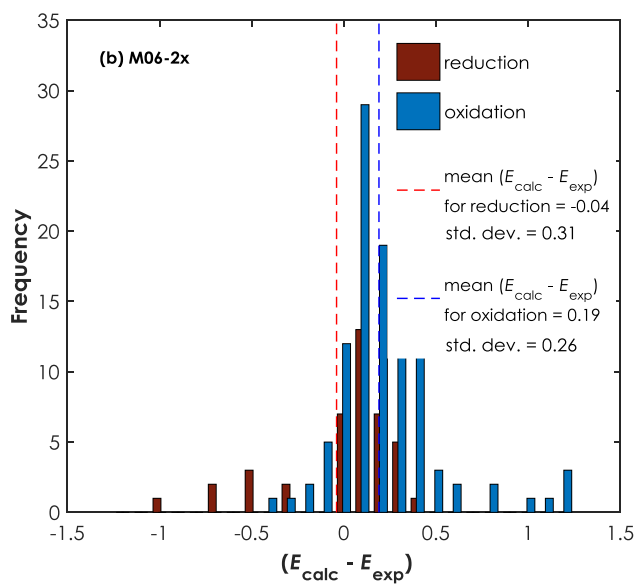
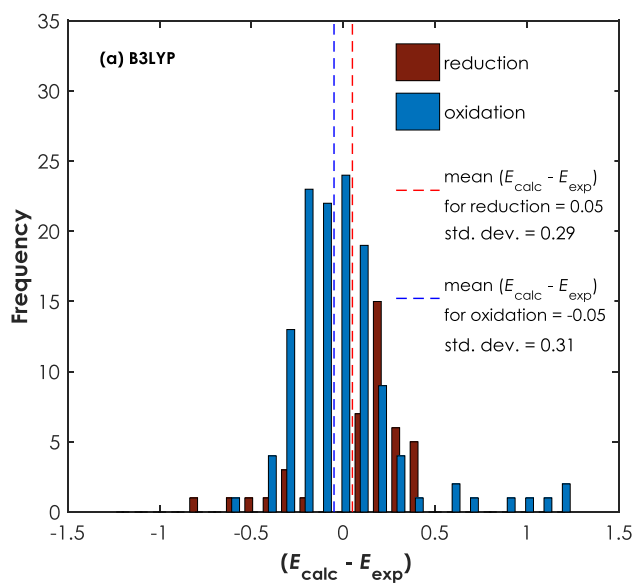


Figure A.18. Histograms in **Figure A.17** separated into the contributions of oxidation and reduction potentials; (a) B3LYP and (b) M06-2X

APPENDIX B: SUPPORTING INFORMATION FOR “MECHANISTIC INSIGHT INTO THE PHOTOREDOX CATALYSIS OF ANTI-MARKOVNIKOV ALKENE HYDROFUNCTIONALIZATION REACTIONS”

B.1 General Information

B.1.1 General Methods

All synthetic manipulations were carried out as reported by our laboratory previously,³¹⁸ using air-free techniques when appropriate. The purity of all synthesized materials was verified by ¹H NMR to be >97% (Bruker model DRX-400, 500, or 600 spectrometer). Chemical shifts are referenced to residual CHCl₃ (7.26 ppm) in the solvent for proton signals and to the carbon resonance (77.16 ppm) of the solvent for ¹³C signals as parts per million downfield from tetramethylsilane. Unless otherwise noted, all solutions used in spectroscopic measurements were prepared in a dry, nitrogen filled glovebox in which O₂ levels were kept below 2.0 ppm at all times. Preparative photolysis experiments utilized a single Par38 Royal Blue Aquarium LED lamp (Model # 6851) fabricated with high-power Cree LEDs as purchased from Ecoxotic (www.ecoxotic.com). For all photolyses, reactions were stirred using a PTFE coated magnetic stir bar on a magnetic stir plate. The lamp was positioned approximately 10 cm from the reaction vial.

B.1.2 Materials.

Spectrophotometric grade acetonitrile (MeCN) and 1,2-dichloroethane (DCE) were purchased from EMD Millipore and were distilled from P₂O₅, sparged with dry Nitrogen or Argon gas for at least 1 hour, and immediately transferred to the glovebox. Solid samples were purified by recrystallization unless otherwise specified. Authentic 9-mesityl-10-methylacridinium tetrafluoroborate (Mes-AcrBF₄) was synthesized as reported previously,³¹⁹ and

highly pure samples were obtained after three successive recrystallizations using an acetonitrile/methanol mixture (MeCN/MeOH = ~5:1) to dissolve the acridinium at room temperature, followed by careful layering with an equal volume of diethyl ether (Et₂O). After an initial period of crystallization, an excess of Et₂O was further layered in order to promote additional crystallization. The solid was collected by vacuum filtration and dried under vacuum for 24 hours. Bis(η^5 -cyclopentadienyl)cobalt (cobaltocene = **CoCp₂**) was purchased from Strem and used without further purification. Diphenyl disulfide (**PhS**)₂ was recrystallized from ethanol/hexanes and dried under vacuum for 24 hours for all studies except crossover experiments. In crossover studies, diphenyl disulfide (**PhS**)₂ and di-*p*-tolyl disulfide (**4-Me-PhS**)₂ were used as received from Sigma-Aldrich (>98% pure). Thiophenol (**PhSH**), Anethole ((*E*)-1-methoxy-4-(prop-1-en-1-yl)benzene, **An**) and β -methylstyrene ((*E*)-prop-1-en-1-ylbenzene, **β MS**) were purchased from Sigma-Aldrich and purified by distillation. Other materials used in Stern-Volmer experiments (5-methyl-2,2-diphenylhex-4-enoic acid, 5-methyl-2,2-diphenylhex-4-en-1-ol, 2-phenylmalononitrile (**PMN**)) were authentic samples used in a previous report from our laboratory.³¹⁸

B.1.3 Synthesized Materials:

9-Xylyl-10-methylacridinium tetrafluoroborate (Xyl-AcrBF₄) was synthesized according to the previously specified method for 9-mesityl-10-methylacridinium tetrafluoroborate,³¹⁹ with 2-bromo-1,3-dimethylbenzene used in place of 2-bromo-1,3,5-trimethylbenzene. **Xyl-Acr⁺** was recrystallized from MeCN/MeOH in the same way as **Mes-Acr⁺**. The ¹H and ¹³C NMR chemical shifts are consistent with those reported for the iodide salt in DMSO-*d*₆.³²⁰ **¹H NMR** (600 MHz, Chloroform-*d*) δ 8.84 (dd, *J* = 9.4, 2.2 Hz, 2H), 8.46 – 8.40 (m, 2H), 7.84 – 7.77 (m, 4H), 7.51 (t, *J* = 7.8 Hz, 1H), 7.34 (d, *J* = 7.7 Hz, 2H), 5.11 (s, 3H),

1.76 (s, 6H). ^{13}C NMR (151 MHz, CDCl_3) δ 162.14, 141.78, 139.62, 136.19, 132.47, 130.45, 128.79, 128.64, 128.43, 125.80, 119.63, 39.28, 20.27.

(E)-5-Phenylpent-4-en-1-ol (R-OH) was synthesized from benzaldehyde according to the procedure reported previously for the synthesis of 5-aryl-2,2-dimethylpent-4-en-1-ols.³¹⁸ The ^1H NMR chemical shifts match those reported in the literature.³²¹ ^1H NMR (500 MHz, Chloroform-*d*) δ 7.39 – 7.35 (m, 2H), 7.32 (dd, $J = 8.6, 6.8$ Hz, 2H), 7.23 (t, $J = 7.3$ Hz, 1H), 6.45 (d, $J = 15.8$ Hz, 1H), 6.26 (dt, $J = 15.8, 6.9$ Hz, 1H), 3.74 (t, $J = 6.4$ Hz, 2H), 2.34 (q, $J = 7.2$ Hz, 2H), 1.79 (p, $J = 6.9$ Hz, 2H), 1.32 (t, $J = 4.6$ Hz, 1H).

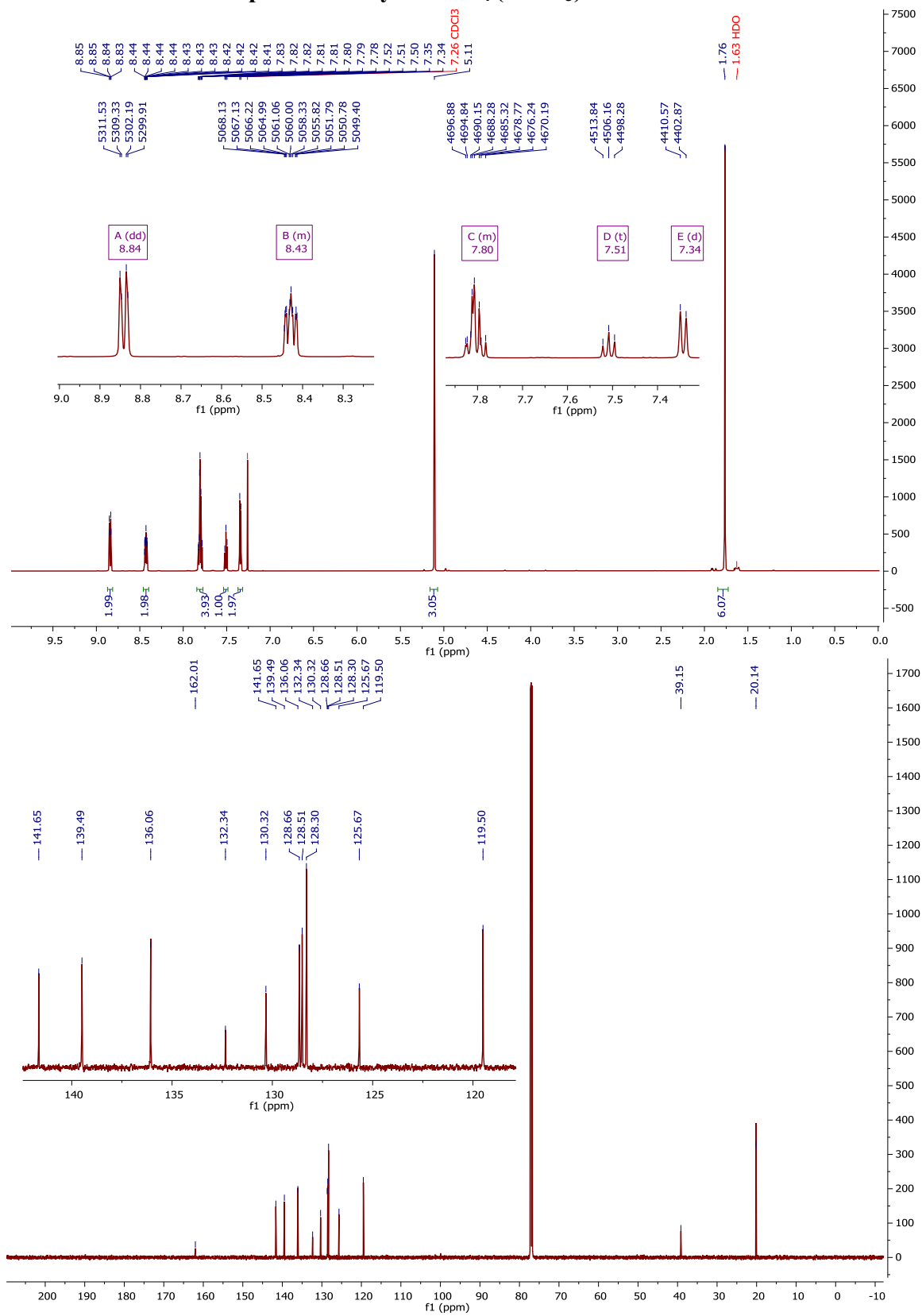
Tert-Butyldimethyl-(E)-(5-phenylpent-4-enyloxy)silane (R-OTBDMS) was synthesized from the corresponding alkenol as reported previously,³²¹ and the ^1H NMR matches the reported chemical shifts.³²¹ ^1H NMR (600 MHz, Chloroform-*d*) δ 7.35 (d, $J = 7.0$ Hz, 2H), 7.30 (t, $J = 7.6$ Hz, 2H), 7.21 (t, $J = 7.3$ Hz, 1H), 6.41 (d, $J = 15.8$ Hz, 1H), 6.25 (dt, $J = 15.8, 6.9$ Hz, 1H), 3.68 (t, $J = 6.4$ Hz, 2H), 2.29 (q, $J = 6.9$ Hz, 2H), 1.72 (p, $J = 6.3$ Hz, 2H), 0.93 (s, 9H), 0.08 (s, 6H).

10-Methylacridinium tetrafluoroborate (AcrBF₄) was synthesized by addition of acridine to trimethyloxonium tetrafluoroborate (Me_3OBF_4) in DCE. The salt was precipitated with Et_2O and recrystallized repeatedly from MeCN/MeOH and Et_2O . The ^1H NMR is consistent with the literature report in DMSO-*d*₆.³²² ^1H NMR (400 MHz, Chloroform-*d*) δ 8.95 (d, $J = 8.3$ Hz, 2H), 8.22 – 8.14 (m, 2H), 8.07 (d, $J = 9.0$ Hz, 2H), 7.92 (br s, 1H), 7.73 (t, $J = 7.7$ Hz, 2H), 4.47 (s, 3H).

10-Methylacridinium Chloride (AcrCl) was employed in the determination of fluorescence quantum yield of Mes-AcrBF₄. AcrCl was obtained by dissolving AcrBF₄ in concentrated aqueous HCl, and crystals were collected after addition of ethanol/diethyl ether

(1:1). After recrystallizing twice from ethanol, analytically pure material was used in subsequent photophysical studies. The absolute fluorescence quantum yield of **AcrCl** in H₂O is widely accepted to be 1.0,⁵⁷ and the quantum yield of **Mes-AcrBF₄** in DCE reported herein is measured relative to the quantum yield of **AcrCl**.

¹H NMR and ¹³C NMR spectra for Xyl-AcrBF₄ (CDCl₃):



B.2 Spectroelectrochemical Measurements

Spectroelectrochemical measurements were performed in a N₂ filled glovebox with the use of a Pine Instruments honeycomb spectroelectrochemical cell in combination with the Wavenow potentiostat from the same manufacturer. Absorption spectra were collected using an Agilent Cary 60 spectrophotometer equipped with optical fiber manufactured by Ocean Optics. The spectrum for neutral **Mes-Acr•** was recorded by performing bulk electrolysis on a solution of Mes-AcrBF₄ (93 μM) in DCE with 0.1 M tetrabutylammonium tetrafluoroborate (TBABF₄) as a supporting electrolyte. When the potential was fixed at -1.0 V (nominal) using a platinum working electrode, complete conversion of **Mes-Acr⁺** to **Mes-Acr•** occurred within 30 seconds. The absorbance spectrum of **Mes-Acr•** at complete conversion was converted to molar absorptivity (ε) using a reference value of 6340 M⁻¹cm⁻¹ at 430 nm for **Mes-Acr⁺** in DCE. The calculated molar absorptivity at 520 nm is 6610 M⁻¹cm⁻¹. The difference spectrum for **Mes-Acr•** (Figure B.10, red) was obtained by subtraction of the absorption spectrum prior to electrolysis from the spectrum after complete conversion to **Mes-Acr•**.

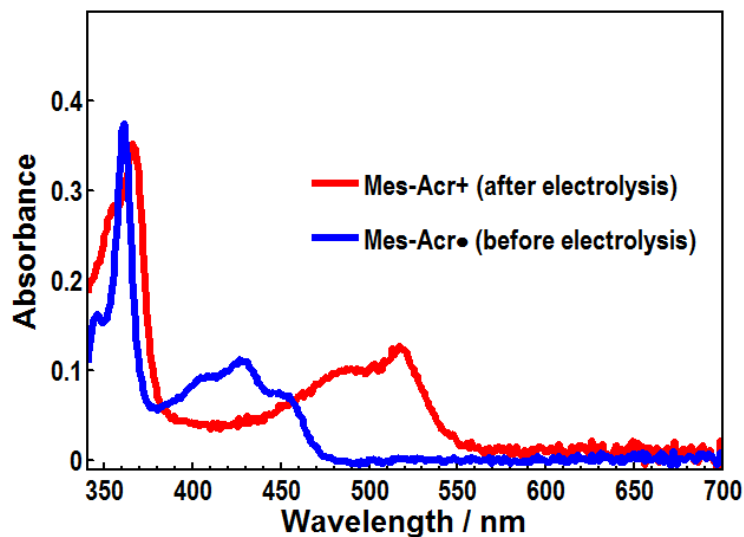


Figure B.1. UV-Vis absorbance spectra collected before (red) and after (blue) bulk electrolysis at a fixed potential of -1.0 V (nominal) on a 93 μM solution of Mes-AcrBF₄ in DCE with 0.1 M TBABF₄ as a supporting electrolyte.

B.3 Electrochemical Measurements

Cyclic Voltammetry was performed using a Pine Instruments Wavenow potentiostat with a standard three electrode setup (working: glassy carbon, reference: Ag/AgCl in 3 M NaCl, counter: platinum). All measurements were taken in N₂-sparged MeCN with 0.1 M tetrabutylammonium hexafluorophosphate (TBAPF₆) as a supporting electrolyte where the analyte concentration was 5-10 mM. The potential was scanned from 1.0 V to a vertex potential of 2.5 V in the forward direction at a sweep rate of 100 mV/s, and the reverse sweep showed no indication of a reversible electrochemical event in all cases. The voltammograms shown below have been corrected by subtracting the background current of the electrolyte solution. The half-wave potential for irreversible oxidation is estimated at $E_{p/2}$ the potential where the current is equal to one-half the peak current of the oxidation event. The values for $E_{p/2}$ are referenced to SCE (Saturated Calomel Electrode) by adding +30 mV to the potential measured against Ag/AgCl (3 M NaCl).

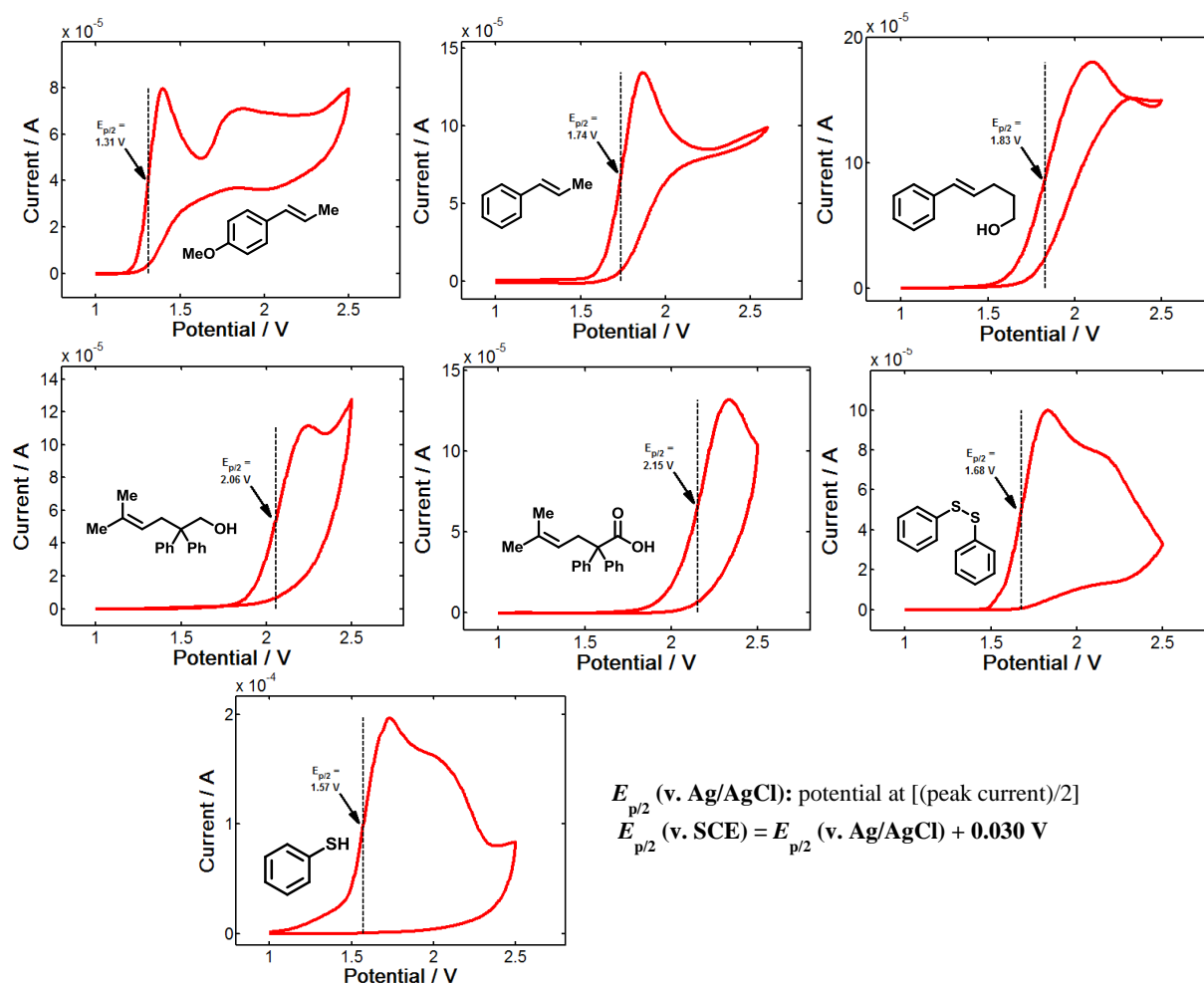


Figure B.2. Cyclic voltammograms for the species examined in this study. The $E_{p/2}$ values shown on each plot referenced to Ag/AgCl in 3 M NaCl. Addition of 30 mV to this value gives the potential v. SCE.

B.4 Photophysical Measurements

All photophysical measurements were taken in 4 ml (nominal volume) quartz cells sealed with a silicone rubber- or PTFE-lined screw cap purchased from Starna Cells, Inc. Solutions were made by dilution and thorough mixing of freshly prepared stock solutions of each component to a total volume of 4.0 mL unless otherwise stated. Background absorbance of the solvent is subtracted from the reported spectra. Duplicate experiments were performed to ensure the reproducibility of all results, and the reported data is the composite of all trials. In most cases,

error is estimated from multiple trials and is represented as the maximum deviation from the average of multiple measurements.

Prior to laser flash photolysis or fluorescence experiments, each sample was evaluated by UV-Vis absorption to verify **Mes-Acr**⁺ concentration. Where relevant, UV-Vis absorption spectra were measured during or after analysis to determine sample degradation. Steady state UV-Vis absorption spectra were recorded on a Varian Cary 50 spectrophotometer or a Hewlett-Packard 8453 Chemstation spectrophotometer. Molar extinction coefficients for Mes-AcrBF₄ in DCE were determined by concentration studies ($\epsilon = 6340 \text{ M}^{-1}\text{cm}^{-1}$ at 430 nm), and all subsequent optical measurements employed sample concentrations in the region where the detector response was found to be linear with respect to absorbance at 430 nm.

B.4.1 Emission Studies

Time-resolved and steady state emission spectra were recorded using an Edinburgh FLS920 spectrometer. The temperature of the cell was controlled with a Quantum Northwest TLC 50 4-position cell holder where the temperature was modulated by a Peltier device. Unless otherwise specified, measurements were taken under ambient conditions. Each sample was stirred continuously with a magnetic stir bar. For collection of steady state fluorescence spectra, the excitation wavelength was set to 450 nm, and a 435 nm low pass optical filter was used to remove extraneous wavelengths from the excitation light. All spectra (1 nm step size, 5 nm bandwidth) are fully corrected for the spectral response of the instrument. Time resolved emission measurements (including Stern-Volmer quenching studies) were made by the time-correlate single photon counting (TCSPC) capability of the same instrument (FLS920) with pulsed excitation light (444.2 nm, typical pulse width = 95 ps) generated by a Edinburgh EPL-445 ps pulsed laser diode operating at a repetition rate of 5 MHz for **Mes-Acr**⁺ or 2 MHz for

Xyl-Acr⁺ and **Acr⁺**. The maximum emission channel count rate was less than 5% of the laser channel count rate, and each data set collected greater than 7500 counts on the maximum channel. The fluorescence lifetime of Mes-AcrBF₄ was found not to depend on stirring, exposure to air, or repetition rate of the laser diode with detection at 500 or 515 nm (20 nm bandwidth). The lifetime of fluorescence was determined by reconvolution fit with the instrument response function using the Edinburgh FS900 software. In all cases, after reconvolution, fluorescence decay was satisfactorily fit with a monoexponential function of the form:

Equation B.1

$$I_t = I_0 e^{-t/\tau}$$

where I is the intensity (counts), and τ is the mean lifetime of fluorescence. Fluorescence lifetimes for **Mes-Acr⁺**, **Xyl-Acr⁺**, and **Acr⁺** were measured with detection at 500 nm with solutions in 4.0 mL DCE at concentrations of 1.60×10^{-5} M in each. Repetition rate was 5 MHz for **Mes-Acr⁺** and 2 MHz for **Xyl-Acr⁺** and **Acr⁺**.

NOTE: While both LE^S and CT^S (for **Mes-Acr⁺**) are reported to decay with a common lifetime of ~6 ns, we observe minor differences in the fluorescence lifetimes when the time resolved emission spectra are measured with the LP920 instrument (**Figure B.4**). Though CT^S appears to decay slightly faster than LE^S (**Figure B.4**), the difference is evidently minimal at 500 and 515 nm, such that the fluorescence decay at these wavelengths follows single exponential kinetics when measured by TCSPC. Nonetheless, we use this difference in fluorescence lifetime to approximate the contribution of CT^S to the steady state fluorescence. The red trace in **Figure B.3** below is produced by normalizing the raw transient emission spectra at 20 ns and 60 ns at to 475 nm, and subtracting the spectrum at 60 ns from the spectrum at 20 ns. Thus, at 60 ns, the emission is almost entirely due LE fluorescence.

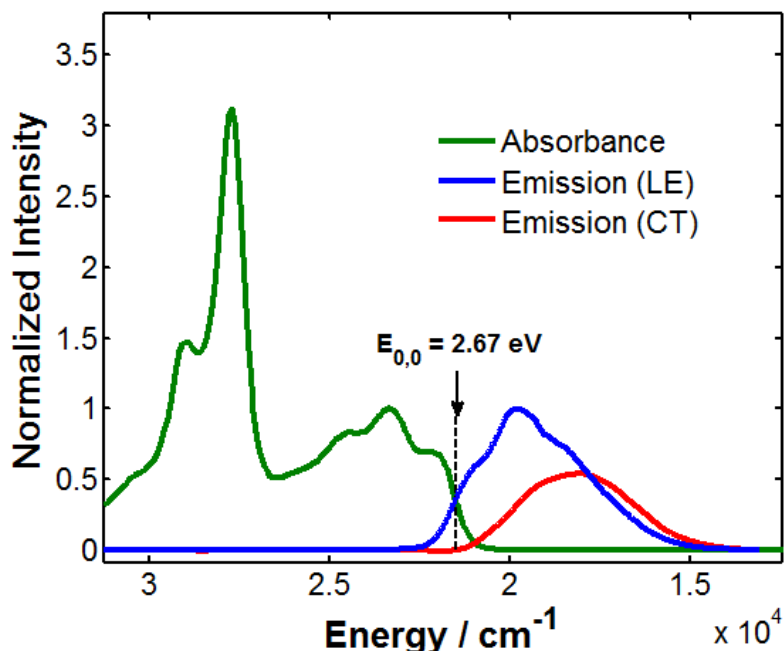


Figure B.3. Steady state absorbance spectrum (red, measured on HP 8453 spectrophotometer) and emission spectra for Mes-Acr^+ (measured on LP920) where locally excited (LE, blue) and charge-transfer (CT, red) fluorescence contributions are separated.

Excitation energy $E_{0,0}$ is determined to be 2.67 eV at the intersection of absorption and LE fluorescence spectra normalized to 1. The calculated $E_{0,0}$ is identical to the value obtained by Verhoeven, et. al.³²³ Accordingly, the excited state reduction potential is calculated to be +2.12 V vs. SCE ($E_{\text{red}}^* = E_{0,0} + E_{\text{red}} = (2.67 - 0.55) \text{ V} = +2.12 \text{ V}$).

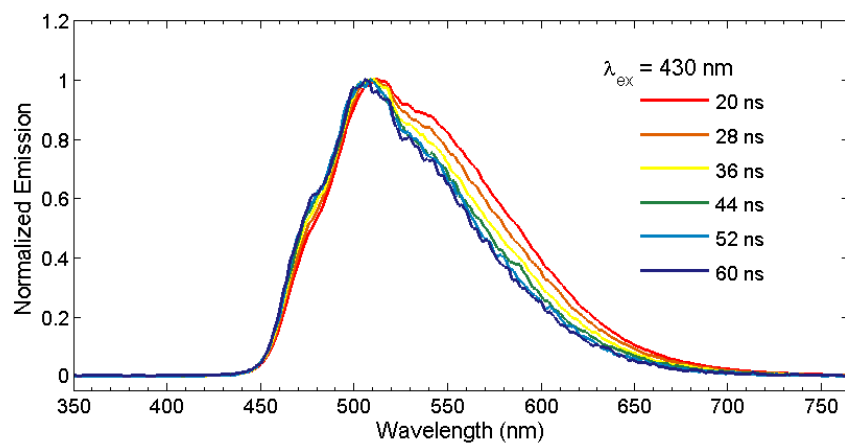


Figure B.4. Time resolved emission spectra for Mes-Acr^+ (50 μM , measured on LP920) normalized at 510 nm to show both LE and CT. Contribution of CT^{S} fluorescence (**Figure B.3**) estimated by subtracting the emission spectrum at 60 ns from the emission spectrum at 20 ns.

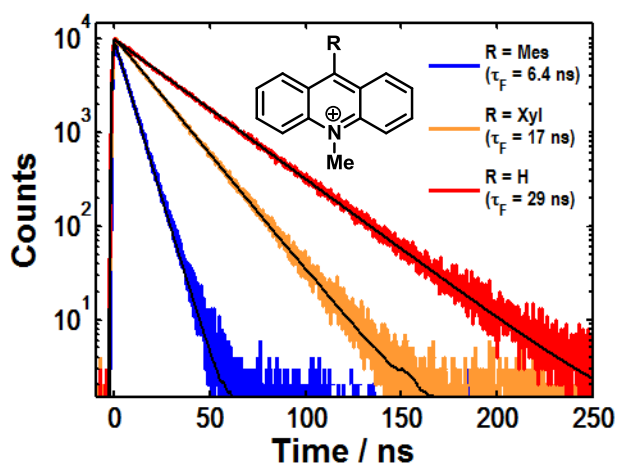


Figure B.5. Fluorescence lifetime of several 10-methyl-acridinium tetrafluoroborate salts measured at 515 nm by Time-Correlated Single Photon Counting (TCSPC). The decays are fit to a monoexponential (black traces) after reconvolution with the instrument response profile.

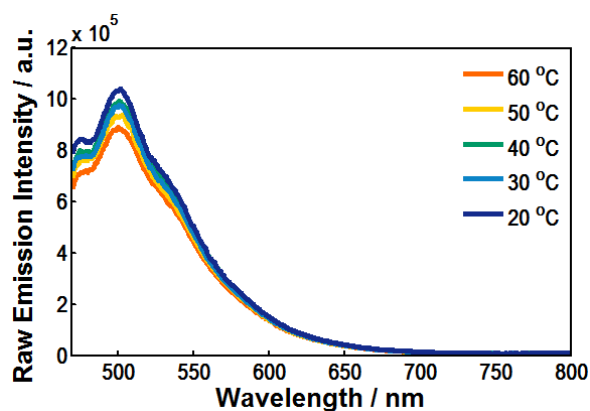


Figure B.6. Raw variable temperature fluorescence spectra of **Xyl-Acr⁺** in DCE.

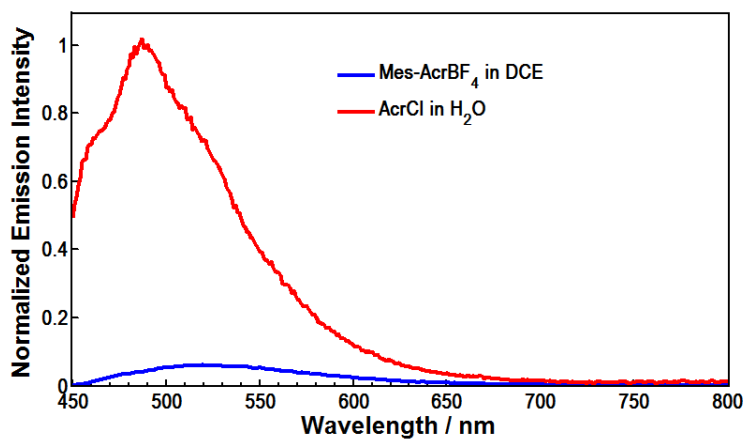


Figure B.7. Absorbance corrected fluorescence spectra for **Mes-AcrBF₄** and **AcrCl** for the determination of the relative quantum yield of fluorescence (Φ_F) for **Mes-Acr⁺** in DCE. The

absolute quantum yield of fluorescence for **AcrCl** in H₂O is 1.0,⁵⁷ and Φ_F for **Mes-Acr⁺** is calculated by dividing the integrated area beneath the blue curve by the integrated area beneath the red curve. Φ_F is calculated to be 0.08 or 8% for **Mes-Acr⁺** in DCE.

B.4.2 Stern-Volmer Analyses

Stern-Volmer experiments were conducted with detection at 515 nm, where the solutions in DCE contained Mes-AcrBF₄ (1.60×10^{-5} M) and a quencher ranging from 3.0×10^{-4} to 1.7×10^{-2} M in concentration. Comparison of UV-Vis absorption spectra taken before and after lifetime quenching studies verified that **Mes-Acr⁺** was unchanged. Stern-Volmer analysis was conducted according to the following relationship:

Equation B.2

$$\frac{\tau_o}{\tau} = 1 + K_{SV}[Q] = 1 + k_q\tau_o[Q]$$

where τ_o and τ are the fluorescence lifetime in the absence and presence of quencher Q , K_{SV} is the Stern-Volmer constant, k_q is the bimolecular quenching constant, and $[Q]$ is the concentration of quencher. An example of the fluorescence lifetime with increasing $[Q]$ is shown in **Figure B.8** ($Q = \text{anethole} = \text{An}$).

Equation B.3 (Calculation of Gibbs Energy for Photoinduced electron transfer)

$$\Delta G_{ET} = f [E_{p/2}(Q/Q^{+\bullet}) - E_{p/2}(\text{Mes-Acr}^+/\text{Mes-Acr}^{\bullet}) - E_{0,0}]$$

$$f = 23.061 \text{ kcal mol}^{-1} \text{ eV}^{-1}$$

$$E_{p/2}(\text{Mes-Acr}^+/\text{Mes-Acr}^{\bullet}) = -0.55 \text{ V}$$

$$E_{0,0} = 2.67 \text{ eV (see Figure B.3)}$$

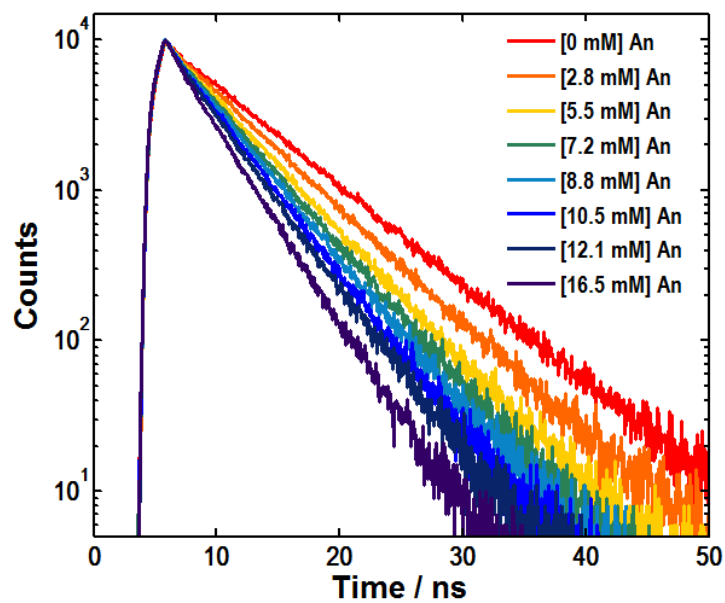


Figure B.8. Fluorescence lifetime of Mes-Acr⁺ (16 μM in DCE) measured at 515 nm at the concentrations of anethole (An) given.

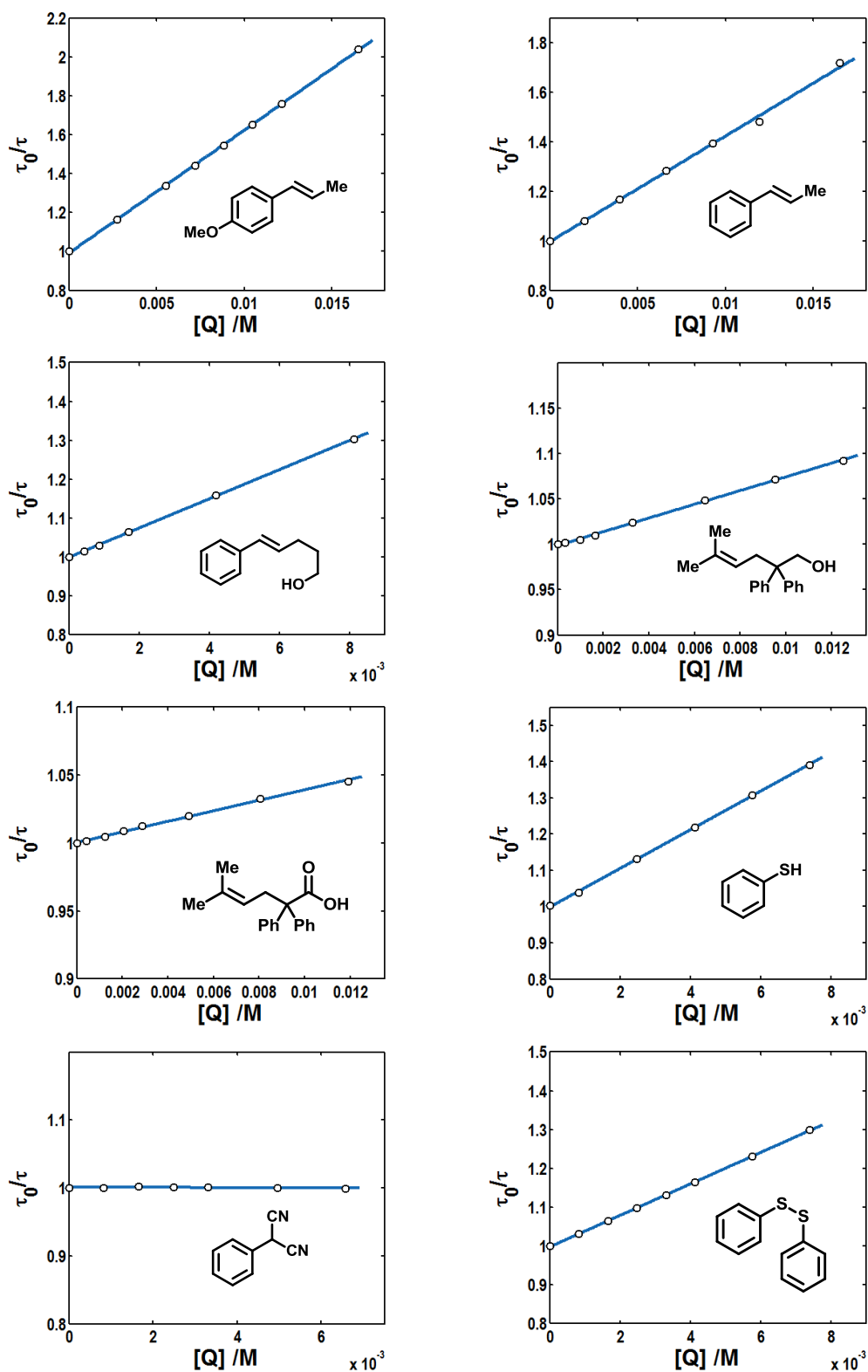


Figure B.9. Stern-Volmer plots of quenching of **Mes-Acr⁺** (16 μ M) fluorescence lifetime for each quencher studied. Fluorescence lifetime was measured by TCSPC with detection at 515 nm (20 nm bandwidth). The Stern-Volmer quenching constant, K_{SV} , was determined by the slope of

the linear regression ($R^2 > 0.99$), where the bimolecular quenching constant, k_q , is equal to K_{SV}/τ_0 .

B.4.3 Laser Flash Photolysis/Transient Absorption experiments

Laser Flash Photolysis/Transient Absorption was performed using the commercially available LP920 system by Edinburgh Instruments, Inc., and the identical system used has been described elsewhere.³²⁴ Laser excitation was provided by a pulsed Nd:YAG laser in combination with an optical parametric oscillator (OPO) for wavelength selection. Probe light was generated by a 450 W Xe lamp, which was pulsed at a rate of 1 Hz. Typical experiments employed laser excitation at 430 nm (3.5 ± 0.1 mJ, 5-7 ns fwhm) with single wavelength transient absorption monitored at the indicated wavelengths (0.3-2.0 nm bandwidths) with a photomultiplier tube (PMT) and transient spectra recorded using a gated CCD at the indicated time delays (10 ns gate width) unless otherwise indicated. The probe light was passed through a 380 nm long-pass filter before reaching the sample to minimize higher energy excitation. A 435 nm long pass filter was placed between the sample and detector for single-wavelength measurements to suppress laser scatter. When collecting transient absorption spectra, only a 380 nm long-pass filter was applied to the probe light. For all records, the probe background was collected between laser shots and subtracted from the signal, and fluorescence background was subtracted where relevant. Transient absorption kinetics were fit with the equations described below using the Levenberg-Marquardt algorithm as implemented in Matlab.

B.4.3.1 With Mes-Acr+

Laser flash photolysis was performed on a 50 μ M solution of Mes-AcrBF₄ in DCE. Transient absorption spectra were collected at time delays ranging from 20 ns to 200 μ s. Verhoeven reports first order (mono-exponential) decay³²³ of the microsecond transient for Mes-

AcrPF₆ in MeCN, while Fukuzumi reports second-order behavior of the transient.³²⁵ In our hands, wide variation was seen when applying a mono-exponential kinetic model to fit the decay of the microsecond transient at wavelengths ranging from 460 to 600 nm. Transient absorption studies conducted immediately after sample preparation in a rigorously oxygen-free glovebox yielded a first-order decay constant of $\tau = 38 \mu\text{s}$ for the signal at 480 nm (**Figure B.11a**). Yet, analysis of the residuals indicates that the mono-exponential model does not adequately describe the signal decay. Considering that Fukuzumi reports second order behavior due to formation of a triplet-triplet dimer,³²⁶ we attempted to fit the transient absorption at 480 nm with a second order kinetic model; however, a satisfactory fit could not be obtained (**Figure B.11b**). Intriguingly, the best fit is obtained when the signal is fit to a kinetic model with both mono-exponential and second-order terms (**Figure B.11c**), possibly indicating that the triplet **T** decays from both the triplet-triplet dimer and the free triplet simultaneously. Importantly, decay of **T** at longer wavelengths (i.e., wavelengths greater than ~ 570 nm) consistently follows monoexponential decay with $\tau_{\text{T}} = 45 \mu\text{s}$, even while higher-order decay components are detected at 480 nm. Parallel studies with samples allowed to stand for greater than 1 hour saw in increasingly diminished lifetimes at all wavelengths, due to the difficulty in completely excluding O₂ from screw-cap sealed cuvettes. With the cuvette open to air, measured lifetimes dropped below $\tau = 5 \mu\text{s}$, consistent with the notion that the microsecond transient is a triplet.

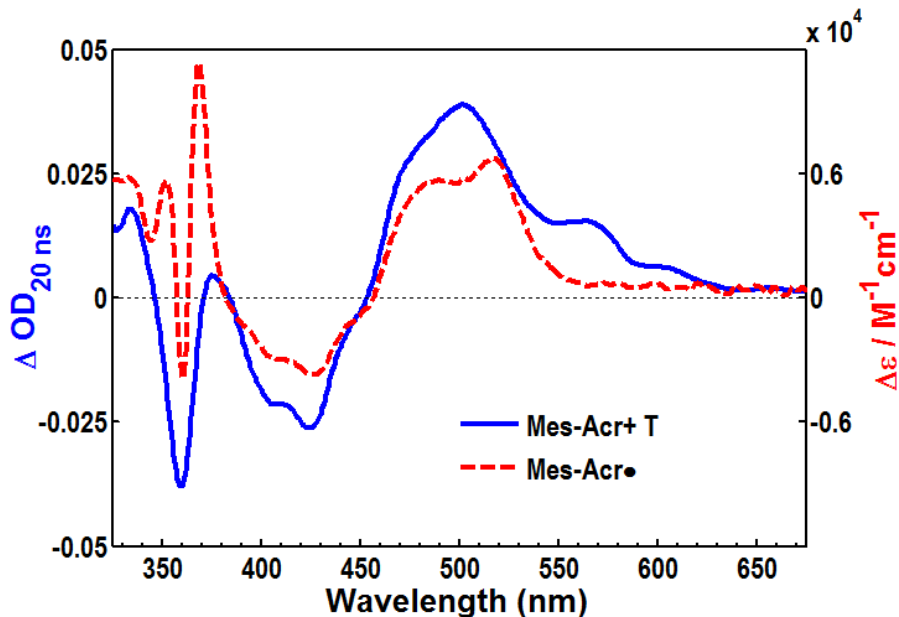


Figure B.10. Transient absorption spectrum (blue) for **Mes-Acr⁺ T** (50 μM in DCE) taken at 20 ns with laser excitation at 430 nm. Difference spectrum for **Mes-Acr•** shown as calculated from spectroelectrochemical records (dashed red).

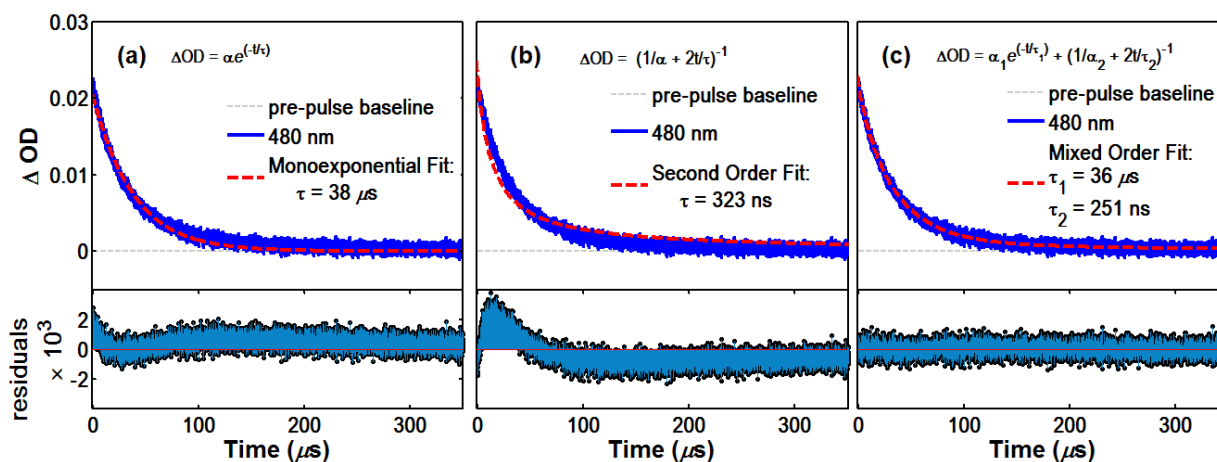


Figure B.11. Transient absorption kinetics for **Mes-Acr⁺** (50 μM in DCE) measured at 480 nm with laser excitation at 430 nm.

Fit to (a) monoexponential decay: $\Delta\text{OD}_{480}(t) = \alpha e^{-\frac{t}{\tau}}$, (b) second order decay: $\Delta\text{OD}_{480}(t) = \frac{1}{\frac{1}{\alpha_0} - 2\frac{t}{\tau}}$ (second order fit: α_0 fixed at 0.023 in order to obtain a reasonable fit), and (c) a mixed order kinetic model with exponential and second-order decay terms: $\Delta\text{OD}_{480}(t) = \alpha_1 e^{-\frac{t}{\tau_1}} + \frac{1}{\frac{1}{\alpha_2} + 2\frac{t}{\tau_2}}$

B.4.3.2 With Mes-Acr⁺/Alkene Cation Radicals:

Mes-Acr⁺ concentration in DCE was 5.0×10^{-5} M (in all cases, absorbance at 430 nm was less than 0.5) for detection of styrenyl cation radicals, with a typical alkene concentration of 5 to 10×10^{-3} M. Transient absorption spectra are corrected to subtract fluorescence at time delays where significant (i.e., $t < 100$ ns). Transient emission spectra were recorded for Mes-Acr⁺ using the same system with excitation at 430 nm (see above **Figure B.4**).

Electron transfer from anethole to singlet Mes-Acr^{+*} is efficient; thus, the transient absorption spectrum at 500 ns contains little contribution from **T**. The differential absorption spectrum for anethole-cation radical is calculated by normalizing the difference spectrum of Mes-Acr• at 520 nm to the observed transient absorption at 500 ns, then subtracting Mes-Acr• from the 500 ns spectrum. When LFP is conducted with Mes-Acr⁺ and β -methylstyrene (**β MS**), (*E*)-5-Phenylpent-4-en-1-ol (**R-OH**), and *tert*-Butyldimethyl-(*E*)-(5-phenylpent-4-enyloxy)silane (**R-OTBDMS**), the transient absorption spectrum at 20 ns contains significant contribution from the **T** in addition to the feature on the low energy side corresponding to the styrenyl cation radical. The spectrum for **T** (**Figure B.10**, blue) was normalized to the observed absorbance at 460 nm (isosbestic point for Mes-Acr• difference spectrum), and this normalized **T** spectrum was subtracted. The difference spectrum for Mes-Acr• was then normalized to the absorbance at 520 nm (under the assumption that the alkene cation radical does not possess a significant absorbance at 520 nm). Subtraction of the normalized Mes-Acr• spectrum yields the absorbance of the **β MS**, **R-OH**, and **R-OTBDMS** cation radicals.

The lifetime of each cation radical was determined by analysis of the single wavelength kinetic decay at 590 nm. In all cases, the signal at 590 nm contains a contribution from **T**, which

decays with a time constant $\tau_T = 45 \mu\text{s}$, relatively unchanged from records where alkenes are absent. For **β MS** and alkene **R-OTBDMS** the decay is fit with a biexponential function:

Equation B.4

$$\Delta\text{OD}_{590}(t) = \alpha_T e^{-\frac{t}{\tau_T}} + \alpha_{\text{CR}} e^{-\frac{t}{\tau_{\text{CR}}}}$$

where τ_T corresponds to decay of **T** and τ_{CR} corresponds to decay of the respective cation radical.

Alkene **R-OH**, however, is fit with a single exponential function corresponding to **T** decay, confirming that cation radical absorption for **R-OH** is essentially completely quenched before the first time point (40 ns). A lower boundary for the rate of cyclization k_2 can be estimated as $2.5 \times 10^7 \text{ s}^{-1}$ (i.e., $1/\tau = 1/(40 \text{ ns})$ or $1/4.0 \times 10^{-8} \text{ s}$).

Previous studies examining quenching of the triplet **T** have demonstrated quenching of the decay lifetime (at 480-520 nm) of **T** at increasing quencher concentrations. The best kinetic model describing the native decay of **T** in DCE contains 2 terms (**Figure B.11c**), and an additional term would be necessary to describe the contribution from **Mes-Acr•**. Additionally, the native decay of **T** is likely to be perturbed when **Mes-Acr•** is present, as **T** is capable of oxidizing **Mes-Acr•**. Thus, we recognized that we could not obtain reliable rate quenching information, because multiple species absorb at the wavelengths of interest. We do, however, show this signal decay at 520 nm for three concentrations of **β MS** (**Figure B.15**). The decay is approximately mono-exponential with a residual signal at $t = 400 \mu\text{s}$ attributed to the persistent radical **Mes-Acr•**. After subtracting the residual signal at $t = 400 \mu\text{s}$ for each decay, it is clear that the signal intensity is diminished at increasing quencher concentration. Although the lifetime of the decay is relatively unchanged, that the magnitude of the transient is diminished can be rationalized by fast reductive quenching of either a singlet state or the triplet by **β MS**.

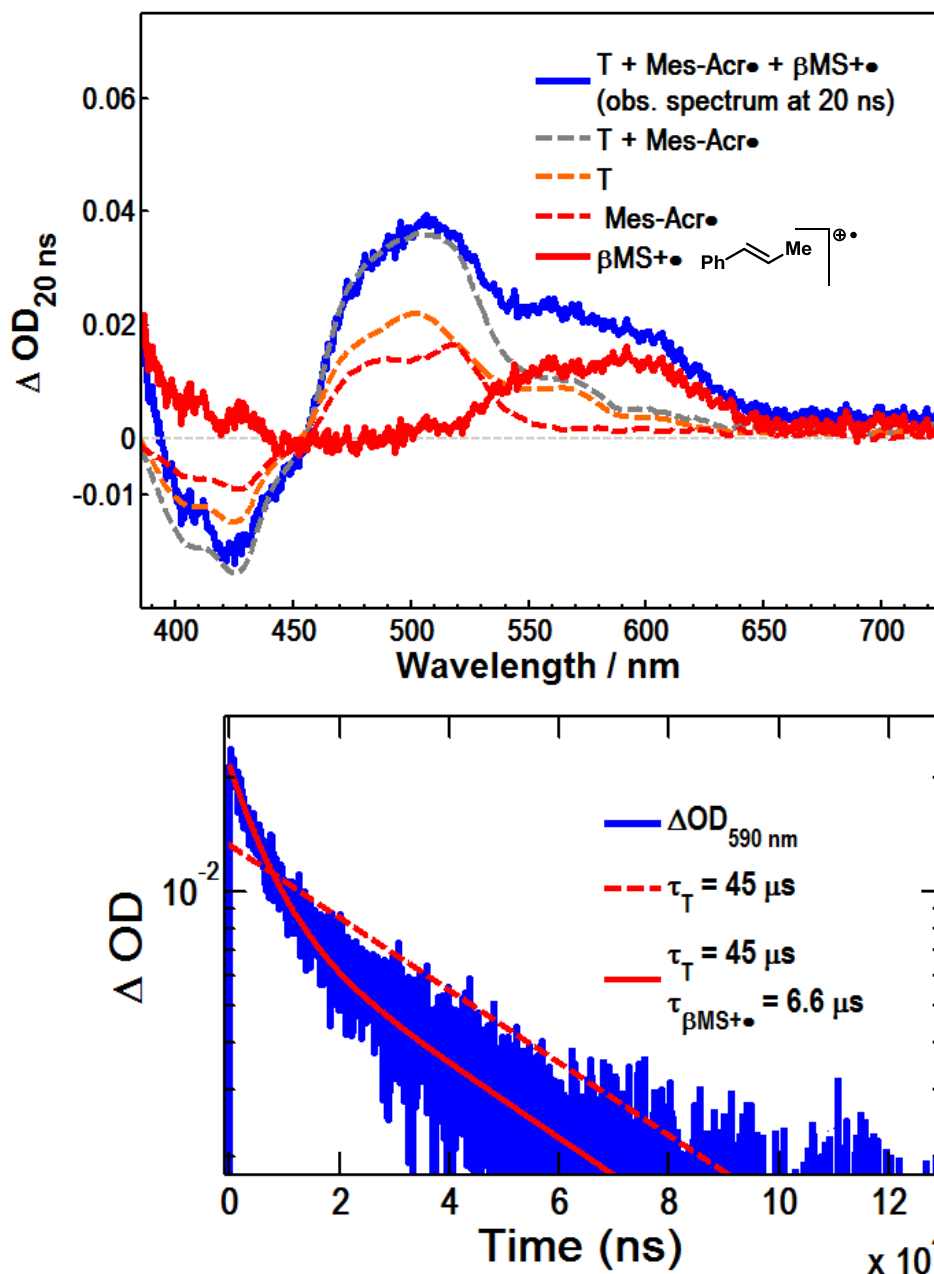


Figure B.12. Detection of the β -methylstyrene cation radical by LFP of a DCE solution containing Mes-AcrBF₄ (50 μM) and β -methylstyrene (βMS , 6 mM). **(a)** Transient absorption spectra showing the contributions of Mes-Acr⁺ T (orange), Mes-Acr[•] (dashed red), and $\beta\text{MS}^+\bullet$ (red). Subtraction of the combined contributions of T and Mes-Acr[•] (gray) give the absorption spectrum for $\beta\text{MS}^+\bullet$. **(b)** Transient absorption kinetics at 590 nm showing the observed signal (blue) fit to a biexponential (solid red) where one decay constant is identical to that of Mes-Acr⁺ T, while the other corresponds to the decay of the cation radical $\beta\text{MS}^+\bullet$ at $\tau = 6.6 \mu\text{s}$.

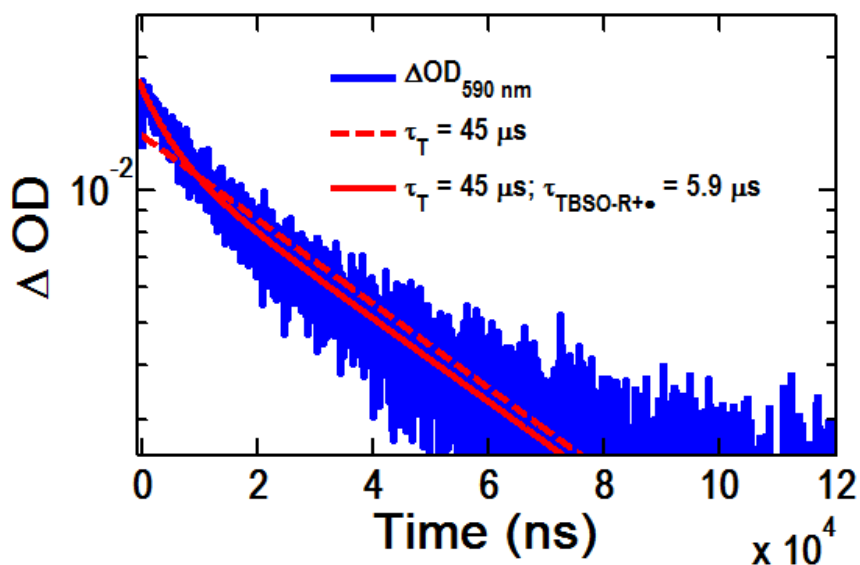
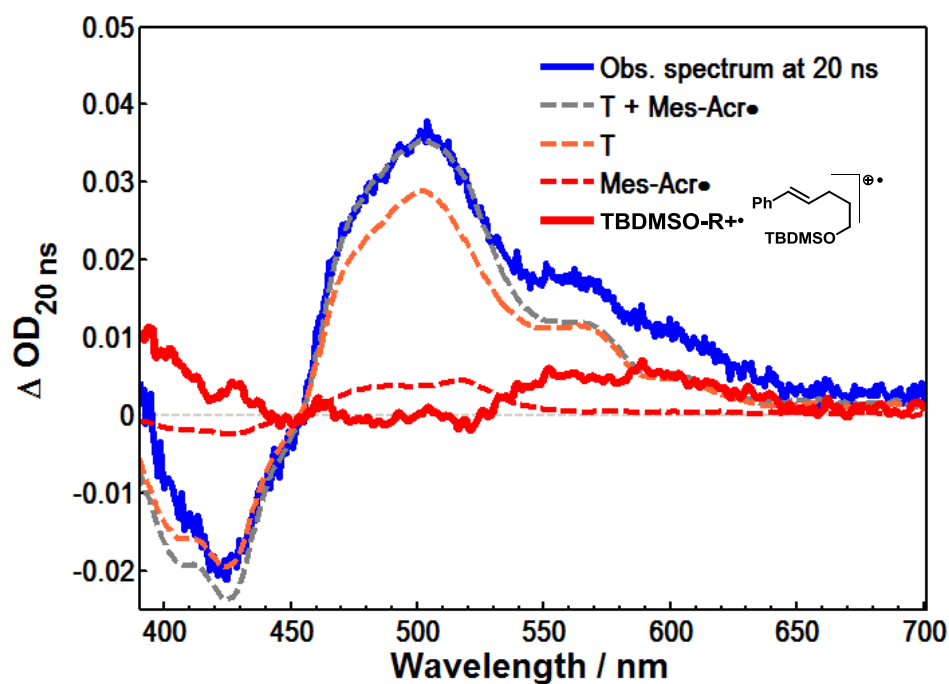


Figure B.13. Detection of the cation radical $\text{R-OTBDMS}^+\cdot$ by LFP of a DCE solution containing Mes-AcrBF₄ (50 μM) and R-OTBDMS (6 mM). (a) Transient absorption spectra showing the contributions of Mes-Acr⁺T (orange), Mes-Acr[•] (dashed red), and R-OTBDMS⁺• (red) are shown. Subtraction of the combined contributions of T and Mes-Acr[•] (gray) give the absorption spectrum for R-OTBDMS⁺• (red, smoothed with Savitsky-Golay filter with a 3rd order polynomial and a frame size of 11). (b) Transient absorption kinetics at 590 nm showing the observed signal (blue) fit to a biexponential (solid red) where one decay constant is identical to that of Mes-Acr⁺T, while the other corresponds to the decay of the cation radical R-OTBDMS⁺• at $\tau = 5.9 \mu\text{s}$.

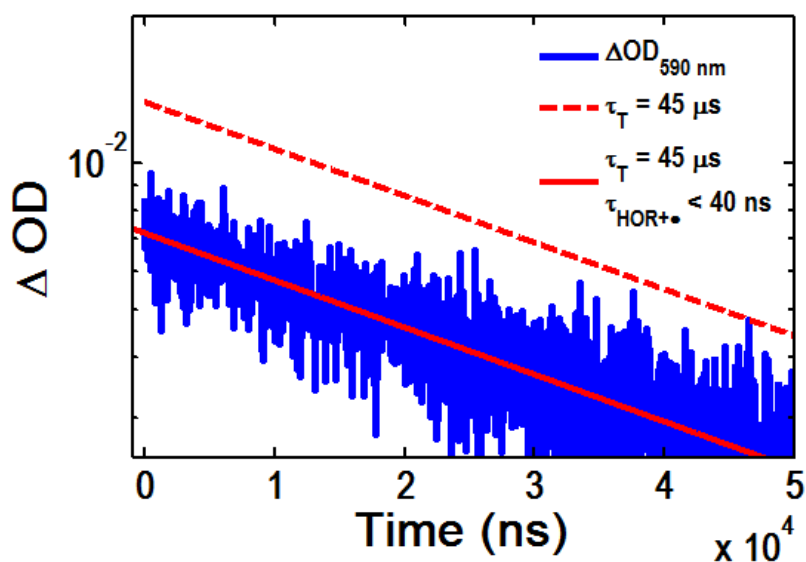
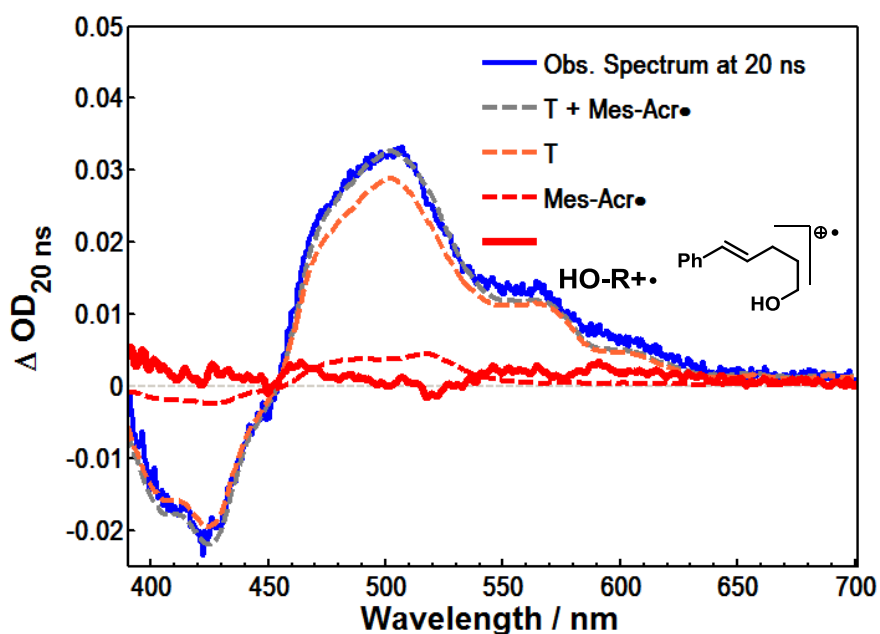


Figure B.14. Detection of the cation radical $\text{ROH}^{\bullet+}$ by laser flash photolysis of a DCE solution containing Mes-AcrBF₄ (50 μM) and alkenol ROH (6 mM).

(a) Transient absorption spectra showing the contributions of $\text{Mes-Acr}^+ \text{T}$ (orange), Mes-Acr^{\bullet} (dashed red), and $\text{ROH}^{\bullet+}$ (red) are shown. Subtraction of the combined contributions of T and Mes-Acr^{\bullet} (dashed gray) give the absorption spectrum for $\text{ROH}^{\bullet+}$ (red, smoothed with Savitsky-Golay filter with a 3rd order polynomial and a frame size of 11). (b) Transient absorption kinetics at 590 nm showing the observed signal (blue) fit to a monoexponential (solid red). The decay constant is identical to that of $\text{Mes-Acr}^+ \text{T}$, confirming that the cation radical $\text{ROH}^{\bullet+}$ is consumed before the response time of the instrument (40 ns) in this experiment.

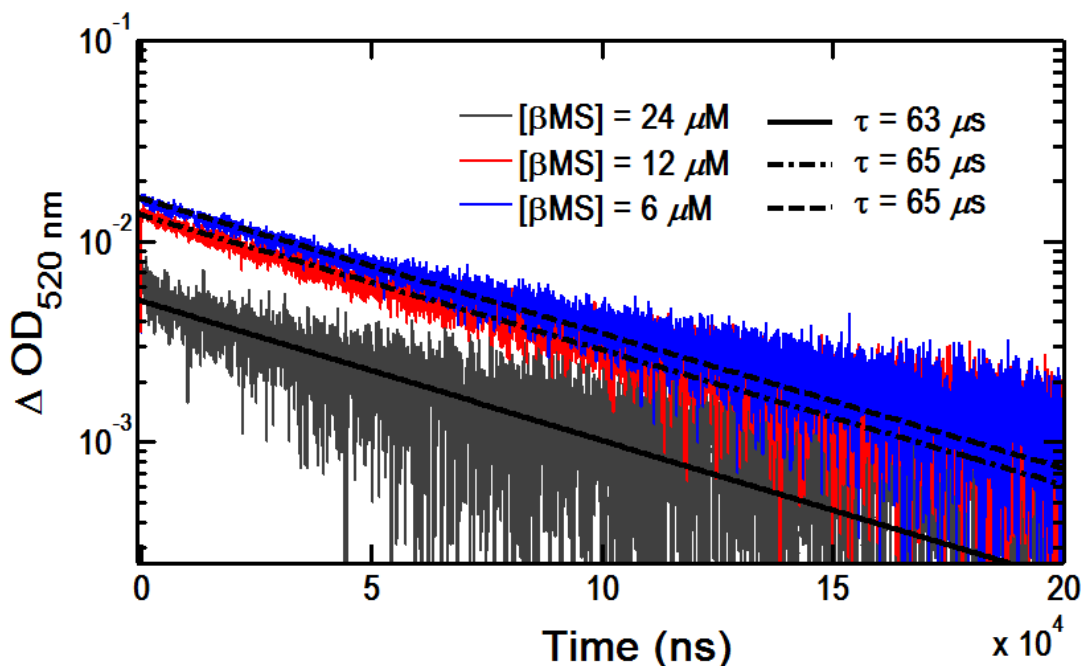


Figure B.15. Dependence of transient absorption kinetics for **Mes-Acr⁺** (75 μM in DCE) with **βMS** (6 to 24 μM) measured at 520 nm with laser excitation at 430 nm.

In all cases, the residual signal at longer time delays after **T** has decayed ($t > 350 \mu\text{s}$) has been subtracted and is attributed to **Mes-Acr \cdot** . This subtraction of the **Mes-Acr \cdot** contribution is an approximation assuming that the concentration of **Mes-Acr \cdot** is invariant with time, although, based on the redox potentials of **T** and **Mes-Acr \cdot** , electron transfer is feasible, if not likely. the contribution of **Mes-Acr \cdot** to the signal at 520 nm is determined by the residual signal at $t = 400 \mu\text{s}$. After subtraction of this constant, the transient signals are modeled by monoexponential

$$\text{decay: } \Delta\text{OD}_{520 \text{ nm}}(t) = \alpha e^{-\frac{t}{\tau}}.$$

B.4.4 Studies involving Mes-Acr•

B.4.4.1 Chemical Reduction of Mes-Acr⁺ to Mes-Acr• using CoCp₂

A 50 μM solution of 9-mesityl-10-methyl-acridinyl radical (**Mes-Acr•**) and bis-cyclopentadiene Cobalt (III) tetrafluoroborate (**CoCp₂⁺**) in DCE was prepared as follows: in a dry, nitrogen filled glovebox, stock solutions of both Mes-AcrBF₄ (10 mM) and **CoCp₂** (20 mM) were prepared by dissolving 20.0 mg Mes-AcrBF₄ (5.01×10^{-5} mol) and **CoCp₂** (1.00×10^{-4} mol) separately in 5.00 mL DCE each. In a 4 mL quartz cell (nominal volume, StarnaCells), 20.0 μL of the Mes-AcrBF₄ stock solution was diluted to a total volume of 4.00 mL for a concentration of [**Mes-Acr⁺**] = 50 μM . To this solution was slowly added 10.0 μL **CoCp₂** stock solution while swirling. Upon addition of **CoCp₂**, the pale yellow **Mes-Acr⁺** solution immediately became light pink in color. Following complete addition of **CoCp₂**, the cell was sealed with a Teflon lined screw cap and the solution swirled excessively to ensure complete mixing. The cell was removed from the glovebox and immediately analyzed by UV-Vis absorption spectroscopy. Complete conversion of **Mes-Acr⁺** to the corresponding acridinyl radical was confirmed by comparison of the absorption spectrum to that of **Mes-Acr•** generated electrochemically (see above). The extinction coefficient of the chemically generated **Mes-Acr•** ($\sim 7000 \text{ M}^{-1} \text{ cm}^{-1}$) matches the value calculated from spectroelectrochemistry. Contribution from the oxidized cobaltocene (**CoCp₂⁺**) to this absorption spectrum was assumed to be very small in the wavelength range of interest. This assumption is supported by literature precedent indicating that the molar extinction coefficient of the cobaltocenium species ($\epsilon_{400-600\text{nm}} < 300 \text{ M}^{-1} \text{ cm}^{-1}$) is <5% compared to **Mes-Acr•** in the visible.^{327,328}

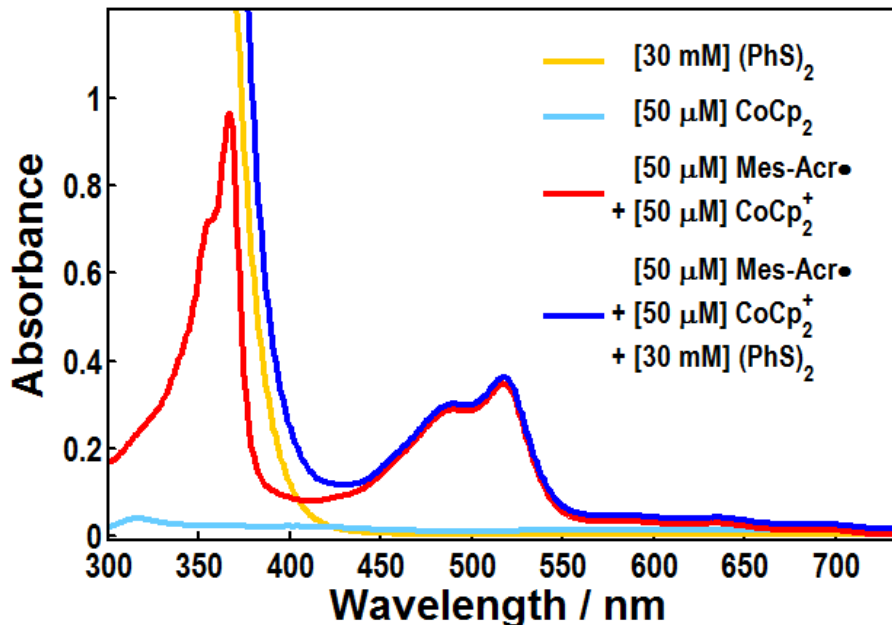


Figure B.16. UV-Vis absorbance spectra for species relevant to Laser Flash Photolysis experiments involving **Mes-Acr•** oxidation.

B.4.4.2 **Mes-Acr•** consumption by LFP-generated **PhS•**

Solutions of **Mes-Acr•**/**CoCp₂BF₄** containing phenyl disulfide (**PhS**)₂ were prepared as described above, with the additional step of adding a microliter quantity of (**PhS**)₂ stock solution to the cell prior to mixing with **CoCp₂** (**[(PhS)₂] = 30 mM**). This solution was kept in the dark until analysis by UV-vis. The resulting UV-vis absorption spectrum closely resembles that of **Mes-Acr•**/**CoCp₂BF₄** (50 μM) with the additional feature of the broad absorption extending into the far UV due to (**PhS**)₂. Comparison to the individual spectra of (**PhS**)₂ and **Mes-Acr•**/**CoCp₂BF₄** precludes the existence of any additional species resulting from a possible background reaction between (**PhS**)₂ and **Mes-Acr•** or **CoCp₂BF₄**. Laser flash photolysis with excitation at 410 nm was performed on this solution in the quartz cell with an average laser pulse energy of 7.0 mJ. A 380 nm long pass optical filter was placed between the probe source and the sample, and a 435 nm long pass filter was placed between the sample and detector. Kinetic

absorption at wavelengths 445 nm and 520 nm were collected with 3-5 laser shots, after which point the net photochemical outcome became non-negligible. New solutions were used for each kinetic measurement, as well as for measurement of the transient difference spectrum taken at 30 μ s. Control experiments where (PhS)₂ is excluded reveal no transient signal differing from baseline absorbance. Laser Flash photolysis with a solution of (PhS)₂ (3.0×10^{-2} M) confirmed that PhS• could be generated with laser pulses at this wavelength.

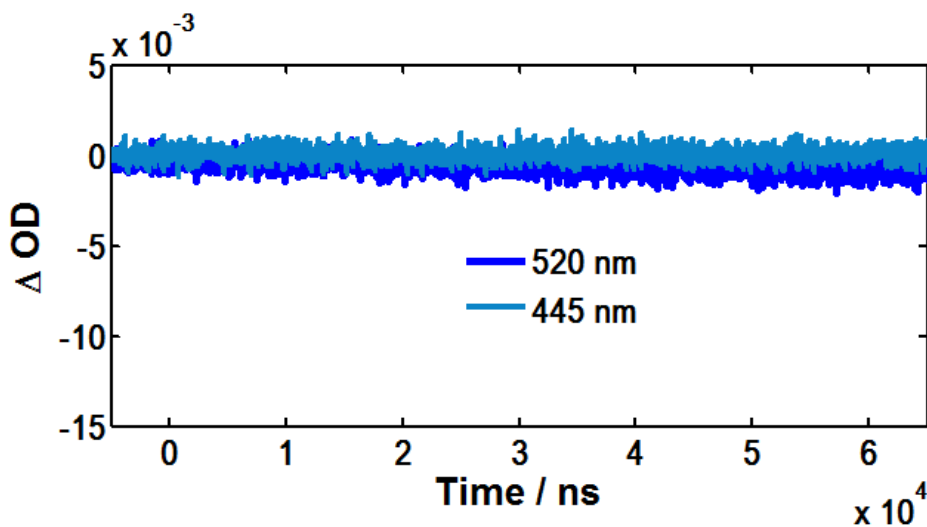


Figure B.17. Laser flash photolysis ($\lambda_{\text{ex}} = 410$ nm, 8.0 mJ) of **Mes-Acr•/CoCp₂BF₄** (50 μ M) containing no (PhS)₂. The absence of an appreciable ΔOD at either wavelength supports the conclusion that bleaching at 520 nm and appearance of a signal at 445 nm is due to electron transfer to PhS•.

Kinetic fitting for the 520 nm transient was fit to a single exponential function of the form:

Equation B.5

$$\Delta OD_{520}(t) = \alpha_1(1 - e^{-k_{\text{obs}}t})$$

where $k_{\text{obs}} = 2.5 \times 10^5 \text{ s}^{-1}$ and $\alpha_1 = -0.0096$.

This corresponds to a final resting concentration $[\text{Mes-Acr}\cdot]_{\infty}$ (i.e., at time delays greater than 50 μs) of:

Equation B.6

$$[\text{Mes-Acr}\cdot]_{\infty} = \alpha_1 / \Delta \epsilon_{(\text{Mes-Acr}\cdot, 520 \text{ nm})} \times \ell = -0.0095 / -6610 \text{ M}^{-1}\text{cm}^{-1} \times 1.00 \text{ cm} = 1.4 \times 10^{-6} \text{ M}$$

The signal at 445 nm is fit to an equation of the form:

Equation B.7

$$\Delta OD_{445}(t) = \alpha_2(1 - e^{-k_{\text{obs}}t}) + \alpha_3 e^{-k_{\text{obs}}t} + \frac{1}{\frac{1}{\alpha_4} + 2k_r t}$$

$$k_{\text{obs}} = 2.5 \times 10^5 \text{ s}^{-1}$$

$$2k_r = 3.5 \times 10^6 \text{ M}^{-1}\text{s}^{-1}$$

$$\alpha_2 = 0.0022$$

$$\alpha_3 = 0.0020$$

$$\alpha_4 = 0.0003$$

Discussion of equation B.7: The pseudo-first order rate constant k_{obs} describes both the appearance of Mes-Acr^+ and the decay of $\text{PhS}\cdot$ in the bimolecular electron transfer reaction.

This rate constant is identical to that obtained by fitting the signal bleach at 520 nm. The second order rate constant $2k_r$ describes decay of $\text{PhS}\cdot$ by a competing bimolecular recombination pathway, which is confirmed to follow second order kinetics in separate experiments (**Figure B.18a**).

The pre-exponential factor α_2 corresponds to the concentration of **Mes-Acr⁺** reached after **PhS•** is completely consumed ($\Delta\varepsilon_{(\text{Mes-Acr}^+, 445 \text{ nm})} \times \ell = 2200 \text{ M}^{-1}$, $[\text{Mes-Acr}^+]_\infty = \sim 1.0 \times 10^{-6} \text{ M}$).

The sum of the pre-exponential factors α_3 and α_4 ($\alpha_3 + \alpha_4 = 0.0023$) corresponds to the concentration of **PhS•** formed upon irradiation with the laser pulse ($\Delta\varepsilon_{(\text{PhS}\cdot, 445 \text{ nm})} \times \ell = 2000 \text{ M}^{-1}$,³²⁹ $[\text{PhS}\cdot]_0 = \sim 1.2 \times 10^{-6} \text{ M}$). Although this scenario requires a more sophisticated model to truly describe the mixed order kinetics of **PhS•** decay, we make the simplification that the pseudo-first order and second order decay modes are separate, where the initial concentration of **PhS•** in each decay term is specified by α_3 and α_4 , respectively, and the molar extinction coefficient of **PhS•**. Under this assumption, approximately 85% of the initially formed **PhS•** is consumed in the pseudo-first order reaction ($[\text{PhS}\cdot]_0(1^{\text{st}}) = \sim 1.0 \times 10^{-6} \text{ M}$) and 15% is consumed through bimolecular recombination ($[\text{PhS}\cdot]_0(2^{\text{nd}}) = \sim 0.2 \times 10^{-6} \text{ M}$).

It should be noted that $[\text{Mes-Acr}\cdot]_\infty$ and $[\text{Mes-Acr}^+]_\infty$ as calculated from α_1 and α_2 , respectively, are expected to be identical, however, some discrepancy is noted. Monitoring at 520 and 445 nm were performed with different samples, and due to the fact that each measurement is the average of only 3-5 laser shots, even small variation in laser pulse energy is expected to give rise to differences in the quantity of **PhS•** generated between experiments. Variation in $[\text{PhS}\cdot]_0$ is expected to only affect the final concentration $[\text{Mes-Acr}^+]_\infty$ and not the observed rate of **Mes-Acr⁺** appearance since $[\text{Mes-Acr}\cdot]_0$ (50 μM) is in large excess of $[\text{PhS}\cdot]_0$ (0.9-1.3 μM) under these conditions.

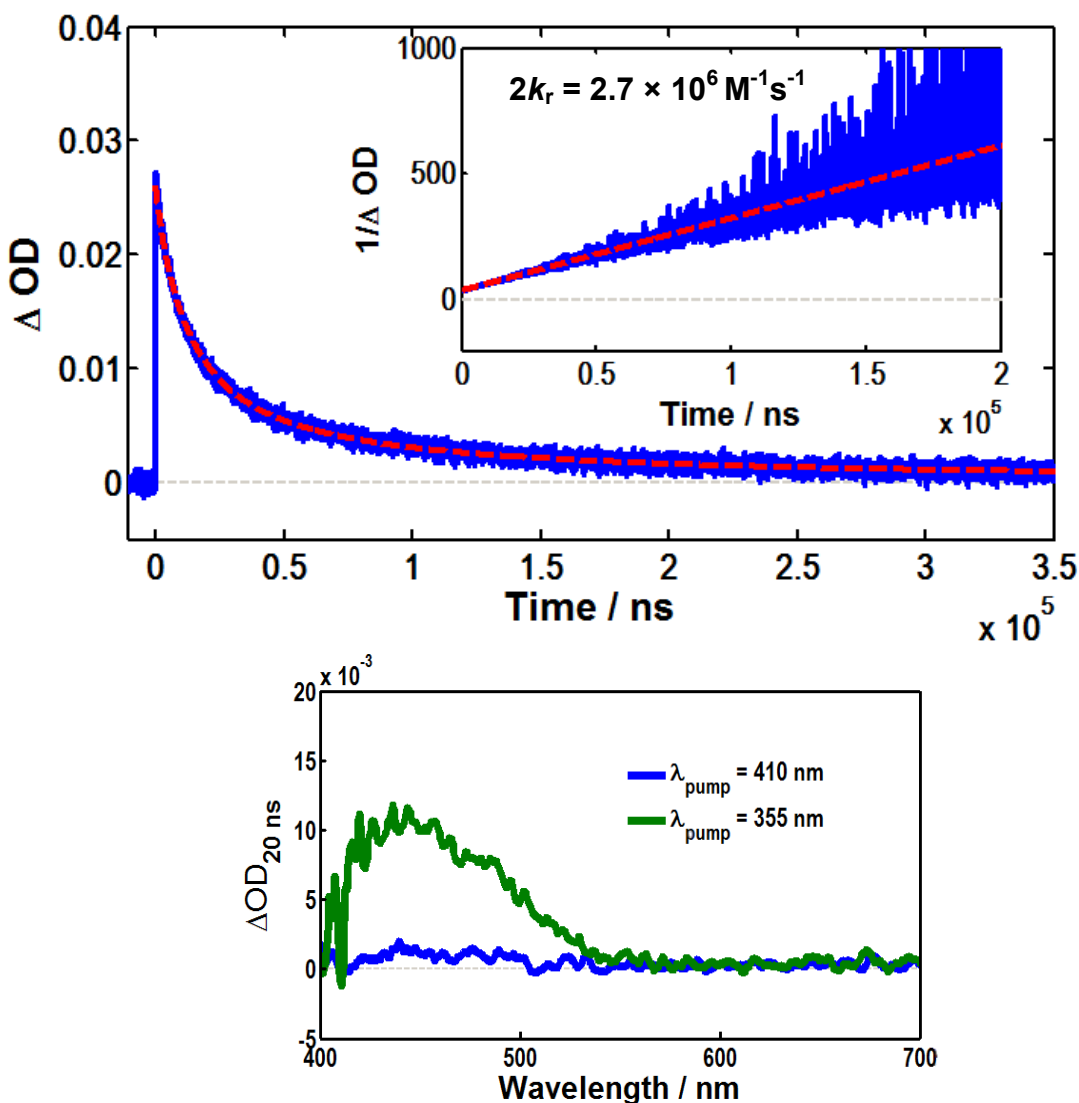


Figure B.18. Laser flash photolysis with $(\text{PhS})_2$ in DCE: (a) Transient decay of signal at 460 nm by second order kinetics, corresponding to recombination of $\text{PhS}\cdot$; $[(\text{PhS})_2] = 30 \text{ mM}$, $\lambda_{\text{pump}} = 355 \text{ nm}$ (b) Transient absorption spectra measured at a 20 ns time delay; green: $[(\text{PhS})_2] = 3 \text{ mM}$; blue: $[(\text{PhS})_2] = 30 \text{ mM}$.

Solutions used in the pseudo-first order study on the rate of $\text{Mes-Acr}\cdot$ oxidation were prepared in a glovebox as described above, wherein the total volume of the solution was 10 mL. $\text{Mes-Acr}\cdot$ concentrations in DCE ranged from 2.5×10^{-5} to $2.5 \times 10^{-4} \text{ M}$, and the concentration of $(\text{PhS})_2$ was $3.0 \times 10^{-3} \text{ M}$. This disulfide concentration was found to give optimal photolytic yield of $\text{PhS}\cdot = \text{ca. } 5 \mu\text{M}$ at a laser excitation wavelength of 355 nm. Solutions were prepared in

flame-dried 20 mL vials sealed with a rubber septum and PTFE tape. Upon removal from the glovebox, the rubber septa were not punctured until introduced into a quartz flow cell through a stainless steel needle connected to the flow cell by FEP tubing. The flow rate through the cell was controlled by positive pressure from a dry, rigorously oxygen free Argon stream, such that each laser pulse irradiated a fresh solution. The average laser pulse energy was 8.0 mJ at 355 nm. For all trials, a 380 nm long pass filter was placed between the probe source and the sample and also between the sample and detector. The reported transient signals with detection at 520 nm are the average of 3-5 laser shots and are fit to a single exponential function as described above (eq. S5).

Based on the molar extinction coefficient reported for **PhS•** at 460 nm ($\sim 2000 \text{ M}^{-1}\text{cm}^{-1}$), the observed transient absorption at 460 nm ($\Delta\text{OD} = 0.010$) for LFP on a solution of **(PhS)₂** in DCE was used in estimating the maximum concentration of **PhS•** to be roughly 5 μM upon disulfide photolysis. This is in good agreement with the observation that the ΔOD reaches a minimum of -0.040 over the range of **Mes-Acr•** concentration (see **Figure B.19** below), corresponding to the consumption of approximately 5-6 μM **Mes-Acr•**. Thus, under these conditions, **Mes-Acr•** is in large excess of **PhS•**.

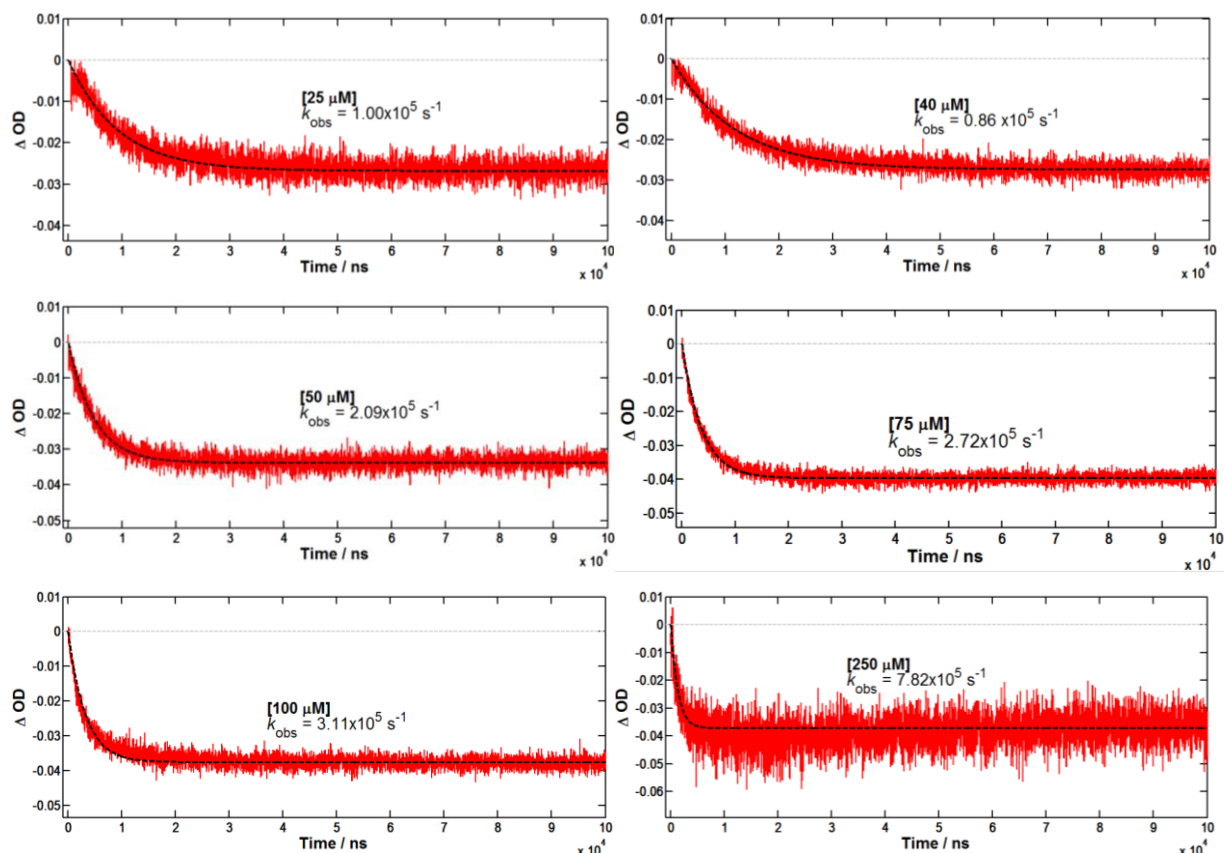


Figure B.19. Transient absorption signals at 520 nm showing consumption of **Mes-Acr•** at increasing rate when **[Mes-Acr•]** is increased. The rate of decay k_{obs} is found by fitting the decay curves to equation B.5 (dashed black trace).

B.5 Disulfide Exchange Experiments

Stock solutions of phenyl disulfide and 4-methylphenyl disulfide were prepared by dissolving 27.3 mg (0.13 mmol) and 30.8 mg (0.13 mmol) of each disulfide (respectively) in 5.0 mL DCE, such that the concentration of each stock solution was 2.5×10^{-2} M. To study the kinetics of exchange, 0.5 mL of each disulfide stock solution were mixed in a flame-dried 1 dram vial containing a Teflon-coated magnetic stir bar and sealed with a Teflon coated septum cap. The total concentration of disulfide was 2.5×10^{-2} M. For experiments where Mes-AcrBF₄ was included, solutions were prepared by mixing 0.5 mL of each disulfide stock solution with 5.0 mg Mes-AcrBF₄ (0.013 mmol), such that the concentration of Mes-AcrBF₄ was 1.3×10^{-2} M. After sealing each vial with PTFE tape, the vials were removed from the glovebox and the Teflon

septum cap was punctured with a needle supplying positive pressure of dry N₂ for the duration of the experiment to exclude oxygen from the reactions. The solutions were stirred on a magnetic stir plate and irradiated using the setup described above. Aliquots (volume < 5 μL) were removed at the time points listed below without ceasing irradiation, quenched by addition to excess diethyl ether and immediately analyzed on an Agilent 5973 GC-MS system. Prior to experimental analysis, calibration curves for (PhS)₂ and (4-Me-PhS)₂ were constructed, and it was determined that the detector response was linear for both disulfides in the range of concentrations relevant in this experiment. Calibration experiments also showed that the detector response factor for (4-Me-PhS)₂ was 1.3 times that of (PhS)₂. In the absence of a calibration standard for 4-Me-PhSSPh, it was assumed that the detector response factor is likewise 1.3 for 4-Me-PhSSPh. Thus, the integrated areas of (4-Me-PhS)₂ and 4-Me-PhSSPh are scaled by a factor of 1/1.3. The theoretical mole fraction of 4-Me-PhSSPh when 1:1 (PhS)₂:(4-Me-PhS)₂ fully exchange to 1:1:2 (PhS)₂:(4-Me-PhS)₂:4-Me-PhSSPh is

Equation B.8

$$\text{mol fraction at equilibrium} = \frac{[\text{4-Me-PhSSPh}]}{[(\text{PhS})_2] + [(\text{4-Me-PhS})_2] + [\text{4-Me-PhSSPh}]} = 0.5$$

Thus, the ratio of mixed to total unmixed disulfide is 1:1. Therefore, conversion to an equilibrium amount of 50 mol% 4-Me-PhSSPh was determined by the expression

Equation B.9

$$\text{conversion} = \frac{[\text{4-Me-PhSSPh}]}{[(\text{PhS})_2] + [(\text{4-Me-PhS})_2]} = \frac{[\text{area 4-Me-PhSSPh}] / 1.3}{[\text{area } (\text{PhS})_2] + [\text{area } (\text{4-Me-PhS})_2] / 1.3}$$

where the area was found by baseline-to-baseline integration of each peak using ChemStation software. Control experiments were performed where (a) light was excluded by wrapping the vial in aluminum foil and placed side-by-side with the irradiated vials or (b) light

was excluded and the vial heated to 50 °C in an oil bath. Both control experiments (a) and (b) contained 0.013 M (PhS)₂ + 0.013 M (4-Me-PhS)₂ and the total volume of the solution was 1.0 mL (as above). In both cases, a negligible amount of (4-Me-PhS)₂ (mol fraction <0.004) was formed by 400 minutes; therefore, we consider these background reactions to be of negligible consequence.

Table B.1. Disulfide exchange amounts as determined by GC-MS

No Mes-AcrBF ₄		w/ 0.013 M Mes-AcrBF ₄	
time / min	$\frac{[\rho\text{-Me-PhSSPh}]}{[(\rho\text{-Me-PhS})_2] + [(\text{PhS})_2]}$	time / min	$\frac{[\rho\text{-Me-PhSSPh}]}{[(\rho\text{-Me-PhS})_2] + [(\text{PhS})_2]}$
0	0.00	0	0.00
5	0.04	5	0.14
10	0.11	10	0.30
25	0.30	25	0.55
45	0.56	45	0.69
75	0.95	75	0.85
115	1.00	115	1.03
240	1.06	240	0.99

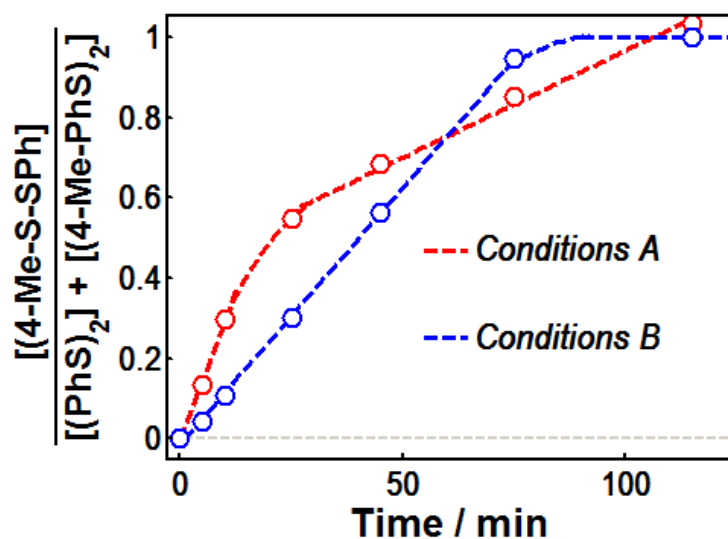


Figure B.20. Plot showing formation of mixed disulfide (4-Me-PhSSPh) under the photolytic conditions: (A) [Mes-AcrBF₄] = 0.013 M (B) no Mes-AcrBF₄. The rate to equilibrium concentration of (4-Me-PhSSPh) is zero-order when Mes-Acr⁺ is excluded, indicating a direct homolytic mechanism for generation of PhS· from (PhS)₂.

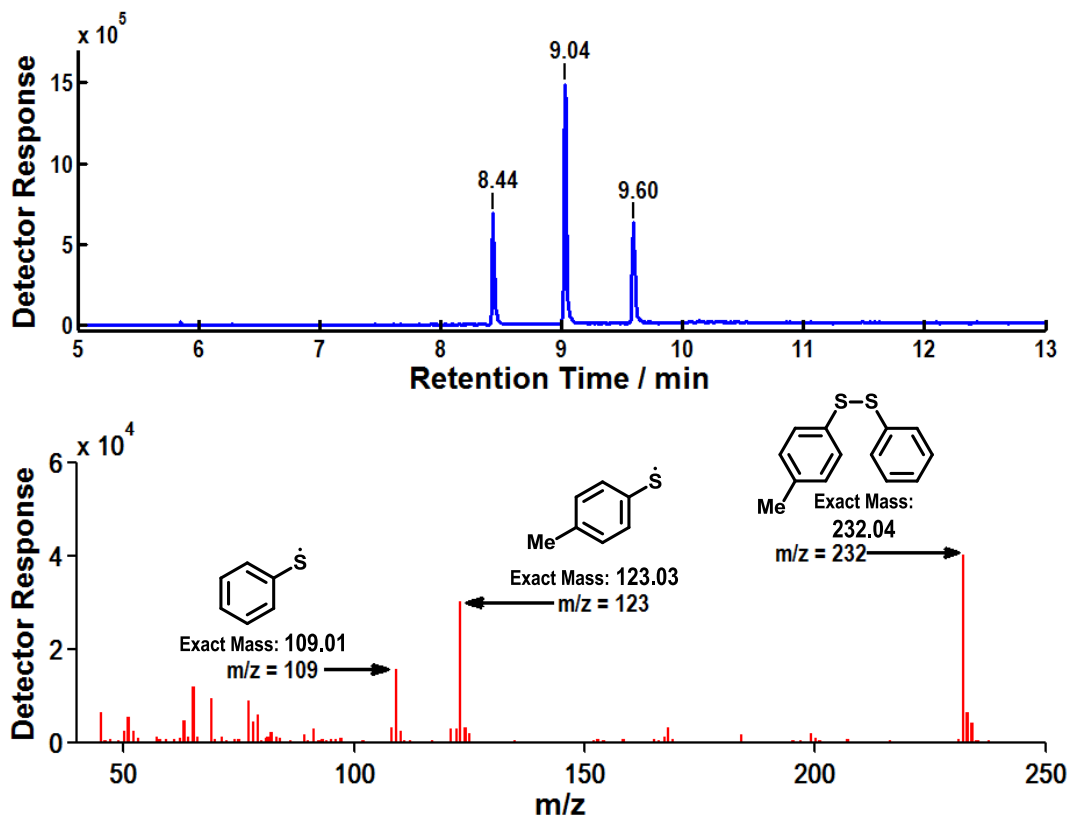


Figure B.21. (a) Example Gas Chromatogram of an aliquot after $t = 240$ min showing $(\text{PhS})_2$ (retention time = 8.44 min), (4-Me-PhSSPh) (retention time = 9.04 min), and $(4\text{-Me-PhS})_2$ (retention time = 9.60 min). (b) Example mass spectrum corresponding to 4-Me-PhSSPh (peak with retention time = 9.04 min) showing $m/z = 232$ for the parent mixed disulfide, and fragments at $m/z = 109$ and 123 for the fragments PhS and 4-Me-PhS , respectively.

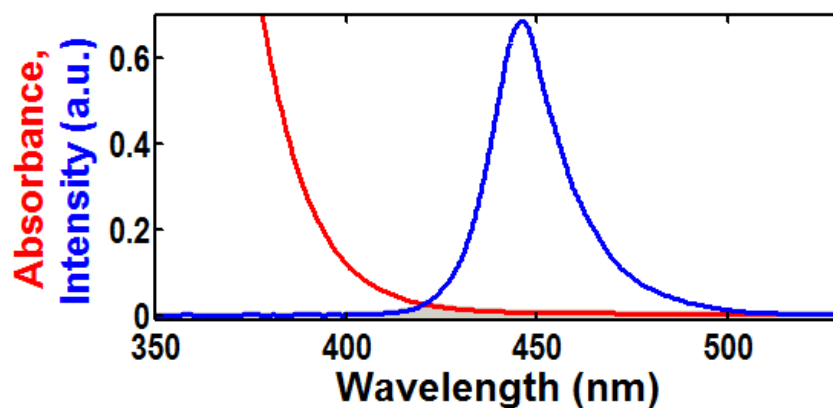


Figure B.22. Absorbance spectrum of 30 mM $(\text{PhS})_2$ in DCE (red) overlaid with the spectral output for the Ecoxotic LED lamp used in photolysis (blue, arbitrary units). The overlap between the traces is highlighted in gray. An Ocean Optics HR4000 spectrometer (Dunedin, FL) was used to measure the emission spectrum of the LED lamp, which was directly oriented toward the aperture of the spectrometer unit at a distance of approximately 10 cm.

B.6 Reaction Progress Monitoring

B.6.1 Gas Chromatography: Alkenol ROH/Product/PhSH/(PhS)₂

Time-monitored conversion was measured by analyzing aliquots with gas chromatography (Agilent 6850 Series II, flame ionization detector).

In a glovebox, two solutions of total volume 1.1 mL DCE were prepared in flame-dried 1 dram borosilicate glass vials with a PTFE coated magnetic stir bar and sealed with a PTFE-lined septum cap:

- (A) 44.5 mg alkenol **ROH** [0.25 M], 5.6 μ L **PhSH** [0.05 M], 5.5 mg Mes-AcrBF₄ [0.013 M], 61 μ L dodecane [0.25 M] (internal standard)
- (B) 44.5 mg alkenol **ROH** [0.25 M], 5.9 mg (**PhS**)₂ [0.025 M], 5.5 mg Mes-AcrBF₄ [0.013 M], 61 μ L dodecane [0.25 M] (internal standard)

After sealing each vial with PTFE tape, the vials were removed from the glovebox and the Teflon septum cap was punctured with a needle supplying positive N₂ pressure to exclude oxygen from the reactions. The solutions were stirred on a magnetic stir plate and irradiated using a single LED lamp. Aliquots (volume < 5 μ L) were removed at the time points listed below without ceasing irradiation, and immediately quenched by dilution with 0.5 mL diethyl ether. Each sample was analyzed by GC within 18 hours, although the makeup of each sample was not found to change upon standing under ambient conditions for a greater period (i.e., 24 hours). Peak areas were found using the OpenLab Software, and were scaled according to the detector response factor for each analyte. The detector response was determined for alkenol **ROH**, the corresponding tetrahydrofuran product, **PhSH**, and (**PhS**)₂ as a burn ratio relative to dodecane (**DD**) as an internal standard. The burn ratio of dodecane to both **ROH** and product was found to be linear when [**DD**]:[**ROH**] and [**DD**]:[**pdt**] ranged from 1 to 0. The conversion was normalized by setting [**DD**]:[**ROH**] at time = 0 to 100%.

B.6.2 UV-Vis Spectroscopy: Mes-Acr⁺/Mes-Acr[•] monitoring during photolysis

Time-evolution spectra were recorded on a Varian Cary 50 spectrophotometer with a scan rate of 1200 nm/min (time resolution is estimated to be ca. 0.5 min).

In a glovebox, two solutions of total volume 2.0 mL DCE were prepared in quartz cells with a PTFE-coated magnetic stir bar and sealed with a PTFE-lined septum cap:

- (A) 81.0 mg alkenol **ROH** [0.25 M], 10.2 μ L **PhSH** [0.05 M], 10.0 mg Mes-AcrBF₄ [0.013 M]
- (B) 81.0 mg alkenol **ROH** [0.25 M], 10.7 mg (**PhS**)₂ [0.025 M], 5.5 mg Mes-AcrBF₄ [0.013 M]

After sealing each cell with a Teflon coated screwcap, the vials were removed from the glovebox and analyzed by UV-Vis while irradiating with a blue LED lamp and continuous stirring. Spectra were collected from 300 to 800 nm with a 1 nm step size and a scan rate of 1200 nm per minute. A spectrum was collected prior to irradiation ($t = 0$) and at subsequent intervals following the start of irradiation (all intervals greater than 1 minute). The cell was irradiated with an incidence perpendicular to the light path of the instrument in order to minimize scatter. It should be noted that although the same lamp was employed in this photolysis as in the experiments described above, the intensity of the light reaching the solution is not likely to be identical to the preparative photolysis conditions, due to the differing materials and shapes of each vessel. However, since **A** and **B** were run under identical conditions (i.e., solution volume, stir rate, distance from lamp to cell are all unchanged), comparison between **A** and **B** is valid. Additional UV-Vis experiments were conducted in the same way as described above, with the exception that the photolysis lamp was turned off upon observation of complete consumption of

both **Mes-Acr⁺** and **Mes-Acr[•]** (ca. 5 min). Spectra were recorded for an additional 8 hours after the lamp was removed and the cell shielded from ambient light.

B.7 Determination of Association Constant for Donor-Acceptor Complex

UV-VIS absorption spectra were collected for solutions of 455 μM **Mes-AcrBF₄** containing **βMS** in the concentrations listed in **Figure B.23**. The Donor-Acceptor complex is detected as a weak new feature on the low energy side of the **Mes-Acr⁺** absorption. The $\Delta\text{Absorbance}$ spectra (spectrum where $[\beta\text{MS}] = 0 \text{ M}$ subtracted from the spectrum for each sample) reveal that the new absorption is centered around 467 nm. The equilibrium constant K_{DA} is defined as $K_{\text{DA}} = [\text{DA}]/[\beta\text{MS}][\text{Mes-Acr}^+]$ where **DA** is assumed to be a binary complex between **βMS** and **Mes-Acr⁺**. K_{DA} is calculated by the Benesi-Hildebrand method^{218,219} according to the equation

Equation B.10

$$\frac{[\text{Mes-Acr}]_0}{\Delta\text{Abs}_{467\text{nm}}} = \frac{1}{\varepsilon_{\text{DA}}K_{\text{DA}}} \cdot \frac{1}{[\beta\text{MS}]} + \frac{1}{\varepsilon_{\text{DA}}}$$

where ε_{DA} is the molar extinction coefficient of **DA**. The best fit line to a plot of $[\text{Mes-Acr}^+]/\Delta\text{Abs}_{467\text{nm}}$ vs. $[\beta\text{MS}]^{-1}$ (Figure B.24) gives ε_{DA} as the reciprocal of the y-intercept, and K_{DA} is obtained as 0.96 M^{-1} .

It should be noted that the Benesi-Hildebrand method is typically calculated using Absorbance, not $\Delta\text{Absorbance}$ as we have done here. However, this method assumes that only the **DA** complex absorbs at the wavelength in question. As **DA** clearly overlaps with the absorption for **Mes-Acr⁺** in this case, using Abs_{467} rather than ΔAbs_{467} is unsuitable.²¹⁹ In order to validate the above calculation, we also calculated K_{DA} by the method of Nash³³⁰ using

Absorbance values, which accounts for **Mes-Acr⁺** absorbance. By the Nash method, we calculate $K_{DA} = 1.1$, which is within reason of the value calculated by the Benesi-Hildebrand method.

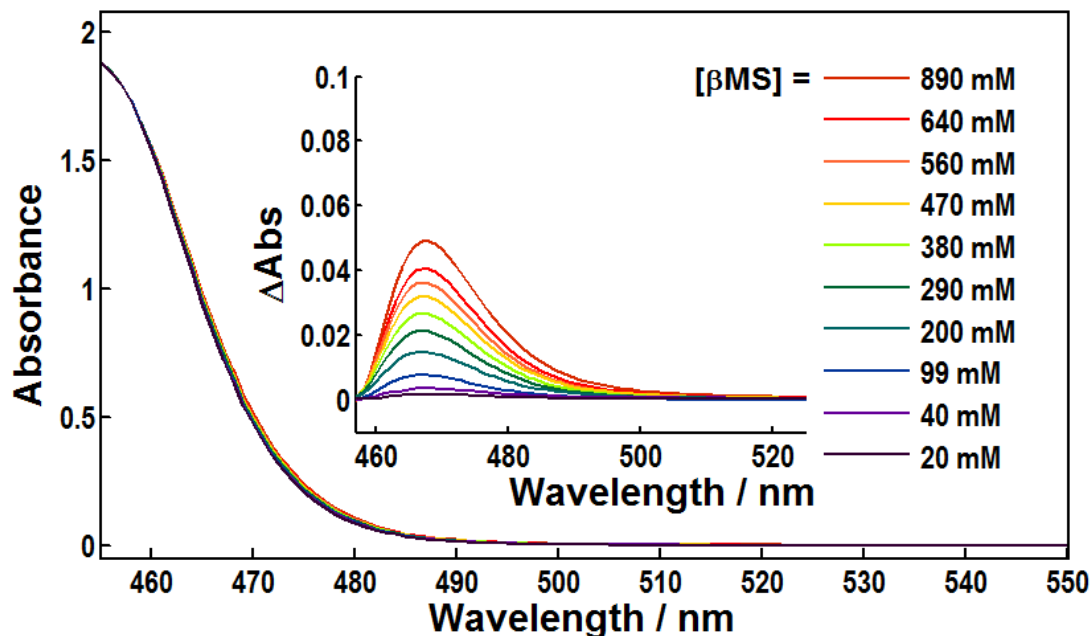


Figure B.23. Absorption spectra for solutions of **Mes-AcrBF₄** in DCE (455 μ M) with β MS. Inset shows Δ Absorbance to emphasize the shape of the new absorption.

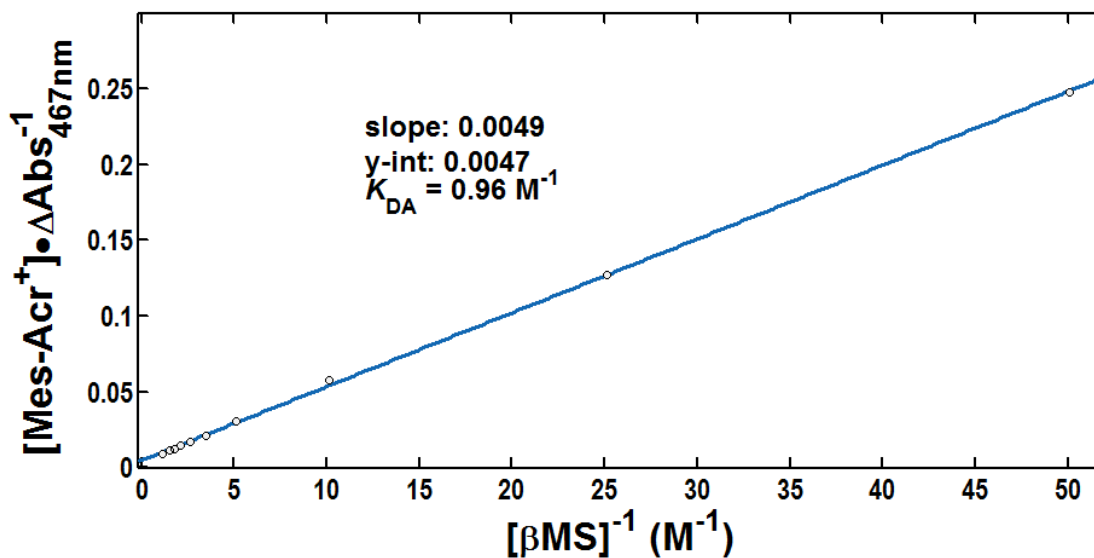


Figure B.24. Benesi-Hildebrand plot for the calculation of K_{DA} by equation B.10.

B.8 Determination of Quantum Yield of Reaction Using Ferrioxalate Actinometry

Potassium ferrioxalate ($\text{K}_3\text{Fe}(\text{C}_2\text{O}_4)_3$) was prepared as the trihydrate by the known method³³¹ and recrystallized three times from H_2O . A 0.15 M aqueous solution (1.0 mL) of $\text{K}_3\text{Fe}(\text{C}_2\text{O}_4)_3$ was irradiated for 60 seconds using the identical photolysis setup described above. The number of mol Fe^{2+} was determined from the absorbance at 510 nm of the tris-phenanthroline- Fe^{2+} after developing the photolyzed solution with a buffered solution of 1,10-phenanthroline.³³² Based on the molar extinction coefficient at 510 ($\epsilon_{510} = 11,110 \text{ M}^{-1}\text{cm}^{-1}$)³³³ and the absolute quantum yield for photolysis of $\text{K}_3\text{Fe}(\text{C}_2\text{O}_4)_3$ at 457.9 nm ($\Phi = 0.85$),³³³ the photon flux was determined to be $6.43 \times 10^{-7} \text{ mol photon s}^{-1}$. Quantum yield of reaction Φ_R was calculated at a given time point using the kinetic data presented in **Figure 3.8** of the text as $\Phi_R = \text{mol pdt/mol photon}$.

B.9 Computational Details

All calculations were implemented in the Gaussian 09 software package,³³⁴ and were performed at the UB3LYP level of theory^{335,336} using the 6-311+G(d) basis set^{337,338} with solvation in DCE evaluated in a self-consistent reaction field (SCRF) with the PCM model.³³⁹ Geometry optimization for structures **SM-a**, **SM-b**, **PDT-a** and **PDT-b** yielded the geometries shown. Transition structures **TS-a** and **TS-b** were located by performing relaxed potential energy scans where the distance between atoms C-12 and H-26 was advanced in 0.1 Å increments. The highest energy structure located from this scan was then submitted to a transition state optimization using the Berny algorithm. Vibrational analysis was performed for all stationary points, where each minimum was confirmed as having only positive vibrational frequencies, and each transition structure possessed a single imaginary frequency. Intrinsic Reaction Coordinate (IRC) calculations in both directions verified that TS structures **TS-a** and **TS-b** led to the minimized structures for the respective reactants and products. Thermochemical values (enthalpies and free energies) at 298.15 K were calculated using scaled vibrational frequencies. Images were generated using the CYLview program.³⁴⁰ Other possible geometries for HAT transfer were also explored, including the pathways where the HAT catalyst is rotated $\sim 180^\circ$ about the X-H (X = S in PhSH or C in PMN) bond in the transition state. This pathway was found to be at least 1.5 kcal mol⁻¹ higher in energy than the pathway explored herein.

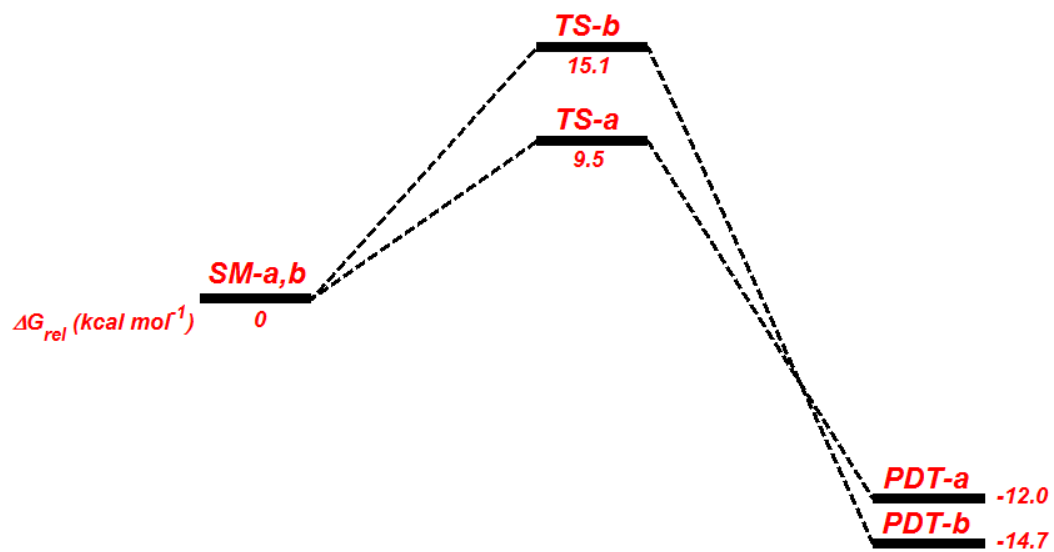
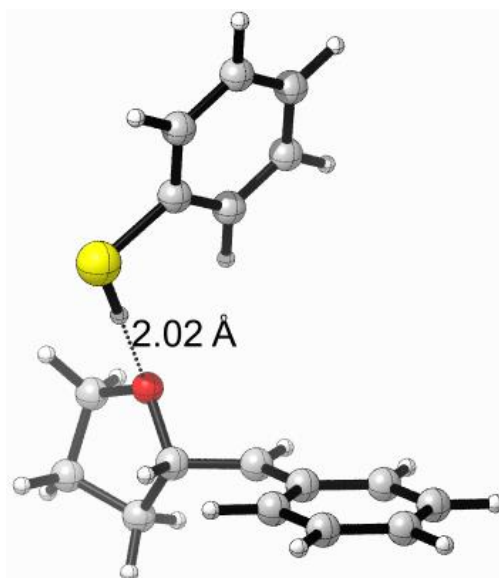


Figure B.25. Relative free energies of calculated structures for H-atom transfer.



SM-a

Table B.2. Thermochemistry for SM-a

H (298 K) = -1132.481289 Hartree $\Delta H_{\text{rel}} = 0 \text{ kcal mol}^{-1}$

G (298 K) = -1132.556371 Hartree $\Delta G_{\text{rel}} = 0 \text{ kcal mol}^{-1}$

Table B.3. Cartesian Coordinates for SM-a

C	-2.91492	-3.27549	-0.5725
C	-2.49141	-2.03754	-1.02368
C	-2.19766	-0.97308	-0.11848
C	-2.36024	-1.24725	1.272013
C	-2.78507	-2.49134	1.711129
C	-3.06738	-3.51633	0.799681
H	-3.12928	-4.06368	-1.28742
H	-2.37745	-1.86118	-2.08908
H	-2.14656	-0.47762	2.004427
H	-2.89704	-2.67116	2.775801
H	-3.39877	-4.48703	1.152441
C	-1.77496	0.273342	-0.63288
H	-1.67367	0.364013	-1.712
C	-1.45207	1.505483	0.135114
H	-1.47261	1.324085	1.213505
C	-2.33804	2.72229	-0.19432
H	-2.6394	2.693222	-1.24616
H	-3.24242	2.738241	0.416315
C	-1.39718	3.904256	0.064554
H	-1.70009	4.816371	-0.45371

H	-1.3411	4.124425	1.134674
C	-0.06317	3.361845	-0.44425
H	0.056271	3.529285	-1.52032
H	0.806328	3.777276	0.07012
O	-0.09291	1.937601	-0.19796
H	1.359932	1.277224	1.048053
C	3.474098	-1.10099	-1.54427
C	2.771805	-0.29248	-0.6514
C	3.218739	-0.15835	0.668922
C	4.370333	-0.84087	1.080128
C	5.064585	-1.6464	0.179496
C	4.621564	-1.78165	-1.13674
H	3.117638	-1.19758	-2.56504
H	1.880916	0.232168	-0.97874
H	4.724461	-0.7446	2.101722
H	5.955437	-2.17019	0.511354
H	5.163519	-2.41002	-1.83546
S	2.36776	0.863701	1.864974

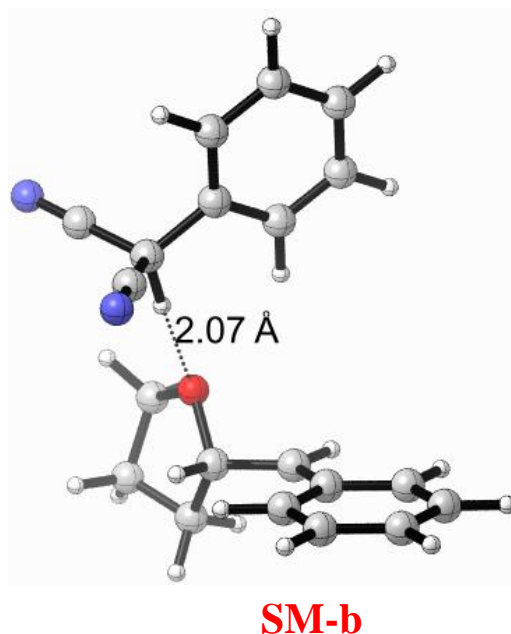


Table B.4. Thermochemistry for SM-b

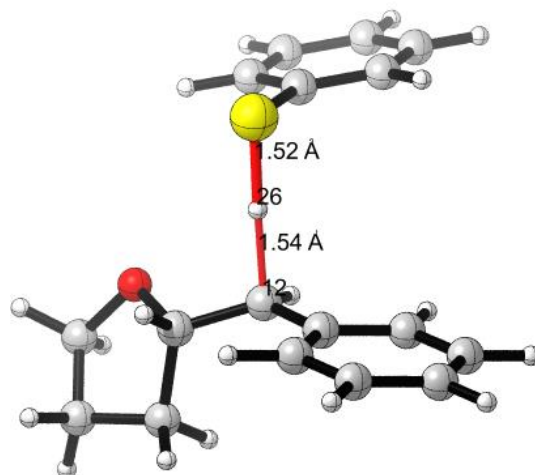
H (298 K) = -958.083907 Hartree $\Delta H_{\text{rel}} = 0 \text{ kcal mol}^{-1}$

G (298 K) = -958.166656 Hartree $\Delta G_{\text{rel}} = 0 \text{ kcal mol}^{-1}$

Table B.5. Thermochemistry for SM-b

C	-3.59317	-2.86292	-0.60984
C	-2.97241	-1.7264	-1.09816
C	-2.53522	-0.68213	-0.22797
C	-2.76902	-0.86663	1.167134
C	-3.39122	-2.00974	1.643643
C	-3.81008	-3.01744	0.766125
H	-3.91287	-3.63872	-1.29849
H	-2.81031	-1.61613	-2.16622
H	-2.45517	-0.10768	1.874199
H	-3.55252	-2.12307	2.711061
H	-4.29585	-3.90896	1.1478
C	-1.91183	0.460523	-0.77858
H	-1.77941	0.490952	-1.85779
C	-1.41861	1.659455	-0.04881
H	-1.47557	1.52208	1.034439
C	-2.11793	2.978362	-0.43317
H	-2.42797	2.947586	-1.48227
H	-3.00618	3.152582	0.176371
C	-1.0134	4.020851	-0.22847
H	-1.18339	4.942712	-0.78851

H	-0.91725	4.27876	0.830289
C	0.221891	3.265697	-0.7118
H	0.344709	3.349363	-1.79751
H	1.149456	3.584548	-0.23179
O	-0.00576	1.878314	-0.37334
H	1.45426	0.895458	0.717771
C	2.751178	-1.80389	-1.87632
C	2.257357	-0.84349	-0.99262
C	2.840698	-0.69585	0.265913
C	3.914664	-1.50595	0.64223
C	4.403905	-2.46286	-0.24332
C	3.822932	-2.61287	-1.50376
H	2.296213	-1.9172	-2.8545
H	1.423549	-0.21134	-1.27852
H	4.371826	-1.3946	1.620596
H	5.238093	-3.09056	0.050922
H	4.206002	-3.3588	-2.19203
C	2.282587	0.369545	1.221802
C	1.729847	-0.22253	2.45029
N	1.277864	-0.69926	3.39697
C	3.289182	1.388353	1.56056
N	4.078925	2.193886	1.79566



TS-a

Table B.6. Thermochemistry for TS-a

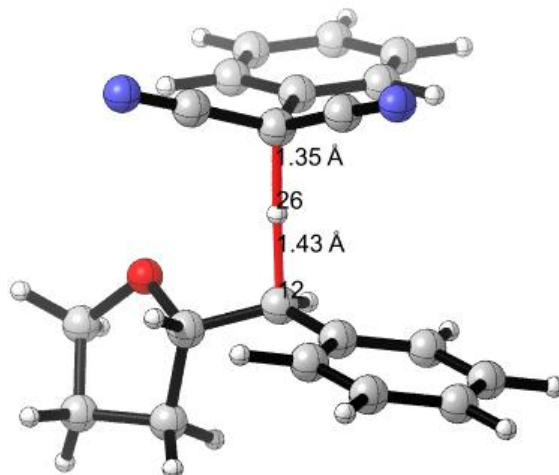
H (298 K) = -1132.470444 Hartree $\Delta H^\ddagger = 6.8 \text{ kcal mol}^{-1}$

G (298 K) = -1132.541164 Hartree $\Delta G^\ddagger = 9.5 \text{ kcal mol}^{-1}$

Table B.7. Cartesian Coordinates for TS-a

C	-1.93903	-3.36468	-0.83898
C	-1.21101	-2.17862	-0.85668
C	-1.54205	-1.10055	0.002905
C	-2.6306	-1.27761	0.893609
C	-3.35643	-2.46659	0.907515
C	-3.01806	-3.51618	0.042934
H	-1.66917	-4.17335	-1.51326
H	-0.37556	-2.06653	-1.54379
H	-2.90554	-0.48229	1.57993
H	-4.18934	-2.57854	1.596869
H	-3.58708	-4.44177	0.057841
C	-0.74106	0.109584	-0.03272
H	-0.04172	0.183905	-0.86831
C	-1.27912	1.443072	0.415861
H	-1.68278	1.37538	1.437355
C	-2.3587	2.039435	-0.51483
H	-2.12869	1.79705	-1.55978
H	-3.35695	1.656942	-0.28443
C	-2.19748	3.543432	-0.25547
H	-2.58587	4.164042	-1.0691
H	-2.71446	3.828437	0.6685
C	-0.67965	3.679811	-0.08983
H	-0.18372	3.873265	-1.05027

H	-0.38906	4.464137	0.617204
O	-0.21012	2.410586	0.41712
H	0.352222	-0.17942	1.021571
C	4.61726	0.61619	-0.27509
C	3.519442	0.651893	0.588909
C	2.819981	-0.52817	0.895577
C	3.243484	-1.7432	0.329634
C	4.344408	-1.77488	-0.53105
C	5.033136	-0.59609	-0.83691
H	5.149198	1.535628	-0.50639
H	3.199533	1.592344	1.027674
H	2.709012	-2.65859	0.567056
H	4.663056	-2.72078	-0.96187
H	5.889483	-0.62231	-1.5057
S	1.433018	-0.49498	2.026403



TS-b

Table B.8. Thermochemistry for TS-b

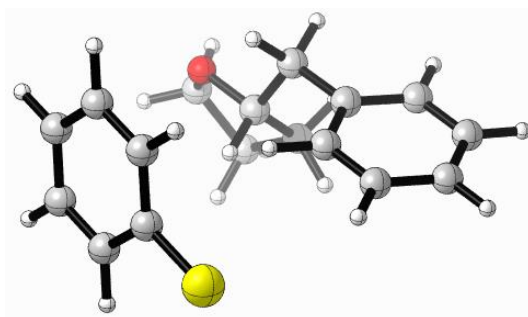
H (298 K) = - 958.065230 Hartree $\Delta H^\ddagger = 11.7 \text{ kcal mol}^{-1}$

G (298 K) = - 958.140052 Hartree $\Delta G^\ddagger = 16.7 \text{ kcal mol}^{-1}$

Table B.9. Cartesian Coordinates for TS-b

C	-3.21006	-2.49167	-1.17379
C	-2.10719	-1.64832	-1.19241
C	-1.95136	-0.62788	-0.22704
C	-2.94638	-0.5028	0.768419
C	-4.0477	-1.34937	0.783591
C	-4.18659	-2.34725	-0.18483
H	-3.31173	-3.26328	-1.92972
H	-1.35315	-1.76413	-1.96483
H	-2.85516	0.255942	1.5374
H	-4.80106	-1.23547	1.55604
H	-5.04734	-3.0072	-0.16755
C	-0.76968	0.224738	-0.27365
H	-0.18553	0.135698	-1.19118
C	-0.79723	1.636247	0.253569
H	-1.1946	1.663465	1.276805
C	-1.58446	2.631426	-0.61901
H	-1.44159	2.394361	-1.67786
H	-2.65408	2.612782	-0.40523
C	-0.90722	3.959142	-0.25812
H	-1.02538	4.721673	-1.03035
H	-1.32161	4.356182	0.672781
C	0.557295	3.54698	-0.06683
H	1.139293	3.667726	-0.98595

H	1.055745	4.099106	0.733746
O	0.548499	2.142887	0.273808
H	0.187673	-0.41124	0.574939
C	4.408314	-0.1545	-0.3831
C	3.300249	-0.08896	0.456892
C	2.350805	-1.11873	0.453039
C	2.525199	-2.20782	-0.41134
C	3.634739	-2.26675	-1.25088
C	4.580827	-1.24199	-1.23981
H	5.1391	0.647017	-0.36592
H	3.173802	0.764703	1.112484
H	1.802088	-3.01611	-0.42562
H	3.760246	-3.11861	-1.91067
H	5.446471	-1.29153	-1.8916
C	1.125604	-1.02874	1.326135
C	0.484766	-2.28539	1.642876
N	-0.0537	-3.28232	1.869327
C	1.23514	-0.19323	2.50048
N	1.296936	0.4832	3.434975



PDT-a

Table B.10. Thermochemistry for PDT-a

H (298 K) = -1132.496244 Hartree $\Delta H_{\text{rxn}} = -9.4 \text{ kcal mol}^{-1}$

G (298 K) = -1132.575477 Hartree $\Delta G_{\text{rxn}} = -12.0 \text{ kcal mol}^{-1}$

Table B.11. Cartesian Coordinates for PDT-a

C	3.216179	-2.60549	0.236605
C	2.978824	-1.31144	0.702076
C	1.690854	-0.76316	0.684504
C	0.642256	-1.55188	0.191892
C	0.87408	-2.84438	-0.27668
C	2.164274	-3.3761	-0.2575
H	4.222686	-3.01136	0.262993
H	3.80564	-0.72206	1.08792
H	-0.36859	-1.15365	0.181495
H	0.045976	-3.43794	-0.65141
H	2.34607	-4.38324	-0.61867
C	1.434448	0.64999	1.1609
H	2.251342	0.990012	1.804838
C	1.271314	1.651353	0.012094
H	0.455879	1.313368	-0.6432
C	2.519252	1.931124	-0.82867
H	3.411121	1.924376	-0.19258
H	2.663859	1.195337	-1.62145
C	2.242579	3.34484	-1.35459
H	3.147385	3.882632	-1.64514
H	1.582006	3.305345	-2.2259
C	1.530368	3.999603	-0.16638
H	2.237315	4.506432	0.499958
H	0.764502	4.719646	-0.46674
O	0.897965	2.931303	0.569059

H	0.520449	0.679736	1.762883
C	-4.18106	0.23357	-0.57692
C	-3.99564	-0.97693	-1.225
C	-3.86222	-2.17988	-0.48199
C	-3.92544	-2.11086	0.935053
C	-4.11171	-0.89504	1.572932
C	-4.23941	0.279873	0.82161
H	-4.28136	1.146619	-1.15361
H	-3.94991	-1.02176	-2.30694
H	-3.82562	-3.02492	1.508727
H	-4.15802	-0.85336	2.6557
H	-4.38399	1.229742	1.32479
S	-3.63363	-3.69145	-1.28266

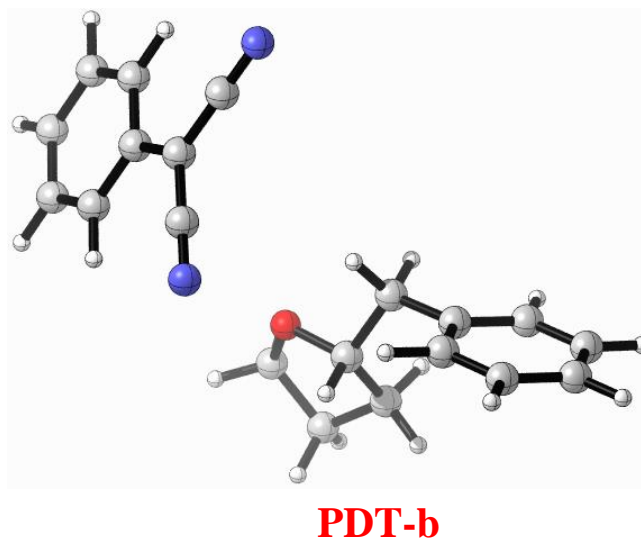


Table B.12. Thermochemistry for PDT-b

H (298 K) = -958.104217 Hartree $\Delta H_{\text{rxn}} = -12.7 \text{ kcal mol}^{-1}$

G (298 K) = -958.190019 Hartree $\Delta G_{\text{rxn}} = -14.7 \text{ kcal mol}^{-1}$

Table B.13. Cartesian Coordinates for PDT-b

C	-4.82164	-1.94528	-1.01597
C	-3.76328	-1.07004	-1.26374
C	-2.64177	-1.03878	-0.42659
C	-2.60758	-1.91421	0.667477
C	-3.66324	-2.78877	0.921187
C	-4.77619	-2.80714	0.079327
H	-5.67937	-1.95545	-1.6813
H	-3.80815	-0.40684	-2.12287
H	-1.74155	-1.91832	1.32364
H	-3.61378	-3.46047	1.772517
H	-5.59693	-3.49039	0.272573
C	-1.50091	-0.0777	-0.68018
H	-1.52658	0.279509	-1.71427
C	-1.51379	1.136742	0.254225
H	-1.49387	0.786894	1.296318
C	-2.66717	2.125835	0.070561
H	-2.9207	2.216395	-0.99137
H	-3.5673	1.824754	0.608975
C	-2.05565	3.432045	0.592224
H	-2.54899	4.32569	0.204557
H	-2.10757	3.467287	1.684461
C	-0.60065	3.318728	0.12485

H	-0.45457	3.776407	-0.85998
H	0.111231	3.768748	0.822022
O	-0.31524	1.908768	0.017348
H	-0.5447	-0.59332	-0.54467
C	4.611704	1.337991	0.768076
C	3.956022	0.154562	1.057265
C	3.953018	-0.90966	0.119707
C	4.631351	-0.73447	-1.11365
C	5.282338	0.454672	-1.38957
C	5.277668	1.495953	-0.45342
H	4.607377	2.144752	1.492125
H	3.441608	0.039997	2.004458
H	4.639932	-1.53631	-1.84308
H	5.797536	0.577648	-2.33543
H	5.789827	2.425587	-0.67498
C	3.279004	-2.14244	0.415053
C	3.264422	-3.22473	-0.49359
N	3.252112	-4.11446	-1.2372
C	2.597528	-2.34917	1.635799
N	2.038488	-2.52102	2.637139

APPENDIX C: SUPPORTING INFORMATION FOR “SITE-SELECTIVE ARENE C-H AMINATION VIA PHOTOREDOX CATALYSIS”

C.1 General Information: Materials and Methods

C.1.1 Materials

Commercially available reagents were purchased from Sigma-Aldrich, Acros, Alfa Aesar, or TCI, Matrix Scientific, Chem Impex International, and Fisher Scientific and were used as received unless otherwise noted. Diethyl ether (Et₂O), dichloromethane (DCM), tetrahydrofuran (THF), toluene, and dimethylformamide (DMF) were dried by passing through activated alumina under nitrogen prior to use. Other common solvents and chemical reagents were purified by standard published methods as noted. The following compounds employed as reagents in the *C-H* amination reactions were obtained from commercial vendors and used as received: 2,2,6,6-Tetramethyl-1-piperidinyloxy (TEMPO), polystyrene-divinylbenzene-bound TEMPO, diacetoxyiodobenzene, potassium persulfate, benzoquinone, (diacetoxyiodo)benzene, anisole, diphenyl ether, biphenyl, 2-chloroanisole, 3-bromoanisole, mesitylene, *m*-xylene, 2,6-dimethoxypyridine, 6-methoxyquinoline, 3,4-dihydrocoumarin, 4-methyl pyrazole, 3-methyl pyrazole, 1,2,3-triazole, 5-methyltetrazole, 1,2,4-triazole, 1,2,3-benzotriazole, 4,5,6,7-tetrahydro-1*H*-indazole, benzimidazole, and imidazole.

C.1.2 General Methods

Proton, carbon, and fluorine nuclear magnetic resonance spectra (¹H NMR, ¹³C NMR, ¹⁹F NMR) were recorded on a Bruker Avance 400 (¹H NMR at 400 MHz, ¹³C NMR at 100 MHz, and ¹⁹F NMR at 376 MHz) or a Bruker Avance III 600 (¹H NMR at 600 MHz and ¹³C NMR at 151 MHz) spectrometer. Chemical shifts for protons are reported in parts per million downfield from

tetramethylsilane and are referenced to residual protium in the solvent (^1H NMR: CHCl_3 at 7.26 ppm). Chemical shifts for carbon signals are reported in parts per million downfield from tetramethylsilane and are referenced to the carbon resonances of the solvent peak (^{13}C NMR: CDCl_3 at 77.16 ppm). Fluorine chemical shifts are referenced to trichlorofluoromethane as an external standard at 0 ppm. ^1H NMR data are reported as follows: chemical shift, multiplicity (s = singlet, d = doublet, t = triplet, q = quartet, hept = heptet, dd = doublet of doublets, ddd = doublet of doublet of doublets, m = multiplet, br s = broad singlet, app = apparent), coupling constants (Hz), and integration. Infrared (IR) spectra were obtained using a Jasco 260 Plus Fourier transform infrared spectrometer. High Resolution Mass Spectra (HRMS) were obtained using a Thermo LTqFT mass spectrometer with electrospray ionization in positive mode. Thin layer chromatography (TLC) was performed on SiliaPlate 250 μm thick silica gel plates provided by Silicycle. Visualization was accomplished with short wave UV light (254 nm), or development with iodine, ninhydrin stain, cerium ammonium molybdate or potassium permanganate solution followed by heating. Column chromatography was performed using SiliaFlash P60 silica gel (40-63 μm) purchased from Silicycle. Unless noted all reactions were run under an atmosphere of oxygen in flame-dried glassware with magnetic stirring. Irradiation of photochemical reactions was carried out using a PAR38 Royal Blue aquarium LED lamp (Model #6851) fabricated with high-power Cree XR-E LEDs as purchased from Ecoxotic (www.ecoxotic.com) with standard borosilicate glass vials purchased from Fischer Scientific. For all photolyses, reactions were stirred using a PTFE coated magnetic stir bar on a magnetic stir plate. Gas chromatography (GC) was performed on an Agilent 6850 series instrument equipped with a split- mode capillary injection system and Agilent 5973 network mass spec detector (MSD). Yield refers to isolated yield of analytically pure material unless otherwise

noted. NMR yields were determined using hexamethyldisiloxane as an internal standard. All other reagents were obtained from commercial sources and used without further purification unless otherwise noted.

C.1.3 Photoreactor Configuration.

Reactions were irradiated using a simple photoreactor consisting of two Par38 Royal Blue Aquarium LED lamps (Model #6851) is shown in which four reactions (2 dram vials) are irradiated simultaneously with a foil barrier preventing irradiation by two lamps. In order to ensure that the reactions are run near room temperature, a simple cooling fan was installed above the reactor to aid in dissipating the heat generated from both nonradiative decay pathways of the excited state catalysts and the heat generated from high power LEDs. An equilibrium temperature of 33 °C was measured with a standard alcohol thermometer. While a number of other blue LED sources are effective, we have found that LED emitters with high luminous flux and narrow viewing angle give the best results.

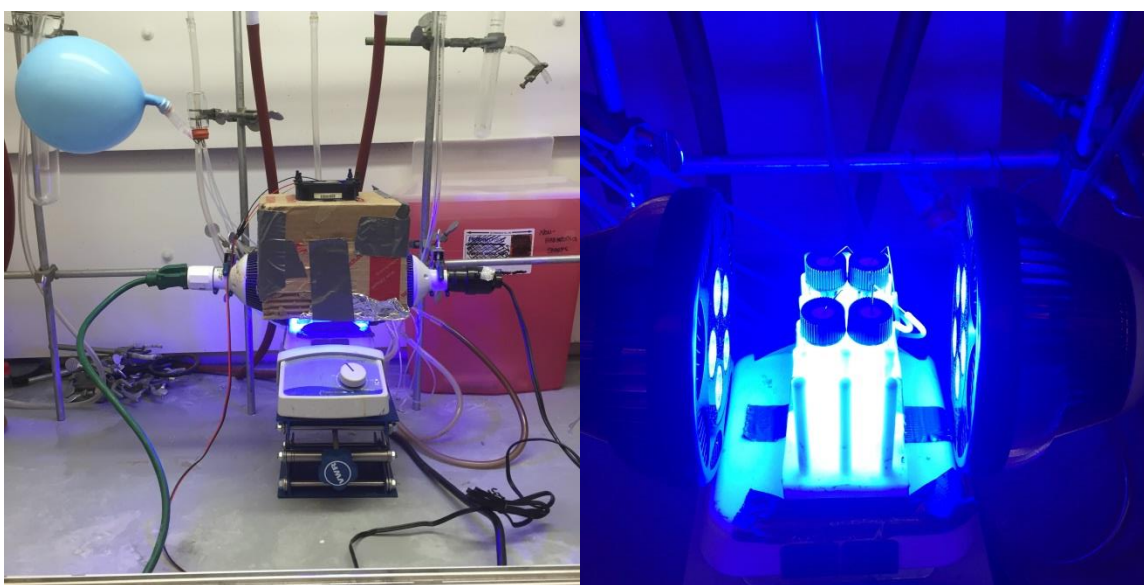
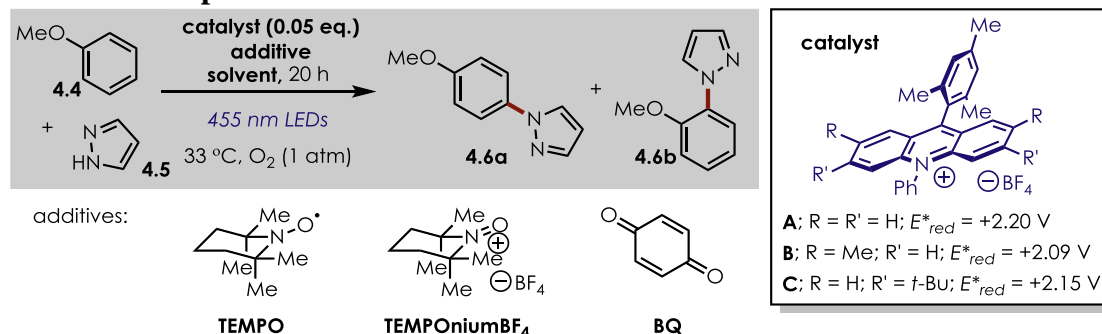


Figure C.1. Photoreactor configuration for aryl amination reactions

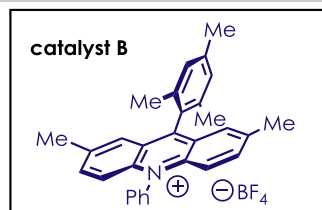
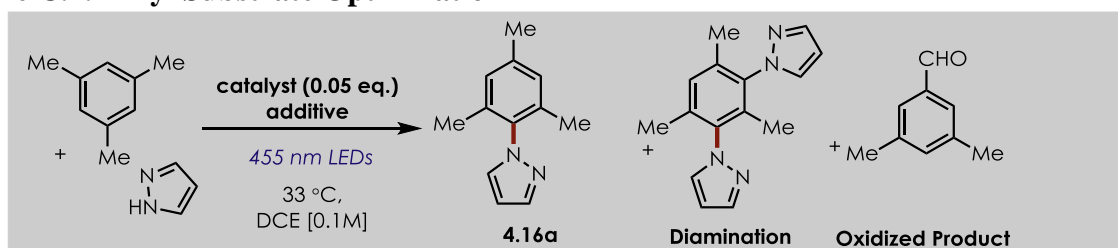
C.2 Additional Optimization Studies

Table C.1. Initial Optimization

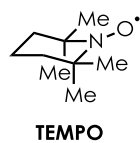


entry	additive	catalyst	solvent [M]	yield	p:o
1	no O ₂	A	DCM [0.25]	2%	–
2	none	A	DCE [0.25]	47%	6.7:1
3	none	A	MeCN [0.25]	6%	2.0:1
4	none	A	MeOH [0.25]	4%	1:2.9
5	none	A	TFE[0.25]	9%	1:25
6	none	B	DCE [0.25]	37%	3.6:1
7	PhI(OAc) ₂ (1.0 eq.)	B	DCE [0.25]	20%	4.1:1
8	BQ (1.0 eq.)	B	DCE [0.25]	18%	6.9:1
9	K ₂ S ₂ O ₈ (1.0 eq.)	B	DCE [0.25]	14%	1.8:1
10	TEMPO (0.1 eq.)	B	DCM[0.25]	65%	6.7:1
11	TEMPO (0.2 eq.)	B	DCM[0.25]	74%	6.2:1
12	TEMPO (0.5 eq.)	B	DCM[0.25]	45%	6.3:1
13	TEMPOoniumBF₄ (0.2 eq.)	B	DCM[0.25]	69%	6.5:1
14	TEMPO (0.2 eq.)	A	DCM[0.1]	61%	6.8:1
15	TEMPO (0.2 eq.)	B	DCM[0.1]	79%	6.7:1
16	TEMPO (0.2 eq.)	C	DCM[0.1]	88%	6.9:1
17	TEMPO (0.2 eq.) (air)*	C	DCM[0.1]	97%	7.5:1
18	polymer-TEMPO (0.2 eq.)	C	DCM[0.1]	65%	6.7:1

Table C.2. Alkyl Substrate Optimization

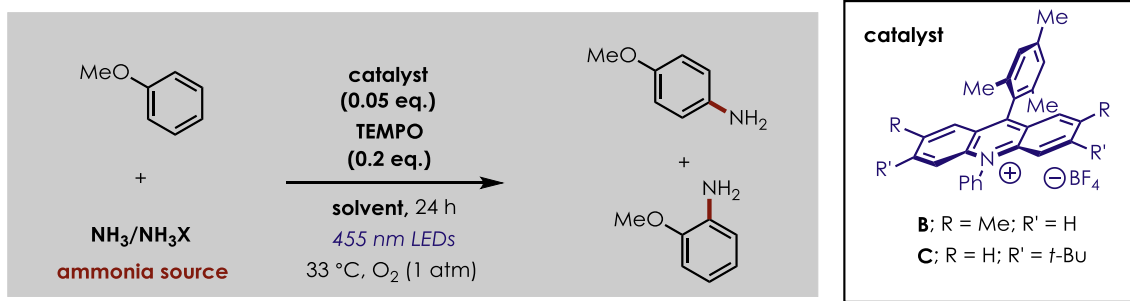


additives:



entry	Atmosphere	Arene:Amine	TEMPO	Time	Yield 4.16a	Yield Diamination	Yield Oxidized
1	O ₂	1:2	None	24 hours	39%	16%	10%
2	O ₂	1:2	0.2 equiv.	24 hours	40%	49%	5%
3	O ₂	2:1	0.2 equiv.	24 hours	78%	12%	20%
4	O ₂	2:1	0.2 equiv.	48 hours	80%	11%	22%
5	N ₂	1:2	0.2 equiv.	24 hours	20%	3%	0%
6	N ₂	1:2	1.0 equiv.	24 hours	52%	3%	0%
7	N ₂	2:1	1.0 equiv.	24 hours	70%	2%	0%
8	N ₂	2:1	1.0 equiv.	48 hours	86%	3%	0%
9	N ₂	1:2	None	24 hours	11%	1%	0%

Table C.3. Aniline Synthesis Optimization



entry	ammonia source	catalyst	solvent [M]	yield†	para:ortho
1	NH ₄ OAc, 2 eq.	B	DCE [0.10]	15%	1:1
2	NH ₄ HCO ₃ , 2 eq.	B	DCE [0.10]	24%	1:1.5
3	(NH ₄) ₂ CO ₃ , 2 eq.	B	DCE [0.10]	35%	1:1
4	(NH ₄) ₂ CO ₃ , 2 eq.	B	MeCN[0.10]	24%	2:1
5	(NH ₄) ₂ SO ₃ , 2 eq.	B	DCE [0.10]	0%	--
6	(NH ₄) ₂ CO ₃ , 2 eq.	B	DCE:H ₂ O [0.10*]	43%	1.6:1
7	(NH ₄) ₂ CO ₃ , 4 eq.	C	DCE:H ₂ O [0.10*]	40%	1.2:1
8	NH₄O₂CNH₂, 4 eq.	C	DCE:H₂O [0.10*]	58%	1.4:1
9	NH ₄ O ₂ CNH ₂ , 2 eq.	C	DCE:H ₂ O [0.10*]	45%	1.5:1
10	NH ₄ O ₂ CNH ₂ , 4 eq.	B	DCE:H ₂ O [0.10*]	47%	1.4:1
11	NH ₄ O ₂ CNH ₂ , 4 eq.	C	TFE [0.10]	7%	--
12	NH ₄ O ₂ CNH ₂ , 4 eq.	C	DCE:TFE [0.10*]	25%	1:1

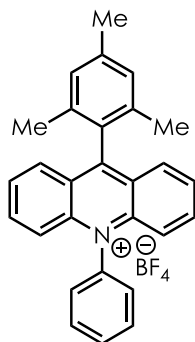
Reactions were performed using anisole (0.460 mmol), catalyst **B** or **C** (5 mol %), TEMPO (20 mol%)

*A 10:1 ratio of DCE:H₂O was utilized as the solvent system.

†Yields determined by GC analysis using 3-bromotoluene as the internal standard

C.3 Synthetic Procedures

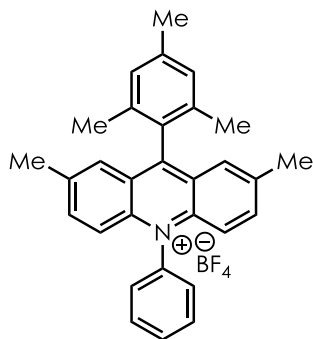
C.3.1 Preparation of Acridinium Photocatalysts



catalyst A

9-Mesityl-10-phenyl acridinium tetrafluoroborate (Catalyst A).

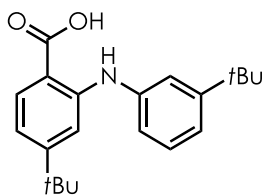
The title compound was prepared as previously reported by our laboratory.¹⁷⁵ The spectral data matched the values reported in the literature.



catalyst B

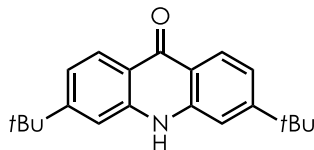
9-Mesityl-2,7-dimethyl-10-phenylacridinium tetrafluoroborate (Catalyst B).

The title compound was prepared as previously reported by our lab.¹⁷⁵ The spectral data matched the values reported in the literature.



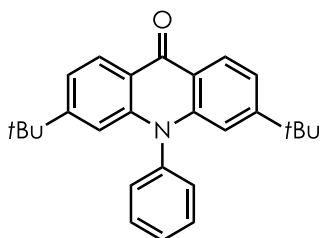
4-(*tert*-butyl)-2-((3-(*tert*-butyl)phenyl)amino)benzoic acid (S1).

To a flame dried 2-neck round bottom flask equipped with a condenser was added potassium carbonate (9.0 g, 65.3 mmol, 1.4 equiv.), copper (594 mg, 9.34 mmol, 0.2 equiv.) and 2-bromo-4-(*tert*-butyl)benzoic acid (12 g, 46.7 mmol, 1.0 equiv.). The setup was evacuated and back filled with nitrogen gas three times for 15 minutes each cycle. *m*-*Tert*-butyl aniline (10.3 mL, 65.3 mmol, 1.4 equiv.) and 1-pentanol (72 mL) were both sparged with nitrogen for 15 minutes. Pentanol was added to the reaction flask followed by the aniline. The solution was heated to 140 °C for 16 hours. The solution was cooled to room temperature and diluted with water (100 mL), washed with 3M HCl (100 mL) and extracted with dichloromethane (3 x 100 mL). The organic layer was washed with ammonium chloride (100 mL), brine (100 mL) and dried over sodium sulfate. The organic solution was concentrated to afford a brown solid. The crude product was recrystallized from methanol to afford the desired aryl amine (10.1 g, 67% yield). ¹H NMR (600 MHz, CDCl₃): δ 11.74 (br s, 1H), 9.32 (s, 1H), 8.00 (d, *J* = 9 Hz, 1H), 7.36-7.35 (m, 2H), 7.32 (t, *J* = 7.8 Hz, 1H), 7.16 (d, *J* = 8.4 Hz, 1H), 7.07 (dd, *J* = 7.8 Hz, *J* = 0.6 Hz, 1H), 6.83 (dd, *J* = 8.4 Hz, *J* = 1.2 Hz, 1H), 1.35 (s, 9H), 1.27 (s, 9H); ¹³C NMR (CDCl₃, 151 MHz): δ 173.4, 159.0, 152.5, 148.6, 140.3, 132.3, 129.0, 120.6, 119.6, 119.5, 115.1, 111.0, 108.0, 35.3, 34.8, 31.4, 30.8. IR (thin film): 3340.10, 2963.09, 2569.68, 2360.44, 1659.45, 1565.92, 1416.46, 1242.90, 963.27, 700.99. HRMS: Calculated for (M+Na)⁺: 348.1940; found: 348.1932.



3,6-di-*tert*-butylacridin-9(10*H*)-one (S2).

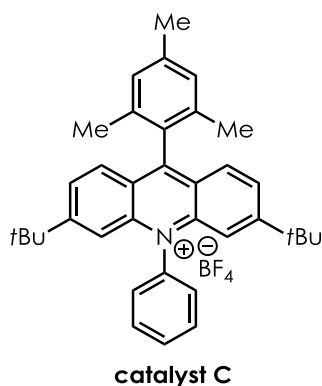
To an Erlenmeyer flask equipped with a stir bar was added sulfuric acid (38 mL), which was heated to 100 °C. 4-(*tert*-butyl)-2-((3-(*tert*-butyl)phenyl)amino)benzoic acid (5.1 g, 15.7 mmol) was added to the sulfuric acid in portions and stirred for 3 hours at 100 °C. The solution was cooled to room temperature and the acidic solution was then poured into water at 0 °C, forming a yellow precipitate. Ammonium hydroxide was added until an alkaline pH persisted. The yellow solid was then filtered over a medium fritted funnel to afford the desired product along with the undesired regioisomer in an 8:1 mixture. Hot filtration from methanol removed insoluble salts, followed by a recrystallization from methanol and dichloromethane to afford the desired acridone (3.6 g, 76% yield). ¹H NMR (400 MHz, 3:1 CDCl₃:MeOD) δ 8.12 (d, *J* = 8.9 Hz, 2H), 7.26 (d, *J* = 1.8 Hz, 2H), 7.29-7.18 (m, 2H), 3.15 (br. s, 1H), 1.16 (d, *J* = 2.5 Hz, 18H). ¹³C NMR (151 MHz, CDCl₃) δ 178.26, 157.33, 141.19, 125.73, 119.82, 118.44, 112.70, 48.73, 35.02, 30.51. IR (thin film): 3087.48, 2962.13, 2321.87, 1632.45, 1594.84, 1552.42, 1368.25, 1235.18, 1094.40 765.60. HRMS: Calculated for (M+H)⁺: 308.2014; found: 308.2004.



3,6-di-*tert*-butyl-10-phenylacridin-9(10*H*)-one (S3).

To a flame-dried round bottom flask was added 3,6-di-*tert*-butylacridin-9(10*H*)-one (3.75 g, 12.2 mmol, 1 equiv.), copper (I) iodide (232 mg, 1.22 mmol, 0.1 equiv.) and potassium carbonate (3.37 g, 24.4 mmol, 2.0 equiv.). Iodobenzene (1.48 mL, 13.3 mmol, 1.1 equiv.) and

2,2,6,6-tetramethylheptane-3,5-dione (0.51 mL, 2.44 mmol, 0.2 equiv.) were added in a nitrogen-filled glovebox along with dimethylformamide (62 mL). The solution was heated to 130 °C for 48 hours. The solution was then cooled to room temperature and quenched with 3M HCl (50 mL). The aqueous solution was extracted with dichloromethane (3x 100 mL). The combined organic layers were washed with sodium bicarbonate (150 ml), ammonium chloride (150 mL), brine, dried over sodium sulfate and then concentrated. The final pale yellow solid (2.95 g, 63% yield) was obtained after flash chromatography (20% EtOAc/Hexanes). **¹H NMR** (400 MHz, CDCl₃) δ 8.50 (d, *J* = 8.5 Hz, 2H), 7.72 (t, *J* = 7.5 Hz, 2H), 7.66 (d, *J* = 7.3 Hz, 1H), 7.40-7.37 (m, 2H), 7.33 (dd, *J* = 8.5, 1.6 Hz, 2H), 6.71 (d, *J* = 1.6 Hz, 2H), 1.20 (s, 18H). **¹³C NMR** (151 MHz, CDCl₃) δ 177.73, 156.93, 143.38, 139.30, 131.01, 130.21, 129.59, 126.98, 119.94, 119.77, 113.03, 35.46, 31.01. **IR** (thin film): 3049.87, 2964.05, 2868.59, 1606.41, 1452.14, 1307.50, 1197.58, 997.02, 867.81, 682.68; **HRMS**: Calculated for (M+H)⁺: 384.2327; found: 384.2319.

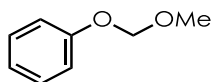


9-Mesityl-3,6-di-*tert*-butyl-10-phenylacridinium tetrafluoroborate (Catalyst C).

To a flame dried round bottom flask equipped with a stir bar was added 3,6-di-*tert*-butyl-10-phenylacridin-9(10*H*)-one (1.5 g, 3.91 mmol, 1.0 equiv.). The acridone was dissolved in dry THF (112 mL). Mesityl magnesium bromide (9.8 mL, 9.8 mmol, 1 M in Et₂O, 2.5 equiv.) was added dropwise and the solution was stirred at room temperature for 24 hours. The solution was

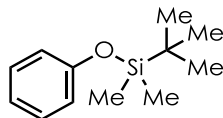
then heated to 50 °C for 72 hours. The red solution was cooled and quenched with sodium bicarbonate (100 mL). The aqueous layer was extracted with DCM (3x 100 mL) followed by a brine wash, drying over sodium sulfate and concentration to afford a red oil. The oil was dried on high vacuum for 4 hours. The oil was then dissolved in ether (67 mL) and tetrafluoroboric acid diethyl ether complex (0.65 mL, 4.7 mmol, 1.2 equiv.) in ether (12.5 mL) was added dropwise and the solution was stirred for 1 hour, during which a precipitate quickly appeared with the addition of acid. The yellow solid that precipitated out was then filtered and washed with ether (200 mL) to afford the final 3,6-di-*tert*-butyl-9-mesityl-10-phenylacridin-10-ium tetrafluoroborate (2.05 g, 92% yield). **¹H NMR** (400 MHz, CDCl₃) δ 7.99-7.93 (m, 2H), 7.93-7.89 (m, 1H), 7.78 (q, *J* = 1.6 Hz, 3H), 7.77-7.70 (m, 2H), 7.41 (d, *J* = 3.2 Hz, 2H), 7.26 (s, 1H), 7.16 (d, *J* = 2.7 Hz, 2H), 2.48 (s, 3H), 1.86 (d, *J* = 3.5 Hz, 6H), 1.29 (d, *J* = 3.5 Hz, 9H). **¹³C NMR** (151 MHz, CDCl₃) δ 163.72, 162.44, 142.25, 140.31, 136.95, 136.25, 131.96, 131.75, 129.40, 129.07, 128.41, 128.12, 127.60, 124.16, 115.19, 36.80, 30.34, 21.42, 20.36. **IR** (thin film): 2965.02, 2863.77, 1615.09, 1540.85, 1436.71, 1252.54, 1055.84, 915.06, 780.06, 728.96; **HRMS**: Calculated for (M-BF₄)⁺: 486.3161; found: 486.3158.

C.3.2 Preparation of Arene Substrates



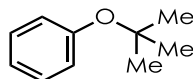
(methoxymethoxy)benzene (S4)

The title compound was prepared according to a published procedure; spectral data were in agreement with literature values.³⁴¹



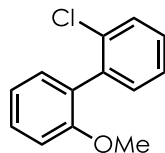
***tert*-butyldimethyl(phenoxy)silane (S5)**

The title compound was prepared according to a published procedure; spectral data were in agreement with literature values.³⁴²



***tert*-butoxybenzene (S6)**

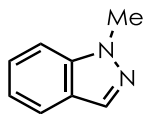
The title compound was prepared according to a published procedure; spectral data were in agreement with literature values.³⁴³



2-chloro-2'-methoxy-1,1'-biphenyl. (S7)

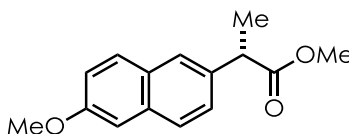
Under an inert atmosphere, 173 mg Tetrakis(triphenylphosphine)palladium(0) (0.15 mmol, 0.03 equiv.) was added to a flame-dried round bottom flask containing a magnetic stir bar, along with 938 mg (2-chlorophenyl)boronic acid (6.0 mmol, 1.2 equiv.) and 1.38 g K₂CO₃ (10. mmol, 2.0 eq.). Separately, a 9:1 (v/v) mixture of THF/H₂O was sparged with nitrogen, then added to the flask containing palladium, boronic acid, and carbonate. The mixture was warmed to 50 °C for 10 minutes while 2-bromoanisole was sparged with nitrogen in a separate vial. 2-Bromoanisole was added, and the reaction was heated at reflux for 26 hours. After cooling to room temperature, 20 mL H₂O was added, along with 10 mL saturated aqueous NH₄Cl. The layers were separated, and the aqueous phase was extracted twice with diethyl ether. The combined extracts were washed with brine and dried with MgSO₄. After filtration and concentration in vacuo, the crude oil was dissolved in pentanes and crystallization occurred when

cooled in a -20 °C freezer. The white crystals were collected by vacuum filtration, washed with cold pentanes, and dried in vacuo to give 930 mg pure material. The spectral data were in agreement with literature values.³⁴⁴



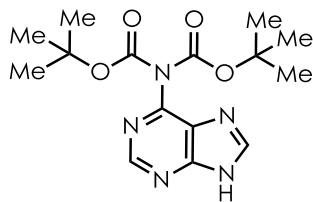
1-methyl-1*H*-indazole (S8).

The title compound was prepared by the published procedure.³⁴⁵ The material was recrystallized from a mixture of ethyl acetate and hexanes and dried in vacuo. The ¹H NMR spectrum matches the reported data.



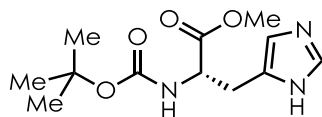
(*S*)-methyl 2-(6-methoxynaphthalen-2-yl)propanoate (S9)

The title compound was prepared according to a published procedure; spectral data were in agreement with literature values.³⁴⁶



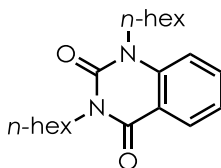
Bis-Boc-adenine (S10)

The title compound was prepared according to a published procedure.³⁴⁷ The material was recrystallized from a mixture of ethyl acetate and hexanes and dried in vacuo. Spectral data were in agreement with literature values.



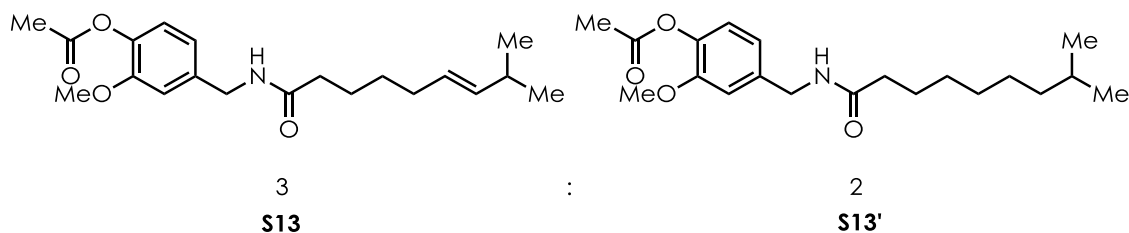
methyl (*tert*-butoxycarbonyl)-*L*-histidinate (S11).

The title compound was prepared by the published procedure.³⁴⁸ The material was recrystallized from a mixture of ethyl acetate and hexanes and dried in vacuo. The ¹H NMR spectrum matches the reported data.³⁴⁹



1,3-dihexylquinazoline-2,4(1*H*,3*H*)-dione (S12).

Benzoyleneurea (1 g, 6.2 mmol, 1.0 equiv.) was dissolved in dry DMF and potassium carbonate was added (2.8 g, 20.1 mmol, 3.3 equiv.). Hexyl bromide (3.5 mL, 24.7 mmol, 4.0 equiv.) was added dropwise and the solution was stirred for 84 hours. The solution was concentrated and then diluted with dichloromethane. The organic solution was washed with water (50 mL), and the aqueous layer was extracted with CH₂Cl₂ (3x 50 mL). The combined organic layers were washed with brine, dried over sodium sulfate and concentrated to give a pale yellow solid. The crude product was purified by flash chromatography (0-20% EtOAc/Hex) to afford the desired pale yellow oil (1.1 g, 54% yield). ¹H NMR (600 MHz, CDCl₃) δ 8.24 (dd, *J* = 7.9, 1.7 Hz, 1H), 7.66 (ddd, *J* = 8.7, 7.2, 1.7 Hz, 1H), 7.33-7.12 (m, 2H), 4.17-4.04 (m, 4H), 1.77-1.61 (m, 4H), 1.42-1.23 (m, 11H), 0.95-0.79 (m, 7H). ¹³C NMR (151 MHz, CDCl₃) δ 161.79, 150.80, 139.89, 134.94, 129.19, 122.68, 115.88, 113.57, 43.84, 42.05, 31.63, 31.63, 31.58, 27.88, 27.37, 26.78, 26.59, 22.69, 22.67, 14.15, 14.11; IR (thin film): 2956.34, 2930.31, 2857.99, 2357.55, 1704.76, 1660.41, 1608.34, 1483.96, 1352.82, 757.89. HRMS: Calculated for (M+H)⁺: 331.2385; found: 331.2379.

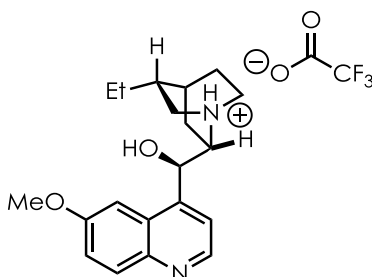


(*E*)-2-methoxy-4-((8-methylnon-6-enamido)methyl)phenyl acetate (S13/S13').

The title compound was synthesized from capsaicin, which was obtained from Sigma-Aldrich as a 2:1 mixture of capsaicin ((*E*)-*N*-(4-hydroxy-3-methoxybenzyl)-8-methylnon-6-enamide) and dihydrocapsaicin (*N*-(4-hydroxy-3-methoxybenzyl)-8-methylnonanamide). The capsaicin was used as received and acylated by the following procedure: 750 mg capsaicin (2.5 mmol, 1.0 equiv.) was cooled to 0 °C in 11 mL DCM, and 262 μ L acetyl chloride was added (3.7 mmol, 1.5 equiv.), followed by 693 μ L trimethylamine. The mixture was stirred for 1 hour at 0 °C, then at ambient temperature for an additional 1 hour. The mixture was diluted with 25 mL DCM and washed with brine, dilute HCl, then saturated aqueous NaHCO₃. The organic phase was again washed with brine and dried with MgSO₄. After concentrating in vacuo, the crude tan solid was recrystallized from a mixture of EtOAc and hexanes, and collected by vacuum filtration, yielding 813 mg of a white solid. The proton NMR spectra indicates that the ratio between *O*-acetyl capsaicin **S13** and *O*-acetyl dihydrocapsaicin **S13'** is identical to the starting material. Note: the indicated proton resonances refer to the title compound; see the included ¹HNMR spectrum below for the resonances of the saturated compound. The carbon resonances listed include the resonances for both the unsaturated and saturated compounds in the mixture.

¹HNMR (600 MHz, CDCl₃) δ 6.98 (d, *J* = 8.0 Hz, 1H), 6.90 (s, 1H), 6.84 (d, *J* = 8.0 Hz, 1H), 5.68 (s, 1H), 5.41 – 5.28 (m, 2H), 4.42 (d, *J* = 5.7 Hz, 2H), 3.82 (s, 3H), 2.31 (s, 3H), 2.21 (t, *J* = 7.4 Hz, 2H), 1.99 (q, *J* = 7.0 Hz, 2H), 1.67 – 1.63 (m, 2H), 1.51 (hept, *J* = 6.7 Hz, 1H), 1.39 (p, *J*

= 7.6 Hz, 2H), 0.95 (d, $J = 6.7$ Hz, 6H). ; ^{13}C NMR (151 MHz, CDCl_3) δ 172.96, 169.29, 151.35, 139.21, 138.25, 137.53, 126.60, 123.01, 120.19, 112.29, 100.12, 56.04, 43.60, 39.10, 37.00, 36.84, 32.38, 31.12, 29.45, 28.09, 27.39, 25.93, 25.40, 22.80, 20.82. IR (thin film): 3287.07, 2928.38, 2359.48, 1766.48, 1642.09, 1511.92, 1388.25, 1272.79, 1195.54, 1035.59. HRMS: Calculated for $(\text{M}+\text{Na})^+$: 370.1995 and 372.2151; found: 370.1987 and 370.2141.



(9S)-10,11-dihydro-6'-methoxycinchonan-9-ol·2,2,2-trifluoroacetic acid (S14).

The title compound was prepared by stirring 1.0 g dihydroquinidine (3.1 mmol, 1.0 equiv.) in a 15:1 (v/v) mixture of $\text{Et}_2\text{O}/\text{MeOH}$ at $0\text{ }^\circ\text{C}$ and adding $237\ \mu\text{L}$ trifluoroacetic acid (3.1 mmol, 1.0 equiv.) slowly. The mixture was stirred for 2 hours and concentrated in vacuo. The crude white foam was recrystallized by dissolving in hot toluene and cooling. The tan solid was collected by vacuum filtration and washed with toluene. The solid was dried in vacuo to give quantitative yield of the salt. ^1H NMR (600 MHz, CDCl_3) δ 12.34 (s, 1H), 8.69 (d, $J = 4.5$ Hz, 1H), 7.86 (d, $J = 9.3$ Hz, 1H), 7.62 (d, $J = 4.4$ Hz, 1H), 7.18 (s, 1H), 6.98 (s, 1H), 6.37 (s, 1H), 5.66 (s, 1H), 4.16 – 3.91 (m, 1H), 3.83 (s, 3H), 3.54 – 3.22 (m, 3H), 3.18 (s, 1H), 2.39 – 2.24 (m, 1H), 1.95 (s, 1H), 1.86 – 1.51 (m, 5H), 1.02 – 0.88 (m, 4H). ^{13}C NMR (151 MHz, CDCl_3) δ 162.93 (q, $J = 34.9$ Hz), 158.20, 146.85, 144.30, 143.27, 131.19, 125.16, 122.30, 118.36, 116.71 (q, $J = 292.7$ Hz), 99.36, 66.40, 60.23, 55.79, 50.03, 49.38, 35.26, 25.16, 24.30, 23.93, 17.68, 11.50. ^{19}F NMR (376 MHz, CDCl_3) δ -75.34. IR (thin film): 3249.47 (br), 2964.05, 2556.18,

2360.44, 1672.95, 1509.99, 1433.82, 1242.90, 1199.51, 834.06. **HRMS**: Calculated for (M-C₂O₂F₃)⁺: 327.2072; found: 327.2067.

C.3.3 Procedures for the Photoredox-Catalyzed Synthesis of Aryl Amines

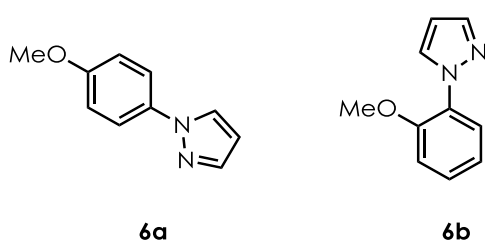
Notes: All isolated yields and regioisomeric ratios reported are the average of duplicate experiments. For inseparable mixtures of regioisomers, analytical data was collected for the sample as isolated from chromatography, which, in most cases, is a mixture of *para*- and *ortho*-isomers.

C.3.3.1 General Method A: Synthesis of 4.6, 4.12-4.15, 4.18-4.32, 4.34-4.37, 4.39-4.41

The synthesis of aryl pyrazoles **4.6a** and **4.6b** from anisole **4.4** and pyrazole **4.5** is representative of the following general procedure using conditions from **Figure 4.2A**:

To a 2 dram vial containing a Teflon-coated magnetic stir bar was added 25 μ mol of Catalyst C (0.05 equiv.), 68 mg of pyrazole (1.0 mmol, 2 equiv.), and 16 mg of (2,2,6,6-tetramethylpiperidin-1-yl)oxyl (0.1 mmol, 0.2 equiv.). Dichloromethane or 1,2-Dichloroethane was added (5.0 mL), followed by the arene (0.5 mmol, 1.0 equiv.). The vial was sealed with a Teflon-lined septum screw cap. The septum was pierced with a disposable steel needle connected to an oxygen-filled balloon. A vent needle was inserted and the reaction medium was sparged for 5 minutes by bubbling oxygen through the mixture. The vent needle was removed, and the oxygen balloon was maintained, providing approximately 1 atm of oxygen to the vial headspace for the course of the reaction. The vial was positioned on a stir plate approximately 10 cm from a Par38 LED lamp supplying blue light ($\lambda = 440\text{-}460$ nm). After irradiation for 20 hours, the reaction mixture was analysed by GC-MS or concentrated in vacuo and purified by column chromatography on silica gel with hexanes/ethyl acetate (or with the eluent noted for each substrate). For reaction optimization as shown in **Figure 4.2A** and **Table C.1**, crude reaction

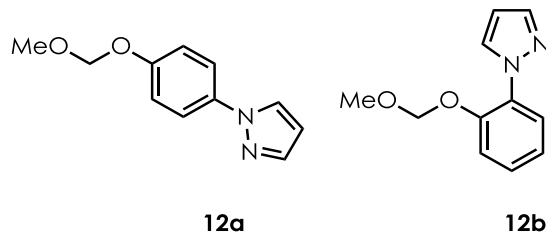
mixtures were analyzed by GC-MS by the following modification to General Procedure A: reactions were run under concentrations given in **Figure 4.2A** and **Table C.1** relative to anisole on a 0.5 mmol scale. Following irradiation for 20 hours, 33 μL 1,3-dimethoxybenzene (0.25 mmol, 0.5 equiv.) was added to the reaction mixture, which was passed through a short pad of silica gel and rinsed with an equal volume of dichloromethane. Samples were analyzed using an Agilent 5973 GC-MS system, wherein product yields and anisole conversions were calculated relative to the internal standard according to the instrument response factors, which were determined separately by construction of calibration curves.



1-(4-methoxyphenyl)-1H-pyrazole (4.6a), 1-(2-methoxyphenyl)-1H-pyrazole (4.6b).

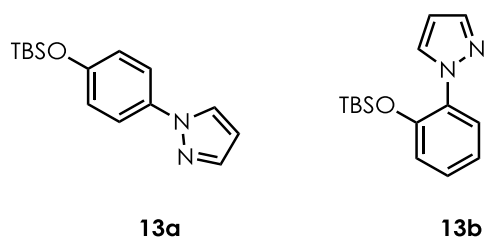
The title compounds were prepared according to **General Method A** with an irradiation time of 20 hours. The crude residue was purified by column chromatography on silica gel with an eluent of 10% to 20% EtOAc/hexanes to yield a pale yellow oil in 88% as an inseparable mixture of **4.6a** and **4.6b**. The *para:ortho* ratio of the inseparable mixture was 6.7:1 as determined by ^1H NMR of the isolated product. The NMR data were consistent with literature values. **4.6a:**³⁵⁰ ^1H NMR (400 MHz, CDCl_3) δ 7.82 (s, 1H), 7.69 (s, 1H), 7.59 (d, $J = 8.9$ Hz, 2H), 6.97 (d, $J = 8.9$ Hz, 2H), 6.43 (s, 1H), 3.84 (s, 3H). ^{13}C NMR (100 MHz, CDCl_3) δ 158.25, 140.64, 134.06, 126.85, 120.91, 114.54, 107.21, 55.60. **4.6b:**³⁵¹ ^1H NMR (400 MHz, CDCl_3) δ 8.03 (s, 1H), 7.72 (m, 1H), 7.69 (m, 2H), 7.30 (m, 1H), 7.06 (m, 1H), 6.43 (s, 1H), 3.87 (s, 3H).

^{13}C NMR (100 MHz, CDCl_3) δ 151.36, 140.10, 131.59, 128.05, 125.31, 121.19, 112.29, 106.20, 55.97.



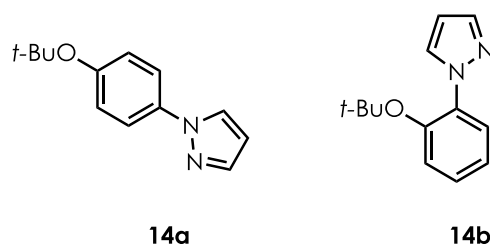
1-(4-(methoxymethoxy)phenyl)-1H-pyrazole (4.12a) and 1-(2-(methoxymethoxy)phenyl)-1H-pyrazole (4.12b).

The title compounds were prepared from **S4** and pyrazole according to **General Method A** with an irradiation time of 20 hours. The crude residue was purified by column chromatography on silica gel with an eluent of 10% to 20% EtOAc/hexanes to yield a pale yellow solid in 52% as an inseparable mixture of **4.12a** and **4.12b**. The *para:ortho* ratio of the mixture was 7.8:1 as determined by ^1H NMR of the isolated product. **4.12a.** ^1H NMR (600 MHz, CDCl_3) δ 7.83 (d, $J = 2.4$ Hz, 1H), 7.69 (d, $J = 1.7$ Hz, 1H), 7.59 (d, $J = 9.0$ Hz, 2H), 7.11 (d, $J = 9.0$ Hz, 2H), 6.43 (d, $J = 2.2$ Hz, 1H), 5.19 (s, 2H), 3.49 (s, 3H). ^{13}C NMR (151 MHz, CDCl_3) δ 155.91, 140.80, 135.03, 126.88, 120.84, 117.08, 107.35, 94.75, 56.15. **4.12b.** ^1H NMR (600 MHz, CDCl_3) δ 8.03 (dd, $J = 2.4, 0.8$ Hz, 1H), 7.74-7.70 (m, 2H), 7.28-7.25 (m, 3H), 6.43 (d, $J = 2.2$ Hz, 1H), 5.19 (s, 2H), 3.42 (s, 3H). ^{13}C NMR (151 MHz, CDCl_3) δ 149.10, 140.24, 135.03, 131.58, 128.16, 125.55, 116.41, 106.38, 95.44, 56.43. **IR** (thin film): 3452.67, 3124.12, 2955.38, 1597.73, 1523.49, 1396.21, 1311.36, 1237.11, 1079.94, 997.98, 752.10; **HRMS**: Calculated for $(\text{M}+\text{H})^+$: 205.0977; found: 205.0970.



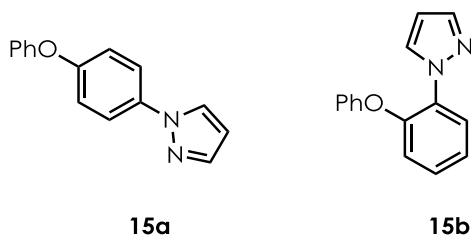
1-(4-((*tert*-butyldimethylsilyl)oxy)phenyl)-1*H*-pyrazole (4.13a) and 1-(2-((*tert*-butyldimethylsilyl)oxy)phenyl)-1*H*-pyrazole (4.13b).

The title compounds were prepared from S5 and pyrazole according to **General Method A** with an irradiation time of 20 hours. The crude residue was purified by column chromatography on silica gel with an eluent of 10% to 20% EtOAc/hexanes to yield a pale yellow oil in 74% as an inseparable mixture of **4.13a** and **4.13b**. The *para:ortho* ratio of the mixture was 9.3:1 as determined by ^1H NMR of the isolated product. **4.13a.** ^1H NMR (600 MHz, CDCl_3) δ 7.83 (s, 1H), 7.70 (s, 1H), 7.56-7.54 (d, $J = 8.1$ Hz, 2H), 6.93-6.92 (d, $J = 8.1$ Hz, 2H), 6.44 (d, $J = 2.1$ Hz, 1H), 1.02 (s, 9H), 0.24 (s, 6H). ^{13}C NMR (151 MHz, CDCl_3) δ 154.11, 140.37, 134.26, 126.57, 120.56, 120.51, 106.93, 25.45, 18.00, -4.65. **4.13b.** ^1H NMR (600 MHz, CDCl_3) δ 7.93 (d, $J = 2.0$ Hz, 1H), 7.70 (s, 1H), 7.63 (d, $J = 7.9$ Hz, 1H), 7.25-7.19 (m, 1H), 7.10-7.05 (m, 1H), 6.99 (dt, $J = 8.1, 1.3$ Hz, 1H), 6.43 (s, 1H), 0.90 (s, 9H), 0.05 (s, 6H). ^{13}C NMR (151 MHz, CDCl_3) δ 147.58, 139.79, 132.08, 131.30, 127.79, 125.88, 121.81, 120.86, 105.79, 25.38, 17.91, -5.02. **IR** (thin film): 2956.34, 2930.31, 2857.99, 1596.77, 1521.56, 1471.42, 1395.25, 1266.04, 913.13, 839.84, 781.99, 747.28; **HRMS**: Calculated for $(\text{M}+\text{H})^+$: 275.1580; found: 275.1575.



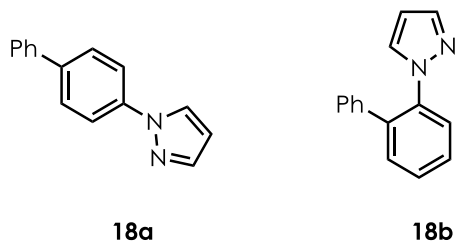
1-(4-(tert-butoxy)phenyl)-1H-pyrazole (4.14a) and 1-(2-(tert-butoxy)phenyl)-1H-pyrazole (4.14b).

The title compounds were prepared from **S6** and pyrazole according to **General Method A** with an irradiation time of 20 hours. The crude residue was purified by column chromatography on silica gel with an eluent of 10% to 20% EtOAc/hexanes to yield a pale yellow solid in 63% as an inseparable mixture of **4.14a** and **4.14b**. The *para:ortho* ratio of the mixture was 6:1 as determined by ^1H NMR of the isolated product. **4.14a.** ^1H NMR (400 MHz, CDCl_3) δ 7.90 (s, 1H), 7.74 (s, 1H), 7.62 (d, $J = 8.4$ Hz, 2H), 7.11 (d, $J = 8.4$ Hz, 2H), 6.48 (s, 1H), 1.41 (s, 9H). ^{13}C NMR (151 MHz, CDCl_3) δ 153.49, 140.43, 135.70, 126.47, 124.62, 119.65, 106.97, 78.58, 28.42. **4.14b.** ^1H NMR (400 MHz, CDCl_3) δ 8.12 (s, 1H), 7.74 (s, 1H), 7.25 (d, $J = 7.8$ Hz, 2H), 7.22-7.19 (m, 2H), 6.46 (s, 1H), 1.17 (s, 9H). ^{13}C NMR (151 MHz, CDCl_3) δ 146.78, 139.72, 135.32, 131.47, 126.86, 125.03, 124.00, 105.73, 80.56, 27.82. **IR** (thin film): 3122.19, 2976.59, 2933.20, 2360.44, 1521.56, 1394.28, 1240.00, 1161.90, 1046.19, 892.88, 750.17; **HRMS**: Calculated for $(\text{M}+\text{Na})^+$: 239.1160; found: 239.1152.



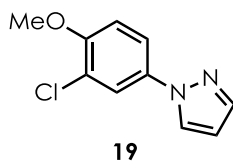
1-(4-phenoxyphenyl)-1H-pyrazole (4.15a) and 1-(2-phenoxyphenyl)-1H-pyrazole (4.15b).

The title compounds were prepared from diphenyl ether and pyrazole according to **General Method A** with an irradiation time of 20 hours. The crude residue was purified by column chromatography on silica gel with an eluent of 10% to 20% EtOAc/hexanes to yield a pale yellow solid in 86% as an inseparable mixture of **4.15a** and **4.15b**. The *para:ortho* ratio of the mixture was 11:1 as determined by ^1H NMR of the isolated product. **4.15a.** ^1H NMR (600 MHz, CDCl_3) δ 7.88 (d, $J = 2.4$ Hz, 1H), 7.73 (d, $J = 1.8$ Hz, 1H), 7.66 (d, $J = 8.9$ Hz, 2H), 7.37 (dd, $J = 8.5, 7.3$ Hz, 2H), 7.14 (td, $J = 7.4, 1.1$ Hz, 1H), 7.11 (d, $J = 8.8$ Hz, 2H), 7.07-7.03 (m, 2H), 6.47 (t, $J = 2.1$ Hz, 1H). ^{13}C NMR (151 MHz, CDCl_3) δ 157.18, 155.80, 141.03, 136.0, 129.96, 126.92, 123.61, 120.98, 119.74, 118.92, 107.60. **4.15b.** ^1H NMR (600 MHz, CDCl_3) δ 8.10 (d, $J = 2.3$ Hz, 1H), 7.94-7.90 (m, 1H), 7.70 (d, $J = 1.7$ Hz, 1H), 7.32 (dd, $J = 8.5, 7.3$ Hz, 2H), 7.27 (d, $J = 3.7$ Hz, 2H), 7.14 (td, $J = 7.4, 1.1$ Hz, 1H), 7.11 (d, $J = 8.8$ Hz, 1H), 6.98 (dd, $J = 7.6, 1.1$ Hz, 2H), 6.38 (d, $J = 2.1$ Hz, 1H). ^{13}C NMR (151 MHz, CDCl_3) δ 156.73, 147.88, 140.55, 132.36, 131.26, 129.61, 127.91, 125.39, 124.60, 120.98, 118.24, 115.54, 106.92. **IR** (thin film): 3056.62, 2359.48, 1589.06, 1521.56, 1488.78, 1395.25, 1236.15, 1046.19, 936.27, 841.78; **HRMS**: Calculated for $(\text{M}+\text{H})^+$: 237.1028; found: 237.1020.



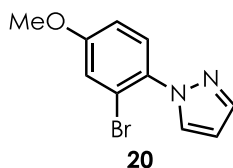
1-([1,1'-biphenyl]-4-yl)-1H-pyrazole (4.18a) and 1-([1,1'-biphenyl]-2-yl)-1H-pyrazole (4.18b).

The title compounds were prepared from biphenyl and pyrazole according to **General Method A** with an irradiation time of 20 hours. The crude residue was purified by column chromatography on silica gel with an eluent of 10% to 20% EtOAc/hexanes to yield a pale yellow solid in 56% as an inseparable mixture of **4.18a** and **4.18b**. The *para:ortho* ratio of the mixture was 7.9:1 as determined by ^1H NMR of the isolated product. **4.18a.** ^1H NMR (600 MHz, CDCl_3) δ 7.97 (s, 1H), 7.79-7.76 (m, 3H), 7.69 (dd, $J = 8.7, 1.9$ Hz, 2H), 7.64-7.62 (m, 2H), 7.48-7.45 (m, 2H), 7.39-7.36 (m, 1H), 6.50 (s, 1H). ^{13}C NMR (151 MHz, CDCl_3) δ 141.29, 140.22, 139.49, 139.44, 128.99, 128.17, 127.61, 127.08, 126.81, 119.5, 107.83. **4.18b.** ^1H NMR (600 MHz, CDCl_3) δ 7.65-7.60 (m, 1H), 7.50-7.44 (m, 2H), 7.32-7.28 (m, 3H), 7.26 (m, 2H), 7.13-7.12 (dd, $J = 6.7, 2.7$ Hz, 2H), 7.08 (m, 1H), 6.20 (q, $J = 1.9$ Hz, 1H). ^{13}C NMR (151 MHz, CDCl_3) δ 140.36, 138.68, 136.78, 131.43, 131.13, 128.64, 128.55, 128.47, 128.35, 127.53, 126.67, 106.48. **IR** (thin film): 3130.87, 3107.72, 2358.52, 1607.38, 1530.24, 1486.85, 1394.28, 1050.05, 836.96, 743.42; **HRMS**: Calculated for $(\text{M}+\text{H})^+$: 221.1079; found: 221.1072.



1-(3-chloro-4-methoxyphenyl)-1H-pyrazole (4.19).

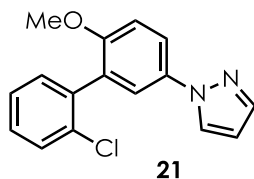
The title compound was prepared from 2-chloroanisole and pyrazole according to **General Method A** with an irradiation time of 44 hours. The crude residue was purified by column chromatography on silica gel with an eluent of 10% to 20% EtOAc/hexanes to give **4.19** as a pale yellow solid in 70% yield. **¹H NMR** (600 MHz, CDCl₃) δ 7.80 (d, *J* = 2.4 Hz, 1H), 7.73 (d, *J* = 2.6 Hz, 1H), 7.68 (d, *J* = 1.8 Hz, 1H), 7.53 (dd, *J* = 9.0, 2.6 Hz, 1H), 6.96 (d, *J* = 8.8 Hz, 1H), 6.43 (s, 1H), 3.91 (s, 3H). **¹³C NMR** (151 MHz, CDCl₃) δ 153.67, 141.07, 134.17, 126.84, 123.20, 121.73, 118.59, 112.40, 107.71, 56.51; **IR** (thin film): 3124.12, 2965.02, 2839.67, 2359.48, 1585.20, 1504.20, 1397.17, 1278.57, 1062.59, 750.17; **HRMS**: Calculated for (M+Na)⁺: 231.0301; found: 231.0294.



1-(2-bromo-4-methoxyphenyl)-1H-pyrazole (4.20).

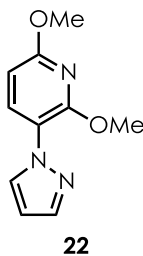
The title compound was prepared from 3-bromoanisole and pyrazole according to **General Method A** with an irradiation time of 44 hours. The crude residue was purified by column chromatography on silica gel with an eluent of 10% to 20% EtOAc/hexanes to give **4.20** as a white solid in 54% yield. **¹H NMR** (600 MHz, CDCl₃) δ 7.71 (dd, *J* = 11.3, 2.1 Hz, 2H), 7.39 (d, *J* = 8.9 Hz, 1H), 7.20 (d, *J* = 2.5 Hz, 1H), 6.93 (dd, *J* = 8.7, 2.5 Hz, 1H), 6.43 (t, *J* = 2.3 Hz, 1H), 3.83 (s, 3H). **¹³C NMR** (151 MHz, CDCl₃) δ 153.71, 141.10, 134.21, 126.85, 123.24, 121.77, 118.62, 112.43, 107.73, 56.55. **IR** (thin film): 3101.94, 2965.02, 2837.74, 1602.56,

1521.56, 1396.21, 1293.04, 1232.29, 1034.62, 850.45, 753.07; **HRMS**: Calculated for (M+H)⁺: 252.9976; found: 252.9971.



1-(2'-chloro-6-methoxy-[1,1'-biphenyl]-3-yl)-1H-pyrazole (4.21).

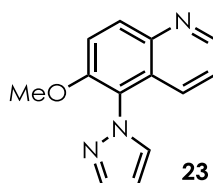
The title compound was prepared from **S7** and pyrazole according to **General Method A** with an irradiation time of 20 hours. The crude residue was purified by column chromatography on silica gel with an eluent of 5% to 10% EtOAc/hexanes to give **4.21** as a white solid in 75% yield. **¹H NMR** (600 MHz, CDCl₃) δ 7.86 (d, *J* = 2.4 Hz, 1H), 7.72 – 7.68 (m, 1H), 7.68 (d, *J* = 2.8 Hz, 1H), 7.52 (d, *J* = 2.8 Hz, 1H), 7.49 – 7.44 (m, 1H), 7.37 – 7.29 (m, 3H), 7.05 (d, *J* = 8.9 Hz, 1H), 6.45 (t, *J* = 2.0 Hz, 1H), 3.83 (s, 3H); **¹³C NMR** (151 MHz, CDCl₃) δ 155.51, 140.85, 136.88, 133.95, 133.70, 131.69, 129.51, 129.43, 129.09, 126.97, 126.69, 122.54, 120.44, 111.64, 107.41, 56.17. **IR** (thin film): 3055.66, 2934.16, 2835.81, 1593.88, 1518.67, 1400.07, 1253.50, 1141.65, 1046.19, 750.17; **HRMS**: Calculated for (M+Na)⁺: 307.0614; found: 307.0606.



2,6-dimethoxy-3-(1H-pyrazol-1-yl)pyridine (22).

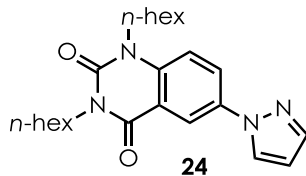
The title compound was prepared from 2,6-dimethoxypyridine and pyrazole according to **General Method A** with an irradiation time of 72 hours. The crude residue was purified by

column chromatography on silica gel with an eluent of hexanes to 10% EtOAc/hexanes to give **4.22** as a white solid in 45% yield. $^1\text{H NMR}$ (600 MHz, CDCl_3) δ 7.98 (d, $J = 2.4$ Hz, 1H), 7.93 (d, $J = 8.4$ Hz, 1H), 7.68 (d, $J = 1.6$ Hz, 1H), 6.45 – 6.37 (m, 2H), 4.02 (s, 3H), 3.96 (s, 3H). $^{13}\text{C NMR}$ (151 MHz, CDCl_3) δ 161.15, 154.17, 140.22, 136.29, 131.06, 117.65, 106.33, 101.58, 54.02, 53.95. **IR** (thin film): 3103.87, 2949.59, 1592.91, 1591.63, 1486.85, 1392.35, 1230.36, 1021.12, 812.85, 753.07; **HRMS**: Calculated for $(\text{M}+\text{Na})^+$: 228.0749; found: 228.0741.



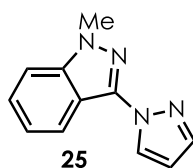
6-methoxy-5-(1H-pyrazol-1-yl)quinoline (4.23).

The title compound was prepared from 6-methoxyquinoline and pyrazole according to **General Method A** with an irradiation time of 20 hours. The crude residue was purified by column chromatography on silica gel with an eluent of 50% to 100% EtOAc/Hexanes to give a yellow oil in 60% yield. $^1\text{H NMR}$ (600 MHz, CDCl_3) δ 8.79 (dt, $J = 4.1, 2.1$ Hz, 1H), 8.21 (d, $J = 9.4$ Hz, 1H), 7.85 (t, $J = 2.1$ Hz, 1H), 7.72-7.62 (m, 2H), 7.58 (d, $J = 9.4$ Hz, 1H), 7.33 (m, 1H), 6.54 (m, 1H), 3.89 (s, 3H). $^{13}\text{C NMR}$ (151 MHz, CDCl_3) δ 152.42, 148.91, 143.37, 140.87, 133.16, 132.07, 131.01, 127.29, 116.62, 106.30, 56.92. **IR** (thin film): 311640, 2941.88, 1618.95, 1506.13, 1398.14, 1325.82, 1267.97, 1091.51, 908.31, 827.31; **HRMS**: Calculated for $(\text{M}+\text{H})^+$: 226.0980; found: 226.0974.



1,3-dihexyl-6-(1H-pyrazol-1-yl)quinazoline-2,4(1H,3H)-dione (4.24).

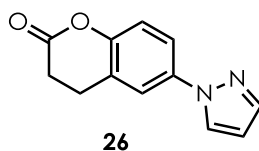
The title compound was prepared from **S12** and pyrazole according to **General Method A** with an irradiation time of 20 hours. The crude residue was purified by column chromatography on silica gel with an eluent of 10% to 20% EtOAc/hexanes to yield a pale yellow oil in 43% as an inseparable mixture of pyrazole addition at the 6 and 8 positions. The ratio of 6-pyrazolyl to 8-pyrazolyl products was determined by ^1H NMR of the isolated product to be greater than 15:1. ^1H NMR (600 MHz, CDCl_3) δ 8.36 (d, $J = 3.0$ Hz, 1H), 8.18-8.17 (m, 1H), 8.00 (d, $J = 2.9$ Hz, 1H), 7.73 (s, 1H), 7.27-7.26 (m, 1H), 6.49 (s, 1H), 4.14-4.07 (m, 4H), 1.73-1.68 (m, 4H), 1.44-1.32 (m, 12H), 0.97-0.84 (m, 6H). ^{13}C NMR (151 MHz, CDCl_3) δ 161.22, 150.43, 141.43, 137.96, 135.49, 126.77, 126.43, 117.76, 116.27, 115.05, 108.17, 44.04, 42.19, 31.54, 31.49, 27.78, 27.36, 26.68, 26.49, 22.60, 14.09, 14.04. IR (thin film): 3122.19, 2930.31, 2857.99, 1703.80, 1659.45, 1524.45, 1480.10, 1394.28, 1045.23, 752.10; HRMS: Calculated for $(\text{M}+\text{Na})^+$: 419.2423; found: 419.2416.



1-methyl-3-(1H-pyrazol-1-yl)-1H-indazole (4.25).

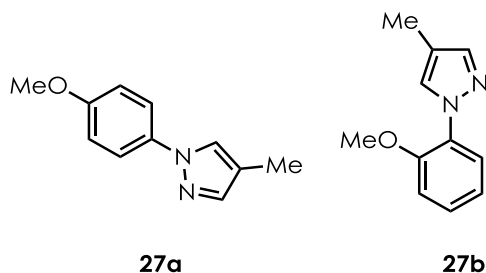
The title compound was prepared from 1-methylindazole (**S8**) and pyrazole according to **General Method A** with an irradiation time of 24 hours. The crude residue was purified by column chromatography on silica gel with an eluent of 10% to 75% EtOAc/hexanes to give **4.25**

as a pale yellow oil in 43%. $^1\text{H NMR}$ (600 MHz, CDCl_3) δ 8.32 (dt, $J = 8.3, 1.0$ Hz, 1H), 8.25 (d, $J = 2.5$ Hz, 1H), 7.81 (d, $J = 2.0$ Hz, 1H), 7.45 (ddd, $J = 8.3, 6.8, 1.1$ Hz, 1H), 7.36 (d, $J = 8.6$ Hz, 1H), 7.24-7.16 (m, 1H), 6.49 (t, $J = 2.1$ Hz, 1H), 4.05 (s, 3H). $^{13}\text{C NMR}$ (151 MHz, CDCl_3) δ 141.68, 141.42, 127.84, 127.58, 122.63, 121.37, 115.20, 109.01, 107.01, 35.65. **IR** (thin film): 3124.12, 3063.37, 2936.09, 1617.98, 1549.52, 1397.17, 1256.40, 1043.30, 919.88, 743.43; **HRMS**: Calculated for $(\text{M}+\text{Na})^+$: 221.0803; found: 221.0796.



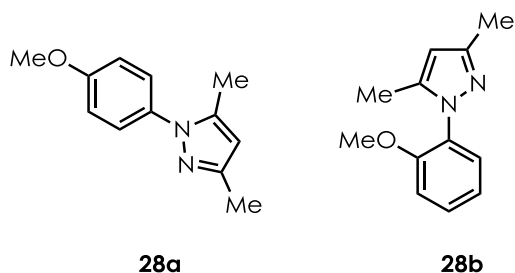
6-(1*H*-pyrazol-1-yl)chroman-2-one (4.26).

The title compound was prepared according to **General Method A** with the following modifications to the procedure: 2 equivalents of 3,4-dihydrocoumarin (1.0 mmol) and 1 equivalent of pyrazole (0.5 mmol) with Catalyst B (0.025 mmol) in DCE (0.1 M) without a cooling fan and with an irradiation time of 44 hours. The title compound was purified by column chromatography on silica gel (25% to 50% EtOAc/Hexanes) to give a yellow solid in 30% yield. $^1\text{H NMR}$ (600 MHz, CDCl_3) δ 7.87 (d, $J = 2.5$ Hz, 1H), 7.71 (d, $J = 1.7$ Hz, 1H), 7.60 (d, $J = 2.6$ Hz, 1H), 7.51 (dd, $J = 8.7, 2.6$ Hz, 1H), 7.11 (d, $J = 8.7$ Hz, 1H), 6.47 (t, $J = 2.2$ Hz, 1H), 3.06 (dd, $J = 8.3, 6.3$ Hz, 2H), 2.81 (dd, $J = 8.3, 6.2$ Hz, 2H). $^{13}\text{C NMR}$ (151 MHz, CDCl_3) δ 168.06, 150.33, 141.28, 136.73, 126.86, 123.94, 119.25, 118.90, 117.85, 107.90, 29.03, 23.93.; **IR** (thin film): 3127.01, 2918.73, 1769.37, 1600.63, 1502.28, 1395.25, 1343.18, 1217.83, 1144.55, 899.63; **HRMS**: Calculated for $(\text{M}+\text{H})^+$: 215.0820; found: 201.0813.



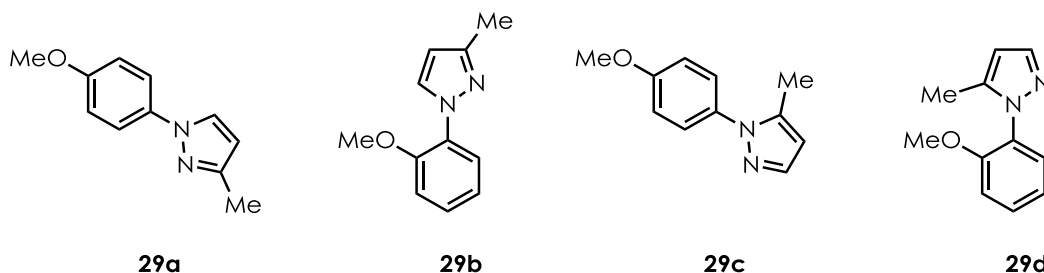
1-(4-methoxyphenyl)-4-methyl-1H-pyrazole (4.27a), 1-(2-methoxyphenyl)-4-methyl-1H-pyrazole (4.27b).

The title compounds were prepared from anisole and 4-methylpyrazole according to **General Method A** with an irradiation time of 20 hours. The crude residue was purified by column chromatography on silica gel with an eluent of hexanes to 20% EtOAc/hexanes to yield a colorless solid in 68% as an inseparable mixture of **4.27a** and **4.27b** in a ratio of 8:1. **4.27a.** ¹H NMR (600 MHz, CDCl₃) δ 7.59 (s, 1H), 7.54 (d, *J* = 9.0 Hz, 2H), 7.49 (s, 1H), 6.94 (d, *J* = 9.0 Hz, 2H), 3.82 (s, 3H), 2.14 (s, 3H). ¹³C NMR (151 MHz, CDCl₃) δ 157.96, 141.30, 134.23, 125.55, 120.44, 117.84, 114.52, 55.61, 9.03. **4.27b.** ¹H NMR (600 MHz, CDCl₃) δ 7.80 (s, 1H), 7.68 (dd, *J* = 7.9, 1.5 Hz, 1H), 7.51 (s, 1H), 7.27 – 7.24 (m, 1H), 7.06 – 7.00 (m, 2H), 3.86 (s, 3H), 2.16 (s, 3H). ¹³C NMR (151 MHz, CDCl₃) δ 151.21, 140.89, 130.24, 130.00, 127.70, 125.05, 121.21, 116.69, 112.27, 55.97, 9.08. **IR** (thin film): 2966.95, 2839.67, 1519.63, 1455.03, 1261.22, 1181.19, 1041.37, 953.63, 829.24, 610.36; **HRMS**: Calculated for (M+Na)⁺: 211.0847; found: 211.0842.



1-(4-methoxyphenyl)-3,5-dimethyl-1H-pyrazole (4.28a), 1-(2-methoxyphenyl)-3,5-dimethyl-1H-pyrazole (4.28b).

The title compounds were prepared from anisole and 4-methylpyrazole according to **General Method A** with an irradiation time of 20 hours. The crude residue was purified by column chromatography on silica gel with an eluent of hexanes to 15% EtOAc/hexanes to yield an oily solid in 85% as an inseparable mixture of **4.28a** and **4.28b** in a ratio of 7.5:1. **4.28a.** ³⁵² **¹H NMR** (600 MHz, CDCl₃) δ 7.32 (d, *J* = 8.9 Hz, 2H), 6.95 (d, *J* = 8.9 Hz, 2H), 5.96 (s, 1H), 3.84 (s, 3H), 2.29 (s, 3H), 2.24 (s, 3H). ¹³**C NMR** (151 MHz, CDCl₃) δ 158.87, 148.63, 139.57, 133.22, 126.49, 114.21, 106.35, 55.64, 13.64, 12.28. **4.28b.** ³⁵³ **¹H NMR** (600 MHz, CDCl₃) δ 7.38 (td, *J* = 8.0, 1.7 Hz, 1H), 7.33 – 7.32 (m, 1H), 7.04 – 6.99 (m, 2H), 5.96 (s, 1H), 3.79 (s, 3H), 2.30 (s, 3H), 2.09 (s, 3H). ¹³**C NMR** (151 MHz, CDCl₃) δ 154.77, 149.03, 141.56, 130.00, 129.37, 128.79, 120.90, 111.97, 105.27, 55.88, 13.80, 11.39.

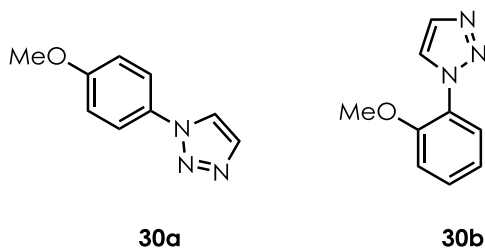


1-(4-methoxyphenyl)-3-methyl-1H-pyrazole (4.29a), 1-(2-methoxyphenyl)-3-methyl-1H-pyrazole (4.29b), 1-(4-methoxyphenyl)-5-methyl-1H-pyrazole (4.29c), 1-(2-methoxyphenyl)-5-methyl-1H-pyrazole (4.29d).

The title compounds were prepared from anisole and 3-methylpyrazole according to **General Method A** with an irradiation time of 20 hours. The crude residue was purified by column chromatography on silica gel with an eluent of hexanes to 50% EtOAc/hexanes from which were isolated two sets of fractions. The first contained an inseparable mixture of *N2* isomers **4.29a** and **4.29b** in 57% yield and a 6:1 ratio. The second contained an inseparable mixture of *N3* isomers **4.29c** and **4.29d** in 16% yield and a 8:1 ratio. The spectral data for the known compounds **4.29b**,³⁵³ **4.29c**,³⁵⁴ and **4.29d**³⁵⁵ were consistent with the literature reports.

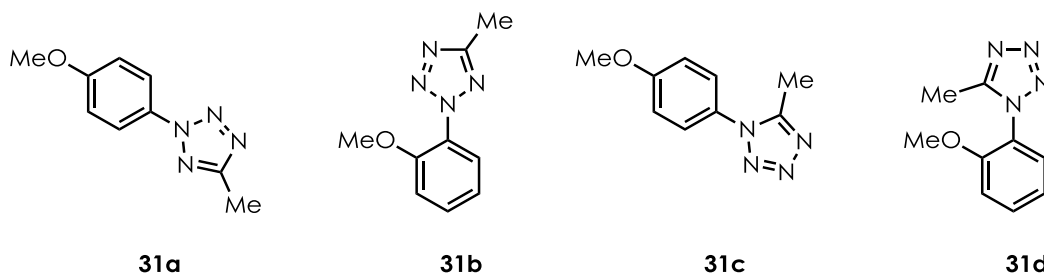
4.29a. ¹H NMR (600 MHz, CDCl₃) δ 7.70 (s, 1H), 7.54 (d, *J* = 8.9 Hz, 2H), 6.94 (d, *J* = 8.9 Hz, 2H), 6.20 (s, 1H), 3.82 (s, 3H), 2.37 (s, 3H). ¹³C NMR (151 MHz, CDCl₃) δ 157.86, 150.00, 134.09, 127.43, 120.53, 114.43, 106.99, 55.53, 13.72. **4.29b.** ¹H NMR (600 MHz, CDCl₃) δ 7.92 (d, *J* = 2.2 Hz, 1H), 7.72 – 7.69 (m, 1H), 7.26 – 7.22 (m, 1H), 7.07 – 6.99 (m, 2H), 6.21 – 6.20 (m, 1H), 3.85 (s, 3H), 2.38 (s, 3H). ¹³C NMR (151 MHz, CDCl₃) δ 151.16, 149.33, 132.31, 129.79, 127.54, 125.07, 121.13, 112.16, 106.14, 55.89, 13.67. **IR** (thin film): 3459.67, 2932.23, 1646.91, 1515.77, 1456.96, 1363.43, 1247.72, 1181.19, 1045.23, 830.21 **HRMS**: Calculated for (M+Na)⁺: 211.0847; found: 211.0841.

4.29c. $^1\text{H NMR}$ (600 MHz, CDCl_3) δ 7.54 (d, $J = 1.6$ Hz, 1H), 7.34 (d, $J = 8.9$ Hz, 2H), 6.97 (d, $J = 8.9$ Hz, 2H), 6.17 (d, $J = 1.3$ Hz, 1H), 3.85 (s, 3H), 2.29 (s, 3H). $^{13}\text{C NMR}$ (151 MHz, CDCl_3) δ 159.09, 139.59, 138.82, 133.17, 126.53, 114.27, 106.42, 55.66, 12.34. **4.29d.** $^1\text{H NMR}$ (600 MHz, CDCl_3) δ 7.59 (d, $J = 1.6$ Hz, 1H), 7.43 – 7.39 (m, 1H), 7.33 – 7.31 (m, 1H), 7.07 – 7.01 (m, 2H), 6.17 – 6.16 (m, 1H), 3.79 (s, 3H), 2.15 (s, 3H). $^{13}\text{C NMR}$ (151 MHz, CDCl_3) δ 154.81, 140.75, 140.00, 130.26, 129.24, 120.92, 112.12, 105.30, 55.93, 11.41.



1-(4-methoxyphenyl)-1H-1,2,3-triazole (4.30a), 1-(2-methoxyphenyl)-1H-1,2,3-triazole (4.30b).

The title compounds were prepared from anisole and 1,2,3-triazole according to **General Method A** with an irradiation time of 20 hours. The crude residue was purified by column chromatography on silica gel with an eluent of hexanes to 15% EtOAc/hexanes to yield a colorless solid in 71% as an inseparable mixture of **4.30a** and **4.30b** in a ratio of 3.5:1. The analytical data matches those reported in the literature for **4.30a** and **4.30b**.³⁵⁶ **4.30a.** $^1\text{H NMR}$ (600 MHz, CDCl_3) δ 7.91 (s, 1H), 7.83 (s, 1H), 7.64 (d, $J = 8.8$ Hz, 2H), 7.03 (d, $J = 8.8$ Hz, 2H), 3.88 (s, 3H). $^{13}\text{C NMR}$ (151 MHz, CDCl_3) δ 159.95, 134.42, 122.46, 121.98, 114.91, 112.38, 55.77. **4.30b.** $^1\text{H NMR}$ (600 MHz, CDCl_3) δ 8.12 (s, 1H), 7.81 (s, 1H), 7.78 (d, $J = 7.9$ Hz, 1H), 7.43 (t, $J = 7.9$ Hz, 1H), 7.14 – 7.05 (m, 2H), 3.89 (s, 3H). $^{13}\text{C NMR}$ (151 MHz, CDCl_3) δ 151.31, 141.52, 133.39, 131.66, 130.64, 130.20, 125.74, 121.37, 56.11.

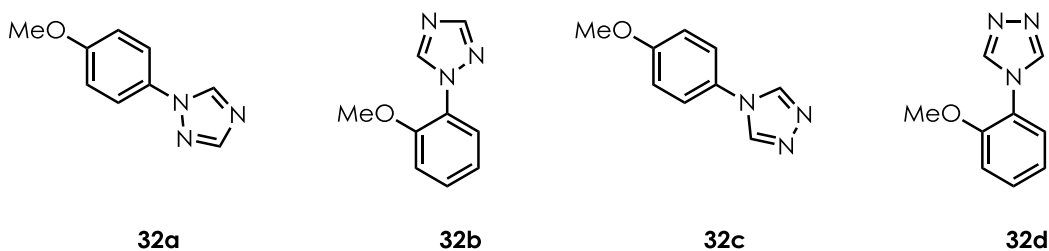


2-(4-methoxyphenyl)-5-methyl-2H-tetrazole (4.31a), 2-(2-methoxyphenyl)-5-methyl-2H-tetrazole (4.31b), 1-(4-methoxyphenyl)-5-methyl-1H-tetrazole (4.31c), 1-(2-methoxyphenyl)-5-methyl-1H-tetrazole (4.31d).

The title compounds were prepared from anisole and 5-methyltetrazole according to **General Method A** with an irradiation time of 20 hours and the modification that 1.25 equiv. 5-methyltetrazole were employed. The crude residue was purified by column chromatography on silica gel with an eluent of hexanes to 50% EtOAc/hexanes to EtOAc from which were isolated two sets of fractions. The first contained an inseparable mixture of *N*2 isomers **4.31a** and **4.31b** in 23% yield and a 1.7:1 ratio. The second contained an inseparable mixture of *N*3 isomers **31c** and **4.31d** in 39% yield and 2.1:1 ratio. The spectral data for the known compounds **4.31a**,³⁵⁷ **4.31c**,³⁵⁸ and **4.31d**³⁵⁸ are consistent with the literature reports. **4.31a.** ¹H NMR (600 MHz, CDCl₃) δ 8.00 (d, *J* = 9.1 Hz, 2H), 7.03 (d, *J* = 9.1 Hz, 2H), 3.88 (s, 3H), 2.62 (s, 3H). ¹³C NMR (151 MHz, CDCl₃) δ 163.11, 160.48, 130.61, 121.40, 114.77, 55.79, 11.13. **4.31b.** ¹H NMR (600 MHz, CDCl₃) δ 7.58 – 7.46 (m, 2H), 7.18 – 7.06 (m, 2H), 3.87 (s, 3H), 2.66 (s, 3H). ¹³C NMR (151 MHz, CDCl₃) δ 162.96, 153.55, 132.00, 127.12, 126.51, 120.84, 112.80, 56.38, 11.16. **IR** (thin film): 2943.80, 2840.63, 1732.73, 1646.91, 1507.10, 1456.96, 1418.39, 1254.47, 1023.05, 837.92; **HRMS**: Calculated for (M+H)⁺: 191.0933; found: 191.0927.

4.31c. ¹H NMR (600 MHz, CDCl₃) δ 7.35 (d, *J* = 7.4 Hz, 2H), 7.05 (d, *J* = 7.3 Hz, 2H), 3.87 (s, 3H), 2.55 (s, 3H). ¹³C NMR (151 MHz, CDCl₃) δ 160.93, 151.78, 126.54, 126.16,

115.07, 55.80, 9.71. **4.31d**. $^1\text{H NMR}$ (600 MHz, CDCl_3) δ 7.54 (t, $J = 8.0$ Hz, 1H), 7.35 – 7.32 (m, 1H), 7.12 – 7.09 (m, 2H), 3.81 (s, 3H), 2.42 (s, 3H). $^{13}\text{C NMR}$ (151 MHz, CDCl_3) δ 153.72, 153.41, 132.44, 128.09, 122.38, 121.23, 112.43, 55.99, 9.12.

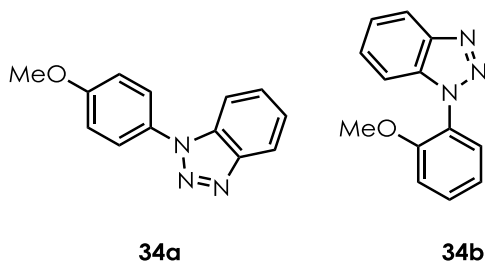


1-(4-methoxyphenyl)-1H-1,2,4-triazole (4.32a), **1-(2-methoxyphenyl)-1H-1,2,4-triazole (4.32b)**, **4-(4-methoxyphenyl)-4H-1,2,4-triazole (4.32c)**, **4-(2-methoxyphenyl)-4H-1,2,4-triazole (4.32d)**.

The title compounds were prepared from anisole and 1,2,4-triazole according to **General Method A** with an irradiation time of 20 hours. The crude residue was purified by column chromatography on silica gel with an eluent of 50% EtOAc/hexanes to 5% MeOH/EtOAc from which were isolated two sets of fractions. The first contained a mixture of *N1* isomers **4.32a** and **4.32b** in 36% yield and a 4.5:1 ratio, but which was separable by additional chromatography. The second contained an inseparable mixture of *N4* isomers **4.32c** and **4.32d** in 40% yield and a 4:1 ratio. The spectral data for the known compounds **4.32a**³⁵⁹ and **4.32b**³⁵⁹ are consistent with the literature reports. Although **4.32c** was reportedly synthesized,³⁶⁰ the analytical data provided by the authors appeared identical to those reported for compound **4.32a**. We provide a correct assignment for **4.32c** with the corresponding spectral data. **4.32a**. $^1\text{H NMR}$ (600 MHz, CDCl_3) δ 8.44 (s, 1H), 8.07 (s, 1H), 7.56 (d, $J = 8.9$ Hz, 2H), 7.00 (d, $J = 8.9$ Hz, 2H), 3.85 (s, 3H). $^{13}\text{C NMR}$ (151 MHz, CDCl_3) δ 159.56, 152.48, 140.90, 130.56, 121.98, 114.92, 55.74. **4.32b**. ^1H

NMR (600 MHz, CDCl₃) δ 8.74 (s, 1H), 8.07 (s, 1H), 7.77 (dd, *J* = 7.9, 1.3 Hz, 1H), 7.39 – 7.32 (m, 1H), 7.10 – 7.07 (m, 2H), 3.92 (s, 3H). **¹³C NMR** (151 MHz, CDCl₃) δ 151.40, 151.04, 144.71, 129.21, 126.44, 124.66, 121.45, 112.31, 56.11.

4.32c. **¹H NMR** (600 MHz, CDCl₃) δ 8.38 (s, 2H), 7.29 (d, *J* = 8.9 Hz, 2H), 7.01 (d, *J* = 8.9 Hz, 2H), 3.85 (s, 3H). **¹³C NMR** (151 MHz, CDCl₃) δ 160.20, 142.01, 126.78, 124.15, 115.41, 55.82. **4.32d.** **¹H NMR** (600 MHz, CDCl₃) δ 8.40 (s, 2H), 7.44 – 7.41 (m, 1H), 7.28 – 7.27 (m, 1H), 7.09 – 7.05 (m, 2H), 3.85 (s, 3H). **¹³C NMR** (151 MHz, CDCl₃) δ 152.42, 143.02, 130.55, 125.26, 121.35, 112.58, 56.04. **IR** (thin film): 3438.46, 3139.54, 1536.99, 2836.77, 1457.92, 1269.90, 1256.40, 1097.30, 1032.69, 831.17; **HRMS**: Calculated for (M+H)⁺: 176.0824; found: 176.0817.

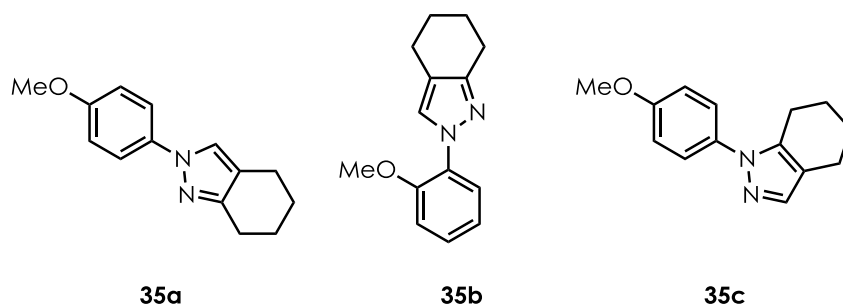


1-(4-methoxyphenyl)-1H-benzo[d][1,2,3]triazole (4.34a), 1-(2-methoxyphenyl)-1H-benzo[d][1,2,3]triazole (4.34b).

The title compounds were prepared from anisole and 1,2,3-benzotriazole according to **General Method A** with an irradiation time of 20 hours. The crude residue was purified by column chromatography on silica gel with an eluent of 5% EtOAc/hexanes to 10% EtOAc/hexanes to yield a colorless solid in 57% yield as an inseparable mixture of **4.34a** and **4.34b** in a ratio of 3:1. The analytical data matches those reported in the literature for **4.34a**.³⁶¹

4.34a. **¹H NMR** (600 MHz, CDCl₃) δ 8.14 (d, *J* = 8.4 Hz, 1H), 7.68 (app d, *J* = 8.9 Hz, 3H), 7.54 (t, *J* = 8.0 Hz, 1H), 7.43 (t, *J* = 7.6 Hz, 1H), 7.12 (d, *J* = 8.9 Hz, 2H), 3.92 (s, 3H). **¹³C NMR**

(151 MHz, CDCl₃) δ 159.88, 146.36, 132.70, 130.04, 128.10, 124.67, 124.32, 120.25, 115.04, 110.33, 55.75. **4.34b**. ¹H NMR (600 MHz, CDCl₃) δ 8.12 (d, *J* = 8.2 Hz, 1H), 7.55 – 7.49 (m, 2H), 7.49 – 7.44 (m, 1H), 7.37 (app t, *J* = 7.4 Hz, 2H), 7.17 – 7.12 (m, 2H), 3.79 (s, 3H). ¹³C NMR (151 MHz, CDCl₃) δ 153.75, 145.74, 134.14, 131.11, 128.19, 127.62, 125.35, 123.92, 121.16, 119.91, 112.43, 111.27, 55.88. IR (thin film): 3064.33, 2934.16, 2358.52, 1613.16, 1517.70, 1454.06, 1253.50, 1067.41, 833.41, 746.32; HRMS: Calculated for (M+H)⁺: 226.0980; found: 226.0975.

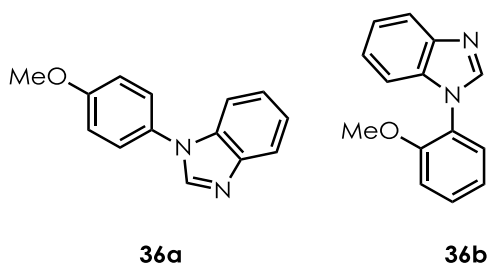


2-(4-methoxyphenyl)-4,5,6,7-tetrahydro-2H-indazole (4.35a), 2-(2-methoxyphenyl)-4,5,6,7-tetrahydro-2H-indazole (4.35b), 1-(4-methoxyphenyl)-4,5,6,7-tetrahydro-1H-indazole (4.35c).

The title compounds were prepared from anisole and 4,5,6,7-tetrahydroindazole according to **General Method A** with an irradiation time of 20 hours. The crude residue was purified by column chromatography on silica gel with an eluent of 5% EtOAc/hexanes to 25% EtOAc/hexanes from which were isolated two sets of fractions. The first contained an inseparable mixture of *N*2 isomers **4.35a** and **4.35b** in 25% yield and a 10:1 ratio. The second contained *N*1 isomer **4.35c** as a single compound in 26% yield. The spectral data for the known compound **4.35c**³⁶² are consistent with the literature report. **4.35a**. ¹H NMR (600 MHz, CDCl₃) δ 7.54 – 7.49 (m, 3H), 6.93 (d, *J* = 9.0 Hz, 2H), 3.82 (s, 3H), 2.77 (t, *J* = 6.3 Hz, 2H), 2.61 (t, *J* =

6.2 Hz, 2H), 1.93 – 1.81 (m, 2H), 1.81 – 1.72 (m, 2H); ^{13}C NMR (151 MHz, CDCl_3) δ 157.72, 150.82, 134.46, 123.93, 120.37, 117.84, 114.50, 55.64, 23.63, 23.61, 20.80. **4.35b.** ^1H NMR (600 MHz, CDCl_3) δ 7.72 (s, 1H), 7.68 (dd, $J = 7.9, 1.6$ Hz, 1H), 7.25 – 7.21 (m, 1H), 7.04 – 6.99 (m, 2H), 3.87 (s, 2H), 2.80 – 2.74 (m, 2H), 2.64 – 2.58 (m, 2H), 1.87 – 1.83 (m, 2H), 1.79 – 1.75 (m, 2H). ^{13}C NMR (151 MHz, CDCl_3) δ 151.09, 150.18, 130.19, 128.64, 127.27, 125.02, 121.23, 116.86, 112.15, 55.98, 23.66, 23.58, 20.85. IR (thin film): 2932.23, 2853.17, 1517.70, 1456.96, 1377.89, 1254.47, 1023.05, 837.92; HRMS: Calculated for $(\text{M}+\text{H})^+$: 251.1160; found: 251.1154.

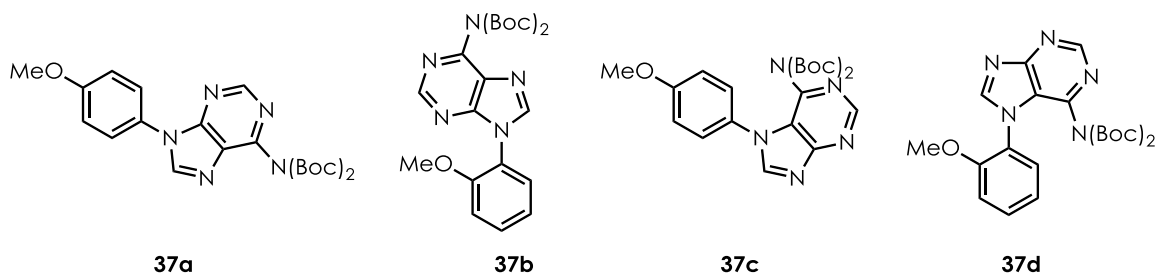
4.35c. ^1H NMR (600 MHz, CDCl_3) δ 7.43 (s, 1H), 7.38 (d, $J = 8.9$ Hz, 2H), 6.95 (d, $J = 8.9$ Hz, 2H), 3.84 (s, 3H), 2.66 (t, $J = 5.8$ Hz, 2H), 2.58 (t, $J = 5.7$ Hz, 2H), 1.82 – 1.75 (m, 4H). ^{13}C NMR (151 MHz, CDCl_3) δ 158.46, 138.40, 138.29, 133.56, 124.84, 117.34, 114.29, 55.67, 23.47, 23.27, 23.03, 20.88.



1-(4-methoxyphenyl)-1H-benzo[d]imidazole (4.36a), 1-(2-methoxyphenyl)-1H-benzo[d]imidazole (4.36b).

The title compounds were prepared from anisole and benzimidazole according to **General Method A** with an irradiation time of 20 hours. The crude residue was purified by column chromatography on silica gel with an eluent of 25% EtOAc/hexanes to 75% EtOAc/hexanes to yield a colorless solid in 72% yield as an inseparable mixture of **4.36a** and

4.36b in a ratio of 5:1. The analytical data matches those reported in the literature for **36a**³⁶³ and **4.36b**.³⁶³ **4.36a.** ¹H NMR (600 MHz, CDCl₃) δ 8.04 (s, 1H), 7.88 – 7.86 (m, 1H), 7.45 – 7.44 (m, 1H), 7.40 (d, *J* = 8.9 Hz, 2H), 7.28 – 7.33 (m, 2H), 7.06 (d, *J* = 8.9 Hz, 2H), 3.87 (s, 3H). ¹³C NMR (151 MHz, CDCl₃) δ 159.37, 143.90, 142.62, 134.29, 129.20, 125.77, 123.57, 122.63, 120.55, 115.17, 110.40, 55.71. **4.36b.** ¹H NMR (600 MHz, CDCl₃) δ 8.07 (s, 1H), 7.88 – 7.86 (m, 1H), 7.45 – 7.42 (m, 1H), 7.41 – 7.39 (m, 1H), 7.33 – 7.27 (m, 3H), 7.13 – 7.08 (m, 2H), 3.78 (s, 3H). ¹³C NMR (151 MHz, CDCl₃) δ 154.00, 143.39, 134.50, 129.78, 127.31, 124.84, 123.29, 122.37, 121.07, 120.30, 112.50, 110.81, 55.79.



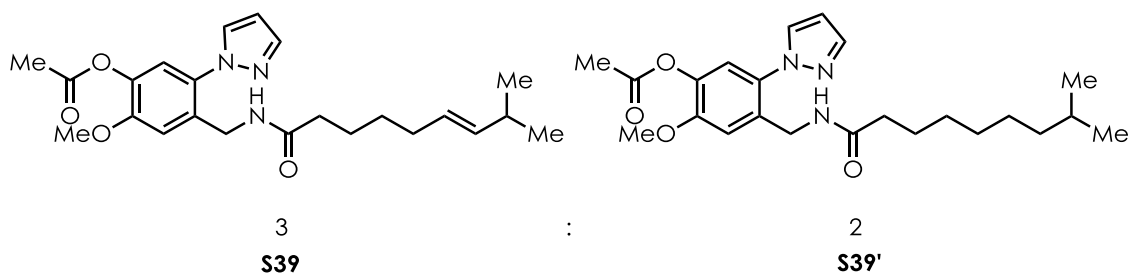
9-(4-methoxyphenyl)-N₆,N₉-bis(*tert*-butoxycarbonyl)-9*H*-purin-6-amine (4.37a), 9-(2-methoxyphenyl)-N₆,N₉-bis(*tert*-butoxycarbonyl)-9*H*-purin-6-amine (4.37b), 7-(4-methoxyphenyl)-N₆,N₇-bis(*tert*-butoxycarbonyl)-7*H*-purin-6-amine (4.37c), 7-(2-methoxyphenyl)-N₆,N₇-bis(*tert*-butoxycarbonyl)-7*H*-purin-6-amine (4.37d).

The title compounds were prepared from anisole and Boc₂-adenine **S10** according to **General Method A** with an irradiation time of 20 hours and the modification that 1.25 equiv. **S10** were employed. The crude residue was purified by column chromatography on silica gel with an eluent of hexanes to 50% EtOAc/hexanes to EtOAc from which were isolated two sets of fractions. The first contained an inseparable mixture of *N*₉ isomers **4.37a** and **4.37b** in 47% yield and a 3:1 ratio. The second contained an inseparable mixture of *N*₇ isomers **4.37c** and **4.37d** in

52% yield and 4:1 ratio. **4.37a.** $^1\text{H NMR}$ (600 MHz, CDCl_3) δ 8.91 (s, 1H), 8.28 (s, 1H), 7.59 (d, $J = 8.9$ Hz, 2H), 7.10 (d, $J = 8.9$ Hz, 2H), 3.89 (s, 3H), 1.49 (s, 18H). $^{13}\text{C NMR}$ (151 MHz, CDCl_3) δ 159.66, 153.69, 153.49, 153.10, 152.61, 152.45, 150.64, 150.49, 150.33, 143.94, 130.52, 129.01, 128.41, 127.47, 126.86, 125.18, 122.29, 121.08, 115.06, 112.33, 83.79, 83.68, 55.61, 27.75, 27.74. **4.37b.** $^1\text{H NMR}$ (600 MHz, CDCl_3) δ 8.87 (s, 1H), 8.28 (s, 1H), 7.57 (d, $J = 5.9$ Hz, 1H), 7.48 (t, $J = 7.9$ Hz, 1H), 7.18 – 7.11 (m, 2H), 3.80 (s, 3H), 1.48 (s, 18H). $^{13}\text{C NMR}$ (151 MHz, CDCl_3) δ 153.69, 153.49, 152.45, 150.33, 145.86, 130.52, 128.41, 126.86, 125.12, 122.29, 121.08, 112.33, 83.68, 55.80, 27.74. **IR** (thin film): 2979.48, 2935.13, 1790.58, 1758.76, 1595.81, 1519.63, 1455.99, 1340.28, 1140.69; **HRMS**: Calculated for $(\text{M}+\text{H})^+$: 442.2090; found: 442.2087.

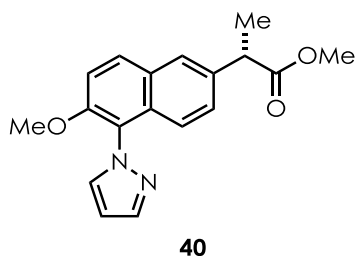
4.37c. $^1\text{H NMR}$ (600 MHz, CDCl_3) δ 9.08 (s, 1H), 8.28 (s, 1H), 7.33 (d, $J = 8.8$ Hz, 2H), 6.99 (d, $J = 8.8$ Hz, 2H), 3.87 (s, 3H), 1.30 (s, 18H). $^{13}\text{C NMR}$ (151 MHz, CDCl_3) δ 163.68, 160.48, 153.06, 149.84, 148.71, 144.26, 127.70, 126.88, 121.51, 115.00, 84.15, 55.83, 27.93.

4.37d. $^1\text{H NMR}$ (600 MHz, CDCl_3) δ 9.06 (s, 1H), 8.33 (s, 1H), 7.48 (t, $J = 8.0$ Hz, 1H), 7.36 – 7.33 (m, 1H), 7.10 – 7.04 (m, 2H), 3.79 (s, 3H), 1.30 (s, 18H). $^{13}\text{C NMR}$ (151 MHz, CDCl_3) δ 163.49, 153.79, 152.77, 150.13, 144.08, 131.04, 127.65, 125.32, 123.49, 121.34, 121.03, 112.41, 83.94, 55.92, 27.85. **IR** (thin film): 3077.83, 2980.45, 2935.13, 2237.99, 1739.48, 1768.40, 1613.16, 1515.77, 1369.21, 1252.54; **HRMS**: Calculated for $(\text{M}+\text{Na})^+$: 464.1910; found: 464.1910.



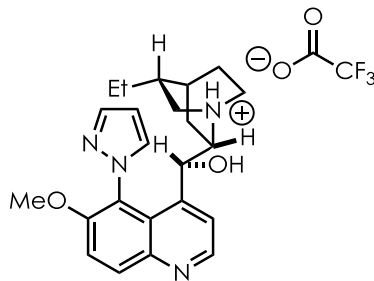
(*E*)-2-methoxy-4-((8-methylnon-6-enamido)methyl)-5-(1*H*-pyrazol-1-yl)phenyl acetate (4.39/4.39').

The title compounds were prepared from anisole and *O*-acetylcapsaicin **S13/S13'** according to **General Method A** with the modification that 1.25 equiv. **S13** were employed for an irradiation time of 40 hours. The crude residue was purified by column chromatography on silica gel with an eluent of hexanes to 75% EtOAc/hexanes giving a white solid in 66% yield. Note: The product contains the same ratio of unsaturated to saturated capsaicin analogues as the starting material **S13/S13'** (~3:2). The provided proton NMR peak list below refers only to the unsaturated product **4.39**; see spectrum for peaks corresponding to saturated product **4.39'**. **¹H NMR** (600 MHz, CDCl₃) δ 7.70 (s, 1H), 7.64 (d, *J* = 2.3 Hz, 1H), 7.19 (d, *J* = 1.9 Hz, 1H), 7.01 (s, 1H), 6.92 (t, *J* = 6.0 Hz, 1H), 6.45 (t, *J* = 2.1 Hz, 1H), 5.38 – 5.28 (m, 2H), 4.23 (d, *J* = 6.3 Hz, 2H), 3.87 (s, 3H), 2.32 (s, 3H), 2.20 – 2.14 (m, 2H), 1.97 (q, *J* = 7.0 Hz, 2H), 1.62 – 1.58 (m, 2H), 1.50 (hept, *J* = 6.7 Hz, 1H), 1.36 (p, *J* = 7.6 Hz, 2H), 0.94 (d, *J* = 6.7 Hz, 6H). **¹³C NMR** (151 MHz, CDCl₃) δ 172.95, 172.83, 168.87, 151.09, 140.87, 138.84, 138.08, 133.08, 132.50, 130.75, 126.75, 119.88, 115.31, 107.11, 100.12, 56.47, 40.00, 39.10, 37.10, 36.96, 32.41, 31.11, 29.77, 29.46, 29.42, 28.09, 27.39, 25.76, 25.27, 22.80, 22.78, 20.75. **IR** (thin film): 3288.04, 2928.38, 2865.70, 1768.40, 1649.80, 1521.56, 1368.25, 1206.26, 1039.44, 755.00; **HRMS**: Calculated for (M+Na)⁺: 436.2213 and 438.2369; found: 436.2200 and 438.2363.



(S)-methyl 2-(6-methoxy-5-(1*H*-pyrazol-1-yl)naphthalen-2-yl)propanoate (4.40).

The title compounds were prepared from pyrazole and naproxen methyl ester **S9** according to **General Method A** with an irradiation time of 20 hours and the modification that 4.0 equiv. of pyrazole were employed. The crude residue was purified by column chromatography on silica gel (25% to 50% EtOAc/Hexanes) to yield a yellow solid in 26%. **¹H NMR** (600 MHz, CDCl₃) δ 7.92 (d, *J* = 9.1 Hz, 1H), 7.86 (d, *J* = 2.0 Hz, 1H), 7.72 (d, *J* = 2.0 Hz, 2H), 7.65 (d, *J* = 2.3 Hz, 1H), 7.40-7.34 (m, 2H), 7.22 (d, *J* = 8.9 Hz, 1H), 6.54 (d, *J* = 2.3 Hz, 1H), 3.87 (s, 3H), 3.65 (s, 3H), 1.56 (d, *J* = 7.3, 3H). **¹³C NMR** (151 MHz, CDCl₃) δ 174.98, 152.61, 140.70, 136.66, 133.06, 131.47, 130.65, 128.97, 127.94, 125.97, 123.24, 122.83, 113.97, 106.10, 57.00, 52.24, 45.39, 18.57. **IR** (thin film): 2949.59, 2844.49, 1732, 1606.41, 1455.99, 1341.25, 1278.57, 1196.61, 1071.26, 755.96; **HRMS**: Calculated for (M+Na)⁺: 333.1216; found: 333.1207.



41

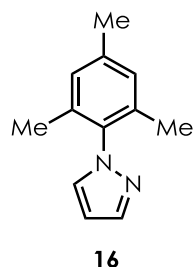
(9*S*)-10,11-dihydro- 6'-methoxy-5'-(1*H*-pyrazol-1-yl)cinchonan-9-ol · 2,2,2-trifluoroacetic acid (4.41).

The title compound was prepared from **S14** using **General Method A** with an irradiation time of 40 hours. The crude residue was purified by column chromatography on silica gel (0% to 5% MeOH/DCM to 5% MeOH/DCM/0.05% TFA) to yield the desired product in 53% as a glassy orange-tinted solid. **¹H NMR** (600 MHz, CDCl₃) δ 10.85 (br s, 1H), 8.83 (d, *J* = 4.5 Hz, 1H), 8.34 (d, *J* = 9.4 Hz, 1H), 7.97 (d, *J* = 4.5 Hz, 1H), 7.94 (d, *J* = 1.8 Hz, 1H), 7.58 (d, *J* = 9.4 Hz, 1H), 7.38 (d, *J* = 2.2 Hz, 1H), 6.89 (br s, 1H), 6.52 (t, *J* = 2.0 Hz, 1H), 4.36 (s, 1H), 3.87 (s, 3H), 3.81 (t, *J* = 10.5 Hz, 2H), 3.68 (t, *J* = 9.8 Hz, 1H), 3.16 – 3.09 (m, 1H), 2.99 (q, *J* = 9.3 Hz, 1H), 1.81 – 1.59 (m, 5H), 1.52 – 1.36 (m, 2H), 0.85 (t, *J* = 7.4 Hz, 3H), 0.41 (dt, *J* = 13.7, 7.7 Hz, 1H). **¹³C NMR** (151 MHz, CDCl₃) δ 162.54 (q, *J* = 35.2 Hz), 156.32, 148.37, 143.69, 143.37, 142.21, 134.37, 134.30, 123.76, 122.24, 121.13, 116.76 (q, *J* = 292.3 Hz), 115.56, 108.15, 66.00, 60.59, 57.02, 51.03, 48.45, 35.46, 25.68, 24.20, 23.68, 18.68, 11.56. **IR** (thin film): 3213.79, 2963.09, 2241.84, 1671.02, 1508.06, 1464.67, 1268.93, 1201.43, 1136.83, 725.10; **HRMS**: Calculated for (M-C₂O₂F₃)⁺: 393.2290; found: 393.2282.

C.3.3.2 General Method B: Synthesis of Alkyl-Substituted Arenes 4.16 and 4.17 and Imidazoles 4.33 and 4.38.

The synthesis of aryl pyrazole **4.16** from mesitylene and pyrazole **4.5** is representative of the following general procedure:

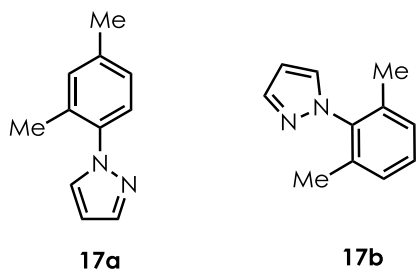
To a 2 dram vial containing a Teflon-coated magnetic stir bar was added 25 μ mol of Catalyst C (0.05 equiv.), 34 mg of pyrazole (0.5 mmol, 1 equiv.), and 16 mg of (2,2,6,6-tetramethylpiperidin-1-yl)oxyl (0.1 mmol, 0.2 equiv.). Dichloromethane or 1,2-Dichloroethane was added (5.0 mL), followed by addition of alkyl arene (1.0 mmol, 2 equiv.). The vial was sealed with a Teflon-lined septum screw cap. The septum was pierced with a disposable steel needle connected to a nitrogen-filled balloon. A vent needle was inserted and the reaction medium was sparged for 5 minutes by bubbling nitrogen through the mixture. The vent needle was removed, and the nitrogen line was maintained, providing approximately 1 atm of nitrogen to the vial headspace for the course of the reaction. The vial was irradiated as described in **General Procedure A** for 44 hours, and the reaction mixture was analysed by GC-MS or concentrated in vacuo and purified by column chromatography on silica gel with the eluent noted for each substrate.



1-mesityl-1H-pyrazole (4.16).

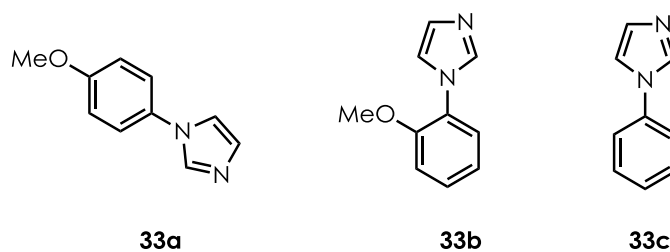
The title compound was prepared using **General Method B** with an irradiation time of 44 hours. The title compound was purified by column chromatography on silica gel (5% to 10%

EtOAc/Hexanes) to yield a yellow oil in 82%. $^1\text{H NMR}$ (400 MHz, CDCl_3) δ 8.17 (s, 1H), 7.86 (d, $J = 2.3$ Hz, 1H), 7.40 (s, 2H), 6.88 (s, 1H), 2.79 (s, 3H), 2.43 (s, 6H). $^{13}\text{C NMR}$ (151 MHz, CDCl_3) δ 140.07, 138.82, 137.05, 135.97, 130.93, 128.85, 105.83, 21.19, 17.30. **IR** (thin film): 3103.87, 2921.63, 2358.52, 1594.84, 1516.74, 1393.32, 1190.83, 1044.26, 852.38, 751.14; **HRMS**: Calculated for $(\text{M}+\text{H})^+$: 187.1235; found: 187.1228.



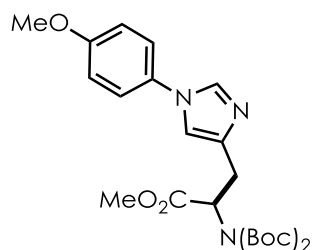
1-(2,4-dimethylphenyl)-1H-pyrazole (4.17a) and 1-(2,6-dimethylphenyl)-1H-pyrazole (4.17b).

The title compounds were prepared from *m*-xylene and pyrazole using Method B with an irradiation time of 44 hours. The title compound was purified by column chromatography on silica gel (5% to 10% EtOAc/Hexanes) to yield a yellow oil in 36%. The ratio of the inseparable mixture was >15:1 as determined by $^1\text{H NMR}$ of the isolated product. **17a.** $^1\text{H NMR}$ (400 MHz, CDCl_3) δ 8.00 (s, 1H), 7.85 (s, 1H), 7.51 (d, $J = 7.4$ Hz, 1H), 7.42 (s, 1H), 7.37 (d, $J = 7.4$ Hz, 1H), 6.72 (s, 1H), 2.68 (s, 3H), 2.50 (s, 3H). $^{13}\text{C NMR}$ (151 MHz, CDCl_3) δ 136.07, 134.08, 133.47, 129.32, 127.74, 126.68, 123.05, 121.93, 102.03, 17.13, 13.90. **17b.** $^1\text{H NMR}$ (400 MHz, CDCl_3) δ 8.04 (s, 1H), 7.74 (s, 1H), 7.25 (s, 3H), 6.75 (s, 1H), 2.31 (s, 6H). $^{13}\text{C NMR}$ (151 MHz, CDCl_3) δ 136.03, 135.21, 132.07, 126.81, 124.91, 124.07, 101.89, 13.28. **IR** (thin film): 3103.94, 2972.73, 2936.09, 2870.52, 1670.05, 1507.10, 1464.67, 1395.25, 1241.93, 1043.30; **HRMS**: Calculated for $(\text{M}+\text{Na})^+$: 195.0898; found: 195.0891.

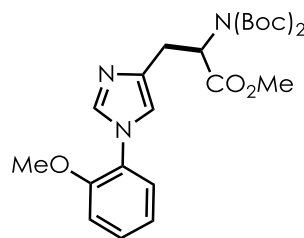


1-(4-methoxyphenyl)-1H-imidazole (4.33a), 1-(2-methoxyphenyl)-1H-imidazole (4.33b), and 1-phenyl-1H-imidazole (4.33c).

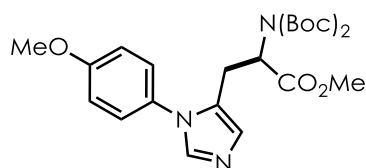
The title compounds were prepared using **General Method B** with the following modifications: 1.0 equiv. anisole and 2.0 equiv. imidazole were irradiated for 20 hours without nitrogen sparging or a balloon of nitrogen over the course of the reaction. Note: **General Method A** was incompatible with imidazole as a substrate, leading to complete suppression of product under the aerobic conditions. The crude residue was purified by column chromatography on silica gel with an eluent of 75% EtOAc/hexanes to EtOAc to 5% MeOH/EtOAc giving an inseparable mixture of **4.33a** and **4.33b** in a ratio of 4:1 in 55% yield, along with the product of *ipso*-substitution, **4.33c** in 7% yield. The spectral data match the literature report for compounds **4.33a**, **4.33b**, and **4.33c**.³⁶⁴ **4.33a**. ¹H NMR (600 MHz, CDCl₃) δ 7.76 (s, 1H), 7.30 (d, *J* = 8.9 Hz, 2H), 7.20 (s, 1H), 7.18 (s, 1H), 6.98 (d, *J* = 8.8 Hz, 2H), 3.85 (s, 3H). **4.33b**. ¹H NMR (600 MHz, CDCl₃) δ 7.78 (s, 1H), 7.37 – 7.34 (m, 1H), 7.29 – 7.28 (m, 1H), 7.21 (s, 1H), 7.16 (s, 1H), 7.07 – 7.02 (m, 2H), 3.85 (s, 3H). **4.33c**. ¹H NMR (600 MHz, CDCl₃) δ 7.86 (s, 1H), 7.48 (t, *J* = 7.8 Hz, 2H), 7.41 – 7.36 (m, 3H), 7.27 (s, 1H), 7.21 (s, 1H). ¹³C NMR (151 MHz, CDCl₃) δ 158.92, 152.58, 137.81, 137.35, 135.86, 135.58, 130.69, 130.40, 130.03, 129.89, 128.96, 128.79, 127.49, 126.50, 125.53, 123.20, 121.47, 121.00, 120.28, 118.77, 118.25, 114.89, 112.34, 55.82, 55.61.



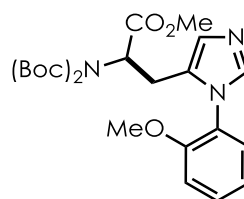
38a



38b



38c



38d

methyl N^{α} -(*tert*-butoxycarbonyl)- N^{ϵ} -(4-methoxyphenyl)-*L*-histidinate (4.38a), methyl N^{α} -(*tert*-butoxycarbonyl)- N^{ϵ} -(2-methoxyphenyl)-*L*-histidinate (4.38b), methyl N^{α} -(*tert*-butoxycarbonyl)- N^{ϵ} -(4-methoxyphenyl)-*L*-histidinate (4.38c), methyl N^{α} -(*tert*-butoxycarbonyl)- N^{ϵ} -(2-methoxyphenyl)-*L*-histidinate (4.38d).

The title compounds were prepared using **General Method B** with the following modifications: 1.0 equiv. anisole and 2.0 equiv. histidine **S11** were irradiated for 20 hours without nitrogen sparging or a balloon of nitrogen over the course of the reaction. Note: **General Method A** was incompatible with **S11** as a substrate, leading to complete suppression of product under the aerobic conditions. The crude residue was purified by column chromatography on silica gel with an eluent of 75% EtOAc/hexanes to EtOAc to 5% MeOH/EtOAc, from which were isolated 2 sets of fractions. The first set contained **4.38a** and **4.38b** in 24% yield and 8:1 ratio. The second set contained **4.38c** and **4.38d** in 24% yield and 5:1 ratio. **4.38a**. **$^1\text{H NMR}$** (600 MHz, CDCl_3) δ 7.66 (s, 1H), 7.25 (d, $J = 8.9$ Hz, 2H), 6.96 (d, $J = 9.0$ Hz, 3H), 5.90 (d, $J = 8.1$ Hz, 1H), 4.65 – 4.53 (m, 1H), 3.84 (s, 3H), 3.72 (s, 3H), 3.15 (dd, $J = 14.8, 5.6$ Hz, 1H), 3.08 (dd, $J = 14.7, 4.8$ Hz, 1H), 1.43 (s, 9H). **$^{13}\text{C NMR}$** (151 MHz, CDCl_3) δ 172.73, 159.00, 155.75,

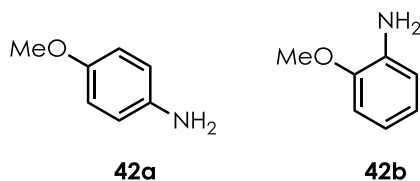
138.41, 135.62, 130.64, 123.07, 116.42, 115.01, 79.80, 55.73, 53.64, 52.39, 30.43, 28.48. **4.38b.** $^1\text{H NMR}$ (600 MHz, CDCl_3) δ 7.69 (s, 1H), 7.35 – 7.32 (m, 1H), 7.25 – 7.22 (m, 1H), 7.05 – 7.00 (m, 2H), 6.97 (s, 1H), 5.56 (d, $J = 8.2$ Hz, 1H), 4.61 – 4.57 (m, 1H), 3.83 (s, 3H), 3.72 (s, 3H), 3.02 (dd, $J = 15.0, 5.0$ Hz, 1H), 2.90 (dd, $J = 15.7, 4.4$ Hz, 1H), 1.44 (s, 9H). $^{13}\text{C NMR}$ (151 MHz, CDCl_3) δ 171.59, 152.52, 137.66, 130.01, 129.00, 127.57, 126.46, 125.41, 121.14, 117.98, 112.46, 80.52, 55.92, 53.74, 52.32, 30.39, 28.40. **IR** (thin film): 3369.07, 2976.59, 2841.60, 1746.23, 1705.73, 1517.70, 1366.32, 1251.58, 1166.72, 1021.12; **HRMS**: Calculated for $(\text{M}+\text{H})^+$: 376.1872; found: 376.1863.

4.38c. $^1\text{H NMR}$ (600 MHz, CDCl_3) δ 7.51 (s, 1H), 7.20 (d, $J = 8.8$ Hz, 2H), 6.99 (d, $J = 8.8$ Hz, 2H), 6.92 (s, 1H), 4.95 (d, $J = 7.9$ Hz, 1H), 4.39 – 4.34 (m, 1H), 3.86 (s, 3H), 3.62 (s, 3H), 3.06 (dd, $J = 15.4, 5.2$ Hz, 1H), 2.97 (dd, $J = 15.5, 6.7$ Hz, 1H), 1.39 (s, 9H). $^{13}\text{C NMR}$ (151 MHz, CDCl_3) δ 171.98, 159.89, 155.04, 138.59, 129.01, 128.50, 127.73, 121.10, 114.88, 80.21, 55.71, 52.72, 52.57, 28.39, 27.14. **4.38d.** $^1\text{H NMR}$ (600 MHz, CDCl_3) δ 7.46 – 7.42 (m, 2H), 7.22 – 7.18 (m, 1H), 7.07 – 7.04 (m, 2H), 6.93 (s, 1H), 5.00 (d, $J = 7.6$ Hz, 1H), 4.41 – 4.33 (m, 1H), 3.81 (s, 3H), 3.63 (s, 3H), 2.94 – 2.90 (m, 2H), 1.39 (s, 9H). $^{13}\text{C NMR}$ (151 MHz, CDCl_3) δ 172.13, 160.77, 154.66, 153.68, 138.73, 130.78, 128.86, 128.08, 127.76, 127.41, 112.25, 80.11, 55.87, 52.89, 52.50, 28.42, 26.83. **IR** (thin film): 3421.10, 2976.59, 1732.73, 1683.55, 1652.70, 1518.67, 1363.43, 1249.65, 1166.72, 1024.98; **HRMS**: Calculated for $(\text{M}+\text{H})^+$: 376.1872; found: 376.1863.

C.3.3.3 General Method C: Synthesis of Anilines 4.42-4.49

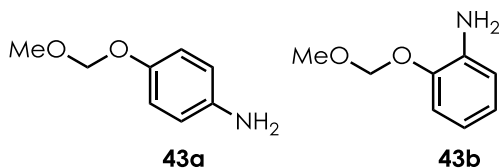
To a vial containing a Teflon-coated magnetic stir bar was added Catalyst B or C (0.05 equiv.), ammonium carbamate (4.0 equiv.), and TEMPO (0.2 equiv.). A 10:1 solvent mixture of 1,2-dichloroethane/water was added (0.1M), followed by the arene (1.0 equiv.). The vial was

sealed with a Teflon-lined septum screw cap, and the reaction mixture was sparged with O₂ and irradiated in the same fashion as **General Method A**.



***p*-anisidine (4.42a) and *o*-anisidine (4.42b).**

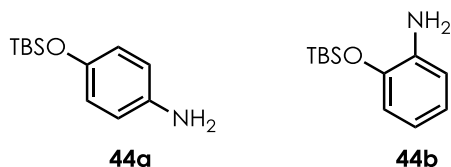
The title compounds were prepared from anisole using **General Method C** with an irradiation time of 24 hours. The reaction was run through a plug of silica, concentrated and the reaction was purified by column chromatography on silica gel (20% EtOAc/Hexanes) to afford a dark-purple solid in 36% yield (**4.42a**) and a dark brown liquid in 22% yield (**4.42b**). The spectral data were in agreement with previously reported literature values.³⁶⁵ **4.42a.** ¹H NMR (600 MHz, CDCl₃) δ 6.76 (d, *J* = 8.8 Hz, 1H), 6.66 (d, *J* = 8.8 Hz, 1H), 3.76 (s, 3H), 3.44 (br s, 2H); ¹³C NMR (151 MHz, CDCl₃) δ 152.95, 140.03, 116.56, 114.94, 55.88. **4.42b.** ¹H NMR (600 MHz, CDCl₃) δ 6.85 - 6.78 (m, 2H), 6.78 - 6.70 (m, 2H), 3.86 (s, 3H), 3.80 (br s, 2H); ¹³C NMR (151 MHz, CDCl₃) δ 147.45, 136.26, 121.20, 118.62, 115.16, 110.56, 55.56.



4-(methoxymethyl)aniline (4.43a) and 2-(methoxymethyl)aniline (4.43b).

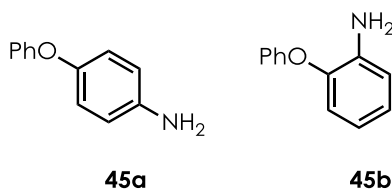
The title compounds were prepared from **S4** using **General Method C** with an irradiation time of 24 hours. The reaction was run through a plug of silica, concentrated and the reaction was purified by column chromatography on silica gel (20% to 50% EtOAc/Hexanes) to afford a

brown oil in 43% yield (**4.43a**) and a yellow oil in 21% yield (**4.43b**). The spectral data were in agreement with previously reported literature values.^{294,366} **4.43a.** ¹H NMR (600 MHz, CDCl₃) δ 6.87 (d, *J* = 8.8 Hz, 2H), 6.63 (d, *J* = 8.8 Hz, 2H), 5.08 (s, 3H), 3.47 (s, 5H). ¹³C NMR (151 MHz, CDCl₃) δ 150.32, 141.33, 117.98, 116.32, 95.62, 55.93. **4.43b.** ¹H NMR (600 MHz, CDCl₃) δ 7.03 (dd, *J* = 8.1, 1.3 Hz, 1H), 6.85 (td, *J* = 7.6, 1.3 Hz, 1H), 6.77 – 6.67 (m, 2H), 5.20 (s, 2H), 3.82 (br s, 2H), 3.51 (s, 3H). ¹³C NMR (151 MHz, CDCl₃) δ 144.93, 136.88, 122.61, 118.65, 115.60, 114.89, 95.21, 56.20.



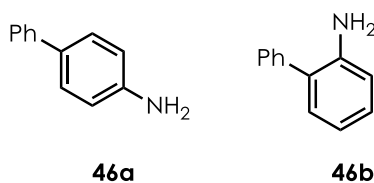
4-((*tert*-butyldimethylsilyl)oxy)aniline (4.44a) and 2-((*tert*-butyldimethylsilyl)oxy)aniline (4.44b).

The title compound was prepared from **S5** using **General Method C** with an irradiation time of 24 hours. The reaction was run through a plug of silica, concentrated and the reaction was purified by column chromatography on silica gel (10 to 20% EtOAc/Hexanes) to afford a brown solid in 35% yield (**4.44a**) and a yellow oil in 9% yield (**4.44b**). The spectral data were in agreement with previously reported literature values.^{367,368} **4.44a.** ¹H NMR (600 MHz, CDCl₃) δ 6.67 (m, 2H), 6.59 (m, 2H), 3.41 (br s, 2H), 0.98 (s, 9H), 0.16 (s, 6H). ¹³C NMR (151 MHz, CDCl₃) δ 148.34, 140.39, 120.80, 116.43, 29.85, 25.89, 18.33, -4.35. **4.44b.** ¹H NMR (600 MHz, CDCl₃) δ 6.79 (td, *J* = 7.5, 1.4 Hz, 1H), 6.76 – 6.71 (m, 2H), 6.63 (ddd, *J* = 7.9, 7.3, 1.7 Hz, 1H), 3.70 (br s, 2H), 1.03 (s, 9H), 0.25 (s, 6H); ¹³C NMR (151 MHz, CDCl₃) δ 143.05, 138.27, 121.95, 118.61, 118.53, 115.78, 25.97, 18.38, -4.10. **IR** (thin film): 3445.17, 2955.38, 2929.34, 2857.02, 1646.91, 1519.63, 1275.68, 1226.50, 923.74, 832.13. **HRMS:** Calculated for (M+H)⁺: 224.1470; found: 224.1464.



4-phenoxyaniline (4.45a) and 2-phenoxyaniline (4.45b).

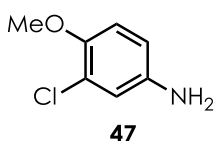
The title compounds were prepared from diphenyl ether using **General Method C** with an irradiation time of 24 hours. The reaction was run through a plug of silica, concentrated and the reaction was purified by column chromatography on silica gel (20% EtOAc/Hexanes) to afford a light brown solid in 46% yield (**4.45a**)³⁶⁹ and a yellow oil in 16% yield (**4.45b**).³⁷⁰ The spectral data were in agreement with previously reported literature values. **4.45a.** ¹H NMR (600 MHz, CDCl₃) δ 7.32 - 7.26 (m, 2H), 7.05 - 6.99 (m, 1H), 6.97 - 6.92 (m, 2H), 6.92 - 6.85 (m, 2H), 6.72 - 6.67 (m, 2H), 3.59 (br s, 2H); ¹³C NMR (151 MHz, CDCl₃) δ 159.02, 148.72, 142.80, 129.65, 122.19, 121.27, 117.34, 116.37. **4.45b.** ¹H NMR (600 MHz, CDCl₃) δ 7.34 - 7.28 (m, 2H), 7.06 (tt, *J* = 7.3, 1.1 Hz, 1H), 7.01 - 6.95 (m, 3H), 6.88 (dd, *J* = 8.0, 1.4 Hz, 1H), 6.83 (dd, *J* = 7.9, 1.6 Hz, 1H), 6.72 (td, *J* = 7.7, 1.6 Hz, 1H), 3.80 (br s, 2H); ¹³C NMR (151 MHz, CDCl₃) δ 157.61, 143.19, 138.86, 129.84, 125.03, 122.76, 120.40, 118.92, 117.23, 116.61.



[1,1'-biphenyl]-4-amine (4.46a) and [1,1'-biphenyl]-2-amine (4.46b).

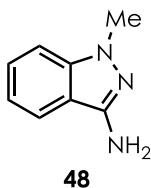
The title compounds were prepared using **General Method C** with an irradiation time of 24 hours. The reaction was run through a plug of silica, concentrated and the reaction was purified by column chromatography on silica gel (20% EtOAc/Hexanes) to afford a brown crystalline solid in 42% yield (**4.46a**) and a brown solid in 11% yield (**4.46b**). The spectral data were in agreement with previously reported literature values.³⁶⁵ **4.46a.** ¹H NMR (600 MHz,

CDCl₃) δ 7.56 (d, J = 7.8 Hz, 2H), 7.48 - 7.35 (m, 4H), 7.33 - 7.24 (m, 1H), 6.78 (d, J = 8.4 Hz, 2H), 3.74 (br s, 2H); ¹³C NMR (151 MHz, CDCl₃) δ 145.93, 141.26, 131.68, 128.76, 128.12, 126.51, 126.36, 115.49. **46b.** ¹H NMR (600 MHz, CDCl₃) δ 7.49 - 7.42 (m, 4H), 7.38 - 7.33 (m, 1H), 7.20 - 7.12 (m, 2H), 6.84 (td, J = 7.4, 1.2 Hz, 1H), 6.78 (dd, J = 8.0, 1.1 Hz, 1H), 3.76 (br s, 2H). ¹³C NMR (151 MHz, CDCl₃) δ 143.62, 139.64, 130.59, 129.22, 128.94, 128.62, 127.77, 127.29, 118.78, 115.72.



3-chloro-4-methoxyaniline (4.47).

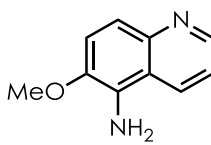
The title compound was prepared using **General Method C** with an irradiation time of 48 hours. The reaction was run through a plug of silica, concentrated and the reaction was purified by column chromatography on silica gel (50% EtOAc/Hexanes) to afford a brown solid in 33% yield. ¹H NMR (600 MHz, CDCl₃) δ 6.78 (d, J = 8.7 Hz, 1H), 6.76 (d, J = 2.8 Hz, 1H), 6.56 (dd, J = 8.7, 2.8 Hz, 1H), 3.83 (s, 3H), 3.47 (br s, 2H); ¹³C NMR (151 MHz, CDCl₃) δ 148.31, 140.86, 123.32, 117.53, 114.39, 114.15, 57.06. **IR** (thin film): 3421.10, 3361.32, 3219.58, 2931.27, 2835.81, 1634.38, 1505.17, 1439.60, 1272.79, 1229.40. **HRMS**: Calculated for (M+H)⁺: 158.0373; found: 158.0366.



1-methyl-1H-indazol-3-amine (4.48).

The title compound was prepared using **General Method C** with an irradiation time of 24 hours. The reaction was run through a plug of silica, concentrated and the reaction was

purified by column chromatography on silica gel (50% to 70% EtOAc/Hexanes) to afford a pink-red crystalline solid in 33% yield. The spectral data were in agreement with previously reported literature values.³⁷¹ $^1\text{H NMR}$ (600 MHz, CDCl_3) δ 7.55 (d, $J = 8.1$ Hz, 1H), 7.36 (dd, $J = 8.1$, 6.9 Hz, 1H), 7.22 (d, $J = 8.6$, 1H), 7.03 (dd, $J = 7.8$, 6.9, 1H), 4.04 (br s, 2H), 3.86 (s, 3H); $^{13}\text{C NMR}$ (151 MHz, CDCl_3) δ 146.99, 141.66, 127.00, 119.62, 118.54, 114.60, 108.79, 34.94.



49

6-methoxy-quinolin-5-amine (4.49).

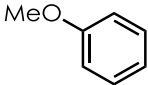
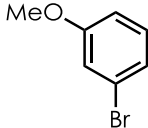
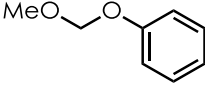
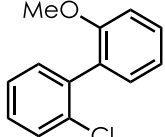
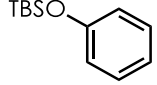
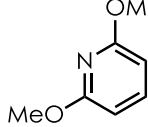
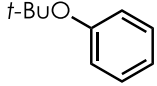
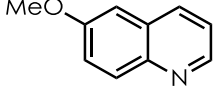
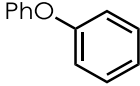
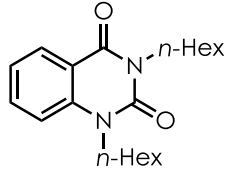
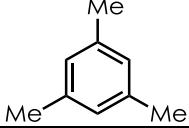
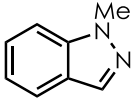
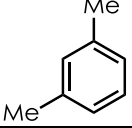
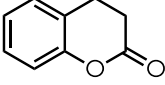
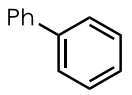
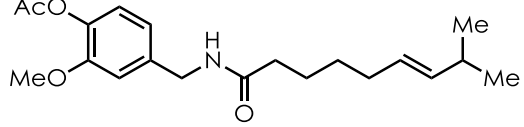
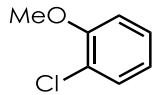
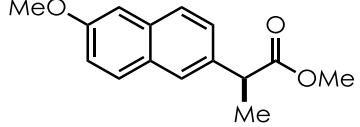
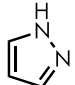
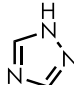
The title compound was prepared using **General Method C** with an irradiation time of 32 hours along with Catalyst B. The reaction was run through a plug of silica, concentrated and the reaction was purified by column chromatography on silica gel (70% EtOAc/Hexanes) to afford a green solid in 36% yield. The spectral data were in agreement with previously reported literature values.³⁷¹ $^1\text{H NMR}$ (600 MHz, CDCl_3) δ 8.78 (dd, $J = 4.1$, 1.6 Hz, 1H), 8.14 (d, $J = 8.6$, 1H), 7.61 (d, $J = 9.1$, 1H), 7.45 (d, $J = 9.1$ Hz, 1H), 7.32 (dd, $J = 8.6$, 4.1 Hz, 1H), 4.27 (br s, 2H), 4.00 (s, 3H); $^{13}\text{C NMR}$ (151 MHz, CDCl_3) δ 148.38, 144.17, 142.72, 129.41, 129.11, 119.79, 119.72, 118.89, 116.52, 56.76.

C.4 Electrochemical Measurements

Electrochemical half peak redox potentials ($E_{p/2}$) were estimated from cyclic voltammograms obtained by the method described previously.⁶¹ Measurements were performed in acetonitrile with tetrabutylammonium hexafluorophosphate (0.1 M) as the electrolyte, and the cyclic voltammograms were collected using a glassy carbon working electrode, a platinum wire counter electrode, and a Ag/AgCl reference electrode in saturated NaCl. The observed half peak

potential was referenced to SCE by addition of 30 mV to the value obtained vs. Ag/AgCl. For a typical measurement, the potential was increased from an initial potential of 0.5 V to a vertex potential of 2.8 V, then returning to a final potential of 0.5 V. With these parameters, all compounds listed in **Table C.4** exhibited irreversible oxidation waves. Excited state reduction potentials for Catalysts A-C are estimated as described in the aforementioned reference from the ground state reduction potentials (Catalyst A: $E_{1/2} = -0.47$ V vs. SCE, Catalyst B: $E_{1/2} = -0.58$ V vs. SCE, Catalyst C: $E_{1/2} = -0.52$ V vs. SCE) and the excited state energy ($E_{0,0}$) of the locally excited singlet state for 9-mesityl-10-methylacridinium tetrafluoroborate.

Table C.4. Electrochemical Half Peak Potentials for ($E_{p/2}$) for the arenes and select amine nucleophiles employed

substrate	$E_{p/2}$ (V vs. SCE)	substrate	$E_{p/2}$ (V vs. SCE)
Arenes			
	1.87		1.96
	1.89		1.86
	1.89		1.59
	1.74		1.66
	1.97		1.92
	2.13		1.60
	2.26		2.19
	1.96		1.74
	2.00		1.43
Representative Amines			
	2.27		2.83

C.5 NMR spectra of new compounds

See Supplementary Materials for Romero, et al.²⁹⁷ which is available online.

APPENDIX D: SUPPORTING INFORMATION FOR MECHANISTIC STUDIES ON ACRIDINIUM-MEDIATED ARENE C-H AMINATION REACTIONS

D.1 Materials

Mes-(*t*-Bu)₂Acr-PhBF₄ was synthesized according to the previously disclosed procedure,²⁹⁷ and samples for use in spectroscopic studies were prepared by layered recrystallization in MeCN/Et₂O. CoCp₂ was purchased from Strem, purified by vacuum sublimation, stored at -20 °C, handled entirely under an atmosphere of N₂, and used within one day of subliming. Spectroscopy grade DCE was used in spectroscopic studies, and was distilled from P₂O₅ before use. For all other reactions, DCE was used as received. TEMPO was purified by sublimation. Anisole was passed through a plug of activated alumina before use. Samples of **pdt** were obtained by scaling up the aryl amination reaction, and sequentially purifying by column chromatography on silica gel, followed by vacuum distillation, then passing the clear oil through activated alumina before use. Proton NMR was used to determine the *para*:-*ortho*- ratio, which was 5:1 in this isolated material.

D.2 Specifications for custom LED array used in test reactions and kinetics

All test reactions and kinetic runs were carried out using a custom-designed LED array pictured in **Figure D.1**, which features four wells to accommodate four 1 or 2 dram vials and provides irradiation from beneath. This array was constructed with 3D-printed parts and the commercially available parts listed below:

1. CREE XT-E Royal Blue LEDs pre-soldered to MCPCB (metal core printed circuit board); purchased from www.rapidled.com (<http://www.rapidled.com/cree-xt-e-royal-blue-led/>)
2. 60 Degree lens designed for use with CREE XT-E LEDs; purchased from www.rapidled.com (<http://www.rapidled.com/60-degree-cree-xp-e-xp-g-lens-optics-white-black/>)

3. Mean Well LPC-35-700 constant current driver; purchased from www.rapidled.com (<http://www.rapidled.com/mean-well-lpc-35-700-constant-current-driver/>)
4. 60 mm Round x 20 mm High heat sink; purchased from www.luxeonstar.com (<http://www.luxeonstar.com/60mm-round-5.8-degree-cw-alpha-heat-sink>)
5. Thermal grease; purchased from www.rapidled.com (<http://www.rapidled.com/thermal-grease-5g/>)

The four LEDs (1) are wired in series with the driver (3), which powers each LED at a constant current of 700 mA. The LEDs are attached to the heatsink (4) with screws and a layer of thermal grease (5) between the MCPCB and the heatsink. The lenses (2) are pressed onto the top of the LED without use of adhesive, and the LEDs, lenses, and heatsink are encased in a 2-part 3D-printed enclosure made with ABS filament. The upper and lower parts of the enclosure are fastened together with 4 screws, holding the lenses firmly in place, each facing upward into a well into which reaction vials are placed, resting directly on the surface of the lens. The upper part of the enclosure contains an air inlet through which pressurized air is introduced and passes over the upper surfaces of the MCPCBs and the heatsink, and the lower part features 12 outlet channels which direct the airflow across the fins of the heatsink.

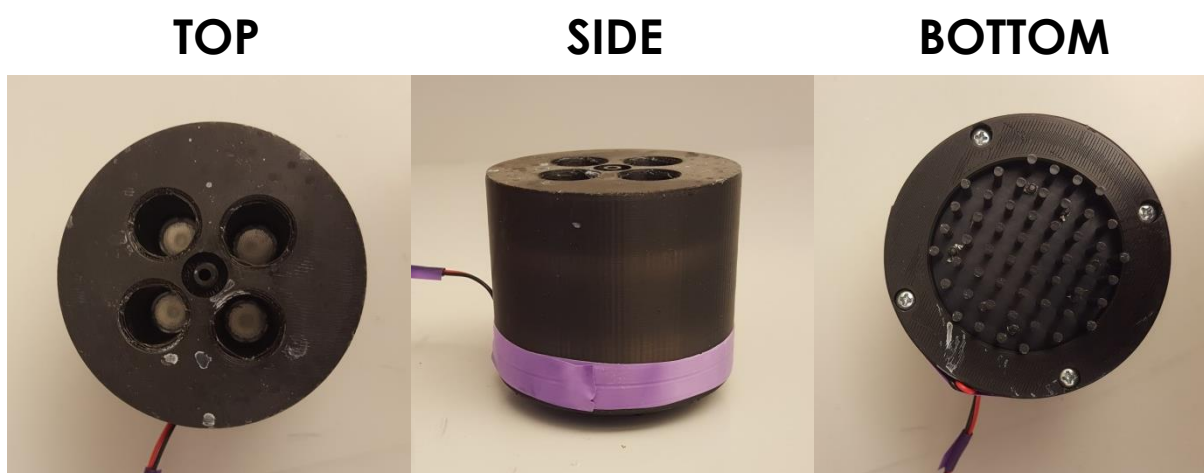


Figure D.1. Custom LED array with irradiation from beneath the vial

D.3 Procedure for kinetic analysis of the photoredox catalyzed aryl amination reaction

Into a flame-dried 2 dram vial containing a magnetic stir bar, the requisite amount of pyrazole, TEMPO, Mes-(*t*-Bu)₂Acr-PhBF₄ and anisole were added to give the concentrations listed in **Scheme 5.7**. Additionally, 0.5 equivalents of 1,3-dichlorobenzene relative to anisole was added as an internal standard. DCE was added to bring the total solution volume to 5.0 mL and the vial was sealed with a PTFE-lined septum cap. The solution was sparged for 60 seconds with a single balloon containing O₂ through a thin gauge needle. After sparging, the needle connected to the balloon was not removed from the reaction headspace for the entire reaction. Before irradiation, a 10 μL aliquot was removed (*t* = 0 min). For all reactions, the stir plate was set to stir at 800 revolutions per minute, and 10 μL aliquots were removed at the given intervals after the sample was placed into a well above a single LED. Prior to this, the LED was turned on for at least 10 minutes to allow for the light output and temperature to stabilize. The temperature was monitored by placing a thermocouple in a separate vial filled with DCE, and was kept below 30.0 °C for the entire reaction. Aliquots were immediately diluted to 1 mL in Et₂O and analyzed by GC (Agilent 6850, FID detector).

The integrated peak areas for anisole, pyrazole, TEMPO, and the *ortho*- and *para*-isomers of **pdt** were normalized to the integrated peak area of the internal standard 1,3-dichlorobenzene and converted to concentration by their instrument response factors.

For each experiment in **Scheme 5.7**, the [anisole] vs. time plot was fit to a multiexponential fit with 4 exponential terms using the Curve Fitting Tool (“cftool”) in MATLAB R2015b of the form:

Equation D.1

$$[\text{anisole}]_t = Ae^{-Bt} + Ce^{-Dt} + Ee^{-Ft} + Ge^{-Ht}$$

This regression equation is arbitrary, insofar as it bears no mathematical relationship to the reaction mechanism. The coefficients for the fit corresponding to each experiment is given in

Table D.1 below:

Table D.1. Coefficient values used to model kinetics by equation D.1

	<i>A</i>	<i>B</i>	<i>C</i>	<i>D</i>	<i>E</i>	<i>F</i>	<i>G</i>	<i>H</i>
"standard"	0.0198	0.0165	0.0165	0.0108	0.0227	0.0925	0.0407	0.0020
"same excess"	0.0178	0.0024	0.0183	0.0158	0.0227	0.0852	0.0200	0.0065
"same excess + pdt "	0.0162	0.0082	0.0158	0.0053	0.0285	0.0015	0.0189	0.0352

Using the “differentiate” MATLAB function, the fit was differentiated with respect to the time points at which each aliquot was taken to give the instantaneous reaction rate at each point:

Equation D.2

$$\text{reaction rate} = -\frac{d[\text{anisole}]}{dt} = \frac{d[\text{para} + \text{ortho}]}{dt}$$

By convention, reaction rate is defined as the opposite of anisole disappearance, determined by the differentiation of equation D.1, in order to return positive rate values for the rate of formation of *para*- + *ortho*- isomers. This relies on the assumption that the mass balance is maintained between anisole, **para**, and **ortho** at all points in the reaction, and we confirm that this is the case under the first two conditions in **Scheme 5.7**, such that:

Equation D.3

$$[\text{anisole}]_0 = [\text{anisole}]_t + [\text{para}]_t + [\text{ortho}]_t$$

The [**para**]:[**ortho**] ratio was determined to be approximately 6:1 at the end of irradiation by ¹H NMR and was found to be constant over the course of reaction, so the mass balance relationship in equation D.3 can be written with [ortho]_t omitted:

Equation D.4

$$[\text{anisole}]_0 = [\text{anisole}]_t + \frac{7}{6}[\text{para}]_t$$

When “rate×[para]” is plotted vs. [anisole], satisfactory overlay is not obtained for the three conditions, as shown in **Figure D.2**.

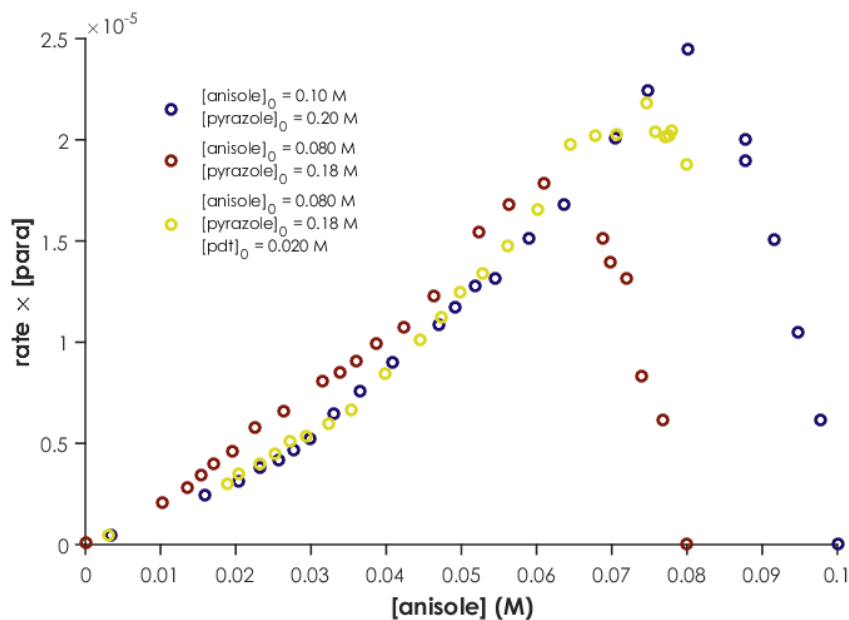


Figure D.2. Graphical rate analysis testing the inverse relationship between rate and [para].

The overlay of the plots in **Figure 5.4** allows for the derivation of the rate law in equation 5.4, with the constants k_A and k_P determined by a simple regression analysis of the combined data from all three experiments in **Scheme 5.7**. The regression analysis was applied to the combined data (i.e., “global fit”) in order to obtain average values for k_A and k_P without propagating the noise inherent to each data set. Once the rate law was derived, we simulated the kinetics ([anisole] vs. time) directly from the rate law using a differential equation solver (the ‘ode23s’ function) in MATLAB. The following code was implemented for the case of the “standard conditions” experiment:

```

tspan = [0 1500];
y0 = 0.1;
p0 = 0.00;
[t,y] = ode23s(@(t,y) -1.293e-5*y./(((y0-y+p0)*6./7).^2+0.000459), tspan, y0);

```


Where “y” corresponds to $[\text{anisole}]_t$, “y0” corresponds to $[\text{anisole}]_0$, “p0” corresponds to $[\text{pdt}]_0$, and the quantity “ $((y_0 - y + p_0) * 6/7)$ ” corresponds to $[\text{para}]$.

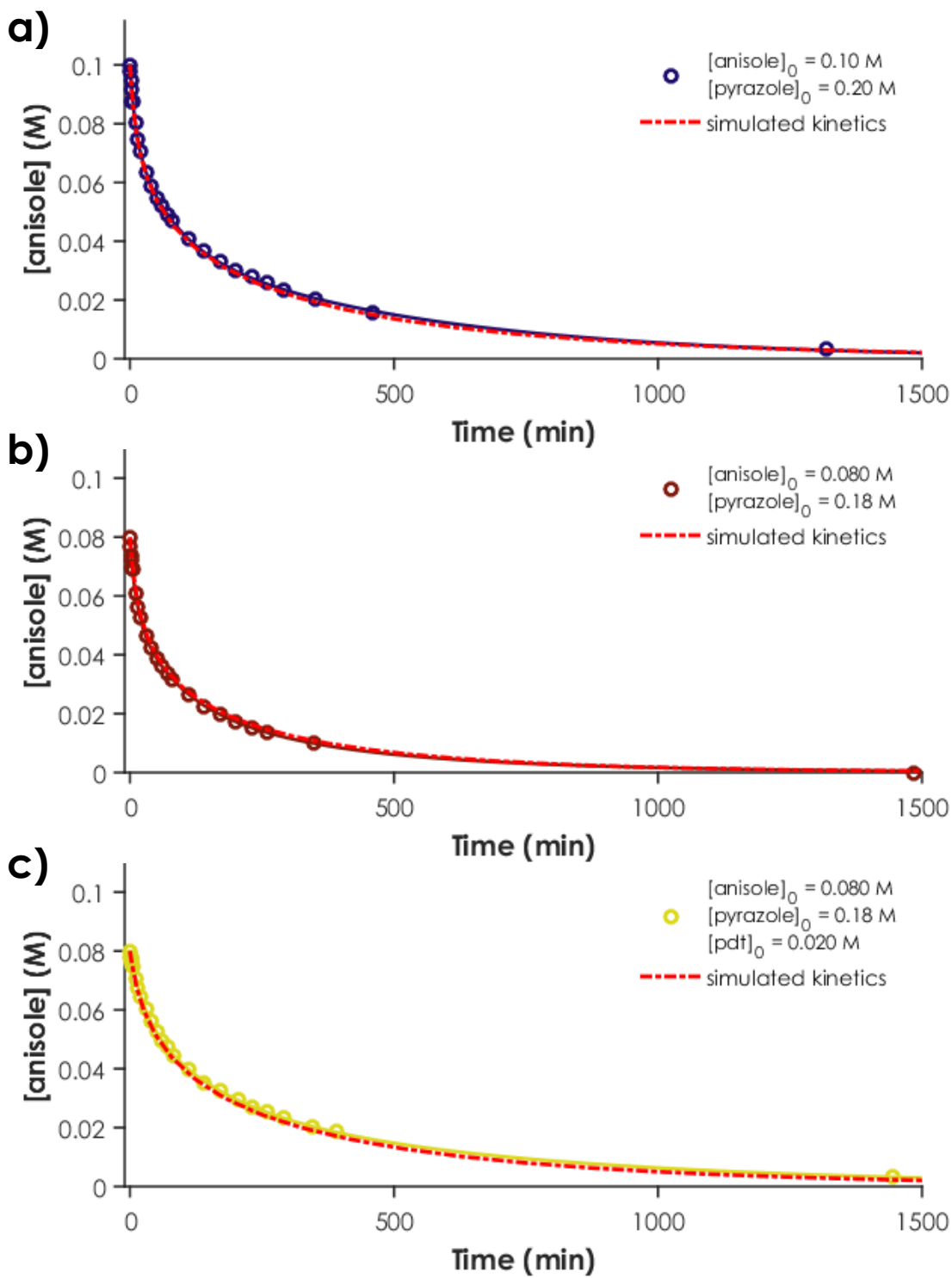


Figure D.3. Simulated kinetics using the experimentally derived rate law (equation 5.3)

The concentration of **[para]** at which the reaction rate is 50% of the initial rate is represented as **[para]_{50%}**. Using the experimentally derived rate law, this condition can be represented by the expression

Equation D.5

$$\frac{k_A[\text{anisole}]_0}{[\text{para}]_0^2 + k_P} = 2 \frac{k_A[\text{anisole}]_{50\%}}{[\text{para}]_{50\%}^2 + k_P}$$

which simplifies to:

Equation D.6

$$\frac{[\text{para}]_{50\%}^2}{k_P} = 2 \frac{([\text{anisole}]_0 - \frac{7}{6}[\text{para}]_{50\%})}{[\text{anisole}]_0} - 1$$

because **[para]₀** = 0 and substitution of **[anisole]_{50%}** according to equation D.4. The positive solution to this quadratic equation is

Equation D.7

$$[\text{para}]_{50\%} = \frac{\sqrt{49k_P^2 - 36k_P[\text{anisole}]_0^2} - 7k_P}{6[\text{anisole}]_0}$$

Along with equation D.4, equation D.7 enables the calculation of **[para]_{50%}** and **[anisole]_{50%}** from a given **[anisole]₀**, and the ratio **[anisole]_{50%}/[para]_{50%}** was calculated accordingly for the the “standard” and “same excess” experiments, returning ratios of 4.8 and 3.9, respectively, with an average ratio of 4.4.

D.4 Analysis of reaction mixtures by HRMS

Reactions were set up as described in the previous section on a 0.5 mmol scale (relative to anisole) and irradiated using the custom LED array described above. Aliquots (10 μL) were taken at time points and finally after 22 hours of irradiation, diluted with MeOH, and the samples

were analyzed using an HPLC system equipped with a photodiode array detector and inline Thermo LTqFT mass spectrometer with electrospray ionization in positive mode.

D.5 Test reaction shown in Scheme 5.9

Reactions were set up as described in the previous section with the following reactant quantities: 0.1 mmol **pdT** (5:1 *p*-: *o*-), 0.9 mmol 4-methylpyrazole, 0.025 mmol Mes-(*t*-Bu)₂Acr-PhBF₄, 0.1 mmol TEMPO (or no TEMPO), and 5.0 mL DCE. These conditions are intended to approximate the concentration at which **pdT** begins to effect product inhibition. The solution was sparged for 5 minutes with N₂ and irradiated using the custom LED array described above for 22 hours. The resulting solution was passed through silica gel and analyzed by GC-MS, which revealed that **pdT** was unchanged in both conditions, and the *m/z* corresponding to **5.14** was not detected.

D.6 Preparation of Mes-(*t*-Bu)₂Acr-Ph•

Mes-(*t*-Bu)₂Acr-Ph• was prepared by chemical reduction of Mes-(*t*-Bu)₂Acr-Ph⁺ in the same fashion as previously reported.⁶¹ In a nitrogen filled glovebox, a sample of equimolar Mes-(*t*-Bu)₂Acr-PhBF₄ (5.0×10^{-5} M) and CoCp₂ (5.5×10^{-5} M, in slight excess to ensure complete reduction of Mes-(*t*-Bu)₂Acr-Ph⁺) was prepared by mixing stock solutions in DCE to give a total solution volume of 4.0 mL. The solution was loaded into a quartz cuvette, which was sealed with a PTFE-lined septum screw cap. After collecting a UV-Vis absorption spectrum of the fully generated acridinyl radical Mes-(*t*-Bu)₂Acr-Ph• (with CoCp₂BF₄ as the byproduct), the solution was sparged for 15 seconds with a balloon of O₂ introduced through the septum by a needle. A UV-Vis spectrum was collected immediately after sparging and shows complete consumption of Mes-(*t*-Bu)₂Acr-Ph•.

D.7 Fluorescence quenching experiments

Stern-Volmer analysis of fluorescence quenching was carried out by measuring fluorescence lifetime in the presence and absence of quencher at various concentrations as described in Appendix B.4.2 using the TCSPC functionality of an Edinburgh FLS920 spectrometer to measure fluorescence lifetime. The solvent used in these experiments was DCE, and the concentration of Mes-(*t*-Bu)₂Acr-PhBF₄ was 2.0×10^{-5} M. Samples were prepared under an atmosphere of N₂ and kept under N₂ at all times. Excitation was provided by a 444 nm laser diode, and emission was measured at 515 nm. Fluorescence lifetimes were calculated by reconvolution fit of the instrument response to a single exponential model (as described in Appendix B.4.2), and a single exponential fit was satisfactory for all decay profiles measured. The fluorescence lifetime of Mes-(*t*-Bu)₂Acr-Ph⁺ in the absence of quencher (τ_0) was 14.40 ns.

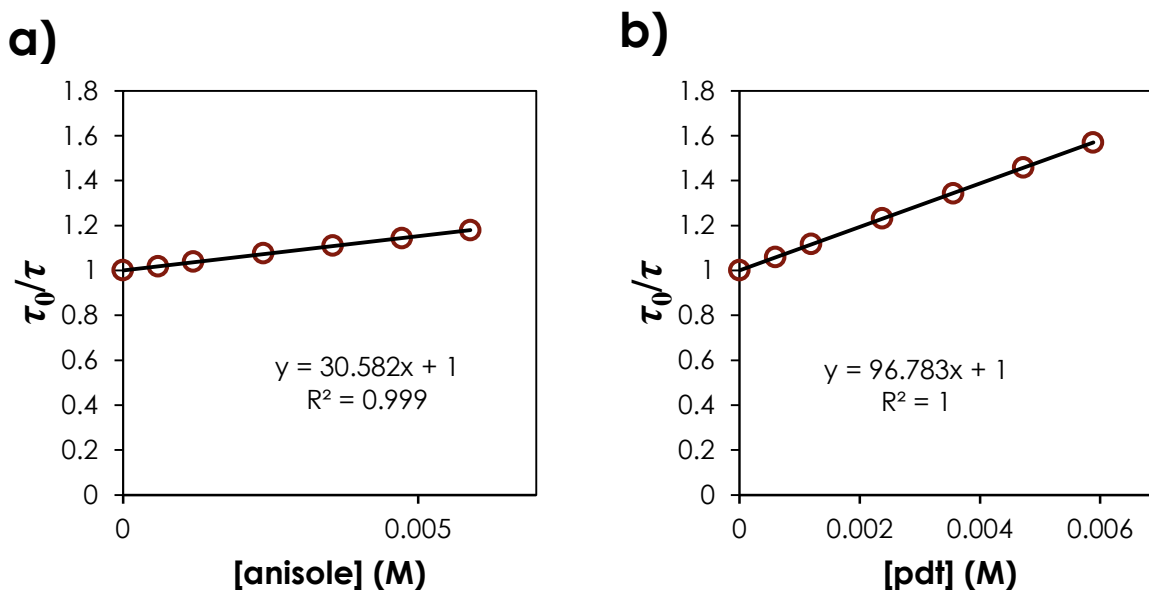
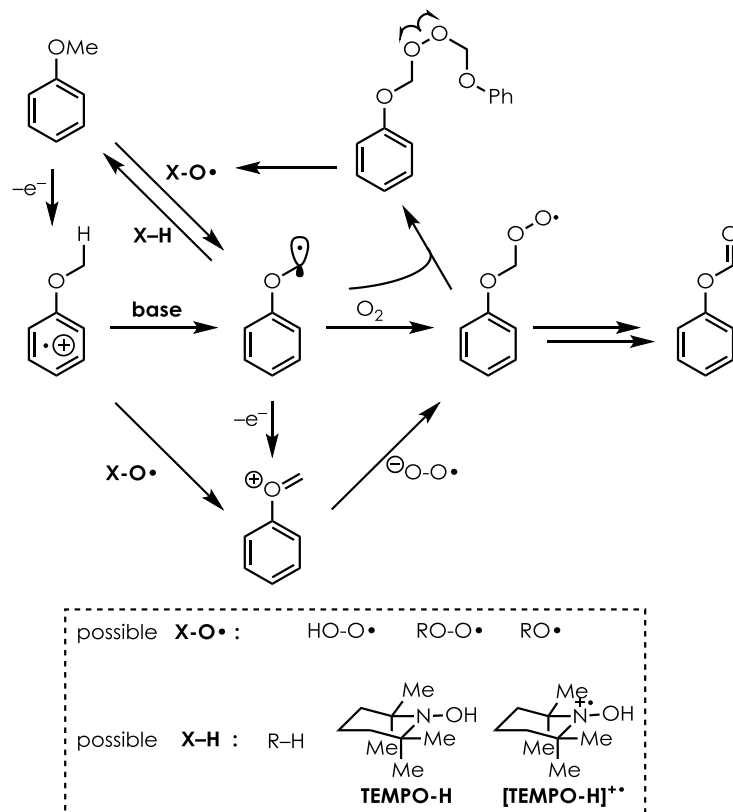


Figure D.4. Stern-Volmer plots of Mes-(*t*-Bu)₂Acr-Ph⁺ fluorescence quenching with the following quenchers: a) anisole and b) pdt

D.8 Additional Schemes and Figures

Scheme D.1. Possible pathways in the oxidative degradation of anisole



REFERENCES

- (1) Romero, N. A.; Nicewicz, D. A. *Chem. Rev.* **2016**, *116* (17), 10075–10166.
- (2) Prier, C. K.; Rankic, D. A.; MacMillan, D. W. C. *Chem. Rev.* **2013**, *113* (7), 5322–5363.
- (3) Xi, Y.; Yi, H.; Lei, A. *Org. Biomol. Chem.* **2013**, *11* (15), 2387–2403.
- (4) Xuan, J.; Xiao, W.-J. *Angew. Chem. Int. Ed.* **2012**, *51* (28), 6828–6838.
- (5) Tucker, J. W.; Stephenson, C. R. J. *J. Org. Chem.* **2012**, *77* (4), 1617–1622.
- (6) Ischay, M. A.; Yoon, T. P. *Eur. J. Org. Chem.* **2012**, *2012* (18), 3359–3372.
- (7) Reckenthäler, M.; Griesbeck, A. G. *Adv. Synth. Catal.* **2013**, *355* (14–15), 2727–2744.
- (8) Narayanam, J. M. R.; Stephenson, C. R. J. *Chem. Soc. Rev.* **2011**, *40* (1), 102.
- (9) Julliard, M.; Chanon, M. *Chem. Rev.* **1983**, *83* (4), 425–506.
- (10) Miranda, M. A.; Garcia, H. *Chem. Rev.* **1994**, *94* (4), 1063–1089.
- (11) Fagnoni, M.; Dondi, D.; Ravelli, D.; Albini, A. *Chem. Rev.* **2007**, *107* (6), 2725–2756.
- (12) Hoffmann, N. *J. Photochem. Photobiol. C Photochem. Rev.* **2008**, *9* (2), 43–60.
- (13) Ravelli, D.; Dondi, D.; Fagnoni, M.; Albini, A. *Chem. Soc. Rev.* **2009**, *38* (7), 1999–2011.
- (14) Ravelli, D.; Fagnoni, M.; Albini, A. *Chem. Soc. Rev.* **2012**, *42* (1), 97–113.
- (15) Marin, M. L.; Santos-Juanes, L.; Arques, A.; Amat, A. M.; Miranda, M. A. *Chem. Rev.* **2012**, *112* (3), 1710–1750.
- (16) Fukuzumi, S.; Ohkubo, K. *Org. Biomol. Chem.* **2014**, *12* (32), 6059–6071.
- (17) Hari, D. P.; König, B. *Chem. Commun.* **2014**, *50* (51), 6688–6699.
- (18) Turro, N. J. *Principles of molecular photochemistry: an introduction*; University Science Books: Sausalito, Calif, 2009.
- (19) Akasaki, I. *Rev. Mod. Phys.* **2015**, *87* (4), 1119–1131.
- (20) Amano, H. *Rev. Mod. Phys.* **2015**, *87* (4), 1133–1138.
- (21) Nakamura, S. *Rev. Mod. Phys.* **2015**, *87* (4), 1139–1151.
- (22) Mangion, D.; Kendall, J.; Arnold, D. R. *Org. Lett.* **2001**, *3* (1), 45–48.

- (23) Ohkubo, K.; Suga, K.; Morikawa, K.; Fukuzumi, S. *J. Am. Chem. Soc.* **2003**, *125* (42), 12850–12859.
- (24) Arnold, D. R.; Maroulis, A. J. *J. Am. Chem. Soc.* **1976**, *98* (19), 5931–5937.
- (25) Görner, H.; Warzecha, K.-D.; Demuth, M. *J. Phys. Chem. A* **1997**, *101* (51), 9964–9973.
- (26) Wang, Y.; Haze, O.; Dinnocenzo, J. P.; Farid, S.; Farid, R. S.; Gould, I. R. *J. Org. Chem.* **2007**, *72* (18), 6970–6981.
- (27) Gould, I. R.; Ege, D.; Moser, J. E.; Farid, S. *J. Am. Chem. Soc.* **1990**, *112* (11), 4290–4301.
- (28) Darmanyán, A. P. *Chem. Phys. Lett.* **1984**, *110* (1), 89–94.
- (29) Kanner, R. C.; Foote, C. S. *J. Am. Chem. Soc.* **1992**, *114* (2), 678–681.
- (30) Heller, H. C. *J. Am. Chem. Soc.* **1967**, *89* (17), 4288–4294.
- (31) Timpe, H.-J.; Kronfeld, K.-P.; Lammel, U.; Fouassier, J.-P.; Lougnot, D.-J. *J. Photochem. Photobiol. Chem.* **1990**, *52* (1), 111–122.
- (32) Timpe, H.-J.; Kronfeld, K.-P. *J. Photochem. Photobiol. Chem.* **1989**, *46* (2), 253–267.
- (33) Suppan, P. *J. Chem. Soc. Faraday Trans. 1 Phys. Chem. Condens. Phases* **1975**, *71* (0), 539–547.
- (34) Ghosh, I.; Mukhopadhyay, A.; Koner, A. L.; Samanta, S.; Nau, W. M.; Moorthy, J. N. *Phys. Chem. Chem. Phys.* **2014**, *16* (31), 16436–16445.
- (35) Xia, J.-B.; Zhu, C.; Chen, C. *J. Am. Chem. Soc.* **2013**, *135* (46), 17494–17500.
- (36) Malval, J.-P.; Jin, M.; Morlet-Savary, F.; Chaumeil, H.; Defoin, A.; Soppera, O.; Scheul, T.; Bouriau, M.; Baldeck, P. L. *Chem. Mater.* **2011**, *23* (15), 3411–3420.
- (37) Del Giacco, T.; Baciocchi, E.; Lanzalunga, O.; Elisei, F. *Chem. – Eur. J.* **2001**, *7* (14), 3005–3013.
- (38) Rathore, R.; Hubig, S. M.; Kochi, J. K. *J. Am. Chem. Soc.* **1997**, *119* (47), 11468–11480.
- (39) Görner, H. *Photochem. Photobiol.* **2006**, *82* (1), 71–77.
- (40) Ohkubo, K.; Fujimoto, A.; Fukuzumi, S. *J. Am. Chem. Soc.* **2013**, *135* (14), 5368–5371.
- (41) Hubig, S. M.; Kochi, J. K. *J. Am. Chem. Soc.* **1999**, *121* (8), 1688–1694.
- (42) Reta, M. R.; Cartana, R.; Anunziata, J. D.; Silber, J. J. *Spectrochim. Acta Part Mol. Spectrosc.* **1993**, *49* (7), 903–912.

- (43) Serpa, C.; Arnaut, L. G. *J. Phys. Chem. A* **2000**, *104* (47), 11075–11086.
- (44) Kasha, M. *Radiat. Res. Suppl.* **1960**, *2*, 243.
- (45) Akaba, R.; Sakuragi, H.; Tokumaru, K. *J. Chem. Soc. Perkin Trans. 2* **1991**, No. 3, 291–297.
- (46) Searle, R.; Williams, J. L. R.; DeMeyer, D. E.; Doty, J. C. *Chem. Commun. Lond.* **1967**, No. 22, 1165–1165.
- (47) Martiny, M.; Steckhan, E.; Esch, T. *Chem. Ber.* **1993**, *126* (7), 1671–1682.
- (48) Parret, S.; Morlet-Savary, F.; Fouassier, J.-P.; Inomata, K.; Matsumoto, T.; Heisel, F. *Bull. Chem. Soc. Jpn.* **1995**, *68* (10), 2791–2795.
- (49) Miranda, M. A.; Izquierdo, M. A.; Pérez-Ruiz, R. *J. Phys. Chem. A* **2003**, *107* (14), 2478–2482.
- (50) Akaba, R.; Kamata, M.; Koike, A.; Mogi, K.-I.; Kuriyama, Y.; Sakuragi, H. *J. Phys. Org. Chem.* **1997**, *10* (11), 861–869.
- (51) Jayanthi, S. S.; Ramamurthy, P. *J. Phys. Chem. A* **1998**, *102* (3), 511–518.
- (52) Baciocchi, E.; Giacco, T. D.; Elisei, F.; Gerini, M. F.; Guerra, M.; Lapi, A.; Liberali, P. *J. Am. Chem. Soc.* **2003**, *125* (52), 16444–16454.
- (53) Fukuzumi, S.; Fujita, M.; Noura, S.; Ohkubo, K.; Suenobu, T.; Araki, Y.; Ito, O. *J. Phys. Chem. A* **2001**, *105* (10), 1857–1868.
- (54) Chao, S. C.; Tretzel, J.; Schneider, F. W. *J. Am. Chem. Soc.* **1979**, *101* (1), 134–139.
- (55) Baciocchi, E.; Del Giacco, T.; Lanzalunga, O.; Mencarelli, P.; Procacci, B. *J. Org. Chem.* **2008**, *73* (15), 5675–5682.
- (56) Kitaguchi, H.; Ohkubo, K.; Ogo, S.; Fukuzumi, S. *J. Phys. Chem. A* **2006**, *110* (5), 1718–1725.
- (57) Weber, G.; Teale, F. W. *J. Trans. Faraday Soc.* **1957**, *53*, 646–655.
- (58) van Willigen, H.; Jones, G.; Farahat, M. S. *J. Phys. Chem.* **1996**, *100* (9), 3312–3316.
- (59) Benniston, A. C.; Harriman, A.; Li, P.; Rostron, J. P.; Verhoeven, J. W. *Chem. Commun.* **2005**, No. 21, 2701–2703.
- (60) Benniston, A. C.; Harriman, A.; Li, P.; Rostron, J. P.; van Ramesdonk, H. J.; Groeneveld, M. M.; Zhang, H.; Verhoeven, J. W. *J. Am. Chem. Soc.* **2005**, *127* (46), 16054–16064.
- (61) Romero, N. A.; Nicewicz, D. A. *J. Am. Chem. Soc.* **2014**, *136* (49), 17024–17035.

- (62) Eisenhart, T. T.; Dempsey, J. L. *J. Am. Chem. Soc.* **2014**, *136* (35), 12221–12224.
- (63) Chan, M. S.; Bolton, J. R. *Photochem. Photobiol.* **1981**, *34* (5), 537–547.
- (64) Parker, C. A.; Joyce, T. A. *Photochem. Photobiol.* **1973**, *18* (6), 467–474.
- (65) Shen, T.; Zhao, Z.-G.; Yu, Q.; Xu, H.-J. *J. Photochem. Photobiol. Chem.* **1989**, *47* (2), 203–212.
- (66) Chambers, R. W.; Kearns, D. R. *Photochem. Photobiol.* **1969**, *10* (3), 215–219.
- (67) Ghosh, T.; Slanina, T.; König, B. *Chem. Sci.* **2015**, *6* (3), 2027–2034.
- (68) Pileni, M. P.; Graetzel, M. *J. Phys. Chem.* **1980**, *84* (19), 2402–2406.
- (69) Lee, W. E.; Galley, W. C. *Biophys. J.* **1988**, *54* (4), 627–635.
- (70) Discekici, E. H.; Treat, N. J.; Poelma, S. O.; Mattson, K. M.; Hudson, Z. M.; Luo, Y.; Hawker, C. J.; Alaniz, J. R. de. *Chem. Commun.* **2015**, *51* (58), 11705–11708.
- (71) Treat, N. J.; Sprafke, H.; Kramer, J. W.; Clark, P. G.; Barton, B. E.; Read de Alaniz, J.; Fors, B. P.; Hawker, C. J. *J. Am. Chem. Soc.* **2014**, *136* (45), 16096–16101.
- (72) Pitre, S. P.; McTiernan, C. D.; Ismaili, H.; Scaiano, J. C. *J. Am. Chem. Soc.* **2013**, *135* (36), 13286–13289.
- (73) Bergmann, K.; O’Konski, C. T. *J. Phys. Chem.* **1963**, *67* (10), 2169–2177.
- (74) Merkelo, H.; Hartman, S. R.; Mar, T.; Singhal, G. S.; Govindjee. *Science* **1969**, *164* (3877), 301–302.
- (75) Wetzler, D. E.; García-Fresnadillo, D.; Orellana, G. *Phys. Chem. Chem. Phys.* **2006**, *8* (19), 2249–2256.
- (76) Timpe, H.-J.; Neuenfeld, S. *J. Chem. Soc. Faraday Trans.* **1992**, *88* (16), 2329–2336.
- (77) Nemoto, M.; Kokubun, H.; Koizumi, M. *Bull. Chem. Soc. Jpn.* **1969**, *42* (5), 1223–1230.
- (78) Zhang, X.-F.; Zhang, I.; Liu, L. *Photochem. Photobiol.* **2010**, *86* (3), 492–498.
- (79) Talla, A.; Driessen, B.; Straathof, N. J. W.; Milroy, L.-G.; Brunsveld, L.; Hessel, V.; Noël, T. *Adv. Synth. Catal.* **2015**, *357* (10), 2180–2186.
- (80) Fidaly, K.; Ceballos, C.; Falguières, A.; Veitia, M. S.-I.; Guy, A.; Ferroud, C. *Green Chem.* **2012**, *14* (5), 1293–1297.
- (81) Martin, M. M.; Lindqvist, L. *J. Lumin.* **1975**, *10* (6), 381–390.

- (82) Yoshioka, E.; Kohtani, S.; Jichu, T.; Fukazawa, T.; Nagai, T.; Takemoto, Y.; Miyabe, H. *Synlett* **2014**, 26 (2), 265–270.
- (83) Yuan, L.; Lin, W.; Yang, Y.; Chen, H. *J. Am. Chem. Soc.* **2012**, 134 (2), 1200–1211.
- (84) Magde, D.; Rojas, G. E.; Seybold, P. G. *Photochem. Photobiol.* **1999**, 70 (5), 737–744.
- (85) Magde, D.; Wong, R.; Seybold, P. G. *Photochem. Photobiol.* **2002**, 75 (4), 327–334.
- (86) Korobov, V. E.; Shubin, V. V.; Chibisov, A. K. *Chem. Phys. Lett.* **1977**, 45 (3), 498–501.
- (87) Yasui, S.; Tsujimoto, M.; Itoh, K.; Ohno, A. *J. Org. Chem.* **2000**, 65 (15), 4715–4720.
- (88) Bergamini, G.; Molloy, J. K.; Fermi, A.; Ceroni, P.; Klärner, F.-G.; Hahn, U. *New J. Chem.* **2012**, 36 (2), 354–359.
- (89) Becker, H.-C.; Broo, A.; Nordén, B. *J. Phys. Chem. A* **1997**, 101 (47), 8853–8860.
- (90) Ford, W. E.; Kamat, P. V. *J. Phys. Chem.* **1987**, 91 (25), 6373–6380.
- (91) Pavlishchuk, V. V.; Addison, A. W. *Inorganica Chim. Acta* **2000**, 298 (1), 97–102.
- (92) Loutfy, R. O.; Loutfy, R. O. *J. Phys. Chem.* **1972**, 76 (11), 1650–1655.
- (93) Schweitzer, C.; Mehrdad, Z.; Noll, A.; Grabner, E.-W.; Schmidt, R. *Helv. Chim. Acta* **2001**, 84 (9), 2493–2507.
- (94) Yamago, S.; Miyazoe, H.; Iida, K.; Yoshida, J. *Org. Lett.* **2000**, 2 (23), 3671–3673.
- (95) Isse, A. A.; Gennaro, A. *J. Phys. Chem. B* **2010**, 114 (23), 7894–7899.
- (96) Yoon, U. C.; Quillen, S. L.; Mariano, P. S.; Swanson, R.; Stavinoha, J. L.; Bay, E. *J. Am. Chem. Soc.* **1983**, 105 (5), 1204–1218.
- (97) Fukuzumi, S.; Kitano, T. *J. Chem. Soc. Perkin Trans. 2* **1991**, No. 1, 41–45.
- (98) Fukuzumi, S.; Nishimine, M.; Ohkubo, K.; Tkachenko, N. V.; Lemmetyinen, H. *J. Phys. Chem. B* **2003**, 107 (45), 12511–12518.
- (99) Fukuzumi, S.; Ohkubo, K.; Suenobu, T.; Kato, K.; Fujitsuka, M.; Ito, O. *J. Am. Chem. Soc.* **2001**, 123 (35), 8459–8467.
- (100) Fox, M. A. *Photochem. Photobiol.* **1990**, 52 (3), 617–627.
- (101) Ohkubo, K.; Fukuzumi, S. *Org. Lett.* **2000**, 2 (23), 3647–3650.
- (102) Fukuzumi, S.; Ohkubo, K.; Suenobu, T. *Acc. Chem. Res.* **2014**, 47 (5), 1455–1464.
- (103) Roth, H.; Romero, N.; Nicewicz, D. *Synlett* **2016**, 27 (5), 714–723.

- (104) Lambert, C. R.; Kochevar, I. E. *Photochem. Photobiol.* **1997**, *66* (1), 15–25.
- (105) Jones II, G.; Wang, X.; Hu, J. *Can. J. Chem.* **2003**, *81* (6), 789–798.
- (106) Park, S. M.; Bard, A. J. *J. Electroanal. Chem. Interfacial Electrochem.* **1977**, *77* (2), 137–152.
- (107) Gosztola, D.; Niemczyk, M. P.; Svec, W.; Lukas, A. S.; Wasielewski, M. R. *J. Phys. Chem. A* **2000**, *104* (28), 6545–6551.
- (108) Lee, S. K.; Zu, Y.; Herrmann, A.; Geerts, Y.; Müllen, K.; Bard, A. J. *J. Am. Chem. Soc.* **1999**, *121* (14), 3513–3520.
- (109) McNaught, A.; Wilkinson, A. In *IUPAC Compendium of Chemical Terminology, 2nd ed. (the “Gold Book”)*; Nič, M., Jirát, J., Košata, B., Jenkins, A., Eds.; Blackwell Scientific Publications: Oxford, 1997.
- (110) McNaught, A.; Wilkinson, A. In *IUPAC Compendium of Chemical Terminology, 2nd ed. (the “Gold Book”)*; Nič, M., Jirát, J., Košata, B., Jenkins, A., Eds.; Blackwell Scientific Publications: Oxford, 1997.
- (111) Rehm, D.; Weller, A. *Berichte Bunsenges. Für Phys. Chem.* **1969**, *73* (8–9), 834–839.
- (112) Rehm, D.; Weller, A. *Isr. J. Chem.* **1970**, *8* (2), 259–271.
- (113) Lakowicz, J. R. *Principles of fluorescence spectroscopy*, 3rd ed.; Springer: New York, 2006.
- (114) Farid, S.; Dinnocenzo, J. P.; Merkel, P. B.; Young, R. H.; Shukla, D.; Guirado, G. *J. Am. Chem. Soc.* **2011**, *133* (30), 11580–11587.
- (115) Farid, S.; Dinnocenzo, J. P.; Merkel, P. B.; Young, R. H.; Shukla, D. *J. Am. Chem. Soc.* **2011**, *133* (13), 4791–4801.
- (116) Richert, S.; Rosspeintner, A.; Landgraf, S.; Grampp, G.; Vauthey, E.; Kattinig, D. R. *J. Am. Chem. Soc.* **2013**, *135* (40), 15144–15152.
- (117) Rosspeintner, A.; Angulo, G.; Vauthey, E. *J. Am. Chem. Soc.* **2014**, *136* (5), 2026–2032.
- (118) Jacques, P.; Burget, D. *J. Photochem. Photobiol. Chem.* **1992**, *68* (2), 165–168.
- (119) Cismesia, M. A.; Yoon, T. P. *Chem. Sci.* **2015**, *6* (10), 5426–5434.
- (120) Rao, P. S.; Hayon, E. *J. Am. Chem. Soc.* **1974**, *96* (5), 1287–1294.
- (121) Wayner, D. D. M.; McPhee, D. J.; Griller, D. *J. Am. Chem. Soc.* **1988**, *110* (1), 132–137.
- (122) Fu, Y.; Liu, L.; Yu, H.-Z.; Wang, Y.-M.; Guo, Q.-X. *J. Am. Chem. Soc.* **2005**, *127* (19), 7227–7234.

- (123) Megerle, U.; Lechner, R.; König, B.; Riedle, E. *Photochem. Photobiol. Sci.* **2010**, *9* (10), 1400–1406.
- (124) Kochi, J. K. *Pure Appl. Chem.* **1991**, *63* (2), 255–264.
- (125) Rosokha, S. V.; Kochi, J. K. *Acc. Chem. Res.* **2008**, *41* (5), 641–653.
- (126) Rosokha, S. V.; Kochi, J. K. *J. Am. Chem. Soc.* **2007**, *129* (12), 3683–3697.
- (127) Rosokha, S. V.; Kochi, J. K. *New J. Chem.* **2002**, *26* (7), 851–860.
- (128) Arceo, E.; Bahamonde, A.; Bergonzini, G.; Melchiorre, P. *Chem. Sci.* **2014**, *5* (6), 2438–2442.
- (129) Nappi, M.; Bergonzini, G.; Melchiorre, P. *Angew. Chem. Int. Ed.* **2014**, *53* (19), 4921–4925.
- (130) Silvi, M.; Arceo, E.; Jurberg, I. D.; Cassani, C.; Melchiorre, P. *J. Am. Chem. Soc.* **2015**, *137* (19), 6120–6123.
- (131) Woźniak, Ł.; Murphy, J. J.; Melchiorre, P. *J. Am. Chem. Soc.* **2015**, *137* (17), 5678–5681.
- (132) Silva, G. P. da; Ali, A.; Silva, R. C. da; Jiang, H.; Paixão, M. W. *Chem. Commun.* **2015**, *51* (82), 15110–15113.
- (133) Gould, I. R.; Farid, S. *Acc. Chem. Res.* **1996**, *29* (11), 522–528.
- (134) Wilkinson, F. *J. Phys. Chem.* **1962**, *66* (12), 2569–2574.
- (135) Zhao, J.; Wu, W.; Sun, J.; Guo, S. *Chem. Soc. Rev.* **2013**, *42* (12), 5323–5351.
- (136) Clennan, E. L.; Pace, A. *Tetrahedron* **2005**, *61* (28), 6665–6691.
- (137) Gorman, A. A.; Rodgers, M. a. J. *Chem. Soc. Rev.* **1981**, *10* (2), 205–231.
- (138) Ohloff, G. *Pure Appl. Chem.* **1975**, *43* (3–4), 481–502.
- (139) Tanielian, C.; Wolff, C. *J. Phys. Chem.* **1995**, *99* (24), 9831–9837.
- (140) Prein, M.; Adam, W. *Angew. Chem. Int. Ed. Engl.* **1996**, *35* (5), 477–494.
- (141) Ni, T.; Caldwell, R. A.; Melton, L. A. *J. Am. Chem. Soc.* **1989**, *111* (2), 457–464.
- (142) Kuriyama, Y.; Arai, T.; Sakuragi, H.; Tokumaru, K. *Chem. Lett.* **1988**, *17* (7), 1193–1196.
- (143) Akaba, R.; Ohshima, K.; Kawai, Y.; Obuchi, Y.; Negishi, A.; Sakuragi, H.; Tokumaru, K. *Tetrahedron Lett.* **1991**, *32* (1), 109–112.
- (144) Keith, J. A.; Carter, E. A. *J. Am. Chem. Soc.* **2012**, *134* (18), 7580–7583.

- (145) Baik, M.-H.; Friesner, R. A. *J. Phys. Chem. A* **2002**, *106* (32), 7407–7412.
- (146) Winget, P.; Weber, E. J.; Cramer, C. J.; Truhlar, D. G. *Phys. Chem. Chem. Phys.* **2000**, *2* (6), 1231–1239.
- (147) Uudsemaa, M.; Tamm, T. *J. Phys. Chem. A* **2003**, *107* (46), 9997–10003.
- (148) Baik, M.-H.; Silverman, J. S.; Yang, I. V.; Ropp, P. A.; Szalai, V. A.; Yang, W.; Thorp, H. *J. Phys. Chem. B* **2001**, *105* (27), 6437–6444.
- (149) Lee, C.; Yang, W.; Parr, R. G. *Phys. Rev. B* **1988**, *37* (2), 785–789.
- (150) Becke, A. D. *J. Chem. Phys.* **1993**, *98* (7), 5648–5652.
- (151) Zhao, Y.; Truhlar, D. G. *Theor. Chem. Acc.* **2007**, *120* (1–3), 215–241.
- (152) Krishnan, R.; Binkley, J. S.; Seeger, R.; Pople, J. A. *J. Chem. Phys.* **1980**, *72* (1), 650–654.
- (153) McLean, A. D.; Chandler, G. S. *J. Chem. Phys.* **1980**, *72* (10), 5639–5648.
- (154) Barone, V.; Cossi, M. *J. Phys. Chem. A* **1998**, *102* (11), 1995–2001.
- (155) Cossi, M.; Rega, N.; Scalmani, G.; Barone, V. *J. Comput. Chem.* **2003**, *24* (6), 669–681.
- (156) *Gaussian 09, Revision D.01*, M. J. Frisch, G. W. Trucks, H. B. Schlegel, G. E. Scuseria, M. A. Robb, J. R. Cheeseman, G. Scalmani, V. Barone, B. Mennucci, G. A. Petersson, H. Nakatsuji, M. Caricato, X. Li, H. P. Hratchian, A. F. Izmaylov, J. Bloino, G. Zheng, J. L. Sonnenberg, M. Hada, M. Ehara, K. Toyota, R. Fukuda, J. Hasegawa, M. Ishida, T. Nakajima, Y. Honda, O. Kitao, H. Nakai, T. Vreven, J. A. Montgomery, Jr., J. E. Peralta, F. Ogliaro, M. Bearpark, J. J. Heyd, E. Brothers, K. N. Kudin, V. N. Staroverov, R. Kobayashi, J. Normand, K. Raghavachari, A. Rendell, J. C. Burant, S. S. Iyengar, J. Tomasi, M. Cossi, N. Rega, J. M. Millam, M. Klene, J. E. Knox, J. B. Cross, V. Bakken, C. Adamo, J. Jaramillo, R. Gomperts, R. E. Stratmann, O. Yazyev, A. J. Austin, R. Cammi, C. Pomelli, J. W. Ochterski, R. L. Martin, K. Morokuma, V. G. Zakrzewski, G. A. Voth, P. Salvador, J. J. Dannenberg, S. Dapprich, A. D. Daniels, Ö. Farkas, J. B. Foresman, J. V. Ortiz, J. Cioslowski, and D. J. Fox, *Gaussian, Inc., Wallingford CT, 2009*.
- (157) Galbraith, J. M.; Iii, H. F. S. *J. Chem. Phys.* **1996**, *105* (2), 862–864.
- (158) Kouroulis, K. N.; Hadjikakou, S. K.; Kourkoumelis, N.; Kubicki, M.; Male, L.; Hursthouse, M.; Skoulika, S.; Metsios, A. K.; Tyurin, V. Y.; Dolganov, A. V.; Milaeva, E. R.; Hadjiliadis, N. *Dalton Trans.* **2009**, No. 47, 10446–10456.
- (159) Lee, D.; Furche, F.; Burke, K. *J. Phys. Chem. Lett.* **2010**, *1* (14), 2124–2129.
- (160) Patterson, E. V.; Cramer, C. J.; Truhlar, D. G. *J. Am. Chem. Soc.* **2001**, *123* (9), 2025–2031.

- (161) Kim, M.-C.; Sim, E.; Burke, K. *Phys. Rev. Lett.* **2013**, *111* (7).
- (162) Rösch, N.; Trickey, S. B. *J. Chem. Phys.* **1997**, *106* (21), 8940–8941.
- (163) Keith, J. A.; Carter, E. A. *J. Chem. Theory Comput.* **2012**, *8* (9), 3187–3206.
- (164) Cramer, C. J. *J. Chem. Soc. Perkin Trans. 2* **1999**, No. 11, 2273–2283.
- (165) Beller, M.; Seayad, J.; Tillack, A.; Jiao, H. *Angew. Chem. Int. Ed.* **2004**, *43* (26), 3368–3398.
- (166) Müller, T. E.; Hultsch, K. C.; Yus, M.; Foubelo, F.; Tada, M. *Chem. Rev.* **2008**, *108* (9), 3795–3892.
- (167) Hintermann, L. In *C-X Bond Formation*; Vigalok, A., Ed.; Topics in Organometallic Chemistry; Springer Berlin Heidelberg, 2010; pp 123–155.
- (168) Utsunomiya, M.; Kuwano, R.; Kawatsura, M.; Hartwig, J. F. *J. Am. Chem. Soc.* **2003**, *125* (19), 5608–5609.
- (169) Utsunomiya, M.; Hartwig, J. F. *J. Am. Chem. Soc.* **2004**, *126* (9), 2702–2703.
- (170) Dong, G.; Teo, P.; Wickens, Z. K.; Grubbs, R. H. *Science* **2011**, *333* (6049), 1609–1612.
- (171) Hamilton, D. S.; Nicewicz, D. A. *J. Am. Chem. Soc.* **2012**, *134* (45), 18577–18580.
- (172) Perkowski, A. J.; Nicewicz, D. A. *J. Am. Chem. Soc.* **2013**, *135* (28), 10334–10337.
- (173) Nguyen, T. M.; Nicewicz, D. A. *J. Am. Chem. Soc.* **2013**, *135* (26), 9588–9591.
- (174) Nguyen, T. M.; Manohar, N.; Nicewicz, D. A. *Angew. Chem. Int. Ed.* **2014**, *53* (24), 6198–6201.
- (175) Wilger, D. J.; Grandjean, J.-M. M.; Lammert, T. R.; Nicewicz, D. A. *Nat. Chem.* **2014**, *6* (8), 720–726.
- (176) Wilger, D. J.; Gesmundo, N. J.; Nicewicz, D. A. *Chem. Sci.* **2013**, *4* (8), 3160–3165.
- (177) Prier, C. K.; Rankic, D. A.; MacMillan, D. W. C. *Chem. Rev.* **2013**, *113* (7), 5322–5363.
- (178) Fukuzumi, S.; Kotani, H.; Ohkubo, K.; Ogo, S.; Tkachenko, N. V.; Lemmetyinen, H. *J. Am. Chem. Soc.* **2004**, *126* (6), 1600–1601.
- (179) Kotani, H.; Ohkubo, K.; Fukuzumi, S. *J. Am. Chem. Soc.* **2004**, *126* (49), 15999–16006.
- (180) Hasobe, T.; Hattori, S.; Kotani, H.; Ohkubo, K.; Hosomizu, K.; Imahori, H.; Kamat, P. V.; Fukuzumi, S. *Org. Lett.* **2004**, *6* (18), 3103–3106.
- (181) Ohkubo, K.; Kotani, H.; Fukuzumi, S. *Chem. Commun.* **2005**, No. 36, 4520–4522.

- (182) Ohkubo, K.; Nanjo, T.; Fukuzumi, S. *Bull. Chem. Soc. Jpn.* **2006**, *79* (10), 1489–1500.
- (183) Fukuzumi, S. *Pure Appl. Chem.* **2007**, *79* (6), 981–991.
- (184) Ohkubo, K.; Iwata, R.; Yanagimoto, T.; Fukuzumi, S. *Chem. Commun.* **2007**, No. 30, 3139–3141.
- (185) Fukuzumi, S.; Kotani, H.; Ohkubo, K. *Phys. Chem. Chem. Phys.* **2008**, *10* (33), 5159–5162.
- (186) Ohkubo, K.; Mizushima, K.; Iwata, R.; Souma, K.; Suzuki, N.; Fukuzumi, S. *Chem. Commun.* **2010**, *46* (4), 601–603.
- (187) Ohkubo, K.; Fujimoto, A.; Fukuzumi, S. *Chem. Commun.* **2011**, *47* (30), 8515–8517.
- (188) Hoshino, M.; Uekusa, H.; Tomita, A.; Koshihara, S.; Sato, T.; Nozawa, S.; Adachi, S.; Ohkubo, K.; Kotani, H.; Fukuzumi, S. *J. Am. Chem. Soc.* **2012**, *134* (10), 4569–4572.
- (189) Verhoeven, J. W.; Ramesdonk, H. J. van; Zhang, H.; Groeneveld, M. M.; Benniston, A. C.; Harriman, A. *Int. J. Photoenergy* **2005**, *7* (2), 103–108.
- (190) Benniston, A. C.; Harriman, A.; Verhoeven, J. W. *Phys. Chem. Chem. Phys.* **2008**, *10* (33), 5156–5156.
- (191) Campbell, J. M.; Xu, H.-C.; Moeller, K. D. *J. Am. Chem. Soc.* **2012**, *134* (44), 18338–18344.
- (192) Smith, J. A.; Moeller, K. D. *Org. Lett.* **2013**, *15* (22), 5818–5821.
- (193) Huang, Y.; Moeller, K. D. *Tetrahedron* **2006**, *62* (27), 6536–6550.
- (194) Tang, F.; Chen, C.; Moeller, K. *Synthesis* **2007**, *2007* (21), 3411–3420.
- (195) Grandjean, J.-M. M.; Nicewicz, D. A. *Angew. Chem. Int. Ed.* **2013**, *52* (14), 3967–3971.
- (196) Zeller, M. A.; Riener, M.; Nicewicz, D. A. *Org. Lett.* **2014**, *16* (18), 4810–4813.
- (197) Mizuno, K.; Tamai, T.; Nishiyama, T.; Tani, K.; Sawasaki, M.; Otsuji, Y. *Angew. Chem. Int. Ed. Engl.* **1994**, *33* (20), 2113–2115.
- (198) Asaoka, S.; Kitazawa, T.; Wada, T.; Inoue, Y. *J. Am. Chem. Soc.* **1999**, *121* (37), 8486–8498.
- (199) Asaoka, S.; Wada, T.; Inoue, Y. *J. Am. Chem. Soc.* **2003**, *125* (10), 3008–3027.
- (200) Nishiyama, Y.; Kaneda, M.; Saito, R.; Mori, T.; Wada, T.; Inoue, Y. *J. Am. Chem. Soc.* **2004**, *126* (21), 6568–6569.

- (201) Nishiyama, Y.; Kaneda, M.; Asaoka, S.; Saito, R.; Mori, T.; Wada, T.; Inoue, Y. *J. Phys. Chem. A* **2007**, *111* (51), 13432–13440.
- (202) Nishiyama, Y.; Wada, T.; Asaoka, S.; Mori, T.; McCarty, T. A.; Kraut, N. D.; Bright, F. V.; Inoue, Y. *J. Am. Chem. Soc.* **2008**, *130* (24), 7526–7527.
- (203) Fukuhara, G.; Mori, T.; Inoue, Y. *J. Org. Chem.* **2009**, *74* (17), 6714–6727.
- (204) Larsen, A. G.; Holm, A. H.; Roberson, M.; Daasbjerg, K. *J. Am. Chem. Soc.* **2001**, *123* (8), 1723–1729.
- (205) Griesbeck, A. G.; Cho, M. *Org. Lett.* **2007**, *9* (4), 611–613.
- (206) Kavarnos, G. J.; Turro, N. J. *Chem. Rev.* **1986**, *86* (2), 401–449.
- (207) Bäckström, H. L. J.; Sandros, K.; Lindgren, J.-E.; Varde, E.; Westin, G. *Acta Chem. Scand.* **1960**, *14*, 48–62.
- (208) Haynes, W. M.; Lide, D. R.; Bruno, T. J. *CRC handbook of chemistry and physics a ready-reference book of chemical and physical data: 2013-2014*; CRC Press: Boca Raton (Fla.); London; New York, 2013.
- (209) Kuruvilla, E.; Ramaiah, D. *J. Phys. Chem. B* **2007**, *111* (23), 6549–6556.
- (210) Jones II, G.; Farahat, M. S.; Greenfield, S. R.; Gosztola, D. J.; Wasielewski, M. R. *Chem. Phys. Lett.* **1994**, *229* (1–2), 40–46.
- (211) Andrews, L.; Harvey, J. A.; Kelsall, B. J.; Duffey, D. C. *J. Am. Chem. Soc.* **1981**, *103* (21), 6415–6422.
- (212) Johnston, L. J.; Schepp, N. P. *J. Am. Chem. Soc.* **1993**, *115* (15), 6564–6571.
- (213) Schepp, N. P.; Johnston, L. J. *J. Am. Chem. Soc.* **1994**, *116* (15), 6895–6903.
- (214) Johnston, L. J.; Schepp, N. P. *Pure Appl. Chem.* **1995**, *67* (1), 71–78.
- (215) Schepp, N. P.; Johnston, L. J. *J. Am. Chem. Soc.* **1996**, *118* (12), 2872–2881.
- (216) Schepp, N. P.; Shukla, D.; Sarker, H.; Bauld, N. L.; Johnston, L. J. *J. Am. Chem. Soc.* **1997**, *119* (43), 10325–10334.
- (217) Shida, T. *Electronic Absorption Spectra of Radical Ions*; Elsevier: Amsterdam, 1988.
- (218) Benesi, H. A.; Hildebrand, J. H. *J. Am. Chem. Soc.* **1949**, *71* (8), 2703–2707.
- (219) Foster, R. *Organic Charge-Transfer Complexes*; Academic Press Inc. Ltd.: London, 1969.
- (220) Bunting, J. W.; Luscher, M. A. *Can. J. Chem.* **1988**, *66* (10), 2532–2539.

- (221) Luo, Y.-R. *Handbook of Bond Dissociation Energies in Organic Compounds*; CRC Press: Boca Raton, FL, 2003.
- (222) Antonello, S.; Daasbjerg, K.; Jensen, H.; Taddei, F.; Maran, F. *J. Am. Chem. Soc.* **2003**, *125* (48), 14905–14916.
- (223) Meneses, A. B.; Antonello, S.; Arévalo, M. C.; González, C. C.; Sharma, J.; Walleto, A. N.; Workentin, M. S.; Maran, F. *Chem. - Eur. J.* **2007**, *13* (28), 7983–7995.
- (224) Giordan, J.; Bock, H. *Chem. Ber.* **1982**, *115* (7), 2548–2559.
- (225) Töteberg-Kaulen, S.; Steckhan, E. *Tetrahedron* **1988**, *44* (14), 4389–4397.
- (226) Lakkaraju, P.; Roth, H. *J. Chem. Soc. Perkin Trans. 2* **1998**, No. 5, 1119–1122.
- (227) Wallace, W. L.; Van Duyne, R. P.; Lewis, F. D. *J. Am. Chem. Soc.* **1976**, *98* (17), 5319–5326.
- (228) Dénès, F.; Pichowicz, M.; Povie, G.; Renaud, P. *Chem. Rev.* **2014**, *114* (5), 2587–2693.
- (229) Armstrong, D. A.; Sun, Q.; Schuler, R. H. *J. Phys. Chem.* **1996**, *100* (23), 9892–9899.
- (230) Ito, O.; Matsuda, M. *J. Am. Chem. Soc.* **1979**, *101* (7), 1815–1819.
- (231) Ito, O. *Res. Chem. Intermed.* **1995**, *21* (1), 69–93.
- (232) Clarke, J. L.; Kastrati, I.; Johnston, L. J.; Thatcher, G. R. *Can. J. Chem.* **2006**, *84* (4), 709–719.
- (233) Scott, T. W.; Liu, S. N. *J. Phys. Chem.* **1989**, *93* (4), 1393–1396.
- (234) Thyron, F. C. *J. Phys. Chem.* **1973**, *77* (12), 1478–1482.
- (235) Sattler, W.; Ener, M. E.; Blakemore, J. D.; Rachford, A. A.; LaBeaume, P. J.; Thackeray, J. W.; Cameron, J. F.; Winkler, J. R.; Gray, H. B. *J. Am. Chem. Soc.* **2013**, *135* (29), 10614–10617.
- (236) Koelle, U.; Infelta, P. P.; Graetzel, M. *Inorg. Chem.* **1988**, *27* (5), 879–883.
- (237) Zheng, S.; Berto, T. C.; Dahl, E. W.; Hoffman, M. B.; Speelman, A. L.; Lehnert, N. *J. Am. Chem. Soc.* **2013**, *135* (13), 4902–4905.
- (238) Riyad, Y. M.; Naumov, S.; Hermann, R.; Brede, O. *Phys. Chem. Chem. Phys.* **2006**, *8* (14), 1697–1706.
- (239) Ito, O.; Matsuda, M. *J. Am. Chem. Soc.* **1979**, *101* (19), 5732–5735.
- (240) Linschitz, H.; Sarkanen, K. *J. Am. Chem. Soc.* **1958**, *80* (18), 4826–4832.

- (241) Zwicker, E. F.; Grossweiner, L. I. *J. Phys. Chem.* **1963**, *67* (3), 549–555.
- (242) Closs, G. L.; Rabinow, B. E. *J. Am. Chem. Soc.* **1976**, *98* (25), 8190–8198.
- (243) Anslyn, E. V. *Modern physical organic chemistry*; University Science: Sausalito, CA, 2006.
- (244) Arnold, D. R.; Chan, M. S.; McManus, K. A. *Can. J. Chem.* **1996**, *74* (11), 2143–2166.
- (245) Bally, T.; Sastry, G. N. *J. Phys. Chem. A* **1997**, *101* (43), 7923–7925.
- (246) Braïda, B.; Hiberty, P. C.; Savin, A. *J. Phys. Chem. A* **1998**, *102* (40), 7872–7877.
- (247) Sodupe, M.; Bertran, J.; Rodríguez-Santiago, L.; Baerends, E. J. *J. Phys. Chem. A* **1999**, *103* (1), 166–170.
- (248) Herbertz, T.; Roth, H. D. *J. Am. Chem. Soc.* **1998**, *120* (46), 11904–11911.
- (249) Zhang, H.-Y.; Sun, Y.-M.; Wang, X.-L. *J. Org. Chem.* **2002**, *67* (8), 2709–2712.
- (250) Valley, N. A.; Wiest, O. *J. Org. Chem.* **2007**, *72* (2), 559–566.
- (251) Um, J. M.; Gutierrez, O.; Schoenebeck, F.; Houk, K. N.; MacMillan, D. W. C. *J. Am. Chem. Soc.* **2010**, *132* (17), 6001–6005.
- (252) Bagnol, L.; Horner, J. H.; Newcomb, M. *Org. Lett.* **2003**, *5* (26), 5055–5058.
- (253) Ditchfield, R.; Hehre, W. J.; Pople, J. A. *J. Chem. Phys.* **1971**, *54* (2), 724–728.
- (254) Hehre, W. J.; Ditchfield, R.; Pople, J. A. *J. Chem. Phys.* **1972**, *56* (5), 2257–2261.
- (255) Franz, J. A.; Suleman, N. K.; Alnajjar, M. S. *J. Org. Chem.* **1986**, *51* (1), 19–25.
- (256) Franz, J. A.; Bushaw, B. A.; Alnajjar, M. S. *J. Am. Chem. Soc.* **1989**, *111* (1), 268–275.
- (257) Bunting, J. W.; Chew, V. S.; Abhyankar, S. B.; Goda, Y. *Can. J. Chem.* **1984**, *62* (2), 351–354.
- (258) Ackmann, A. J.; Fréchet, J. M. J. *Chem. Commun.* **1996**, No. 5, 605–606.
- (259) Zhou, D.; Khatmullin, R.; Walpita, J.; Miller, N. A.; Luk, H. L.; Vyas, S.; Hadad, C. M.; Glusac, K. D. *J. Am. Chem. Soc.* **2012**, *134* (28), 11301–11303.
- (260) Hagel, M.; Liu, J.; Muth, O.; Estevez Rivera, H. J.; Schwake, E.; Sripanom, L.; Henkel, G.; Dyker, G. *Eur. J. Org. Chem.* **2007**, *2007* (21), 3573–3582.
- (261) Lyons, T. W.; Sanford, M. S. *Chem. Rev.* **2010**, *110* (2), 1147–1169.

- (262) Shul'Pin, G. B. In *Transition Metals for Organic Synthesis*; Beller, M., Bolm, C., Eds.; Wiley-VCH Verlag GmbH, 2004; pp 215–241.
- (263) Wolfe, J. P.; Wagaw, S.; Marcoux, J.-F.; Buchwald, S. L. *Acc. Chem. Res.* **1998**, *31* (12), 805–818.
- (264) Hartwig, J. F. *Acc. Chem. Res.* **1998**, *31* (12), 852–860.
- (265) Lam, P. Y. S.; Vincent, G.; Clark, C. G.; Deudon, S.; Jadhav, P. K. *Tetrahedron Lett.* **2001**, *42* (20), 3415–3418.
- (266) Sanjeeva Rao, K.; Wu, T.-S. *Tetrahedron* **2012**, *68* (38), 7735–7754.
- (267) Tsang, W. C. P.; Munday, R. H.; Brasche, G.; Zheng, N.; Buchwald, S. L. *J. Org. Chem.* **2008**, *73* (19), 7603–7610.
- (268) Tran, L. D.; Roane, J.; Daugulis, O. *Angew. Chem. Int. Ed.* **2013**, *52* (23), 6043–6046.
- (269) Xu, H.; Qiao, X.; Yang, S.; Shen, Z. *J. Org. Chem.* **2014**, *79* (10), 4414–4422.
- (270) Matsubara, T.; Asako, S.; Ilies, L.; Nakamura, E. *J. Am. Chem. Soc.* **2014**, *136* (2), 646–649.
- (271) Allen, L. J.; Cabrera, P. J.; Lee, M.; Sanford, M. S. *J. Am. Chem. Soc.* **2014**, *136* (15), 5607–5610.
- (272) Kim, H. J.; Kim, J.; Cho, S. H.; Chang, S. *J. Am. Chem. Soc.* **2011**, *133* (41), 16382–16385.
- (273) Kantak, A. A.; Potavathri, S.; Barham, R. A.; Romano, K. M.; DeBoef, B. *J. Am. Chem. Soc.* **2011**, *133* (49), 19960–19965.
- (274) Boursalian, G. B.; Ngai, M.-Y.; Hojczyk, K. N.; Ritter, T. *J. Am. Chem. Soc.* **2013**, *135* (36), 13278–13281.
- (275) Foo, K.; Sella, E.; Thomé, I.; Eastgate, M. D.; Baran, P. S. *J. Am. Chem. Soc.* **2014**, *136* (14), 5279–5282.
- (276) Kawakami, T.; Murakami, K.; Itami, K. *J. Am. Chem. Soc.* **2015**, *137* (7), 2460–2463.
- (277) Narayanam, J. M. R.; Stephenson, C. R. J. *Chem Soc Rev* **2011**, *40* (1), 102–113.
- (278) Nicewicz, D. A.; Nguyen, T. M. *ACS Catal.* **2014**, *4* (1), 355–360.
- (279) Qin, Q.; Yu, S. *Org. Lett.* **2014**, *16* (13), 3504–3507.
- (280) Brachet, E.; Ghosh, T.; Ghosh, I.; König, B. *Chem. Sci.* **2015**, *6* (2), 987–992.
- (281) Pandey, G.; Sridhar, M.; Bhalerao, U. T. *Tetrahedron Lett.* **1990**, *31* (37), 5373–5376.

- (282) Morofuji, T.; Shimizu, A.; Yoshida, J. *J. Am. Chem. Soc.* **2013**, *135* (13), 5000–5003.
- (283) Morofuji, T.; Shimizu, A.; Yoshida, J. *J. Am. Chem. Soc.* **2014**, *136* (12), 4496–4499.
- (284) Morofuji, T.; Shimizu, A.; Yoshida, J. *Chem. – Eur. J.* **2015**, *21* (8), 3211–3214.
- (285) Ohkubo, K.; Mizushima, K.; Iwata, R.; Fukuzumi, S. *Chem. Sci.* **2011**, *2* (4), 715–722.
- (286) Ohkubo, K.; Fujimoto, A.; Fukuzumi, S. *J. Phys. Chem. A* **2013**, *117* (41), 10719–10725.
- (287) Hess, W. P.; Tully, F. P. *J. Phys. Chem.* **1989**, *93* (5), 1944–1947.
- (288) Pan, X.-M.; Schuchmann, M. N.; von Sonntag, C. *J. Chem. Soc. Perkin Trans. 2* **1993**, No. 3, 289–297.
- (289) Baur, J. E.; Wang, S.; Brandt, M. C. *Anal. Chem.* **1996**, *68* (21), 3815–3821.
- (290) Schmittel, M.; Burghart, A. *Angew. Chem. Int. Ed. Engl.* **1997**, *36* (23), 2550–2589.
- (291) Bordwell, F. G.; Cheng, J. P. *J. Am. Chem. Soc.* **1989**, *111* (5), 1792–1795.
- (292) Vitaku, E.; Smith, D. T.; Njardarson, J. T. *J. Med. Chem.* **2014**, *57* (24), 10257–10274.
- (293) Ritchie, T. J.; Macdonald, S. J. F.; Peace, S.; Pickett, S. D.; Luscombe, C. N. *MedChemComm* **2012**, *3* (9), 1062–1069.
- (294) Vo, G. D.; Hartwig, J. F. *J. Am. Chem. Soc.* **2009**, *131* (31), 11049–11061.
- (295) DelPesco, T. W. U.S. Patent 4031106, June 21, 1977. 4031106.
- (296) Del Pesco, T. W. U.S. Patent 4001260, January 4, 1977. 4001260.
- (297) Romero, N. A.; Margrey, K. A.; Tay, N. E.; Nicewicz, D. A. *Science* **2015**, *349* (6254), 1326–1330.
- (298) Mori, Y.; Sakaguchi, Y.; Hayashi, H. *J. Phys. Chem. A* **2000**, *104* (21), 4896–4905.
- (299) Marx, L.; Schöllhorn, B. *New J. Chem.* **2006**, *30* (3), 430–434.
- (300) Semmelhack, M. F.; Chou, C. S.; Cortes, D. A. *J. Am. Chem. Soc.* **1983**, *105* (13), 4492–4494.
- (301) Warren, J. J.; Tronic, T. A.; Mayer, J. M. *Chem. Rev.* **2010**, *110* (12), 6961–7001.
- (302) Sawyer, D. T.; Gibian, M. J.; Morrison, M. M.; Seo, E. T. *J. Am. Chem. Soc.* **1978**, *100* (2), 627–628.
- (303) Goolsby, A. D.; Sawyer, D. T. *Anal. Chem.* **1968**, *40* (1), 83–86.

- (304) Andrieux, C. P.; Hapiot, P.; Saveant, J. M. *J. Am. Chem. Soc.* **1987**, *109* (12), 3768–3775.
- (305) Hansen, L. D.; Baca, E. J.; Scheiner, P. *J. Heterocycl. Chem.* **1970**, *7* (4), 991–996.
- (306) Catalan, J.; Claramunt, R. M.; Elguero, J.; Laynez, J.; Menendez, M.; Anvia, F.; Quian, J. H.; Taagepera, M.; Taft, R. W. *J. Am. Chem. Soc.* **1988**, *110* (13), 4105–4111.
- (307) Mader, E. A.; Manner, V. W.; Markle, T. F.; Wu, A.; Franz, J. A.; Mayer, J. M. *J. Am. Chem. Soc.* **2009**, *131* (12), 4335–4345.
- (308) Amorati, R.; Pedulli, G. F.; Pratt, D. A.; Valgimigli, L. *Chem. Commun.* **2010**, *46* (28), 5139–5141.
- (309) Haidasz, E. A.; Meng, D.; Amorati, R.; Baschieri, A.; Ingold, K. U.; Valgimigli, L.; Pratt, D. A. *J. Am. Chem. Soc.* **2016**, *138* (16), 5290–5298.
- (310) Benniston, A. C.; Elliott, K. J.; Harrington, R. W.; Clegg, W. *Eur. J. Org. Chem.* **2009**, *2009* (2), 253–258.
- (311) Decker, H.; Schenk, C. *Berichte Dtsch. Chem. Ges.* **1906**, *39* (1), 748–752.
- (312) Raskosova, A.; Stößer, R.; Abraham, W. *Chem. Commun.* **2013**, *49* (38), 3964–3966.
- (313) Blackmond, D. G. *Angew. Chem. Int. Ed.* **2005**, *44* (28), 4302–4320.
- (314) Baxter, R. D.; Sale, D.; Engle, K. M.; Yu, J.-Q.; Blackmond, D. G. *J. Am. Chem. Soc.* **2012**, *134* (10), 4600–4606.
- (315) Wadt, W. R.; Hay, P. J. *J. Chem. Phys.* **1985**, *82* (1), 284–298.
- (316) Hay, P. J.; Wadt, W. R. *J. Chem. Phys.* **1985**, *82* (1), 270–283.
- (317) Hay, P. J.; Wadt, W. R. *J. Chem. Phys.* **1985**, *82* (1), 299–310.
- (318) Hamilton, D. S.; Nicewicz, D. A. *J. Am. Chem. Soc.* **2012**, *134* (45), 18577–18580.
- (319) Wilger, D. J.; Gesmundo, N. J.; Nicewicz, D. A. *Chem. Sci.* **2013**, *4* (8), 3160–3165.
- (320) Kuruvilla, E.; Ramaiah, D. *J. Phys. Chem. B* **2007**, *111* (23), 6549–6556.
- (321) Seiders, J. R.; Wang, L.; Floreancig, P. E. *J. Am. Chem. Soc.* **2003**, *125* (9), 2406–2407.
- (322) Horn, M.; Schappele, L. H.; Lang-Wittkowski, G.; Mayr, H.; Ofial, A. R. *Chem. – Eur. J.* **2013**, *19* (1), 249–263.
- (323) Benniston, A. C.; Harriman, A.; Li, P.; Rostron, J. P.; van Ramesdonk, H. J.; Groeneveld, M. M.; Zhang, H.; Verhoeven, J. W. *J. Am. Chem. Soc.* **2005**, *127* (46), 16054–16064.

- (324) Knauf, R. R.; Brennaman, M. K.; Alibabaei, L.; Norris, M. R.; Dempsey, J. L. *J. Phys. Chem. C* **2013**, *117* (48), 25259–25268.
- (325) Fukuzumi, S.; Kotani, H.; Ohkubo, K.; Ogo, S.; Tkachenko, N. V.; Lemmetyinen, H. *J. Am. Chem. Soc.* **2004**, *126* (6), 1600–1601.
- (326) Fukuzumi, S.; Kotani, H.; Ohkubo, K. *Phys. Chem. Chem. Phys.* **2008**, *10* (33), 5159.
- (327) Koelle, U.; Infelta, P. P.; Graetzel, M. *Inorg. Chem.* **1988**, *27* (5), 879–883.
- (328) Sattler, W.; Ener, M. E.; Blakemore, J. D.; Rachford, A. A.; LaBeaume, P. J.; Thackeray, J. W.; Cameron, J. F.; Winkler, J. R.; Gray, H. B. *J. Am. Chem. Soc.* **2013**, *135* (29), 10614–10617.
- (329) Riyad, Y. M.; Naumov, S.; Hermann, R.; Brede, O. *Phys. Chem. Chem. Phys.* **2006**, *8* (14), 1697.
- (330) Nash, C. P. *J. Phys. Chem.* **1960**, *64* (7), 950–953.
- (331) Johnson, R. C. *J. Chem. Educ.* **1970**, *47* (10), 702.
- (332) Kirk, A. D.; Namasivayam, C. *Anal. Chem.* **1983**, *55* (14), 2428–2429.
- (333) Demas, J. N.; Bowman, W. D.; Zalewski, E. F.; Velapoldi, R. A. *J. Phys. Chem.* **1981**, *85* (19), 2766–2771.
- (334) *Gaussian 09, Revision D.01*, M. J. Frisch, G. W. Trucks, H. B. Schlegel, G. E. Scuseria, M. A. Robb, J. R. Cheeseman, G. Scalmani, V. Barone, B. Mennucci, G. A. Petersson, H. Nakatsuji, M. Caricato, X. Li, H. P. Hratchian, A. F. Izmaylov, J. Bloino, G. Zheng, J. L. Sonnenberg, M. Hada, M. Ehara, K. Toyota, R. Fukuda, J. Hasegawa, M. Ishida, T. Nakajima, Y. Honda, O. Kitao, H. Nakai, T. Vreven, J. A. Montgomery, Jr., J. E. Peralta, F. Ogliaro, M. Bearpark, J. J. Heyd, E. Brothers, K. N. Kudin, V. N. Staroverov, R. Kobayashi, J. Normand, K. Raghavachari, A. Rendell, J. C. Burant, S. S. Iyengar, J. Tomasi, M. Cossi, N. Rega, J. M. Millam, M. Klene, J. E. Knox, J. B. Cross, V. Bakken, C. Adamo, J. Jaramillo, R. Gomperts, R. E. Stratmann, O. Yazyev, A. J. Austin, R. Cammi, C. Pomelli, J. W. Ochterski, R. L. Martin, K. Morokuma, V. G. Zakrzewski, G. A. Voth, P. Salvador, J. J. Dannenberg, S. Dapprich, A. D. Daniels, Ö. Farkas, J. B. Foresman, J. V. Ortiz, J. Cioslowski, and D. J. Fox, *Gaussian, Inc., Wallingford CT, 2009*.
- (335) Becke, A. D. *J. Chem. Phys.* **1993**, *98* (7), 5648–5652.
- (336) Lee, C.; Yang, W.; Parr, R. G. *Phys. Rev. B* **1988**, *37* (2), 785–789.
- (337) Krishnan, R.; Binkley, J. S.; Seeger, R.; Pople, J. A. *J. Chem. Phys.* **1980**, *72* (1), 650–654.
- (338) McLean, A. D.; Chandler, G. S. *J. Chem. Phys.* **1980**, *72* (10), 5639–5648.

- (339) Tomasi, J.; Mennucci, B.; Cammi, R. *Chem. Rev.* **2005**, *105* (8), 2999–3094.
- (340) Legault, C. Y. *CYLview, 1.0b; Université de Sherbrooke, 2009* (<http://www.cylview.org>).
- (341) Seganish, W. M.; DeShong, P. J. *Org. Chem.* **2004**, *69* (20), 6790–6795.
- (342) Baker, M. S.; Phillips, S. T. *J. Am. Chem. Soc.* **2011**, *133* (14), 5170–5173.
- (343) Bartoli, G.; Bosco, M.; Locatelli, M.; Marcantoni, E.; Melchiorre, P.; Sambri, L. *Org. Lett.* **2005**, *7* (3), 427–430.
- (344) Ullah, E.; McNulty, J.; Robertson, A. *Eur. J. Org. Chem.* **2012**, *2012* (11), 2127–2131.
- (345) Ben-Yahia, A.; Naas, M.; El Kazzouli, S.; Essassi, E. M.; Guillaumet, G. *Eur. J. Org. Chem.* **2012**, *2012* (36), 7075–7081.
- (346) Bodnar, B. S.; Vogt, P. F. *J. Org. Chem.* **2009**, *74* (6), 2598–2600.
- (347) Dey, S.; Garner, P. *J. Org. Chem.* **2000**, *65* (22), 7697–7699.
- (348) Abdo, M.-R.; Joseph, P.; Boigegrain, R.-A.; Liautard, J.-P.; Montero, J.-L.; Köhler, S.; Winum, J.-Y. *Bioorg. Med. Chem.* **2007**, *15* (13), 4427–4433.
- (349) Taylor, C. M.; De Silva, S. T. *J. Org. Chem.* **2011**, *76* (14), 5703–5708.
- (350) Chevallier, F.; Halauko, Y. S.; Pecceu, C.; Nassar, I. F.; Dam, T. U.; Roisnel, T.; Matulis, V. E.; Ivashkevich, O. A.; Mongin, F. *Org. Biomol. Chem.* **2011**, *9* (12), 4671–4684.
- (351) Teo, Y.-C.; Yong, F.-F.; Poh, C.-Y.; Yan, Y.-K.; Chua, G.-L. *Chem. Commun.* **2009**, No. 41, 6258–6260.
- (352) DeAngelis, A.; Wang, D.-H.; Buchwald, S. L. *Angew. Chem. Int. Ed.* **2013**, *52* (12), 3434–3437.
- (353) Schneider, Y.; Prévost, J.; Gobin, M.; Legault, C. Y. *Org. Lett.* **2014**, *16* (2), 596–599.
- (354) Zhu, L.; Li, G.; Luo, L.; Guo, P.; Lan, J.; You, J. *J. Org. Chem.* **2009**, *74* (5), 2200–2202.
- (355) Furuta, Y.; Komatsu, K.; Kaya, A.; Takahata, S.; Tabata, Y. Topical Liquid Agent for the Treatment of Dermatophytosis. US2014030209 (A1), January 30, 2014.
- (356) Kumar, A. S.; Ghule, V. D.; Subrahmanyam, S.; Sahoo, A. K. *Chem. – Eur. J.* **2013**, *19* (2), 509–518.
- (357) Onaka, T.; Umemoto, H.; Miki, Y.; Nakamura, A.; Maegawa, T. *J. Org. Chem.* **2014**, *79* (14), 6703–6707.
- (358) Gaydou, M.; Echavarren, A. M. *Angew. Chem. Int. Ed.* **2013**, *52* (50), 13468–13471.

- (359) Kommu, N.; Ghule, V. D.; Kumar, A. S.; Sahoo, A. K. *Chem. – Asian J.* **2014**, *9* (1), 166–178.
- (360) Xu, Z.-L.; Li, H.-X.; Ren, Z.-G.; Du, W.-Y.; Xu, W.-C.; Lang, J.-P. *Tetrahedron* **2011**, *67* (29), 5282–5288.
- (361) Gann, A. W.; Amoroso, J. W.; Einck, V. J.; Rice, W. P.; Chambers, J. J.; Schnarr, N. A. *Org. Lett.* **2014**, *16* (7), 2003–2005.
- (362) Cho, C. S.; Patel, D. B. *Tetrahedron* **2006**, *62* (26), 6388–6391.
- (363) Yang, K.; Qiu, Y.; Li, Z.; Wang, Z.; Jiang, S. *J. Org. Chem.* **2011**, *76* (9), 3151–3159.
- (364) Wentzel, M. T.; Hewgley, J. B.; Kamble, R. M.; Wall, P. D.; Kozlowski, M. C. *Adv. Synth. Catal.* **2009**, *351* (6), 931–937.
- (365) Collman, J. P.; Zhong, M. *Org. Lett.* **2000**, *2* (9), 1233–1236.
- (366) Shimizu, Y.; Morimoto, H.; Zhang, M.; Ohshima, T. *Angew. Chem. Int. Ed.* **2012**, *51* (34), 8564–8567.
- (367) Nojiri, A.; Kumagai, N.; Shibasaki, M. *Angew. Chem. Int. Ed.* **2012**, *51* (9), 2137–2141.
- (368) Rahaim, R. J.; Maleczka, R. E. *Org. Lett.* **2005**, *7* (22), 5087–5090.
- (369) Macías, F. A.; Marín, D.; Oliveros-Bastidas, A.; Chinchilla, D.; Simonet, A. M.; Molinillo, J. M. G. *J. Agric. Food Chem.* **2006**, *54* (4), 991–1000.
- (370) Yao, L.; Zhou, Q.; Han, W.; Wei, S. *Eur. J. Org. Chem.* **2012**, *2012* (35), 6856–6860.
- (371) Liu, H.-J.; Hung, S.-F.; Chen, C.-L.; Lin, M.-H. *Tetrahedron* **2013**, *69* (19), 3907–3912.